

Experimental investigation and extended simulation of turbocharger non-adiabatic performance

Vom Fachbereich Maschinenbau
der Universität Hannover
zur Erlangung des akademischen Grades
Doktor-Ingenieur
genehmigte Dissertation

von

MSc Eng. Sameh Shaaban
geboren am 01.02.1970 in Kairo, Ägypten

2004

Stichworte für die Dokumentation:

Turbolader, diabatisches Verhalten, Simulation, Radialverdichter, radiale Turbine

Key words:

Turbocharger, non-adiabatic performance, simulation, centrifugal compressor, radial turbine, micro compressor.

1. Referent: Prof. Dr.-Ing. J. Seume
2. Referent: Prof. Dr.-Ing. H. Pucher
Tag der Promotion: 14.12.2004

Abstract

Turbocharging is nowadays considered the most commonly used method of engine supercharging. One of the important factors affecting the turbocharger performance is the heat transfer inside the turbocharger and from the turbocharger to the ambient. Heat transfer takes place due to the high temperature gradient between the turbine and the other components of the turbocharger as well as between the turbine and the ambient. This heat transfer causes underestimation of the measured compressor efficiency and overestimation of the turbine efficiency. This results in an inaccurate estimation of the compressor power and the turbine power. Therefore, the measured turbocharger performance maps are not accurate enough to simulate the turbocharger performance in engine simulation programs. Furthermore, the measured turbocharger performance maps provide the turbocharger performance for very few operating points in comparison with the engine operating points.

The present research work aims at investigating the turbocharger non-adiabatic performance. It also aims at extending the simulation of the turbocharger performance down to very low turbocharger rotational speeds as well as compressor operation in the fourth quadrant of the performance map. The turbocharger performance simulation is based on physically meaningful models for the aerodynamic performance of radial turbomachines. The aerodynamic performance of micro radial compressors is also experimentally investigated.

Three different turbochargers are investigated in the present research work. The experimental investigation is conducted using two different combustion chamber test rigs. Models and correlations for the estimation of the amount of heat transfer between the components of the turbocharger as well as between the turbine and the ambient are developed. Empirical loss correlations are obtained for micro radial compressors. Correlations for estimating the slip factor of radial compressors are also presented. A program for predicting the actual performance of micro radial compressors in low rotational speed operating range is introduced. A turbocharger performance simulation program is also presented. This program is designed to operate as a stand alone program or as two subroutines in the engine simulation programs.

Kurzfassung

Turboaufladung ist heutzutage die am häufigsten verwendete Methode für die Aufladung von Verbrennungsmotoren. Wärmeübertragung innerhalb des Turboladers und vom Turbolader an die Umgebung ist einer der wichtigen Faktoren, die das Turboladerverhalten beeinflussen. Sie findet wegen des hohen Temperaturgradienten zwischen der Turbine und den anderen Turboladerbestandteilen sowie zwischen der Turbine und der Umgebung statt. Diese Wärmeübertragung führt zur Unterschätzung des Verdichterwirkungsgrades und Überschätzung des Turbinenwirkungsgrades. Die berechnete Verdichter- bzw. Turbinenleistung mit Hilfe der gemessenen Kennfelder wird deswegen zu groß geschätzt. Das bedeutet, dass die gemessenen Kennfelder nicht genau genug für die Simulation des Turboladerverhaltens in Motorsimulationsprogrammen sind. Außerdem stellen die gemessenen Kennfelder das Turboladerverhalten nur für wenige Betriebspunkte dar.

Ziel der vorliegenden Arbeit ist, das diabate Verhalten des Turboladers zu untersuchen und die Simulation des Turboladers bis zu sehr niedrigen Drehzahlen zu erweitern. Die Simulation des Verdichters deckt auch den Verdichterbetrieb im vierten Quadranten des Kennfeldes ab. Die Erweiterung der Kennfelder basiert auf physikalisch sinnvollen Modellen für das aerodynamische Verhalten der Radialturbomaschinen. Das aerodynamische Verhalten der Mikroradialverdichter wird auch untersucht.

Drei Turbolader werden im Rahmen der vorliegenden Arbeit untersucht. Die experimentelle Untersuchung wird mit zwei unterschiedlichen Brennkammerprüfständen durchgeführt. Modelle bzw. empirische Korrelationen für die Bestimmung der Wärmeübertragung innerhalb des Turboladers und vom Turbolader an die Umgebung werden entwickelt. Des Weiteren werden empirische Korrelationen für die Bestimmung der aerodynamischen Verluste und des Minderleistungsfaktors erstellt. Ein Programm für die Vorhersage des Radialverdichterverhaltens im niedrigen Drehzahlbereich wird erstellt. Ein anderes Programm für die Erweiterung der gemessenen Kennfelder bis zu sehr niedrigen Drehzahlen wird erarbeitet. Dieses Programm dient sowohl als Stand-Alone Programm als auch als Subroutinen in Programmen zur Simulation des Motors.

Acknowledgment

The present research work is developed during my work as research assistance in the institute of turbomachinery (IfS), Hanover University. The research work was supervised by Prof. Dr.-Ing. J. Seume.

I would like to express my thanks and gratitude to Prof. Dr.-Ing. J. Seume for the continuous support, the helpful advice, and the valuable guidance throughout the present research work.

I thank Prof. Dr.-Ing. M. Rautenberg for the discussions during the research work. I also thank Prof. Dr.-Ing. H. Pucher and Prof. Dr.-Ing. J. Linnhoff for the support during the development of the "TC_2003" program. My thanks are also to Dr.-Ing. R. Baar, VW-company, for the support.

I would like to express my thanks and gratitude to Prof. Dr.-Ing. H. Heikal and Prof. Dr. Eng. A. Abdelhafiz for the continuous support during my study in Egypt. I would also like to thank Prof. Dr.-Ing. A. Mobarak for the information and discussions during his visit to Germany.

I thank all my colleagues in the institute of turbomachinery for the valuable discussions. My thanks are also to the technical staff of the institute of turbomachinery for the technical support during my research work.

Finally, I would like to express my special thanks to my family for the patience and encouragement.

Hanover, December 2004

Sameh Shaaban

Table of contents

Abstract	i
Kurzfassung	ii
Acknowledgment	iii
Table of contents	v
List of figures	viii
List of tables	xx
List of symbols	xxi
1. INTRODUCTION	1
1.1 Introduction.....	1
1.2 Turbocharging.....	3
1.3 Mechanical design of the turbocharger.....	4
1.3.1 The radial compressor of the turbocharger.....	4
1.3.2 The radial turbine of the turbocharger.....	5
1.3.3 Turbocharger bearing system.....	6
1.4 Methods of controlling the turbocharger.....	6
1.4.1 By-pass control.....	7
1.4.2 Variable geometry control.....	7
1.5 Turbocharger performance maps.....	8
1.5.1 Compressor performance map.....	8
1.5.2 Turbine performance map.....	9
1.6 Adiabatic versus non-adiabatic turbocharger performance.....	11
1.7 Methods of turbocharger performance simulation.....	13
1.8 Importance of the present research work.....	14
1.9 Aim of the present research work.....	18
2. LITERATURE SURVEY	20
2.1 Turbocharger non-adiabatic performance.....	20
2.2 Turbocharger performance simulation.....	21
2.2.1 Compressor performance simulation.....	21
2.2.2 Turbine performance simulation.....	23
2.3 Aerodynamic losses.....	24
2.4 Slip factor.....	27
3. TEST-RIG AND ERROR ANALYSIS	31
3.1 Introduction.....	31
3.2 Small combustion chamber test rig.....	31
3.2.1 Design of the small combustion chamber test rig.....	31

3.2.2 Instrumentation	34
3.3 Large combustion chamber test rig	35
3.3.1 Design of the large combustion chamber test rig	35
3.3.2 Instrumentation	35
3.4 Test turbochargers	37
3.5 Experimental error analysis	39
4. PARAMETER STUDY OF THE TURBOCHARGER NON-ADIABATIC	
PERFORMANCE	41
4.1 Introduction	41
4.2 Modeling of turbocharger non-adiabatic performance	41
4.3 Effect of heat transfer on the compressor and the turbine aerodynamic work	43
4.4 Effect of heat transfer on the measured compressor and turbine efficiencies	47
4.4.1 Compressor heat number	51
4.4.2 Fraction of heat transfer before the compressor impeller	52
4.4.3 Compressor peripheral Mach number	53
4.4.4 Impeller flow coefficient	55
4.4.5 Impeller slip factor	55
4.4.6 Blade angle at the impeller outlet	57
5. EXPERIMENTAL RESULTS AND ANALYSIS	60
5.1 Compressor non-adiabatic performance	60
5.1.1 Single entry turbocharger compressor	60
5.1.1.1 Effect of exhaust gas temperature at the turbine entry	60
5.1.1.2 Effect of lubrication oil	68
5.1.1.3 Effect of turbine guide-vane position	73
5.1.2 Twin entry turbocharger compressor	73
5.2 Turbine non-adiabatic performance	75
5.2.1 Single entry turbine	76
5.2.1.1 Effect of turbine guide-vane position	76
5.2.1.2 Effect of exhaust gas temperature at the turbine inlet	77
5.2.1.3 Effect of heat transfer to the compressor	79
5.2.2 Twin entry turbine	82
5.2.2.1 Turbine reduced mass flow rate	82
5.2.2.2 Turbine efficiency	85
5.3 Amount of heat transfer in/from the single entry turbocharger	87
5.4 Aerodynamic performance of micro compressors	93
6. EXTENSION OF THE TURBOCHARGER PERFORMANCE MAPS	97
6.1 Introduction	97

6.2	Modeling of the heat transfer inside the turbocharger	97
6.3	Heat transfer to the oil	104
6.4	Turbine heat transfer	104
6.5	Compressor aerodynamic performance	105
6.6	Compressor aerodynamic losses	110
6.6.1	Overall aerodynamic losses	110
6.6.2	Impeller aerodynamic losses	111
6.6.3	Diffuser aerodynamic losses	115
6.6.4	Volute aerodynamic losses	118
6.6.5	Effect of aerodynamic losses on the overall compressor performance	123
6.7	Slip factor	123
6.8	Part load performance prediction of small turbocharger compressors	127
6.9	Turbine performance simulation	131
6.9.1	Turbine mass flow rate	131
6.9.2	Turbine heat efficiency	136
6.10	Turbocharger performance simulation program	137
6.10.1	Description of the "TC_2003" program	137
6.10.2	Compressor subroutine	140
6.10.3	Turbine subroutine	145
6.10.4	Program results	148
7.	CONCLUSIONS AND RECOMMENDATIONS FOR FUTURE WORK	152
A.	Appendix	155
	References	217

List of figures

Figure 1-1	Methods of engine supercharging (<i>Malobabic, 1989</i>).....	1
Figure 1-2	Typical arrangement of an engine fitted with a mechanically driven supercharger (<i>Watson and Janota, 1982</i>)	2
Figure 1-3	Typical arrangement of an engine fitted with turbocharger (<i>Watson and Janota, 1982</i>).....	2
Figure 1-4	Typical turbocharger design	4
Figure 1-5	Multiple entry volute casing; a. double entry, b. twin entry (<i>Zinner, 1980</i>)	6
Figure 1-6	Principle of adjustable turbine guide vanes control	8
Figure 1-7	Mechanisms of heat transfer in/from the turbocharger	12
Figure 1-8	Schematic diagram of compressor map	15
Figure 1-9	Engine operating range during engine dynamic test superimposed on a compressor performance map (<i>Pucher et al. 2001</i>)	17
Figure 2-1	Comparison between the ideal and the actual velocity triangle at the impeller outlet	27
Figure 3-1	Isometric view and layout of the small combustion chamber test rig	32
Figure 3-2	Schematic of the small combustion chamber test rig.....	34
Figure 3-3	Layout of the large combustion chamber test rig.....	36
Figure 3-4	Schematic of large combustion chamber test rig.....	36
Figure 3-5	Overview of the GT1749V 55 Trim and the K29 turbochargers.....	37
Figure 3-6	Locations of static pressure taps in the vaneless diffuser of the GT1749V 70 Trim turbocharger.....	38
Figure 3-7	GT1749V 70 Trim turbocharger with static pressure tapes at diameter ratio 1.26 and 1.6.....	39
Figure 4-1	Schematic h-s diagram of the compression process in an adiabatic and a non-adiabatic compressor	42
Figure 4-2	Ratio of compressor heat efficiency to compressor adiabatic efficiency as a function of compressor heat number and fraction of heat transfer before the impeller.....	45
Figure 4-3	Ratio of turbine heat efficiency to turbine adiabatic efficiency as a function of turbine heat number and fraction of heat transfer before the turbine rotor	46
Figure 4-4	Variation of the ratio of compressor non-adiabatic efficiency to compressor adiabatic efficiency with the compressor heat number	51
Figure 4-5	Percentage error of the measured product of the turbine efficiency	

	and the mechanical efficiency as a function of the compressor heat number	52
Figure 4-6	Variation of the ratio of compressor non-adiabatic efficiency to compressor adiabatic efficiency with the fraction of heat transfer before the compressor impeller	53
Figure 4-7	Variation of the ratio of compressor non-adiabatic efficiency to compressor adiabatic efficiency with the compressor peripheral Mach number	54
Figure 4-8	Percentage error of the measured product of the turbine efficiency and the mechanical efficiency as a function of the compressor peripheral Mach number.....	55
Figure 4-9	Variation of the ratio of compressor non-adiabatic efficiency to compressor adiabatic efficiency with the compressor impeller flow coefficient	56
Figure 4-10	Percentage error of the measured product of the turbine efficiency and the mechanical efficiency as a function of the compressor impeller flow coefficient	56
Figure 4-11	Variation of the ratio of compressor non-adiabatic efficiency to compressor adiabatic efficiency with the compressor slip factor	57
Figure 4-12	Percentage error of the measured product of the turbine efficiency and the mechanical efficiency as a function of the compressor slip factor	58
Figure 4-13	Variation of the ratio of compressor non-adiabatic efficiency to compressor adiabatic efficiency with the blade angle at impeller outlet.....	58
Figure 4-14	Percentage error of the measured product of the turbine efficiency and the mechanical efficiency as a function of the blade angle at impeller outlet.....	59
Figure 5-1	Variation of the compressor total pressure ratio with the compressor reduced mass flow rate at different compressor reduced rotational speeds and total temperatures at the turbine entry for the GT1749V 55 Trim compressor	61
Figure 5-2	Variation of the compressor non-adiabatic efficiency with the compressor reduced mass flow rate at different compressor reduced rotational speeds and total temperatures at the turbine entry for the GT1749V 55 Trim compressor	62
Figure 5-3	Variation of the compressor heat number with the compressor	

	stage flow coefficient at different compressor reduced rotational speeds and total temperatures at the turbine entry for the GT1749V 55 Trim compressor	64
Figure 5-4	Ratio of the compressor non-adiabatic efficiency to the compressor adiabatic efficiency at different compressor reduced rotational speeds and total temperatures at the turbine entry for the GT1749V 55 Trim compressor	66
Figure 5-5	Difference between the compressor non-adiabatic efficiency and the adiabatic efficiency of the GT1749V 55 Trim turbocharger at exhaust gas temperature $T_{0t} = 973$ K	67
Figure 5-6	Ratio of the compressor heat efficiency to the compressor adiabatic efficiency of the GT1749V 55 Trim turbocharger at different rotational speeds and exhaust gas temperatures at the turbine entry	68
Figure 5-7	Ratio of the amount of heat transfer to the oil to the compressor power at different turbocharger normalized rotational speeds and exhaust gas temperatures at the turbine entry	70
Figure 5-8	Amount of heat transfer to the oil as a fraction of the total power added to the oil at different turbocharger normalized rotational speeds.....	71
Figure 5-9	Ratio of the compressor casing temperature to the total air temperature at the compressor outlet.....	72
Figure 5-10	Variation of the compressor total pressure ratio with the compressor reduced mass flow rate at different compressor reduced rotational speeds and total temperatures at the turbine entry for the K29 compressor	74
Figure 5-11	Variation of the compressor non-adiabatic efficiency with the compressor reduced mass flow rate at different compressor reduced rotational speeds and total temperatures at the turbine entry for the K29 compressor	75
Figure 5-12	Variation of the turbine reduced mass flow rate with the turbine total-to-static pressure ratio at different values of the turbine rotational speed parameter and inlet guide-vane positions	76
Figure 5-13	Variation of the product of the turbine efficiency and the mechanical efficiency with the turbine total-to-static pressure ratio at different values of the turbine rotational speed parameter and inlet guide-vane positions of the GT1749V 55 Trim turbocharger	77

Figure 5-14	Variation of the turbine reduced mass flow rate with the turbine total-to-static pressure ratio at different values of the turbine rotational speed parameter and exhaust gas temperatures at the turbine entry of the GT1749V 55 Trim turbocharger	78
Figure 5-15	Effect of the exhaust gas temperature at the turbine entry on the product of the turbine efficiency and the mechanical efficiency of the GT1749V 55 Trim turbocharger.....	79
Figure 5-16	Percentage error in the estimated turbine efficiency due to the amount of heat transfer to the compressor of the GT1749V 55 Trim turbocharger.....	80
Figure 5-17	Comparison between the turbine non-adiabatic efficiency, the measured turbine heat efficiency, and the actual turbine heat efficiency of the GT1749V 55 Trim turbocharger.....	81
Figure 5-18	Declaration of the effect of the rotor passage aerodynamic losses on the entry mass flow rate of the K29 turbine	84
Figure 5-19	Ratio of the entry flow rate to the total turbine mass flow rate of the K29 turbine as a function of the entry isentropic pressure ratio at turbocharger rotational speed 81404 rpm.....	85
Figure 5-20	Heat efficiency of the K29 turbine as a function of the blade speed parameter at different entry pressure ratios.....	87
Figure 5-21	Turbocharger as a thermodynamic system	87
Figure 5-22	Range of heat transfer by convection and radiation from the turbine to the ambient as a fraction of the total amount of heat transfer from the turbine of the GT1749V 55 Trim turbocharger.....	89
Figure 5-23	Range of heat transfer from the turbine to the oil as a fraction of the total amount of heat transfer from the turbine of the GT1749V 55 Trim turbocharger.....	89
Figure 5-24	Range of heat transfer from the turbine to the compressor as a fraction of the total amount of heat transfer from the turbine of the GT1749V 55 Trim turbocharger.....	90
Figure 5-25	Range of total amount of heat transfer from the turbine as a fraction of the fluid power supplied to the turbine of the GT1749V 55 Trim turbocharger.....	91
Figure 5-26	Turbine power as a fraction of the fluid power supplied to the turbine of the GT1749V 55 Trim turbocharger.....	92
Figure 5-27	Ratio of the total amount of heat transfer from the turbine to the turbine power of the GT1749V 55 Trim turbocharger	92

Figure 5-28	Range of power lost at the turbine outlet as a fraction of the fluid power supplied to the turbine of the GT1749V 55 Trim turbocharger	93
Figure 6-1	Schematic diagram of the different heat transfer mechanisms in the bearing housing	98
Figure 6-2	Flow chart for the program “V-Diffuser”	108
Figure 6-3	Overall loss coefficient of the GT1749V 70 Trim compressor.....	111
Figure 6-4	Impeller loss coefficient of the GT1749V 70 Trim compressor	112
Figure 6-5	Schematic diagram of the velocity triangle at the impeller inlet during off-design operation.....	113
Figure 6-6	Diffuser loss coefficient of the GT1749V 70 Trim compressor.....	115
Figure 6-7	Diffuser pressure coefficient of the GT1749V 70 Trim compressor	116
Figure 6-8	Volute loss coefficient of the GT1749V 70 Trim compressor.....	119
Figure 6-9	Volute pressure coefficient of the GT1749V 70 Trim compressor	120
Figure 6-10	Combined pressure coefficient of the volute and the diffuser of the GT1749V 70 Trim compressor	120
Figure 6-11	Variation of the slip factor with the impeller flow coefficient for three different impellers	125
Figure 6-12	Flow chart for the program “CPLP-Prediction”	129
Figure 6-13	Variation of the turbine discharge coefficient with the Reynolds number at the turbine inlet for different guide-vane positions of the GT1749V 55 Trim turbine	133
Figure 6-14	Variation of the turbine discharge coefficient with the Reynolds number for the K29 turbine at entry pressure ratio 1.0	135
Figure 6-15	Schematic of the “TC_2003” program	138
Figure 6-16	Schematic diagram for the modeling of the non-adiabatic work coefficient in the “TC_2003” program	142
Figure 6-17	Schematic diagram of a compressor performance line with a negative slope near the surge point.....	144
Figure A-1	Error analysis of the measured total pressure ratio, reduced rotational speed, and reduced mass flow rate of the GT1749V 55 Trim compressor	156
Figure A-2	Error analysis of the measured isentropic efficiency of the GT1749V 55 Trim compressor	156
Figure A-3	Error analysis of the measured total-to-static pressure ratio, reduced rotational speed, and reduced mass flow rate of the GT1749V 55 Trim turbine	157

Figure A-4	Error analysis of the estimated product of total-to-static turbine efficiency and mechanical efficiency of the GT1749V 55 Trim turbocharger	157
Figure A-5	Error analysis of the measured total pressure ratio, reduced rotational speed, and reduced mass flow rate of the K29 compressor.....	158
Figure A-6	Error analysis of the measured isentropic efficiency of the K29 compressor.....	158
Figure A-7	Error analysis of the measured total-to-static pressure ratio, reduced rotational speed, and reduced mass flow rate of the K29 turbine	159
Figure A-8	Error analysis of the estimated product of total-to-static turbine efficiency and mechanical efficiency of the K29 turbocharger	159
Figure A-9	Schematic h-s diagram of the expansion process in a non-adiabatic turbine	160
Figure A-10	Temperature difference between the turbine casing and the compressor casing of the GT1749V 55 Trim compressor	160
Figure A-11	Normalized compressor casing temperature of the GT1749V 55 Trim compressor	161
Figure A-12	Normalized turbine casing temperature of the GT1749V 55 Trim turbocharger	161
Figure A-13	Comparison between the measured and the calculated ratio of the bearing frictional power to the compressor power of the GT1749V 55 Trim turbocharger.....	162
Figure A-14	Non-adiabatic Compressor efficiency of the GT1749V 70 Trim turbocharger with insulation and without insulation	162
Figure A-15	comparison of the measured compressor non-adiabatic efficiency at turbine inlet guide-vane positions 100% open and 0% open and exhaust gas temperature at the turbine entry of 973 K.....	163
Figure A-16	Schematic diagram of the K29 twin entry turbine	163
Figure A-17	Effect of the turbine entry pressure ratio on the measured compressor efficiency of the K29 turbocharger	164
Figure A-18	Variation of the turbine heat number with the turbine total-to-static pressure ratio at different values of the turbine rotational speed parameter and exhaust gas temperatures at the turbine entry of the GT1749V 55 Trim turbine	164
Figure A-19	Variation of the reduced mass flow rate with the turbine	

	total-to-static pressure ratio of the K29 turbine at entry pressure ratio 0.6	165
Figure A-20	Variation of the reduced mass flow rate with the turbine total-to-static pressure ratio of the K29 turbine at entry pressure ratio 0.7	165
Figure A-21	Variation of the reduced mass flow rate with the turbine total-to-static pressure ratio of the K29 turbine at entry pressure ratio 0.8	166
Figure A-22	Variation of the reduced mass flow rate with the turbine total-to-static pressure ratio of the K29 turbine at entry pressure ratio 0.9	166
Figure A-23	Variation of the reduced mass flow rate with the turbine total-to-static pressure ratio of the K29 turbine at entry pressure ratio 1.0	167
Figure A-24	Variation of the reduced mass flow rate with the turbine total-to-static pressure ratio of the K29 turbine at entry pressure ratio 1.1	167
Figure A-25	Variation of the reduced mass flow rate with the turbine total-to-static pressure ratio of the K29 turbine at entry pressure ratio 1.2	168
Figure A-26	Variation of the reduced mass flow rate with the turbine total-to-static pressure ratio of the K29 turbine at entry pressure ratio 1.3	168
Figure A-27	Variation of the reduced mass flow rate with the turbine total-to-static pressure ratio of the K29 turbine at entry pressure ratio 1.4	169
Figure A-28	Ratio of the entry flow rate to the total turbine mass flow rate of the K29 turbine as a function of the entry isentropic pressure ratio at turbocharger rotational speed 40429 rpm.....	169
Figure A-29	Ratio of the entry flow rate to the total turbine mass flow rate of the K29 turbine as a function of the entry isentropic pressure ratio at turbocharger rotational speed 60854 rpm.....	170
Figure A-30	Ratio of the entry flow rate to the total turbine mass flow rate of the K29 turbine as a function of the entry isentropic pressure ratio at turbocharger rotational speed 102000 rpm.....	170
Figure A-31	Variation of the product of the turbine efficiency and the mechanical efficiency of the K29 turbocharger with the mean	

	total-to-static pressure ratio at different values of the turbine rotational speed parameter and entry pressure ratio 1.0	171
Figure A-32	Product of the turbine efficiency and the mechanical efficiency of the K29 turbine at different exhaust gas temperatures at the turbine entry	171
Figure A-33	Measured performance map of the GT1749V 70 Trim compressor at exhaust gas temperature at the turbine entry $T_{\text{gt}} = 311 \text{ K}$	172
Figure A-34	Measured performance map of the GT1749V 70 Trim compressor at exhaust gas temperature at the turbine entry $T_{\text{gt}} = 873 \text{ K}$	172
Figure A-35	Diffuser static pressure distribution at diameter ratios $\lambda=1.26$ and 1.6 for the GT1749V 70 Trim compressor at 60000 rpm	173
Figure A-36	Diffuser static pressure distribution at diameter ratios $\lambda=1.26$ and 1.6 for the GT1749V 70 Trim compressor at 80000 rpm	174
Figure A-37	Diffuser static pressure distribution at diameter ratios $\lambda=1.26$ and 1.6 for the GT1749V 70 Trim compressor at 100000 rpm	175
Figure A-38	Diffuser static pressure distribution at diameter ratios $\lambda=1.26$ and 1.6 for the GT1749V 70 Trim compressor at 120000 rpm	176
Figure A-39	Diffuser static pressure distribution at diameter ratios $\lambda=1.26$ and 1.6 for the GT1749V 70 Trim compressor at 140000 rpm	177
Figure A-40	Diffuser static pressure distribution at diameter ratios $\lambda=1.26$ and 1.6 for the GT1749V 70 Trim compressor at 160000 rpm	178
Figure A-41	Comparison between the static pressure distribution at diameter ratios $\lambda = 1.26$ and 1.6 for the GT1749V 70 Trim compressor at 60000 rpm	179
Figure A-42	Comparison between the static pressure distribution at diameter ratios $\lambda = 1.26$ and 1.6 for the GT1749V 70 Trim compressor at 80000 rpm	179
Figure A-43	Comparison between the static pressure distribution at diameter ratios $\lambda = 1.26$ and 1.6 for the GT1749V 70 Trim compressor at 100000 rpm	180
Figure A-44	Comparison between the static pressure distribution at diameter ratios $\lambda = 1.26$ and 1.6 for the GT1749V 70 Trim compressor at 120000 rpm	180
Figure A-45	Comparison between the static pressure distribution at diameter ratios $\lambda = 1.26$ and 1.6 for the GT1749V 70 Trim compressor at 140000 rpm	181
Figure A-46	Comparison between the static pressure distribution at diameter	

	ratios $\lambda = 1.26$ and 1.6 for the GT1749V 70 Trim compressor at 160000 rpm	181
Figure A-47	Different flow regimes at the diffuser inlet along the compressor surge line	182
Figure A-48	Comparison between the estimated first temperature distribution coefficient and the predicted one.....	182
Figure A-49	Comparison between the estimated second temperature distribution coefficient and the predicted one	183
Figure A-50	Comparison between the measured compressor adiabatic efficiency and the calculated compressor adiabatic efficiency of the GT1749V 55 Trim compressor	183
Figure A-51	Comparison between the predicted oil Nusselt number and the estimated oil Nusselt number	184
Figure A-52	Comparison between the measured total temperature at the turbine outlet and the estimated one for the GT1749V 55 Trim turbine	184
Figure A-53	Comparison between the measured volute loss coefficient and the calculated one for the large centrifugal compressor with external volute.....	185
Figure A-54	Comparison between the measured flow angle at the volute inlet and the calculated one for the large centrifugal compressor with external volute	185
Figure A-55	Comparison between the estimated impeller loss coefficient using the program “V-Diffuser” and the calculated one.....	186
Figure A-56	Comparison between the estimated diffuser loss coefficient using the program “V-Diffuser” and the calculated one.....	186
Figure A-57	Comparison between the estimated dissipation coefficient using the program “V-Diffuser” and the calculated one.....	187
Figure A-58	Schematic diagram of the volute	187
Figure A-59	Comparison between the measured volute loss coefficient and the calculated one for the large centrifugal compressor with external volute.....	188
Figure A-60	Comparison between the estimated volute loss coefficient using the program “V-Diffuser” and the calculated one for the GT1749V 70 Trim compressor with central volute.....	188
Figure A-61	Variation of the fractional total pressure loss and the compressor adiabatic efficiency with the impeller flow coefficient for the	

	GT1749V 70 Trim compressor at 100000 rpm	189
Figure A-62	Variation of the fractional total pressure loss and the compressor adiabatic efficiency with the impeller flow coefficient for the GT1749V 70 Trim compressor at 160000 rpm	189
Figure A-63	Variation of the fractional total pressure loss and the compressor adiabatic efficiency with the impeller flow coefficient for the large centrifugal compressor with radial impeller.....	190
Figure A-64	Variation of the fractional total pressure loss and the compressor adiabatic efficiency with the impeller flow coefficient for the large centrifugal compressor with backswept impeller	190
Figure A-65	Comparison between the estimated slip factor using the program “V-Diffuser” and the calculated one for the GT1749V 70 trim impeller.....	191
Figure A-66	Comparison between the estimated slip factor using the program “V-Diffuser” and the calculated one for the large radial impeller.....	191
Figure A-67	Comparison between the estimated slip factor using the program “V-Diffuser” and the calculated one for the large backswept impeller.....	192
Figure A-68	Comparison between the predicted compressor performance and the measured compressors performance at 60000 rpm for the GT1749V 70 Trim compressor	192
Figure A-69	Comparison between the predicted compressor performance and the measured compressors performance at 50000, and 0 rpm for the GT1749V 55 Trim compressor	193
Figure A-70	Comparison between the predicted compressor performance and the measured compressors performance at 40000 rpm for the K29 compressor.....	193
Figure A-71	Comparison between the predicted compressor performance and the measured compressors performance at 50000 rpm for the VNT12 compressor.....	194
Figure A-72	Comparison between the predicted compressor performance and the measured compressors performance at 50000 rpm for the K03 compressor.....	194
Figure A-73	Variation of the Reynolds number exponent with the turbine area ratio	195
Figure A-74	Comparison between the measured turbine mass flow rate and the estimated turbine mass flow rate of the GT1749V 55 Trim turbine.....	195

Figure A-75	Comparison between the measured turbine entry mass flow rate and the estimated turbine entry flow rate for entry A of the K29 turbine at entry pressure ratio 1.0.....	196
Figure A-76	Comparison between the measured turbine entry mass flow rate and the estimated turbine entry flow rate for entry B of the K29 turbine at entry pressure ratio 1.0.....	196
Figure A-77	Comparison between the measured turbine entry mass flow rate and the estimated turbine entry flow rate for entry A of the K29 turbine under partial admission conditions	197
Figure A-78	Comparison between the measured turbine entry mass flow rate and the estimated turbine entry flow rate for entry B of the K29 turbine under partial admission conditions	197
Figure A-79	Comparison between the actual heat efficiency of the GT1749V 55 Trim turbine and the calculated turbine heat efficiency at guide-vane position 10% open	198
Figure A-80	Comparison between the actual heat efficiency of the GT1749V 55 Trim turbine and the calculated turbine heat efficiency at guide-vane position 20% open	198
Figure A-81	Comparison between the actual heat efficiency of the GT1749V 55 Trim turbine and the calculated turbine heat efficiency at guide-vane position 40% open	199
Figure A-82	Comparison between the actual heat efficiency of the GT1749V 55 Trim turbine and the calculated turbine heat efficiency at guide-vane position 60% open	199
Figure A-83	Comparison between the actual heat efficiency of the GT1749V 55 Trim turbine and the calculated turbine heat efficiency at guide-vane position 80% open	200
Figure A-84	Comparison between the actual heat efficiency of the GT1749V 55 Trim turbine and the calculated turbine heat efficiency at guide-vane position 100% open	200
Figure A-85	Comparison between the actual heat efficiency of the K29 turbine and the calculated turbine heat efficiency.....	201
Figure A-86	Extended compressor performance map of the GT1749V 70 trim compressor at an exhaust gas temperature 305 K.....	202
Figure A-87	Comparison between the measured performance lines and the extrapolated as well as the interpolated performance lines for the GT1749V 70 trim compressor	203

Figure A-88	Extended compressor performance map of the GT1749V 70 Trim compressor at an exhaust gas temperature 873 K.....	204
Figure A-89	Estimated compressor heat efficiency using the hot measurements as input to the program.....	205
Figure A-90	Estimated compressor non-adiabatic efficiency using the cold measurements as input to the program.....	205
Figure A-91	Extended compressor performance map for the GT1749V 55 Trim compressor.....	206
Figure A-92	Comparison between the interpolated performance line and the measured performance line of the GT1749V 55 Trim compressor at 140000 rpm	207
Figure A-93	Estimated compressor performance of the GT1749V 55 Trim compressor at very low rotational speeds and compressor operation in the forth quadrant of the map.....	207
Figure A-94	Estimated compressor heat efficiency using the hot measurements as input to the program for the GT1749V 55 Trim compressor	208
Figure A-95	Estimated compressor non-adiabatic efficiency using the cold measurements as input to the program for the GT1749V 55 Trim compressor.....	208
Figure A-96	Extended compressor performance map for the K29 compressor	209
Figure A-97	Extended compressor performance map for the VNT12 compressor.....	210
Figure A-98	Extended compressor performance map for the K03 compressor	211
Figure A-99	Extended turbine performance map of the GT1749V 55 Trim turbine at an exhaust gas temperature 873 K.....	212
Figure A-100	Extended turbine performance map of the K29 turbine at an exhaust gas temperature 873 K and entry pressure ratio $\pi_{\text{entry}}=1$	213
Figure A-101	Comparison between the measured turbine performance lines and the interpolated performance lines for the GT1749V 55 trim turbine ..	214
Figure A-102	Comparison between the measured turbine performance lines and the extrapolated performance lines for the GT1749V 55 trim turbine	215
Figure A-103	Comparison between the measured turbine mass flow rate and the extrapolated mass flow rate for the K29 turbine under partial admission conditions	216

List of tables

Table 6-1	Percentage error in estimating the slip factor at the compressor design point.....	127
Table A-1	Main dimensions of the investigated turbochargers.....	155
Table A-2	Main dimensions of the VNT12 and K03 compressors.....	155

List of symbols

Symbol	Unit	Meaning	Defined by eq.
A	m ²	area	
A _B	m ²	bearing cross sectional area	(6.4)
A _{GV}	m ²	throat area of the inlet guide vanes	
AR _T	-	turbine area ratio	
b	m	width	
b _{dif, mean}	m	diffuser width at mean diffuser diameter	
C _d	-	discharge coefficient	
C _p	-	pressure coefficient	(6.86),(6.96), (6.97)
c	m/s	absolute velocity	
c _{1u}	m/s	swirl velocity at impeller inlet	
c _{2m}	m/s	meridional velocity at impeller outlet	(2.9)
c _{2u}	m/s	swirl velocity at impeller outlet	
C _{dis}	-	dissipation coefficient	
C _f	-	friction coefficient	
c _p	J/(kg K)	specific heat at constant pressure	
c _s	m/s	turbine spouting velocity	(1.20)
c _{slip}	m/s	slip velocity	(2.6)
cl	m	clearance	
D	m	diameter	
D _h	m	hydraulic diameter	
GVP	%	Guide-vane position	
h	J/kg	specific enthalpy	
h _{con}	W/(m ² K)	coefficient of heat transfer by free convection	
h _{oil}	W/(m ² K)	coefficient of heat transfer by forced convection to the oil	
K	-	empirical coefficient	
K _{C, before}	-	fraction of heat transfer before the compressor impeller	
K _{T, before}	-	fraction of heat transfer before the turbine wheel	
k _B	W/(m K)	bearing housing thermal conductivity	

Symbol	Unit	Meaning	Defined by eq.
L	m	length	
L_B	m	bearing housing length	
\dot{m}	Kg/s	mass flow rate	
Mu_2	-	compressor peripheral Mach number	(1.17)
Nu	-	Nusselt number	
n	rpm	rotational speed	
$n_{red, C}$	rpm	compressor reduced rotational speed	(1.6)
$n_{rsp, T}$	rpm/K ^{0.5}	turbine rotational speed parameter	(1.13)
P	m	perimeter	
Pr	-	Prandtl number	
p	Pa	pressure	
Q	W	heat transfer rate	
$Q_{B, fri}$	W	bearing frictional power	
q	J/kg	specific amount of heat transfer	
R	J/(kg K)	gas constant	
Re	-	Reynolds number	
r	m	radius	
Sr	-	Strouhal number	
T	K	temperature	
u	m/s	peripheral velocity	
u/c_s	-	turbine blade speed parameter	
\dot{V}	m ³ /s	volume flow rate	
W	J/kg	work	
\dot{W}	W	power	
w	m/s	relative velocity	
x	m	distance along x-axis	
z	-	number of blades	

Greek:

α	°	flow angle	
β	°	relative flow angle	
β_{1b}	°	blade angle at impeller inlet	
β_{2b}	°	blade angle at impeller outlet	
Δ	-	difference, systematic error	
δ	-	random error	(3.3)

Symbol	Unit	Meaning	Defined by eq.
ε_T	-	turbine emissivity	
Φ_T	-	turbine flow function	(2.3), (2.4)
ϕ_2	-	impeller flow coefficient	(1.16)
ϕ_{stage}	-	stage flow coefficient	(1.15)
η	-	efficiency	
η_{heat}	-	efficiency used for estimating the actual power	(4.8), (4.18)
η_m	-	mechanical efficiency	(1.10)
η_{turbo}	-	turbocharger efficiency	(1.9)
κ	-	specific heat ratio	
λ	-	diameter ratio	(3.2)
μ	-	slip factor	(2.7)
ν	m^2/s	kinematic viscosity	
π	-	pressure ratio	(1.4), (1.7)
π	-	circle constant	
π_{entry}	-	entry total pressure ratio (twin entry turbines)	(5.7)
θ	$^\circ$	circumferential angle	
ρ	kg/m^3	density	
σ	$\text{W}/(\text{m}^2 \text{K}^4)$	Stefan-Boltzmann constant	
ω	s^{-1}	angular velocity	
ξ	-	loss coefficient	(6.68),(6.69), (6.70),(6.71)
Ψ	-	work coefficient	(1.18)
ψ	-	compressor pressure coefficient	(1.19)
Ψ_{AB}	-	entry isentropic enthalpy ratio (twin entry turbines)	(5.14)
$\Psi_{T, \text{stator}}$	-	Velocity coefficient of the turbine stator	
$\Psi_{T, \text{rotor}}$	-	Velocity coefficient of the turbine wheel	
ζ_h	-	heat number	(4.17),(4.19)
\mathcal{R}_T	-	turbine degree of reaction	

Subscripts:

1	compressor inlet
2	compressor impeller outlet and diffuser inlet

Symbol	Unit	Meaning	Defined by eq.
3		compressor diffuser outlet and volute inlet	
4		inlet of the compressor volute exit cone	
5		compressor outlet	
6		turbine inlet	
7		inlet of the turbine wheel	
8		turbine outlet	
A		entry A of the twin entry turbine	
ac		actual	
adi		adiabatic	
after		after the wheel	
air		air	
atm		atmospheric	
B		entry B of the twin entry turbine	
b		blade	
before		before the wheel	
bl		blade loading	
C		compressor	
c		casing	
cal		calculated	
cl		clearance	
con		convection heat transfer	
cone		compressor volute exit cone	
cor		corrected	
dia		non-adiabatic	
dif		diffuser	
diff		diffusion	
diskf		disk friction	
eddy		eddy	
eff		effective	
exh		exhaust gas	
fri		friction	
hom		homogeneous	
i		inner, inlet	
ideal		ideal	

Symbol	Unit	Meaning	Defined by eq.
imp		impeller	
inc		incidence	
is		isentropic	
loss		aerodynamic loss	
max		maximum	
mean		mean value	
measured		obtained from measurements	
mix		mixing	
non-hom		non-homogeneous	
o		outer, outlet	
oil		lubrication oil	
opt		optimum	
pass		passage	
pre		pressure side	
r		radial direction	
rad		radiation heat transfer	
red		reduced	
ref		reference	
rel		relative	
rms		root mean square	
s		static	
shaft		turbocharger shaft	
suc		suction side	
surface		surface area	
T		turbine	
t		total	
u		peripheral direction	
vol		volute	
*		heat transfer is tacked into consider	
x		x-direction	

1. INTRODUCTION

1.1 Introduction

Engine supercharging can be defined as the introduction of air (or air/fuel mixture) into an engine cylinder at a density higher than ambient (*Watson and Janota, 1982*). It aims at increasing the amount of air supplied to an engine of a given size; hence more fuel can be burnt. This increases the power output of the engine as a result of increasing the amount of burnt fuel. It is evident that the principle objective is to increase the engine power output, not to improve the engine efficiency. However, the engine efficiency may benefit (*Watson and Janota, 1982*).

Engine supercharging can be achieved using many different methods of supercharging. The applied methods of supercharging are summarized in Figure 1-1 (*Malobabic, 1989*). These methods can be classified into mechanical supercharging, turbocharging, COMPREX-supercharging, and others.

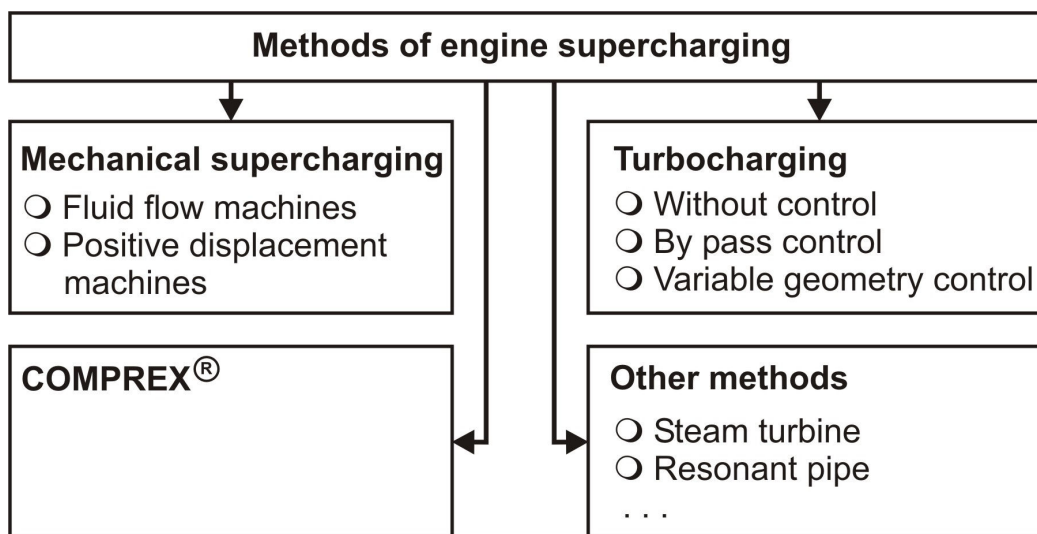


Figure 1-1 Methods of engine supercharging (*Malobabic, 1989*)

Mechanical supercharging uses a rotary or positive displacement compressor to compress the air swallowed by engine. The power required to drive this compressor is directly taken from engine crank shaft. Consequently, compressor rotational speed is directly related to engine rotational speed. *Watson and Janota (1982)* show a typical arrangement of an engine fitted with a mechanically driven supercharger (Figure 1-2). Mechanical supercharging has been used many times in the past, particularly in piston aircraft engines.

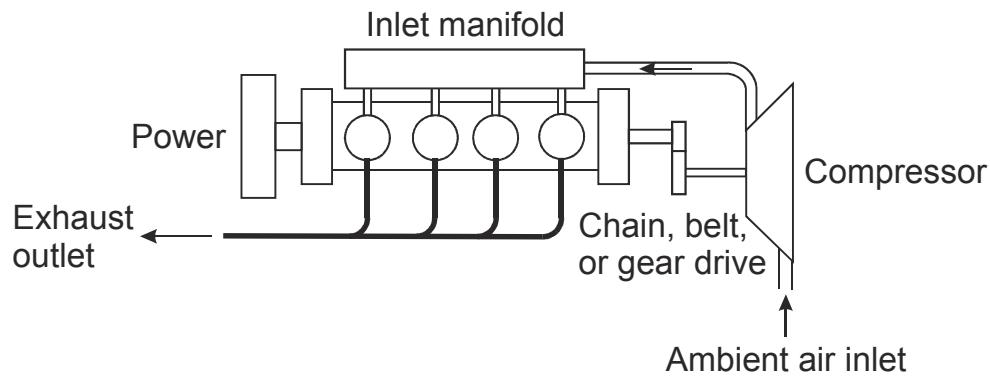


Figure 1-2 Typical arrangement of an engine fitted with a mechanically driven supercharger (*Watson and Janota, 1982*)

Turbocharging is nowadays considered the most commonly used method of engine supercharging. The idea behind turbocharging is to utilize the waste exhaust gas energy to drive a turbine directly coupled to a centrifugal compressor. It is evident here that the power required to drive the compressor is taken from the exhaust gas rather than from the engine as in mechanical supercharging. This waste exhaust gas energy is about 30% of the total energy of a typical diesel engine at rated power (*EPA, 1998*). Thus, turbocharged engines have a favorable power density and overall efficiency compared with mechanically supercharged engines (*Challen and Baranescu, 1999*). Figure 1-3 (*Watson and Janota, 1982*) shows a typical arrangement of a turbocharged engine. Turbocharger is the subject of the current research work and it will be considered in more detail in the following sections.

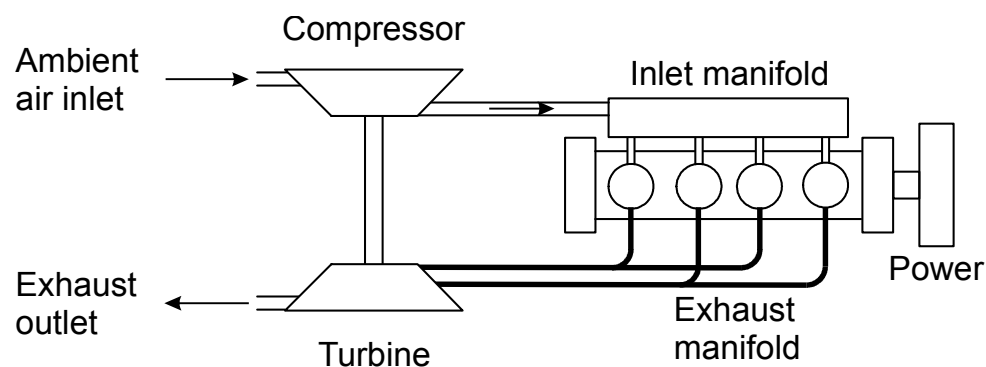


Figure 1-3 Typical arrangement of an engine fitted with turbocharger (*Watson and Janota, 1982*)

Complex supercharger makes use of the fact that if two fluids having different pressures are brought into direct contact in long narrow channels, equalization of pressure occurs faster than mixing (*İçingür et al., 2003*). The idea behind complex superchargers is to use pressure waves to compress the intake air (or mixture). These waves are generated by means of direct contact between the exhaust gas and the intake air in long narrow flow channels. More details about complex

superchargers can be found in Gyarmathy (1983), Mayer (1981), Kirchhofer (1977), and Kirchhofer and Spinnler (1986).

Other methods of supercharging have been investigated, such as resonant pipe supercharging, and steam turbine supercharging.

1.2 Turbocharging

Turbocharging was first proposed in patents by Büchi as long ago as 1905 and 1909 (*Weaving, 1990*). It has been extensively used with diesel engines as a superior boosting system. This is because it allows a significant increase in the maximum power rating with a decrease in gaseous and particulate emissions (*Flotho et al., 2000; Merker and Kessen, 1999; Merker and Stiesch, 1999*). Recently, the application of turbocharging has been extended to cover spark ignition engines (S.I.E) as well as diesel engines. Turbocharging of S.I.E aims at increasing the power to weight ratio; i.e. achieving a compact engine, and maximizing the fuel economy while preserving or even improving the existing performance characteristics (*Hemmerlein, 1994*).

Turbocharging is currently the most commonly used method for engine supercharging. The reasons of the current turbocharging dominance are:

- a. Turbocharging reduces the weight and bulk of the engine for a given power output (*Taylor, 1977*). Therefore, turbocharged engines are compact in size. The compact engine size results in a reduction in engine heat losses as well as friction losses.
- b. Turbocharging improves the fuel economy due to the utilization of the engine exhaust gas energy.
- c. Turbocharging results in a decrease in gaseous and particulate emissions (*Flotho et al., 2000; Merker and Kessen, 1999; Merker and Stiesch, 1999*).
- d. The turbocharger delivers boost in response to engine demand.
- e. The space required to fit a turbocharger is small.
- f. The turbocharger prevents loss of engine power at high altitudes.
- g. The turbocharger has a high flexibility of control (*General Electric, 1943*).

However, the turbocharger has the following disadvantages (*Weaving, 1990*):

- a. It takes time to go from one operating state to another in response to engine demand, the well publicized 'turbo lag'.
- b. The turbocharger compressor is limited by choke, poor efficiencies at high flow rates, and surge at low flow rates so that the compressor operating range is limited and this affects the allowable engine speed range.

1.3 Mechanical design of the turbocharger

A typical turbocharger design is shown in Figure 1-4. The turbocharger consists mainly of an exhaust gas driven turbine and a radial air compressor. The turbine and the compressor are mounted at opposite ends of a common shaft and enclosed in a cast housing. A shaft nut or threaded wheel is used to join the compressor wheel and the turbine wheel. The shaft is enclosed in a bearing housing and supported with a bearing. This bearing is designed for high rotational speeds. Lubrication oil fills the clearance between the bearing and the shaft. This oil filled clearance is very important to the turbocharger mechanical efficiency and life. Seal systems separate the bearing housing from both the turbine and the compressor. The seals restrict the oil from entering the compressor and the turbine areas. They also reduce the flow of gases from the turbine or the compressor into the bearing housing.

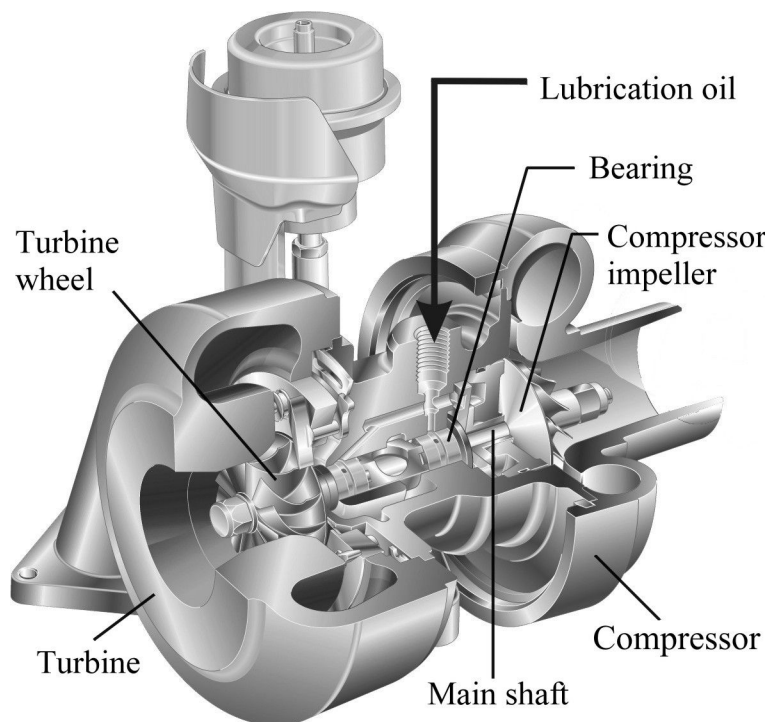


Figure 1-4 Typical turbocharger design

The main components of the turbocharger are discussed in brief in the following sections.

1.3.1 The radial compressor of the turbocharger

Early turbocharger designs had used radial flow, backswept, and shrouded impellers. Later on, unshrouded impellers replaced shrouded impellers. The application of unshrouded impellers results in impeller weight reduction. This enables

turbochargers to rotate at higher rotational speeds, hence producing higher boosting pressure ratios ($> 2:1$). The application of unshrouded impellers also reduces windage losses and improves the turbocharger response to engine demand.

It is also a common practice to increase the number of impeller blades with the application of splitter blades. This provides more guidance to the flow towards the impeller exit, and minimizes blockage at the compressor eye. However, increasing the blade number is limited by the increase in manufacturing costs, impeller weight, hub stresses, and inertia (*Rodgers, 2000*). A blade number higher than certain optimum blade number results in a reduction of the compressor efficiency as a result of the increased aerodynamic friction losses. The optimal blade number is a function of compressor specific speed, blade angle at the impeller outlet, and circumferential Mach number at the impeller outlet (*Rodgers, 2000*).

The radial compressor diffuser may be a vaned or vaneless diffuser. A compressor with a vaned diffuser has higher peak efficiency than that with a vaneless diffuser. This is mainly because the vanes reduce the tangential velocity component more rapidly than a vaneless space, thereby increase the diffusion rate and reduce the flow path length. Thus losses are reduced leading to more efficient diffusion (*Watson and Janota, 1982*). However, vaneless diffusers provide a wider stable operating range than that of vaned diffusers. This wide stable operating range is very important for automotive engines, where the variations in speed and load range are large. Moreover, vaneless diffusers have the advantages of reducing the effect of dirt accumulation, and have lower noise levels. Thus vaneless diffusers are commonly used in the radial compressor of the turbocharger. However, engines with a narrow operating range of speed and load can be equipped with vaned diffuser compressors.

1.3.2 The radial turbine of the turbocharger

Radial inflow turbines are widely used in turbochargers. However, very large engines can also use axial or mixed flow turbines. The main advantages of radial inflow turbines versus axial flow turbines are (*Weaving, 1990*):

- a. A single piece casting
- b. More appropriate flow characteristics
- c. Lower manufacturing cost
- d. Simple entry and exit ducting

Turbine casing can be either single entry or multiple-entry. The latter is required to achieve separation of gas pulses in the exhaust manifold. Multiple-entry volute

casing may be either “double entry volute casing” or “twin entry volute casing”. Figure 1-5 (Zinner, 1980) shows double entry and twin entry volute casings. Double entry volute casing separates the exhaust gas circumferentially, while twin entry volute casing separates the flow meridionally. Most of the multiple-entry automotive turbochargers have twin entry volute casings (Weaving, 1990). This is because they are more effective and have lower losses compared with double entry volute casings (Weaving, 1990).

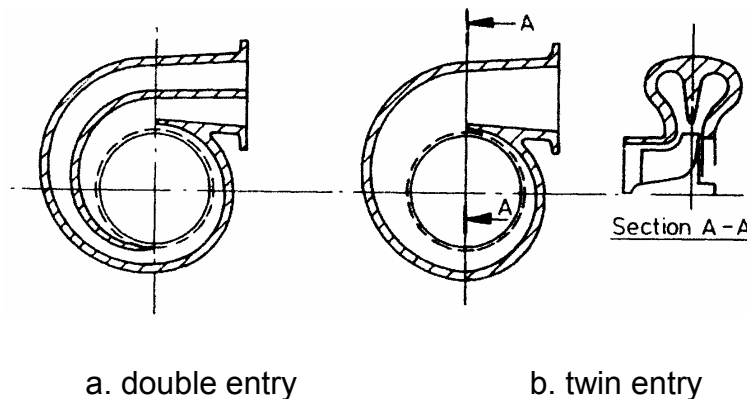


Figure 1-5 Multiple entry volute casing; a. double entry, b. twin entry (Zinner, 1980)

1.3.3 Turbocharger bearing system

Turbocharger bearing may be a roller bearing or a journal bearing. A roller bearing gives higher mechanical efficiency (Watson and Janota, 1982). However it cannot meet the durability requirements at the currently encountered very high rotational speeds, and it is more expensive. Journal bearings are found in the majority of small automotive turbochargers.

More details about turbocharger bearing systems are found in Watson and Janota (1982), Challen and Baranescu (1999), and Weaving (1990).

1.4 Methods of controlling the turbocharger

One of the most important advantages of the turbocharger is the flexibility of control (General Electric, 1943). This is due to the fact that the turbocharger rotational speed depends on the available energy at the turbine inlet rather than the engine rotational speed as in mechanical supercharging (Pucher, 2000). The control of the turbocharger aims at adjusting the boost pressure according to the engine demand. The principal methods of controlling the turbocharger can be classified into by-pass control, and variable geometry control.

1.4.1 By-pass control

By pass control of the turbocharger uses a pneumatic or electric by pass valve located at the turbine inlet to control the turbocharger. This by pass valve opens or closes according to engine demand. The idea behind by pass control is to allow the use of a turbocharger with a smaller turbine. A small turbine gives better engine acceleration at low engine rotational speeds, i.e. low exhaust gas flow rates. However, small turbine wheels may be destroyed with increasing the engine rotational speed and load. This is mainly because of the high exhaust gas pressure as well as the high thermal stresses. To avoid this, the by pass valve opens and only a part of the exhaust gas flows through the turbine. It is clear that the by pass control causes significant waste of the exhaust gas energy at high engine rotational speeds and full load (*Hagelstein et al., 2000*).

1.4.2 Variable geometry control

Variable geometry turbocharging involves the use of a turbocharger with adjustable geometry. This adjustable geometry feature can be applied to the compressor as well as to the turbine. The compressor geometry can be adjusted using:

- a. Adjustable compressor inlet guide vanes
- b. Adjustable diffuser vane angle
- c. Adjustable diffuser width.

The Turbine geometry can be adjusted by means of:

- a. Adjusting the volute geometry
- b. Adjusting the turbine guide vanes angle.

Variable geometry turbochargers with variable turbine guide vanes (VTG) are the most commonly used design. Figure 1-6 shows the principle of turbocharger control using adjustable turbine guide vanes. The control of the VTG-turbocharger takes place by means of opening or closing the guide vanes. This changes the angle of the guide vanes as well as the turbine effective flow area. By these means the pressure ratio across the turbine, and thus the boost pressure, can be maintained at high levels down to much lower engine rotational speeds (*Challen and Baranescu, 1999*). Experimental investigations showed a better engine dynamic performance with variable geometry turbochargers than that with by pass controlled turbochargers (*Chapman and Brentano, 2000*)

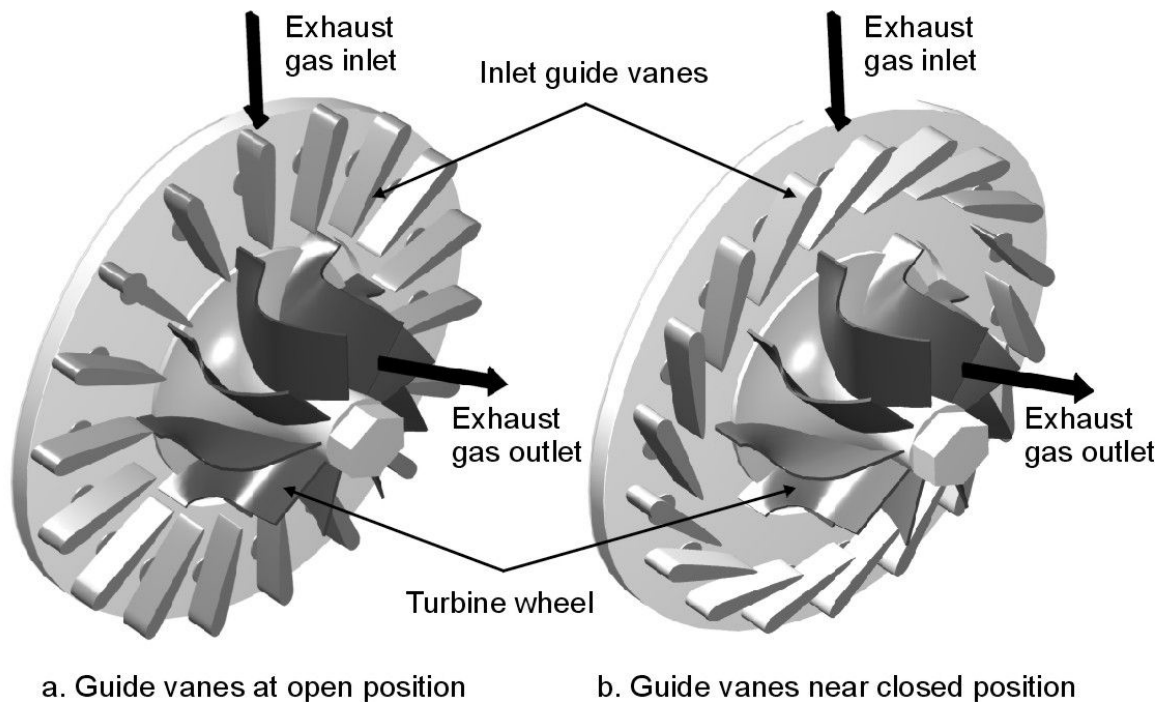


Figure 1-6 Principle of adjustable turbine guide vanes control

1.5 Turbocharger performance maps

Turbocharger performance is presented in the form of separate compressor and turbine performance maps. These maps are normally provided by the turbocharger's manufacturer or measured in laboratory using combustion chamber test rigs.

1.5.1 Compressor performance map

The Compressor performance map presents the compressor characteristics at different compressor operating points. It normally includes the following measured data:

- Compressor reduced mass flow rate or volume flow rate $\dot{m}_{red,C}$ or $\dot{V}_{red,C}$ (abscissa)
- Compressor total pressure ratio $\pi_{t,C}$ (ordinate)
- Compressor isentropic total-to-total efficiency $\eta_{is,C}$
- Compressor reduced rotational speed $n_{red,C}$.

Compressor reduced mass flow rate is given according to SAE 9222 by

$$\dot{m}_{red,C} = \dot{m}_C \frac{\sqrt{T_{1t}/T_{1t,ref}}}{p_{1t}/p_{1t,ref}} \quad (1.1)$$

Compressor reduced volume flow rate is given according to SAE 9222 by

$$\dot{V}_{\text{red,C}} = \dot{V}_{1,\text{C}} / \sqrt{T_{1\text{t}}/T_{1\text{t,ref}}} \quad (1.2)$$

with

$$\dot{V}_{1,\text{C}} = \frac{\dot{m}_{\text{C}}}{\frac{p_{1\text{t}}}{R_{\text{air}} T_{1\text{t}}}} \quad (1.3)$$

Compressor total pressure ratio is given by

$$\pi_{\text{t,C}} = \frac{p_{5\text{t}}}{p_{1\text{t}}} \quad (1.4)$$

Compressor isentropic total-to-total efficiency is given by

$$\eta_{\text{is,C}} = \frac{\Delta h_{\text{is,C}}}{\Delta h_{\text{ac,C}}} = \frac{c_{\text{p,air}} T_{1\text{t}} \left[\pi_{\text{t,C}}^{(\kappa_{\text{air}} - 1)/\kappa_{\text{air}}} - 1 \right]}{c_{\text{p,air}} (T_{5\text{t}} - T_{1\text{t}})} \quad (1.5)$$

An evaluation of compressor efficiency based on equation (1.5) assumes that all kinetic energy at the compressor outlet can be used. However, air delivered from the turbocharger to the inlet manifold of an engine is brought almost to rest without doing useful work (*Watson and Janota, 1982; Challen and Baranescu, 1999*). Thus the total-to-static isentropic compressor efficiency is a more appropriate definition of turbocharger compressor efficiency. Unfortunately many turbocharger manufacturers quote total-to-total efficiency for turbocharger compressors (*Watson and Janota, 1982; Challen and Baranescu, 1999*).

Compressor reduced rotational speed is given according to SAE 9222 by

$$n_{\text{red,C}} = \frac{n}{\sqrt{T_{1\text{t}}/T_{1\text{t,ref}}}} \quad (1.6)$$

1.5.2 Turbine performance map

Turbine performance map presents the turbine characteristics at different turbine operating points. It normally includes the following measured data:

- Turbine total-to-static pressure ratio $\pi_{6\text{t8s,T}}$
- Turbine reduced mass flow rate $\dot{m}_{\text{red,T}}$
- The product of turbine isentropic total-to-static efficiency and turbocharger mechanical efficiency $\eta_{\text{is,T}} \cdot \eta_{\text{m}}$
- Turbine rotational speed parameter $n_{\text{rsp,T}}$

e. Guide-vane position GVP (only for a turbine with variable guide vanes).

Turbine total-to-static pressure ratio is given by

$$\pi_{6t8s,T} = \frac{p_{6t}}{p_8} \quad (1.7)$$

Turbine reduced mass flow rate is given by

$$\dot{m}_{red,T} = \dot{m}_T \frac{\sqrt{T_{6t}}}{p_{6t}} \quad (1.8)$$

Direct estimation of the turbine efficiency using the measured temperature at the turbine outlet yields a highly overestimated turbine efficiency. This is mainly because the temperature difference across the turbine results from the expansion of the exhaust gas in the turbine as well as the high turbine heat losses. Malobabic (1989) showed that the estimated turbine efficiency using the measured temperature at the turbine outlet can be higher than 100%. Therefore, turbine performance maps include the product of the turbine isentropic total-to-static efficiency and the turbocharger mechanical efficiency. This product can be estimated from measurements by means of defining a turbocharger overall efficiency in the form

$$\eta_{turbo} = \frac{\dot{m}_C c_{p,air} T_{1t} \left(\pi_{t,C}^{(\kappa_{air}-1)/\kappa_{air}} - 1 \right)}{\dot{m}_T c_{p,exh} T_{6t} \left(1 - \left(\pi_{6t8s,T} \right)^{-(\kappa_{exh}-1)/\kappa_{exh}} \right)} \quad (1.9)$$

The turbocharger mechanical efficiency is given by

$$\eta_m = \dot{W}_C / \dot{W}_T \quad (1.10)$$

Multiplying equation (1.9) by $\eta_m \dot{W}_T / \dot{W}_C$ and rearranging

$$\eta_{turbo} = \eta_{is,T} \eta_m \eta_{is,C} \quad (1.11)$$

or

$$\eta_{is,T} \eta_m = \eta_{turbo} / \eta_{is,C} \quad (1.12)$$

Equation (1.12) is used for the estimation of the product of the turbine total-to-static efficiency and the turbocharger mechanical efficiency from the measured data.

The turbine rotational speed parameter is given by

$$\eta_{rsp,T} = \frac{n}{\sqrt{T_{6t}}} \quad (1.13)$$

1.6 Adiabatic versus non-adiabatic turbocharger performance

Adiabatic turbocharger performance takes place in the absence of heat transfer between the components of the turbocharger and between the turbocharger and its ambient. It is therefore evident that adiabatic turbine performance is not likely to occur during normal operation of the turbine due to the high temperature of the exhaust gas. Even if the surface area of the turbine was insulated, heat transfer would take place from the turbine to the lubrication oil as well as to the compressor. However, adiabatic turbine performance can be achieved in the laboratory by supplying the turbine with compressed air instead of the hot exhaust gases. This type of experiments is normally called “cold measurements”. Compressor performance likewise is actually non-adiabatic due to heat transfer from the turbine to the compressor. Adiabatic compressor performance can also be achieved by means of cold measurements. It is very important in this case to keep the oil temperature lower than the air temperature in the compressor to avoid heat transfer from the oil to the compressor. Pucher et al. (2003a) showed that adiabatic compressor performance can also be assumed during normal operation of the turbocharger with hot exhaust gases at sufficiently high turbocharger rotational speed.

The complex turbocharger geometry introduces many possible heat transfer mechanisms inside the turbocharger as well as from the turbocharger to the ambient as shown in Figure 1-7. Heat transfer between the components of the turbocharger as well as between the turbocharger and the ambient can be classified into:

- a. Heat transfer from the turbine to the compressor
- b. Heat transfer from the turbine to the oil
- c. Heat transfer from the turbine to the ambient
- d. Heat transfer from the turbine to the cooling water (for water cooled turbochargers)
- e. Heat transfer from the compressor to the ambient
- f. Heat transfer between the compressor and the oil
- g. Heat transfer between the turbocharger and the engine block

Heat transfer from the turbine to the compressor takes place by means of conduction, convection, and radiation. However, the surface area available for convection and radiation between the turbine and the compressor is normally smaller than that available for conduction heat transfer. The bright compressor casing (emissivity ≈ 0.63) reduces radiation heat transfer from the turbine to the compressor furthermore. Heat transfer from the turbine to the oil takes place by means of forced convection in the clearance between shaft and bearing. This means that turbocharger lubrication oil also works as a cooling fluid. The lubrication oil as a cooling fluid reduces the amount of heat transfer by conduction from the turbine to

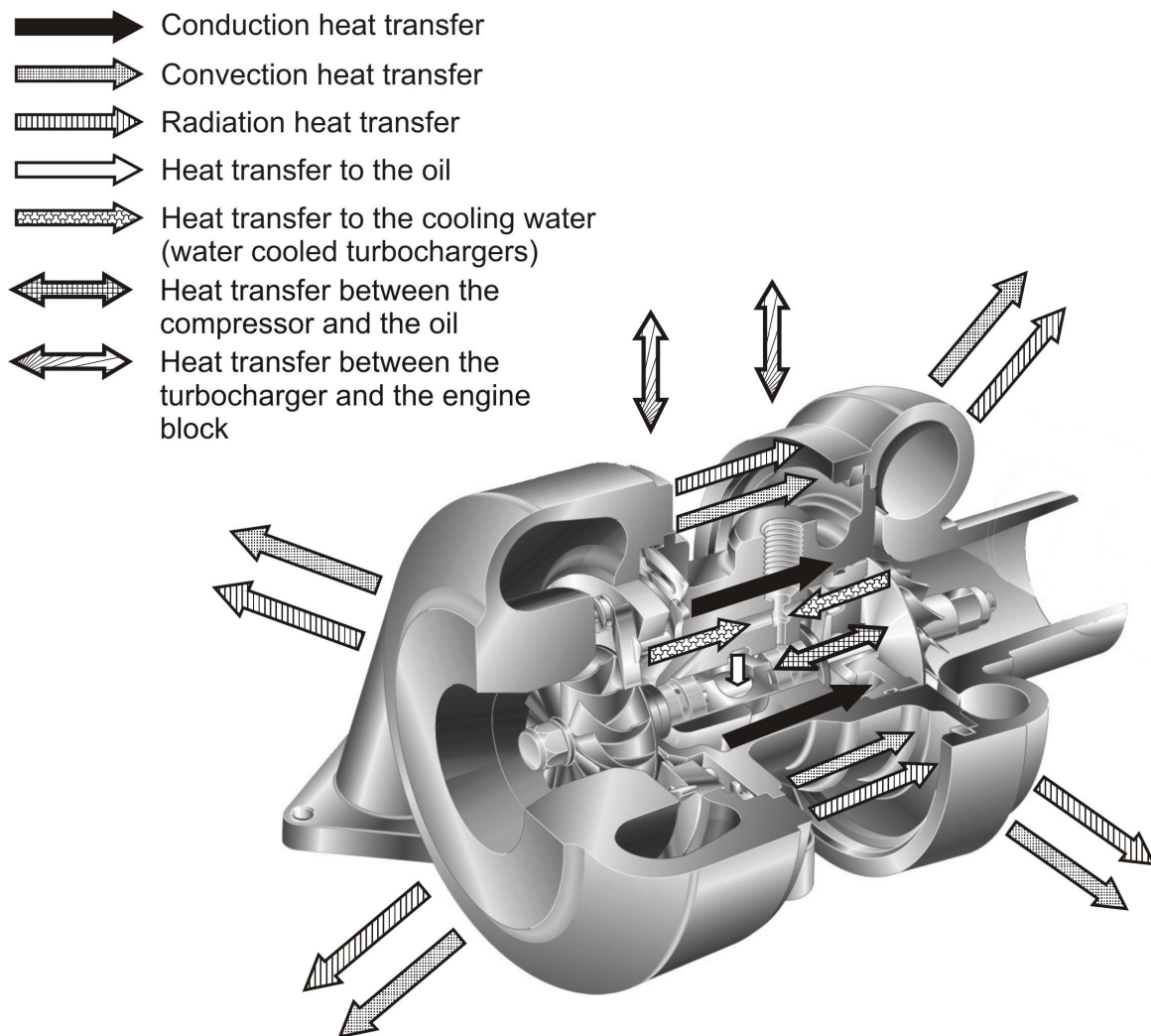


Figure 1-7 Mechanisms of heat transfer in/from the turbocharger

the compressor.

Heat transfer from the turbine to the ambient takes place by means of radiation and free convection. These two mechanisms are very important for the turbine heat transfer because of the high temperature of the turbine casing. Heat transfer from the compressor to the ambient takes place likewise by means of radiation and free convection. Radiation heat transfer from the compressor is very small because of the low emissivity of the bright compressor casing as well as the low temperature difference between the compressor casing and the ambient. This applies particularly for the small turbochargers. The low temperature difference between the compressor casing and the ambient and the small compressor surface area also result in a small amount of heat transfer by free convection from the compressor to the ambient.

Heat transfer to the compressor results in an increase in the total temperature at the

compressor outlet and hence an underestimation of the isentropic compressor efficiency according to equation (1.5). The underestimated isentropic compressor efficiency results consequently in an overestimated turbine efficiency according to equation (1.12). Therefore, modeling of the turbocharger non-adiabatic performance aims at estimating the actual turbine power and compressor power by estimating the actual compressor efficiency. Equation (1.5) can be rewritten as

$$\eta_{is,C} = \frac{\Delta h_{is,C}}{\Delta h_{ac,C}} = \frac{c_{p,air} T_{1t} \left(\pi_{t,C}^{(\kappa_{air} - 1)/\kappa_{air}} - 1 \right)}{c_{p,air} (T_{5t,adi} - T_{1t}) + q_C} \quad (1.14)$$

It is evident that the actual compressor efficiency can be estimated by subtracting the effect of heat transfer to the compressor from equation (1.14). Consequently, the actual turbine efficiency can be estimated using equation (1.12).

1.7 Methods of turbocharger performance simulation

Methods of turbocharger performance simulation can be classified into mathematical interpolation, operational similarity, mean value modeling, and CFD modeling. Mathematical interpolation makes use of the common mathematical interpolation methods to estimate the turbocharger operating characteristics. It is evident here that no physical basis is considered in this method. Moreover, mathematical interpolation cannot be used for the extrapolation of performance maps.

Operational similarity makes use of the common dimensionless groups to estimate every operating point. In this method, the turbocharger performance maps are presented as functions of different dimensionless groups. The most commonly used dimensionless groups for the compressor are

1. Stage flow coefficient

$$\phi_{stage,C} = \frac{\dot{V}_{1,C}}{\frac{\pi}{4} D_2^2 u_2} \quad (1.15)$$

2. Impeller flow coefficient

$$\phi_2 = c_{2m}/u_2 \quad (1.16)$$

3. Peripheral Mach number

$$Mu_2 = \frac{u_2}{\sqrt{\kappa_{air} R_{air} T_{1t}}} \quad (1.17)$$

4. Work coefficient

$$\Psi = \frac{c_{p,air} (T_{5t} - T_{1t})}{u_2^2} \quad (1.18)$$

5. Compressor pressure coefficient

$$\psi = \frac{\Delta p_t}{0.5 \rho_1 u_2^2} \quad (1.19)$$

The most commonly used dimensionless group with turbines is the turbine blade speed parameter. It is defined as the ratio of peripheral speed at the turbine wheel inlet u_7 to the spouting velocity c_s

$$c_s = \sqrt{2c_{p,exh} T_{6t} \left[1 - (\pi_{6t8s})^{-(\kappa_{exh}-1)/\kappa_{exh}} \right]} \quad (1.20)$$

Operational similarity can be used efficiently for interpolating the performance maps. However, extrapolating the compressor map with this method may result in extremely wrong estimated compressor characteristics. This occurs particularly at low compressor rotational speeds. This is because the peripheral Mach number tends to zero while the stage flow coefficient and the impeller flow coefficient tend to infinity.

Mean value modeling predicts the operating characteristics by means of modeling the flow in the compressor and the turbine along a mean streamline. It takes into consideration both the aerodynamic losses and the slip factor of radial turbomachines. This method can be used efficiently in the interpolation and the extrapolation of the performance maps by choosing probable models for the slip factor and the aerodynamic losses.

CFD codes can be used efficiently for predicting certain turbocharger operating points. However, the very long calculation time currently makes it impossible to use CFD codes with engine simulation programs.

1.8 Importance of the present research work

Engine simulation programs have provided a very significant tool for the development of turbocharged engines. These programs were very simple at the early beginning in such a way that they consider only the thermodynamic properties before and after cylinder. With increasing the computers capabilities, they have been developed and extended to include the simulation of the engine together with its manifolds and turbocharger. The simulation of turbocharger performance aims at providing the required boundary conditions for engine simulation. Most of the existing engine

simulation models are based on performance maps provided by the manufacturer or measured in laboratory. These maps cover only a limited turbocharger operating range. Therefore, they cannot be used to simulate the turbocharger performance at every engine rotational speed. A measured compressor map is limited by:

- Surge line at low flow rate
- Minimum measurable rotational speed n_{\min}
- Maximum measurable rotational speed n_{\max}
- Test rig resistance curve and/or compressor choking at high flow rate.

Figure 1-8 shows a schematic diagram of a compressor map with its four different limiting boundaries.

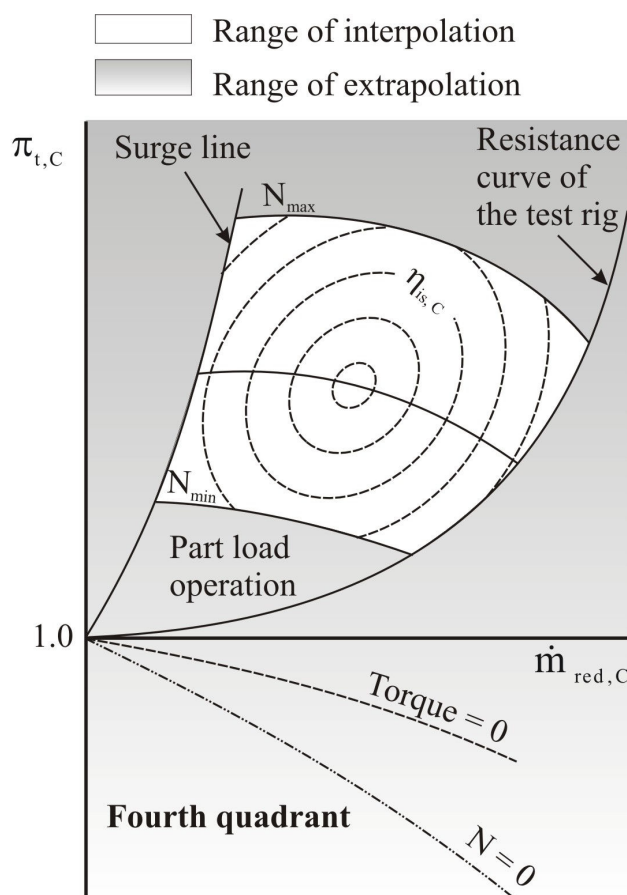


Figure 1-8 Schematic diagram of compressor map

The surge line represents the limit of the compressor stable operation. This stable operation depends on both the compressor and its ducting; i.e. it is a system characteristic. The minimum measurable rotational speed is governed by poor measuring accuracy at low rotational speed. This is because compressor total pressure ratio, temperature difference across the compressor, and compressor mass

flow rate decrease with decreasing the rotational speed. This results in an increase in the measuring error, and hence a poor measuring accuracy at low rotational speeds. Maximum measurable rotational speed depends on the ability of a test rig to provide the turbine with the power required to drive the compressor at high rotational speeds. It is also restricted by the maximum allowable turbocharger rotational speed. Test rig resistance curve represents the characteristics of the compressor ducting with a fully opened throttle valve. These characteristics differ from one test rig to the other as well as from the test rig to the engine.

Moreover, sudden engine acceleration results in a sudden increase in the amount of air swallowed by the engine. This may result in a compressor operation with total pressure ratio less than or equal to unity $\pi_{t, c} \leq 1$. This means that the operation of the compressor with an engine can extend into the fourth quadrant of the compressor map. This quadrant is not normally covered in the available compressor maps. This is mainly because of the zero or negative isentropic compressor efficiency normally encountered in this quadrant ($\pi_{t, c} \leq 1$). The compressor operates in the fourth quadrant of the map either as a throttle to the flow or as an abnormal turbine. The distinction between these two compressor operating regimes depends on the compressor torque. The compressor operates as a throttle valve when the compressor torque is greater than or equal to zero and the compressor total pressure ratio is less than unity $\pi_{t, c} \leq 1$. The measured compressor efficiency under these conditions is normally negative. Since negative compressor efficiency has no physical meaning, the compressor under these conditions is said to operate as a throttle valve. This means that the compressor is doing nothing other than increasing the losses in the engine intake manifold. The compressor can also operate in the fourth quadrant of the map as an abnormal turbine. This operating regime takes place when the compressor torque is less than zero and the compressor total pressure ratio is less than unity $\pi_{t, c} \leq 1$. The air expands through the compressor and delivers useful work to the compressor shaft. This means that the compressor operates as a turbine but with rotational speed in the opposite direction to that of a normal radial turbine. Therefore, the compressor is said to operate as an abnormal turbine.

A measured compressor performance map also provides information concerning the compressor performance only at few measured operating points. This may be suitable for the simulation of an engine running only at constant speed and load. This is because the turbocharger in this case operates at a single operating point. However, engines for automotive and traction application have a wide speed and load range. This means that the turbocharger operates at many operating points in response to the varying engine demand. Figure 1-9 (*Pucher et al. 2001*) shows an

engine operating range superimposed on a compressor performance map. The solid lines represent the measured compressor performance map using combustion chamber test rig. The symbols represent the compressor operation according to the varying engine demand. It is evident in Figure 1-9 (*Pucher et al. 2001*) that:

- Compressor performance is known only for very few engine operating points.
- Many operating points have their rotational speed lower than the minimum measured rotational speed. This occurs mainly during engine part load operation.
- Compressor operating range can be extended down to the fourth quadrant of the compressor map ($\pi_{t,c} \leq 1$).
- Some operating points are located beyond the measured surge line using the combustion chamber test rig.
- It is also possible that the compressor operates at rotational speed higher than the maximum measured rotational speed.

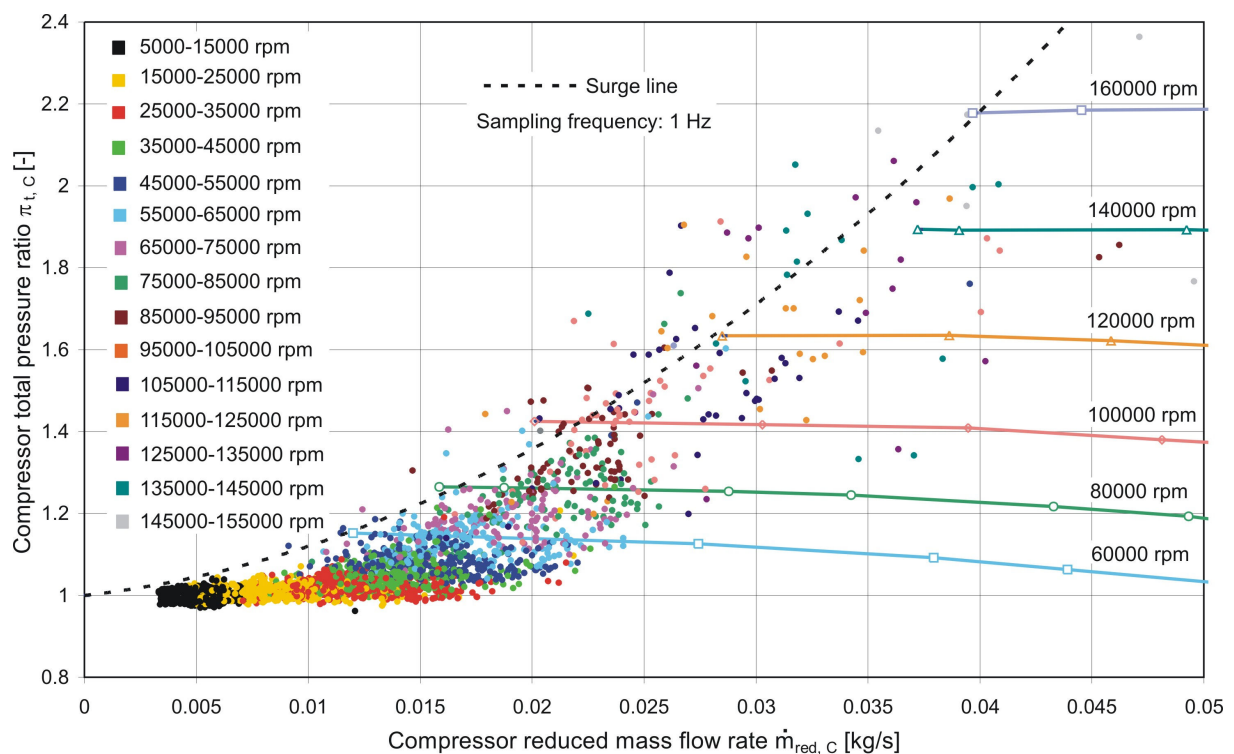


Figure 1-9 Engine operating range during engine dynamic test superimposed on a compressor performance map (*Pucher et al. 2001*)

Another significant factor in the simulation of the compressor performance is the heat transfer between the hot turbine and the cold compressor. This heat transfer causes an overestimation of the calculated compressor power using the measured compressor isentropic efficiency. This is because the measured air temperature difference across the compressor in this case results from the compressor aerodynamic work and the amount of heat transfer from the turbine to the

compressor. Therefore, the measured isentropic efficiency of the compressor will be lower than the one measured if the compressor was adiabatic. This also affects the estimated turbine efficiency according to equation (1.12) and hence the estimated turbine power. So that the amount of heat transfer from the turbine to the compressor should be subtracted from the estimated compressor total enthalpy difference in order to estimate the actual compressor power and turbine power. Turbine power and compressor power are very important for engine simulation programs. This is mainly because they are further used in iterating calculations to estimate the turbocharger rotational speed (*Linnhoff, 1985*). Therefore, inaccurate estimation of the turbine power and/or the compressor power results in a bad estimation of the engine boundary conditions.

Turbine performance likewise is known only at a few measured operating points. These operating points are governed by the power required to drive the compressor at different rotational speeds and flow rates during measurements. This means that turbine performance maps cannot provide any information regarding the turbine performance when the operating points are located between two measured performance lines or outside the measured range.

The previous discussion highlights the importance of a physically meaningful simulation of the turbocharger performance maps to enable inter- and extrapolation of the turbocharger performance maps. This physically meaningful simulation should also allow the estimation of the turbocharger performance at very low rotational speeds. Furthermore, the extrapolation of the compressor map should be extended down to compressor operation in the fourth quadrant of the map. Turbocharger non-adiabatic behavior must also be considered to obtain accurate estimation of the compressor power and the turbine power. This requires the investigation of the complex heat transfer process between the components of the turbocharger as well as between the turbocharger and the ambient.

1.9 Aim of the present research work

The present research work aims at investigating the turbocharger non-adiabatic performance. It also aims at providing a physically meaningful method of turbocharger performance simulation. This method takes into account both the non-adiabatic turbocharger performance as well as the aerodynamic performance of the compressor and the turbine respectively. It uses the measured performance maps as basis for the interpolation and extrapolation of the turbine and the compressor maps. The extrapolation of the compressor map aims at extending the compressor performance prediction down to the fourth quadrant of the map.

Three different turbochargers are investigated in the present research work. The first two turbochargers are the GT1749V 55 Trim and the GT1749V 70 Trim turbochargers from the company Honeywell Garrett. These turbochargers have a single entry turbine with variable inlet guide vanes. They are mainly used with turbocharged passenger car engines. The third turbocharger is a K29 turbocharger from the company 3K Borg Warner Turbo Systems GmbH. This turbocharger has a turbine with twin entry casing. It is mainly used with turbocharged truck and heavy diesel engines.

Two different combustion chamber test rigs are used in the present research work. The first one is used for the investigation of the single entry turbochargers. The second test rig is used for the investigation of the turbocharger with twin entry turbine. The following parameters are investigated:

- a. Effect of exhaust gas temperature on the turbocharger non-adiabatic performance.
- b. Effect of inlet guide vane position on the turbine performance as well as the turbocharger non-adiabatic performance.
- c. Effect of total pressure ratio between the inlet pipes of the twin entry turbine on the turbine performance as well as the turbocharger non-adiabatic performance.
- d. The performance of the GT1749V 55 Trim compressor at very low rotational speeds as well as in the fourth quadrant of the compressor map.
- e. The aerodynamic performance of micro compressors.

The compressor performance at very low rotational speeds and fourth quadrant of the compressor map is measured by the Technical University Berlin. These measurements are conducted in cooperation with the institute of turbomachinery IfS, University of Hanover, in the framework of a research project for the "Forschungsvereinigung Verbrennungskraftmaschinen FVV" (*Pucher et al., 2003b*).

2. LITERATURE SURVEY

2.1 Turbocharger non-adiabatic performance

Turbocharger non-adiabatic performance results from the heat transfer between the components of the turbocharger and between the turbocharger and its ambient. Chapman et al. (2002) investigated the effect of heat transfer on the turbocharger performance using a water cooled turbocharger. They found that the oil and water cavities surrounding the rotor assembly acts as a thermal barrier to allow virtually no heat transfer between the turbine and the compressor. Pucher and Nickel (2002) investigated the effect of oil inlet temperature on the measured isentropic compressor efficiency at a rotational speed of 60000 rpm using air at 295K to drive the turbine (cold measurements). They showed that increasing the oil inlet temperature from 55°C to 85°C results in 10% decrease in the measured compressor isentropic efficiency. However, no significant effect of oil temperature was recorded when the inlet temperature was increased from 75°C to 85°C. They reported that this decrease in the measured compressor isentropic efficiency is due to heat transfer from the oil to the compressor during the cold measurements. They concluded that the measured compressor efficiency is a function of the oil inlet temperature at low turbocharger rotational speeds.

Malobabic et al. (1983) reported that the heat transfer to the compressor has a negative influence on the compression process, not only with respect to the increase of the compressor outlet temperature but also with respect to the required mechanical power. They also reported that the turbine power is reduced due to the heat loss to the ambient and to the compressor during the expansion process. Therefore, the turbocharger will operate at a considerably lower speed which in turn influences the charging process (*Malobabic et al., 1983*). Rautenberg and Kämmer (1984) modelled the non-adiabatic turbocharger performance by decomposing the amount of heat transfer to the compressor into three portions. The first portion Q_{before} takes place before the impeller, the second portion Q_{imp} takes place during the compression process in the impeller, and the third portion Q_{after} takes place after the impeller. They applied the same principle to the heat transfer from the turbine and presented thermodynamic analysis of the non-adiabatic compression and expansion processes. This concept will be used in Section 4.2 below.

Malobabic and Rautenberg (1987) showed that the estimated non-adiabatic turbine efficiency using the measured turbine inlet and outlet temperatures is considerably higher than the adiabatic turbine efficiency. They found that the non-adiabatic turbine efficiency was greater than 100% for a wide range of operating points. They also

showed that non-adiabatic turbine efficiency increases hyperbolically in the direction of higher temperatures and lower mass flow rates. They concluded that non-adiabatic turbine efficiency is not a measure of the aerodynamic quality and/or the mechanical power output of the turbine. Hagelstein et al. (2002) reported that the nature of heat flow in the turbocharger is extremely complex and the solution by a real, significant infinitesimal calculation (CFD) is almost impossible. They simplified the heat model of Rautenberg and Kämmer (1984) and decomposed the amount of heat transfer to the compressor into two portions only. The first portion Q_{before} takes place before the compressor impeller, while the second portion Q_{after} takes place after the compressor. They considered the compression process in the impeller to be adiabatic. Hagelstein et al. (2002) also presented thermodynamic analysis of the non-adiabatic compressor performance using the modified model of Rautenberg and Kämmer (1984).

Baar and Lücking (2002) presented thermodynamic analysis of the turbocharger non-adiabatic performance by applying heat balance to the turbocharger. Bohn et al. (2003a, 2003b, 2003c) performed 3D conjugate calculation for a passenger car turbocharger. They developed a complex 3D model that includes the compressor, the oil cooled bearing housing, and the turbine.

Chapman et al. (2002) investigated the effect of heat transfer on the turbine and the compressor efficiencies of a water cooled turbocharger both numerically and experimentally. They estimated the amount of heat transfer inside/from the turbocharger by applying heat balance to the turbocharger using the experimental data. The amount of heat transfer was also estimated by the CFD code during the numerical investigation. The CFD code provides polynomial expressions for estimating the amount of heat transfer in the turbine and the compressor at each operating point. Chapman et al. (2002) applied these polynomial expressions to correct both the turbine and the compressor efficiencies. They showed that heat transfer rates into and out of the turbocharger significantly affect the turbocharger efficiency.

2.2 Turbocharger performance simulation

Turbocharger performance simulation aims at predicting the turbocharger operating characteristics at every engine operating point. It implies the simulation of both the compressor performance map and the turbine performance map.

2.2.1 Compressor performance simulation

Many different models have been presented for the simulation of compressor performance. Most of these models are based on the measured compressor

performance maps. Zinner (1980, 1961) presented diagrams for the estimation of turbocharger operating points. These diagrams are based on energy balance of the turbocharger and continuity. Kurzke (1996) discussed the extrapolation of compressor maps towards very low rotational speed. He also discussed the problems of reading the compressor maps by the simulation programs due to the shape of the performance lines at the choking and the surge limits. He showed that a compressor map in the standard form cannot be directly used in performance calculations. Therefore, he presented a method to allow the reading of compressor maps independently of the shape of the performance lines. Werner (2001) presented a method for predicting the compressor performance using the performance maps. Chesse et al. (2000) applied a mathematical model for the estimation of compressor operating points. They estimated the mass flow rate and the isentropic efficiency using two dimensional interpolation of the compressor map in matrix form. They calculated the compressor power for operating points beyond the surge line of the manufacturer performance map using the simplified equation

$$\dot{W}_C = K_C n^2 \quad (2.1)$$

They reported that the factor K_C is specific to the compressor being used.

Kouremenos et al. (1994) simulated the compressor performance using the method of operational similarity. They assumed the compressor to be adiabatic. They presented polynomial equations for the compressor efficiency and the normalized isentropic total enthalpy difference as functions of the flow coefficient. The coefficients of these polynomial equations were estimated from the measured compressor map using the least squares method. Kouremenos et al. (1994) reported that this method can predict the turbocharger operation at any point from 50% up to 100% of load reliably. Willems and Jager (2000) approximated the compressor pressure coefficient by a cubic polynomial in the stage flow coefficient. The unknown parameters in this cubic polynomial were also estimated from the measured compressor map. The same approach was also used by Hild et al. (1998) to simulate the compressor performance. Staudacher et al. (2003) compared the extrapolation using the conventional compressor map parameters with that using dimensionless parameters. They showed that the latter with high quality initial data represents the most accurate solution. They also reported that the extrapolation using conventional map parameters is only possible if values of pressure ratio and reduced mass flow rate of the rotational speed line $n=0$ are known.

Many authors have used mean value modeling for the simulation of compressor performance. Aungier (2000, 1995) presented aerodynamic performance prediction models for centrifugal compressors. These models make use of empirical correlations for the aerodynamic losses and the impeller slip factor. Mueller et al.

(1998) presented mean value modeling for the turbocharger compressor assuming the compressor to be adiabatic. Mean value modeling of compressor performance was also used by Kolmanovsky and Stefanopoulou (2000).

Miersch et al. (2000) modelled the compressor as a simple throttle valve in order to estimate the compressor flow rate as a function of the compressor static pressure ratio. They performed a coordinate transformation in order to enable the estimation of the pressure ratio at part load as well as in the fourth quadrant of the compressor map. Storset et al. (2000) modelled the flow through the compressor by means of compressor mass flow parameter. This parameter depends on compressor static pressure ratio and rotational speed. They considered the compressor efficiency to be constant at steady state engine operation. Fiaschi et al. (2001) presented and analyzed five different functions representing the polytropic efficiency versus the stage flow coefficient. These functions are based on physically meaningful models and include terms for friction losses, incidence effect, choking flow limit, disk friction, and leakage losses.

Swain (1990), Swain and Connor (1992), Came et al. (1996), and Swain and Meese (1998) presented simplified models for predicting centrifugal compressor performance. The impeller efficiency in these models was considered to be function of the peak impeller efficiency, flow rate at peak impeller efficiency, flow rate, and choking flow rate. Gravdahl et al. (2002) modelled the compression process as an isentropic compression from the total pressure and the total temperature at the compressor inlet to the total pressure at the compressor outlet. This isentropic compression is followed by an isobaric entropy increase. They considered this entropy increase to be due to shock loss, and fluid friction loss.

Most of the information available for the performance in the fourth quadrant of the performance map concerns pumps (*Senoo and Yamaguchi, 1986; Engeda, 1987; Martin, 1983; Martin, 2000*) or axial flow compressors (*Riegler et al., 2000*). Very little data is available for the radial flow compressors.

2.2.2 Turbine performance simulation

Zinner (1980, 1961), and Bulaty (1974) estimated the turbine flow rate by modeling the turbine as an isentropic nozzle with an effective flow area $A_{\text{eff}, T}$ and a discharge coefficient $C_{d, T}$

$$\dot{m}_T = C_{d, T} A_{\text{eff}, T} \frac{p_{6t}}{\sqrt{R_{\text{exh}} T_{6t}}} \Phi_T \quad (2.2)$$

The turbine flow function Φ_T in equation (2.2) is given by

$$\Phi_T = \sqrt{\frac{2 \kappa_{\text{exh}}}{\kappa_{\text{exh}} - 1} \left(\pi_{6t8s}^{-2/\kappa_{\text{exh}}} - \pi_{6t8s}^{-(\kappa_{\text{exh}}+1)/\kappa_{\text{exh}}} \right)} \quad 1 \leq \pi_{6t8s} < \left(\frac{\kappa_{\text{exh}} + 1}{2} \right)^{\kappa_{\text{exh}} - 1} \quad (2.3)$$

$$\Phi_T = \sqrt{\kappa_{\text{exh}} \left(\frac{2}{\kappa_{\text{exh}} + 1} \right)^{\kappa_{\text{exh}} - 1}} \quad \pi_{6t8s} \geq \left(\frac{\kappa_{\text{exh}} + 1}{2} \right)^{\kappa_{\text{exh}} - 1} \quad (2.4)$$

Values of the discharge coefficient and the effective flow area can be estimated from the measured turbine performance map. Kolmanovsky et al. (1999) corrected the turbine flow function by inserting additional functions of the guide-vane position. They also presented the turbine effective flow area as a polynomial function of guide-vane position. Rodgers (2003) reported that the attainable efficiency of radial turbines is dominated by the turbine blade speed parameter, turbine exit flow coefficient c_{8m}/u_7 , and turbine specific speed. He also reported that extensive experimental results and analysis for a wide variety of radial turbine designs confirm the dominance of the turbine blade speed parameter on the radial turbine efficiency. Therefore, turbine blade speed parameter is the most commonly used parameter for describing the turbine efficiency.

Bulaty (1974) applied a polynomial function for the ratio of turbine efficiency to maximum turbine efficiency in terms of the ratio of turbine blade speed parameter to turbine blade speed parameter at maximum efficiency. Malobabic and Rautenberg (1985) presented an equation for estimating the turbine efficiency as a function of the turbine blade speed parameter and the turbine diameter ratio. They obtained this equation by assuming inlet flow without incidence and outlet flow without swirl at the turbine design point. Kolmanovsky et al. (1999) presented the turbine efficiency as a polynomial function of the turbine blade speed parameter and the guide-vane position. They obtained the coefficients of this polynomial by fitting the experimental data. The same approach was also used by Hild et al. (1998).

Mean value modeling of turbine performance using empirical loss correlations was applied by Chen and Winterbone (1990) and Baines (1998). Balje (1981) presented detailed performance analysis of radial inward flow turbines.

Ghasemi et al. (2002) presented models for predicting the performance of twin entry turbines under steady state and partial admission operating conditions.

2.3 Aerodynamic losses

Aerodynamic losses in turbomachines can be classified into volute losses, diffuser

losses for compressors or stator losses for turbines, and rotor losses. Rotor losses in turn can be classified into incidence, friction, passage, disk friction, tip clearance, secondary flow, blade loading, and diffusion loss. Additional shock losses take place when the fluid Mach number exceeds unity.

Aerodynamic losses of radial turbomachines were reviewed by Logan (2003), and Whitfield and Baines (1990). Denton (1993) discussed the origins and effects of losses in turbomachines. He presented models for estimating viscous effects in boundary layers, viscous effects in mixing processes, shock waves, tip clearance loss, and miscellaneous losses. Japikse (1996), and Aungier (2000, 1995) presented correlations for predicting the aerodynamic losses of centrifugal compressors.

Incidence losses take place at the rotor inlet due to mismatch between the flow angle and the blade angle. The historical incidence loss model considers this loss to be proportional to the kinetic energy based on normal component of the relative velocity at the rotor inlet (*Whitfield and Baines, 1990*). Japikse (2000) reported that this model appears to work sensibly for an important part of the impeller loss process. However, a single preferred value for the optimum incidence angle varies substantially (*Japikse, 2000*). The optimum incidence angle is the flow angle by which the incidence loss is zero. Whitfield and Baines (1990) obtained an expression for the optimum incidence angle by applying the steady incompressible continuity equation to the flow at the rotor inlet. Other incidence loss correlations are also presented by Aungier (2000, 1995), and Gravdahl et al. (2002).

Rodgers (1991) derived a simple correlation for the centrifugal compressor efficiency decrement due to inducer shroud relative Mach number greater than unity. He also presented correlation for predicting the effect of changing the Reynolds number on centrifugal compressor efficiency. Lohmberg et al. (2001) presented a model for estimating shock losses in a high pressure ratio turbocharger. This model was obtained by applying simplifying assumptions such that the flow at the impeller inlet can be approximated with that across normal shock waves.

Impeller friction loss is mostly modelled with an equivalent pipe flow model (*Rodgers, 2000; Whitfield and Baines, 1990*). Rodgers (2000) treated the impeller passage as curved pipe bend and presented correlations for estimating friction, secondary flow, windage, and shock losses. Lütke (1999, 1989) presented correlations for estimating the friction power loss of centrifugal compressors as well as disk friction loss.

Zangeneh et al. (1998) reported that numerical prediction of pump impellers showed a good correlation between the intensity of secondary flows and the gradient of the

static pressure coefficient on the suction surface of the impeller.

Senoo and Ishida (1987, 1986) reported that the tip clearance causes change of the input power and increase in the pressure loss. They presented expressions for estimating the effect of tip clearance and blade loading on compressor performance. Expressions for predicting the effect of blade loading and tip clearance were also presented by Aungier (2000, 1995) and Denton (1993).

Stanitz (1952a) developed an analysis method for predicting the performance of vaneless diffusers. He assumed one dimensional compressible flow with friction, heat transfer, and area change in vaneless diffusers. Traupel (1977, 1962) presented a model for predicting the performance of vaneless diffusers assuming one dimensional compressible flow and uniform velocity distribution at the diffuser inlet. This model is based on the solution of conservation equations of the flow in vaneless diffusers. He considered the losses in vaneless diffusers to be due to friction and energy dissipation. He also reported that the friction coefficient can be calculated using pipe flow models while the dissipation coefficient can be calculated using the relation

$$C_{dis} = C_f + 0.0015 \quad (2.5)$$

Japikse (1984) presented detailed analyses of design technology and performance prediction of diffusers. Rodgers (1984) analyzed the performance of vaneless parallel wall diffusers. He showed that vaneless diffuser losses at peripheral Mach numbers less than 1.2 and optimum or lower specific speeds are essentially due to internal friction. He also presented a correlation for estimating the loss coefficient of a parallel wall vaneless diffuser as a function of friction coefficient, width to diameter ratio, diffuser diameter ratio, and absolute flow angle at the impeller outlet. Heyes (1998) reported that the impeller outlet flow has a strong influence on the diffuser performance. He also reported that a good diffuser recovery can be obtained if the impeller outlet flow is uniform in its flow velocity and direction. Dou and Mizuki (1998) analyzed the flow in parallel wall vaneless diffusers with large width to radius ratio using 3D boundary layer theory. Based on experimental observations of Sideris and Van den Braembussche (1987), Van den Braembussche (1990) assumed the swirl velocity at the impeller outlet to be constant along the impeller circumference. Meese and Swain (2001) conducted experimental analysis and analytical investigation for the vaneless diffusers of two automotive turbochargers. They measured the static pressure distribution at the diffuser inlet and outlet and assumed one dimensional flow. They applied the loss coefficient of Rodgers (1984) to predict the vaneless diffuser losses. They also derived an expression for the length of the flow path from diffuser inlet to outlet assuming free vortex flow. Analysis of vaneless diffuser

performance using the measured static pressure distribution at the diffuser inlet and outlet was also presented by Rautenberg et al. (1998, 1974) for symmetric vaneless diffusers, and Seume et al. (2003) for asymmetric vaneless diffusers.

Hagelstein et al. (2000) presented experimental and numerical investigations for an external volute of rectangular cross section. They showed that the volute losses at high mass flow rate are about twice the value at the design point. Sideris and Van den Braembussche (1986) reported that the volute acts like a diffuser at smaller mass flow rates and this results in a static pressure rise between volute inlet and outlet. At higher mass flow rates, the volute is too small and the flow accelerates resulting in a decreasing static pressure from volute inlet to outlet (*Sideris and Van den Braembussche 1986*). Van den Braembussche (1990), Van den Braembussche et al. (1999), Rautenberg et al. (1998), and Seume et al. (2003) presented models for the analysis and prediction of the flow in centrifugal compressor volutes. These models take into account the vortical structure of the flow which has been observed during 3D flow measurements.

2.4 Slip factor

The slip factor accounts for the reduction in the anticipated swirl velocity at the impeller outlet due to imperfect guidance of the flow by the blades. Figure 2-1 shows the difference between the actual and the ideal velocity triangles at the impeller outlet. The ideal velocity triangle at the impeller outlet is achieved only by perfectly guiding the flow through the impeller. The relative flow angle at the impeller outlet coincides with the blade angle at the impeller outlet in this case. This velocity triangle is called ideal because the actual relative flow angle at the impeller outlet is always

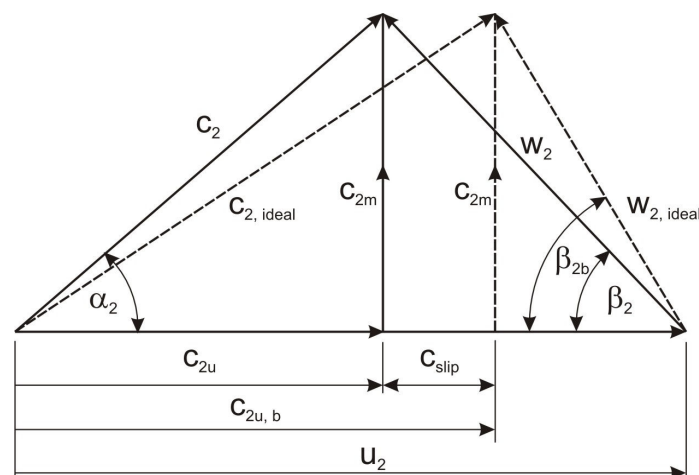


Figure 2-1 Comparison between the ideal and the actual velocity triangle at the impeller outlet

lower than the blade angle due to imperfect guidance of the flow. The two angles will coincide with each other only with the application of infinite number of blades. However, the blade number cannot exceed a certain optimum number (Rodgers, 2000). Therefore, deviation of the actual relative flow angle from the blade angle takes always place at the impeller outlet. This deviation results in reduction of the actual swirl velocity. Therefore, a slip velocity always exists at the impeller outlet. The slip velocity is defined as the difference between the ideal swirl velocity and the actual swirl velocity at the impeller outlet

$$C_{slip} = C_{2u,b} - C_{2u} \quad (2.6)$$

The slip factor of a centrifugal compressor is defined as the ratio of the actual swirl velocity at the impeller outlet to the ideal swirl velocity

$$\mu = \frac{C_{2u}}{C_{2u,b}} = 1 - \frac{C_{slip}}{C_{2u,b}} \quad (2.7)$$

The ideal swirl velocity is given by

$$C_{2u,b} = u_2 - \frac{C_{2m}}{\tan \beta_{2b}} \quad (2.8)$$

The meridional velocity at the impeller outlet is given by

$$C_{2m} = \dot{m}/(\rho_2 A_2) \quad (2.9)$$

Many factors affect the flow guidance, and hence the slip factor. Wiesner (1967) considered the slip factor to be a function of blade number, blade angle at the impeller outlet, and the impeller diameter ratio. Balje (1981) reported that the assumption of Wiesner (1967) appears to be a highly simplifying assumption in view of the complex flow mechanism within and behind the impeller. Balje (1981) and Ziegler et al. (2002) reported that the slip factor is influenced by the downstream conditions for vaneless or vaned diffusers. Eckardt (1980) showed that the blade shape also affects the slip factor. He concluded that additional consideration of the impeller blade shape will be mandatory for more accurate slip correlations. Balje (1981), Harada (1988), Oh and Oh (2000), and Oh (2001) reported that the slip factor is also influenced by the blade loading.

Several efforts have been made to obtain accurate estimation of the slip factor under different geometrical and operating conditions. As early as 1927, Stodola (1945) derived an expression for the estimation of the slip velocity in the form

$$C_{slip} = \frac{\pi u_2 \sin \beta_{2b}}{z} \quad (2.10)$$

Busemann (1928) analyzed the flow in impellers with logarithmic blades to obtain a

somewhat more accurate model for the slip factor. He presented a model that requires a family of curves for the estimation of the slip factor. Stanitz (1952b) presented theoretical analysis of radially bladed impellers using finite difference method. He showed that the slip factor for radially bladed impellers can be presented by

$$\mu = 1 - \frac{0.63 \pi}{z} \quad (2.11)$$

Whitfield and Baines (1990) reported that Stanitz correlation was an exact solution and was not applied to conditions beyond those of the theoretical analysis. Wiesner (1967) approximated successfully the Busemann slip factor by a simple empirical equation. He compared the slip factor with the test data of more than 60 impellers at the best efficiency point and obtained the simple empirical correlation

$$\mu = 1 - \frac{\sqrt{\sin \beta_{2b}}}{z^{0.7}} \quad (2.12)$$

He also presented a correction procedure for diameter ratios larger than a limiting diameter ratio ε_{Lim} in the form

$$\mu = \left(1 - \frac{\sqrt{\sin \beta_{2b}}}{z^{0.7}} \right) \left(1 - \left(\frac{\varepsilon - \varepsilon_{Lim}}{1 - \varepsilon_{Lim}} \right)^3 \right) \quad (2.13)$$

where

$$\varepsilon_{Lim} = \exp(-8.16 \sin \beta_{2b} / z) \quad (2.14)$$

and

$$\varepsilon = D_1 / D_2 \quad (2.15)$$

Based on the results of Busemann (1928), Aungier (2000, 1995) presented a more accurate approximation to the limiting diameter ratio in the form

$$\varepsilon_{Lim} = \frac{\mu - \mu^*}{1 - \mu^*} \quad (2.16)$$

where

$$\mu^* = \sin(19^\circ + 0.2\beta_{2b}) \quad (2.17)$$

A corrected slip factor for $\varepsilon > \varepsilon_{Lim}$ was given by Aungier (2000, 1995) in the form

$$\mu_{cor} = \mu \left(1 - \left(\frac{\varepsilon - \varepsilon_{Lim}}{1 - \varepsilon_{Lim}} \right)^{\sqrt{\beta_{2b}/10}} \right) \quad (2.18)$$

Theoretical correlations for estimating the slip factor were also presented by Harada (1988), Oh and Oh (2000), and Oh (2001).

3. TEST-RIG AND ERROR ANALYSIS

3.1 Introduction

Two test rigs are used in the present research work. The first one is used for the performance investigation of turbochargers with single entry turbines. The second one is used for turbochargers with twin entry turbines. Each test rig uses a combustion chamber for the production of exhaust gas at high temperature “hot measurements”. This means that the performance of the turbocharger during measurements is quasi stationary. “Cold measurements” can also be performed on both test rigs. In this case the combustion chamber is switched off and compressed air is used to drive the turbine. Cold measurements are very important for the investigation of the turbocharger adiabatic performance, while hot measurements are very important for the investigation of the turbocharger non-adiabatic performance. Hot measurements are also important for the performance investigation at high turbocharger rotational speeds. This is mainly because the fluid power supplied to the turbine during cold measurements is normally insufficient to drive the turbocharger at high rotational speeds.

The first test rig has a combustion chamber with a lower capacity compared to that of the second one. Therefore, it cannot be used for investigating truck- and racing car turbochargers. This is mainly because the fluid power required to drive these turbochargers is normally higher than the capacity of the small combustion chamber test rig.

3.2 Small combustion chamber test rig

3.2.1 Design of the small combustion chamber test rig

Small combustion chamber test rig is used for investigating passenger car turbochargers with single entry turbines. Figure 3-1 shows the lay-out of this test rig. A main valve controls the flow rate of the air supplied to the test rig. The supplied air is divided into combustion air and by-pass air. The combustion air mixes with the fuel in the combustion chamber to form a fuel-air mixture. This mixture is burnt in the combustion chamber using a spark plug. By-pass air mixes with the hot exhaust gases at the rear part of the combustion chamber to control the exhaust gas temperature. A combustion chamber by-pass valve controls the amount of by-pass air. Opening the combustion chamber by-pass valve increases the amount of by-pass air and hence reduces the exhaust gas temperature.

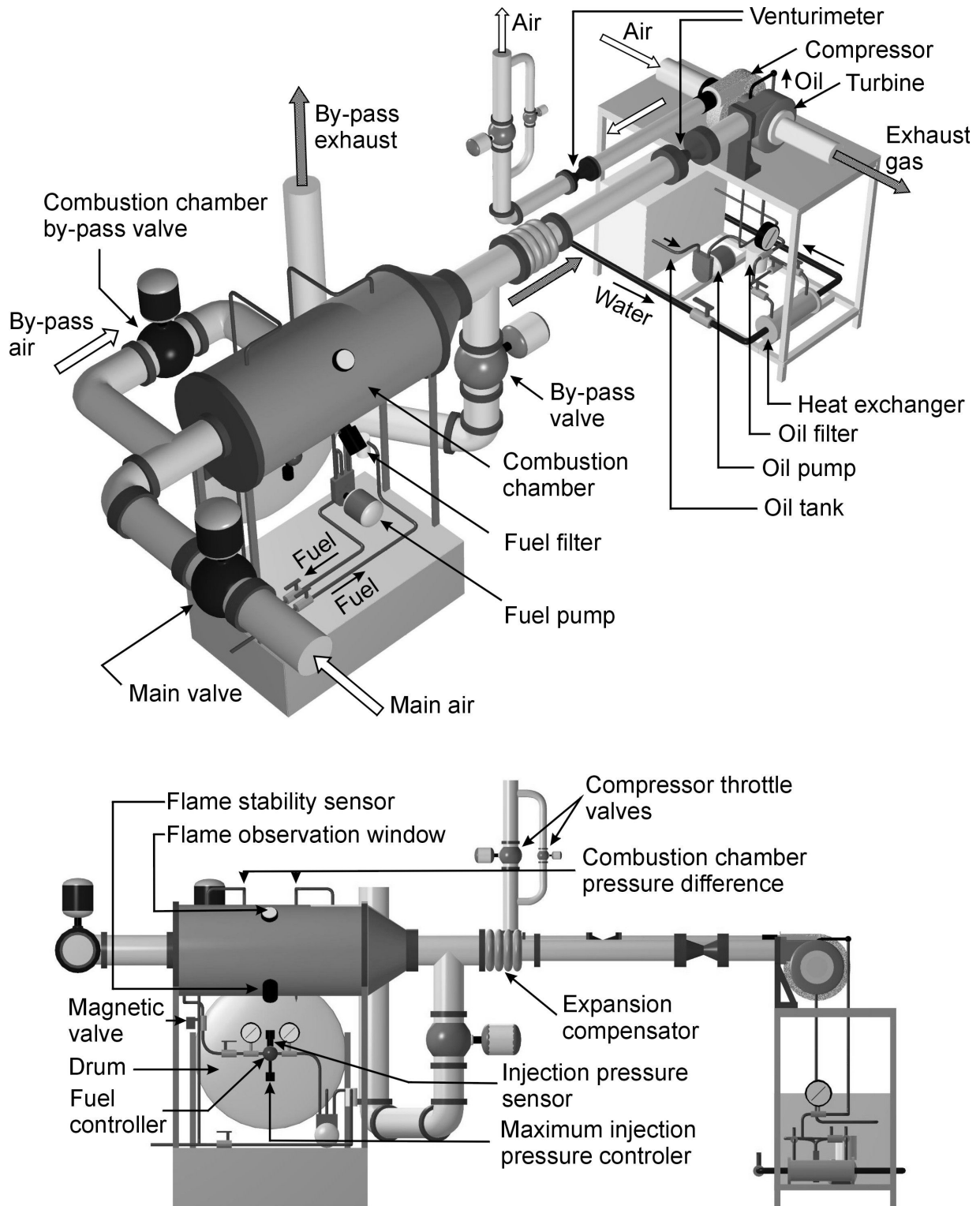


Figure 3-1 Isometric view and layout of the small combustion chamber test rig

Fuel is supplied to the combustion chamber by means of a rotary pump which delivers fuel at 25 bar. Fuel injection pressure and mass flow rate are regulated using a drum with fuel controller to achieve stoichiometric combustion during measurements. A diaphragm separates the drum into two sides. Each side receives a static pressure signal from the combustion chamber. This imposes a pressure difference between the two sides of the diaphragm. The pressure difference causes the diaphragm to deform. A rod contacting the diaphragm at the centre point is used to transport the diaphragm deformation into a small throttle valve. Thereby, fuel injection pressure and flow rate are proportional to the pressure difference of the combustion chamber. The maximum allowable injection pressure is controlled with an electronic controller. This controller sends a control signal to switch the combustion chamber off if the injection pressure exceeds the maximum allowable injection pressure. The maximum allowable injection pressure of the small combustion chamber is adjusted at 22 bar. The combustion chamber is also provided with a flame stability sensor. This sensor detects the fluctuations in the flame temperature based on the radiation properties of the flame. It also sends a control signal to switch the combustion chamber off if the temperature fluctuations exceed some limiting value. A glass window is also used to observe the flame quality.

A by-pass valve located after the combustion chamber is used to control the turbine operation. It is similar in principle to the by-pass control of turbochargers. The by-pass valve opens to reduce the flow rate of the exhaust gas through the turbine. This reduces the turbocharger rotational speed.

A flexible pipe joint is used to reduce the effect of pipe thermal expansion on the measured turbocharger. It is compressed or expanded to maintain the distance between the combustion chamber and the turbocharger almost constant during measurements. The combustion chamber and the hot pipes are thermally insulated.

Two throttle valves are used to control the compressor operating points. The larger one is normally used in the operating range extending from the choking limit to shortly before the surge limit. The smaller one is used at surge point to achieve accurate estimation of the surge point.

A rotary pump is used to pump the oil into the turbocharger bearing. The oil is stored in oil tank and heated in the tank, if necessary, by means of electrical heater. A counter flow heat exchanger is used to maintain the oil inlet temperature within ± 5 °C. The oil pipe line can be adjusted using set of valves to allow the oil to by-pass the heat exchanger and flows directly into the bearing. Oil filter is used to clarify the oil before entering the bearing housing.

3.2.2 Instrumentation

Figure 3-2 shows a schematic of the small combustion chamber test rig together with its measuring points. Two venturimeters are used for estimating the turbine and the compressor mass flow rate. Static pressure measurements are carried out using four static pressure taps of 0.5 mm diameter at each measuring location. These taps are uniformly distributed around the pipe circumference. Total pressure probes and total temperature probes are used to measure the total pressure and the total temperature, respectively. Total temperature probes have Ni-CrNi-thermocouples (K-type) and use ice as a reference point for the temperature measurements.

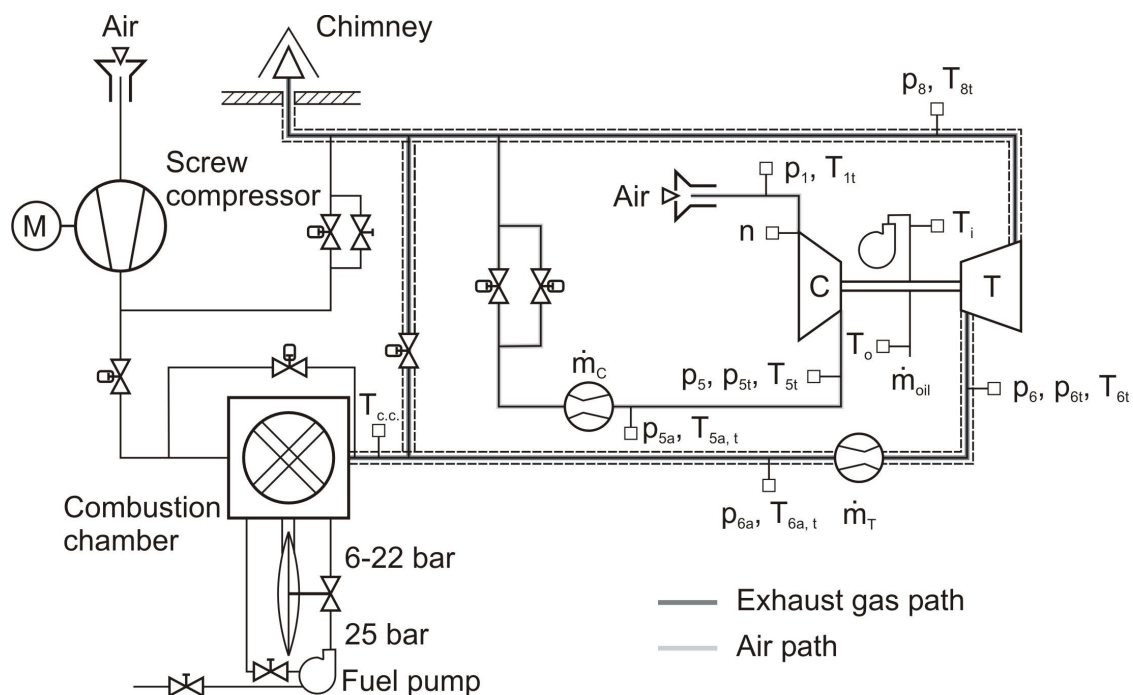


Figure 3-2 Schematic of the small combustion chamber test rig

Pressure transducers with different measuring ranges are used to sense the pressure signals and convert them into electrical signals. Depending on the level of the measured pressure, transducers with measuring ranges of 0–0.350 bar and 0–2 bar are used with the small combustion chamber test rig. Turbocharger rotational speed is measured with an eddy current sensor with a maximum linearity of $\pm 0.2\%$ of the full scale reading (± 800 rpm). Oil volume flow rate is measured with a turbine flow-meter with a linearity of $\pm 0.15\% \dots \pm 1\%$ of the measuring range.

Static pressure and total temperature are measured at the compressor inlet. These measurements together with the mass flow rate enable the estimation of total pressure at the compressor inlet. Static pressure, total pressure, and total

temperature are measured at the compressor outlet. Total pressure at the compressor outlet is also estimated from the measured static pressure, total temperature, and mass-flow rate. The estimated value is compared with the measured one to assure the accuracy of measurements. Total temperature and static pressure are measured at the venturimeter inlet to estimate the fluid density. Pressure difference across the venturimeter is measured to estimate the mass flow rate. Static pressure, total pressure, and total temperature are measured at the turbine inlet while static pressure and total temperature are measured at the turbine outlet.

A data-acquisition system is used to collect the measured data and send them to a computer. A computer program, written in HP VEE visual programming language, is used to collect and present the measured data during the experiment.

3.3 Large combustion chamber test rig

3.3.1 Design of the large combustion chamber test rig

Large combustion chamber test rig is used mainly for the investigation of turbochargers with twin entry turbines. It is also used for investigating turbochargers with fluid power demand higher than the capacity of the small combustion chamber test rig. Figure 3-3 shows the construction of the large combustion chamber test rig. The principle of this test rig is very similar to that of the small combustion chamber test rig. However, an injection pump is used to feed the combustion chamber with the required fuel. Injection pressure of the large combustion chamber ranges from 50 to 200 bar. Fuel flow rate and injection pressure are varied by varying the stroke length of the injection pump. Two pipes are feeding the twin entry turbine. Each pipe has a valve to control the flow rate and the total pressure through the pipe. The two valves are used together to adjust the total pressure ratio between the two pipes. By this means, twin entry turbine performance under partial admission conditions can be investigated. A compact oil system with integrated heating system is used to feed the turbocharger with oil.

3.3.2 Instrumentation

Figure 3-4 shows a schematic diagram of the large combustion chamber test rig with its measuring points. The instrumentation of this test rig is also very similar to that of the small combustion chamber test rig. However, a nozzle flow meter is located at the suction side of the compressor to estimate the compressor flow rate. An inductive sensor with a magnetic nut attached to the shaft is used to measure the turbocharger

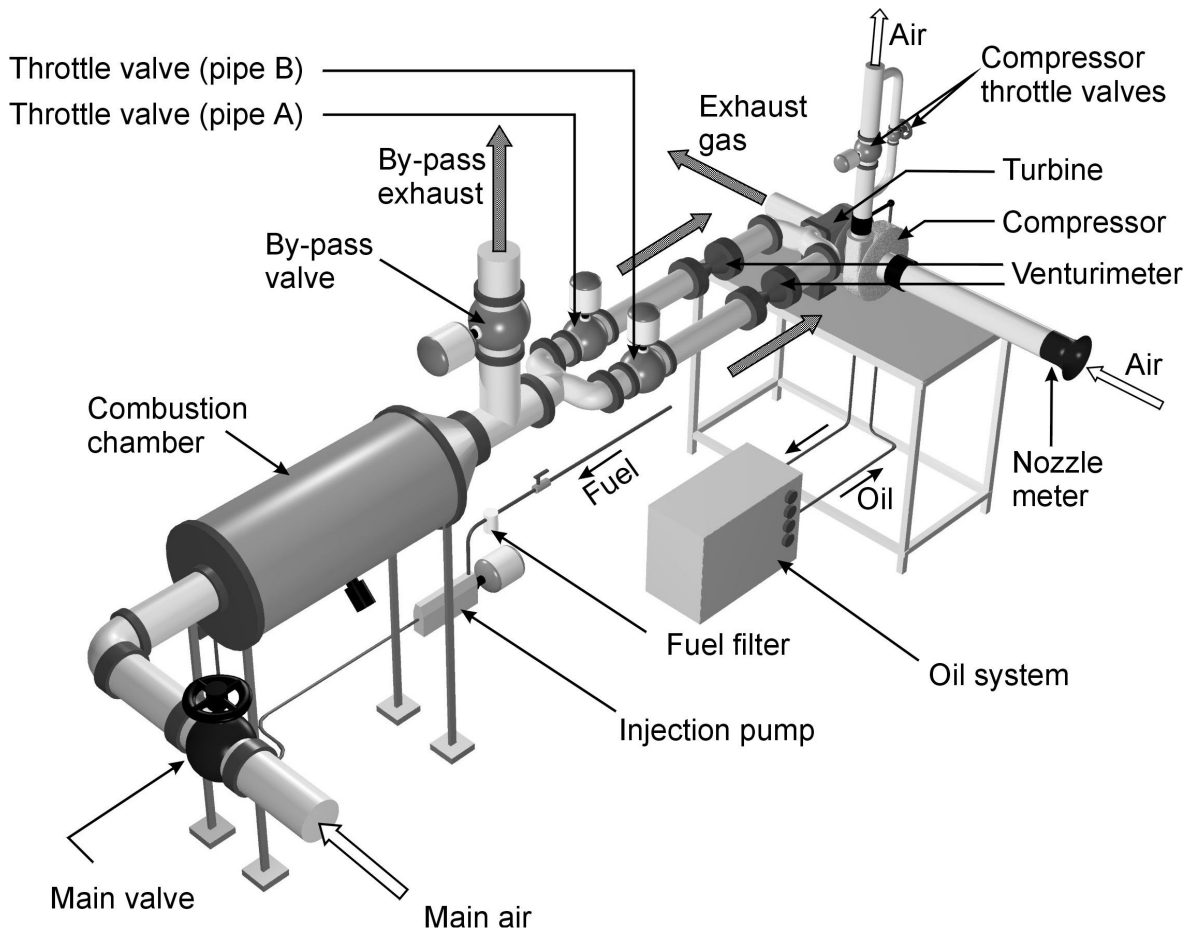


Figure 3-3 Layout of the large combustion chamber test rig

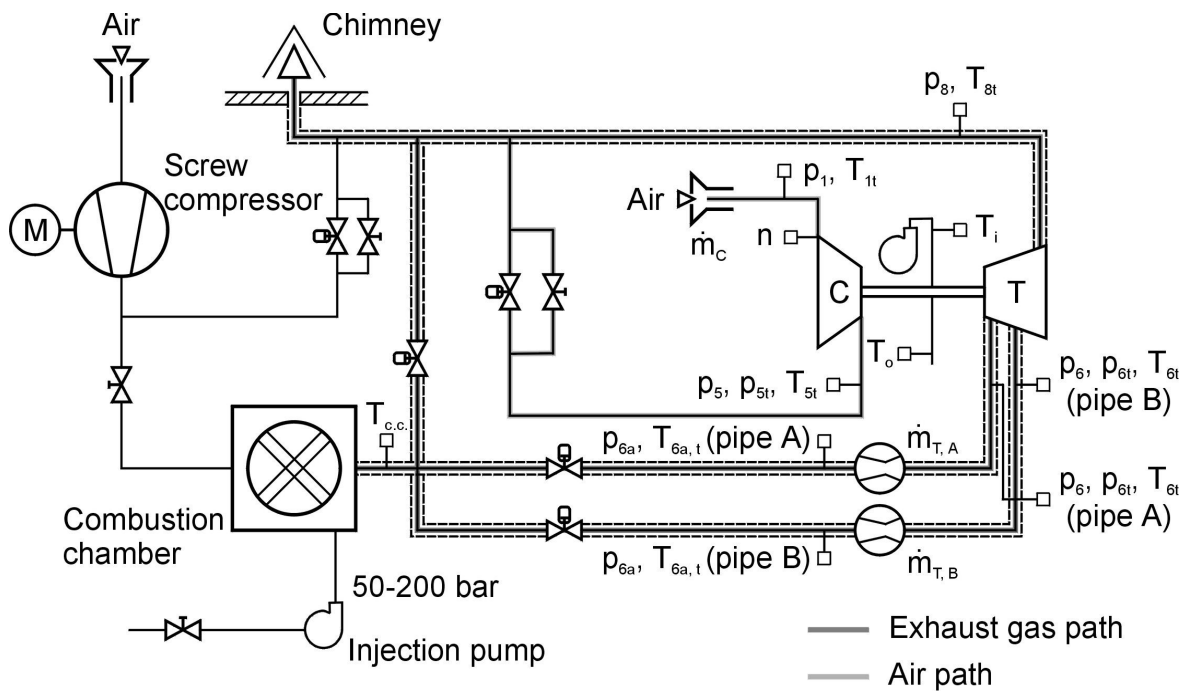


Figure 3-4 Schematic of large combustion chamber test rig

rotational speed.

3.4 Test turbochargers

Three turbochargers are investigated in the present research work. Two of them have a single entry turbine with adjustable guide vanes. These turbochargers are the GT1749V 55 Trim turbocharger and the GT1749V 70 Trim turbocharger by Honeywell Garrett. The turbocharger trim is defined on the basis of the compressor impeller area ratio

$$\text{Trim} = \frac{A_2}{A_1} \cdot 100 \quad (3.1)$$

The third turbocharger has a twin entry turbine without guide vanes. This turbocharger is the K29 turbocharger of the company Borger Warner Turbo Systems GmbH. The GT1749V 55 Trim and the K29 turbochargers are used mainly in the investigation of the turbocharger non-adiabatic performance. Figure 3-5 shows an overview of these turbochargers while Table A-1 shows the main dimensions of the three turbochargers investigated. The main dimensions of the GT1749V 55 Trim turbocharger and the GT1749V 70 Trim turbocharger are very similar.

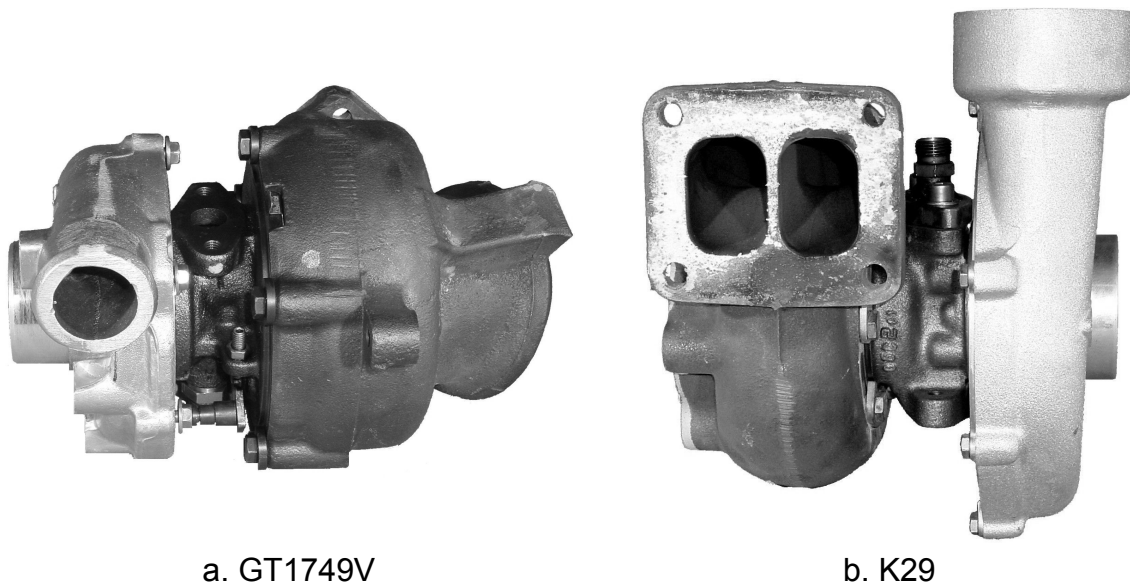


Figure 3-5 Overview of the GT1749V 55 Trim and the K29 turbochargers

The GT1749V 70 Trim turbocharger is used mainly for the investigation of the aerodynamic losses and the slip factor of micro compressors. Therefore, additional static pressure taps are located in the back side of the vaneless diffuser at diameter ratio $\lambda=1.26$ and 1.6 , where

$$\lambda = D/D_2 \quad (3.2)$$

Each measuring location has 8 static pressure taps with 0.5 mm inner diameter. These taps are uniformly distributed around the circumference of the vaneless diffuser. Figure 3-6 shows the locations of the static pressure taps in the vaneless diffuser of the GT1749V 70 Trim compressor.

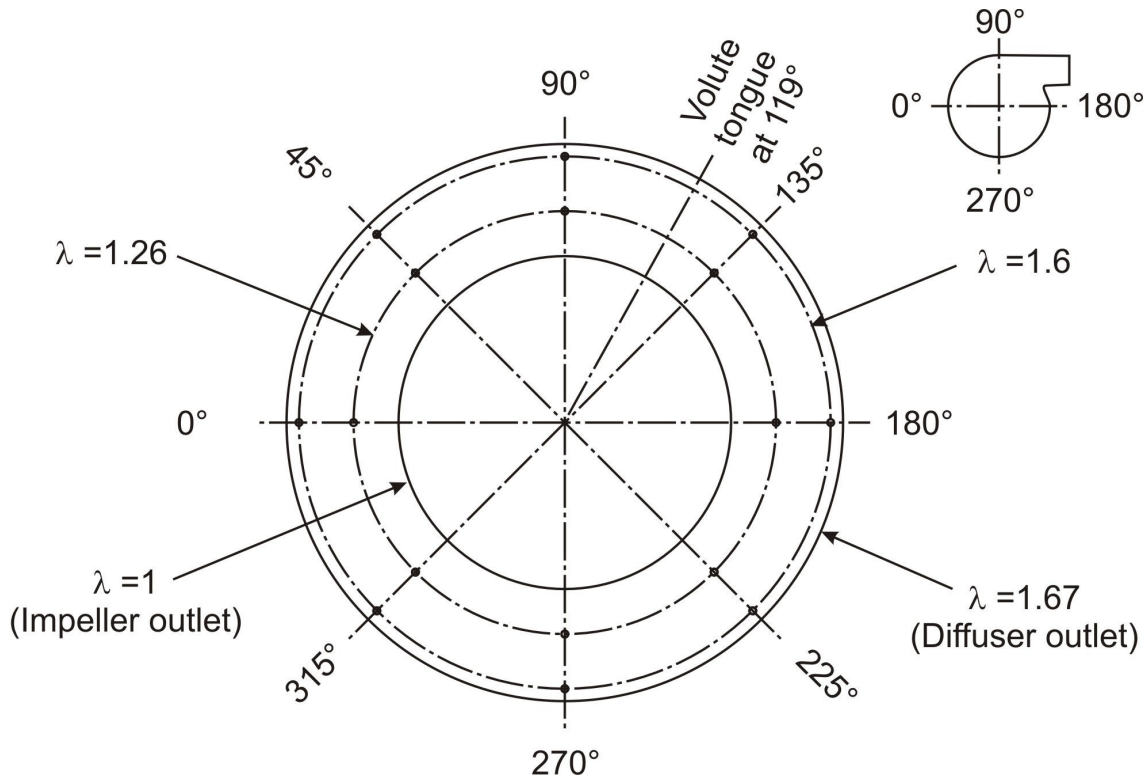


Figure 3-6 Locations of static pressure taps in the vaneless diffuser of the GT1749V 70 Trim turbocharger

The manufacturing of these taps was very difficult because of the complex and small geometry of the turbocharger. This applies especially to the static pressure taps at diameter ratio 1.26. Locating these taps in the front side of the compressor was not possible because of the volute casing. It was also very difficult to locate these taps in the back side of the vaneless diffuser because of the bearing housing. Therefore, a 5-axis milling machine was used to create grooves in the back side of the diffuser wall. These grooves are extended from the required measuring location to another location where enough space is available. It was also not possible to locate the static pressure taps at a diameter ratio less than 1.26. This is because the diffuser wall is not thick enough to accommodate the grooves. Static pressure tubes with 0.5 mm inner diameter are located in these grooves and later covered with epoxy filled with aluminum oxide Al_2O_3 which can withstand a maximum temperature of $250^\circ C$. Figure 3-7 shows the GT1749V 70 Trim turbocharger with the static pressure taps in

the back side of the vaneless diffuser. The pressure taps were checked after manufacturing and it was found that the taps at 180° are blocked. It was not possible to repair these taps or even to create new taps because of the very limited available space.

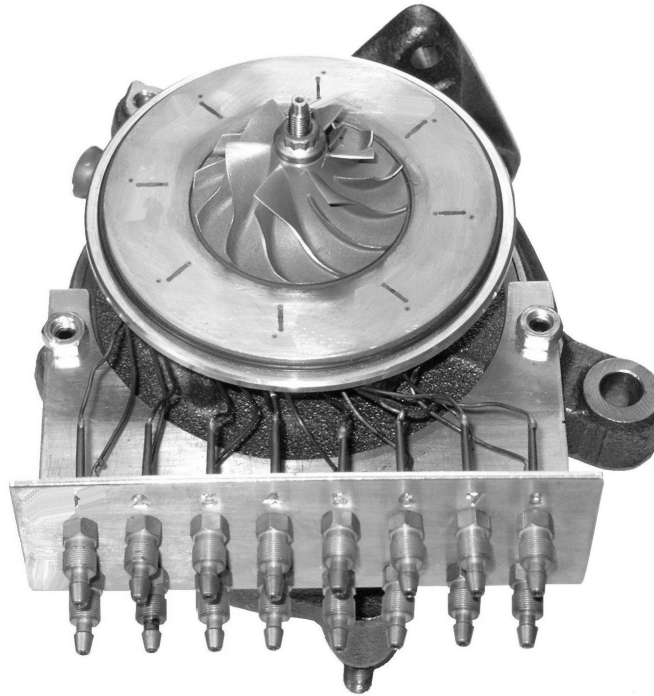


Figure 3-7 GT1749V 70 Trim turbocharger with static pressure tapes at diameter ratio 1.26 and 1.6

3.5 Experimental error analysis

Experimental error analysis aims at estimating the maximum probable error associated with the measurements. It is presented in the present research work on the basis of the differential method for the propagation of errors (*Beckwith, 1982*). This method is based on Taylor's theorem and presents the maximum probable error of a function $f(x_1, x_2, \dots, x_n)$ in the form

$$\delta f = \sqrt{\left(\delta x_1 \frac{\partial f}{\partial x_1}\right)^2 + \left(\delta x_2 \frac{\partial f}{\partial x_2}\right)^2 + \dots + \left(\delta x_n \frac{\partial f}{\partial x_n}\right)^2} \quad (3.3)$$

where

- x_i nominal values of variables
- δx_i discrete errors
- δf overall error.

Equation (3.3) is used for the estimation of the maximum probable measuring error. Figure A-1 to Figure A-8 present the estimated error of the measured compressor and turbine maps of the GT1749V 55 Trim and the K29 turbochargers. The maximum probable errors of the measured maps are satisfactory. However, the maximum probable error of the compressor efficiency at $n_{red,C} = 60000$ rpm for the GT1749V 55 Trim turbocharger and $n_{red,C} = 40000$ rpm for K29 turbocharger is quite high. This is mainly because of the low temperature difference and pressure ratio across the compressor at low rotational speeds. The high probable error of the compressor efficiency results in a higher probable error in the estimated product of the turbine efficiency and the mechanical efficiency. This is mainly because this product is estimated from the turbocharger efficiency and the compressor efficiency, equation (1.12). Therefore, the probable error of the estimated product of the turbine efficiency and the mechanical efficiency is always higher than that of the compressor efficiency.

4. PARAMETER STUDY OF THE TURBOCHARGER NON-ADIABATIC PERFORMANCE

4.1 Introduction

Turbocharger non-adiabatic performance takes place during normal operation of the turbocharger due to the high temperature gradient between the hot turbine and the ambient as well as between the turbine and the compressor. The temperature gradient causes heat transfer between the components of the turbocharger as well as between the turbocharger and the ambient. The amount of heat transfer between the components of the turbocharger causes a deviation of the measured turbocharger performance from the actual performance.

The complex turbocharger geometry introduces many geometrical and operating parameters that affect the turbocharger non-adiabatic performance. The purpose of the present parameter study is to analyse the turbocharger non-adiabatic performance and define the parameters affecting this performance. It also helps to understand and estimate the effect of each parameter on the turbocharger performance.

4.2 Modeling of turbocharger non-adiabatic performance

The complex turbocharger geometry results in very complex heat transfer mechanisms inside the turbocharger. First, heat is transferred by conduction from the turbine casing to the bearing housing. The lubrication oil removes part of this conduction heat transfer and hence reduces the amount of heat transfer from the bearing housing to the compressor. This means that the lubrication oil also acts as a cooling fluid. The amount of heat transfer from the bearing housing to the compressor causes deviation of the measured compressor efficiency from the actual compressor efficiency because the measured total temperature difference across the compressor in this case results from the compressor aerodynamic work and the amount of heat transfer to the compressor. Therefore, the measured compressor efficiency under non-adiabatic operating conditions is lower than the actual compressor efficiency. This underestimated compressor efficiency causes an overestimation of the product of the turbine total-to-static efficiency and the mechanical efficiency according to equation (1.12). The deviation of the measured compressor efficiency from the actual one can be analysed with the help of Figure 4-1. This figure shows a schematic h-s diagram for the compression process in an adiabatic and a non-adiabatic compressor. In the absence of heat transfer to the compressor, the compression process would follow the path 1-5_{adi}. The true total

temperature at the compressor outlet is therefore higher than the adiabatic total temperature due to the amount of heat transfer to the compressor. The effect of heat transfer to the compressor on the compressor performance is modelled by assuming the compression process through the impeller to be adiabatic (*Hagelstein et al., 2002*). The amount of heat transfer to the compressor is divided into two fractions. The first fraction of heat transfer takes place at constant pressure before the impeller inlet. This amount of heat transfer causes the total temperature to increase from T_{1t} to T_{1t^*} . The air is then compressed adiabatically in the impeller and this causes the total temperature at the impeller outlet to increase to $T_{5t,adi}$. The second fraction of heat transfer takes place at constant pressure after the impeller. This fraction causes the total temperature to increase from $T_{5t,adi}$ to T_{5t} .

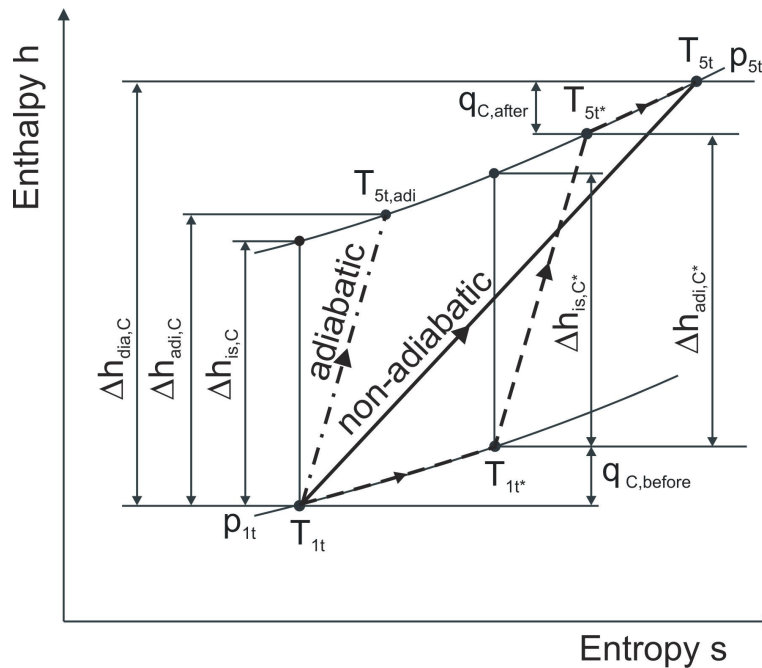


Figure 4-1 Schematic h-s diagram of the compression process in an adiabatic and a non-adiabatic compressor

The application of this model introduces three different expressions for the compressor efficiency. These three definitions allow the description of the compressor non-adiabatic performance. The first expression for the compressor efficiency is called the adiabatic compressor efficiency. This is the compressor efficiency in the absence of heat transfer to the compressor

$$\eta_{adi,C} = \frac{\Delta h_{1s,C}}{\Delta h_{adi,C}} = \frac{\Delta h_{1s,C^*}}{\Delta h_{adi,C^*}} \quad (4.1)$$

where

$$\Delta h_{is,C} = c_{p,air} T_{1t} \left(\pi_{t,C}^{\frac{\kappa_{air}-1}{\kappa_{air}}} - 1 \right) \quad (4.2)$$

$$\Delta h_{adi,C} = c_{p,air} (T_{5t,adi} - T_{1t}) \quad (4.3)$$

$$\Delta h_{is,C^*} = c_{p,air} T_{1t^*} \left(\pi_{t,C}^{\frac{\kappa_{air}-1}{\kappa_{air}}} - 1 \right) \quad (4.4)$$

$$\Delta h_{adi,C^*} = c_{p,air} (T_{5t,adi^*} - T_{1t^*}) \quad (4.5)$$

The second expression for the compressor efficiency is called the compressor non-adiabatic or diabatic efficiency $\eta_{dia,C}$. This is the measured compressor efficiency under non-adiabatic operating conditions

$$\eta_{dia,C} = \frac{\Delta h_{is,C}}{\Delta h_{dia,C}} \quad (4.6)$$

where

$$\Delta h_{dia,C} = c_{p,air} (T_{5t} - T_{1t}) \quad (4.7)$$

The third expression for the compressor efficiency is called the compressor heat efficiency. This expression is used to define the actual compressor work under non-adiabatic operating conditions

$$\eta_{heat,C} = \frac{\Delta h_{is,C}}{\Delta h_{adi,C^*}} \quad (4.8)$$

The denominator of equation (4.8) represents the actual compressor aerodynamic work under non-adiabatic operating conditions.

The same model can be applied to the expansion process through the turbine as shown in Figure A-9.

4.3 Effect of heat transfer on the compressor and the turbine aerodynamic work

Heat transfer between the components of the turbocharger as well as between the turbocharger and the ambient can affect the aerodynamic work of the compressor and the turbine. This causes the heat efficiency of both the turbine and the

compressor to be less than the adiabatic one. The actual compressor aerodynamic work can be presented from equation (4.1) as

$$\Delta h_{adi,C^*} = \Delta h_{is,C^*} / \eta_{adi,C} \quad (4.9)$$

Substituting equation (4.9) in equation (4.8)

$$\eta_{heat,C} = \frac{\Delta h_{is,C}}{\Delta h_{is,C^*} / \eta_{adi,C}} \quad (4.10)$$

Rearranging equation (4.10)

$$\frac{\eta_{heat,C}}{\eta_{adi,C}} = \frac{\Delta h_{is,C}}{\Delta h_{is,C^*}} = \frac{T_{1t}}{T_{1t^*}} \quad (4.11)$$

The total temperature at the impeller inlet under non-adiabatic operating conditions is given by

$$T_{1t^*} = T_{1t} + q_{C,before} / c_{p,air} \quad (4.12)$$

The specific amount of heat transfer to the compressor before the impeller is given by

$$q_{C,before} = Q_{C,before} / \dot{m}_C \quad (4.13)$$

The specific amount of heat transfer to the compressor before the impeller represents a fraction $K_{C,before}$ of the total specific heat transfer to the compressor

$$q_{C,before} = K_{C,before} q_C \quad (4.14)$$

Therefore, equation (4.12) can be rewritten as

$$T_{1t^*} = T_{1t} + K_{C,before} q_C / c_{p,air} \quad (4.15)$$

Substituting equation (4.15) in equation (4.11) and rearranging

$$\frac{\eta_{heat,C}}{\eta_{adi,C}} = \frac{T_{1t}}{T_{1t} + K_{C,before} q_C / c_{p,air}} = \frac{1}{1 + K_{C,before} \zeta_{h,C}} \quad (4.16)$$

The compressor heat number $\zeta_{h,C}$ is defined as

$$\zeta_{h,C} = \frac{q_C}{c_{p,air} T_{1t}} \quad (4.17)$$

Equation (4.16) shows that the amount of heat transfer to the compressor causes an increase in the compressor aerodynamic work and hence in the compressor power demand. This increase in the compressor power demand under non-adiabatic conditions also depends on the distribution of the heat transfer. Figure 4-2 shows the ratio of the compressor heat efficiency to the compressor adiabatic efficiency as a function of the compressor heat number and the fraction of heat transfer before the impeller. The compressor heat efficiency equals the compressor adiabatic efficiency at zero heat number and/or heat transfer to the compressor only after the impeller ($K_{C,before} = 0$). This is because zero compressor heat number means adiabatic compression in the compressor and zero heat transfer before the impeller means adiabatic compression in the impeller. Therefore, heat transfer to the diffuser and the volute of the compressor do not affect the compressor power demand.

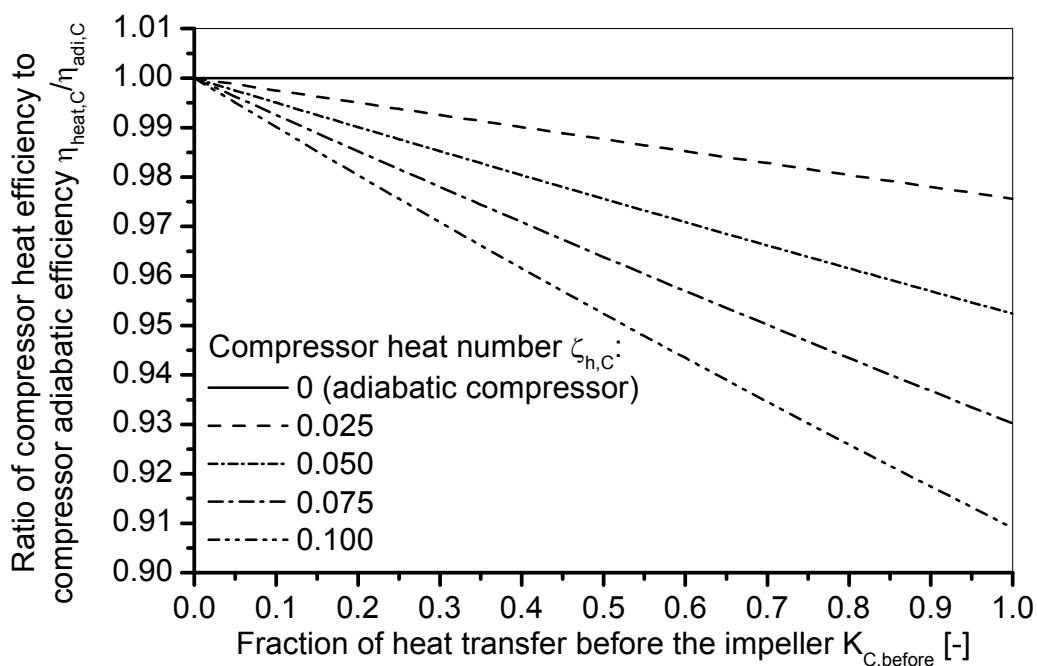


Figure 4-2 Ratio of compressor heat efficiency to compressor adiabatic efficiency as a function of compressor heat number and fraction of heat transfer before the impeller

Increasing the fraction of heat transfer before the impeller results in an increase in the power demand of the compressor and hence a decrease in the compressor heat efficiency under non-adiabatic operating conditions. The decrease in the compressor heat efficiency becomes more significant with increasing compressor heat number. It can also be observed in Figure 4-2 that the fraction of heat transfer before the

impeller can be assumed to equal 0.5 for values of the heat number less than 0.025 without any significant error.

The ratio of turbine heat efficiency to turbine adiabatic efficiency can be likewise presented as

$$\frac{\eta_{\text{heat},T}}{\eta_{\text{adi},T}} = 1 - K_{T,\text{before}} \zeta_{h,T} \quad (4.18)$$

where $K_{T,\text{before}}$ is the fraction of heat transfer before the turbine rotor. The turbine heat number presents the total amount of heat transfer from the turbine in non dimensional form

$$\zeta_{h,T} = \frac{q_T}{c_{p,\text{exh}} T_{6t}} \quad (4.19)$$

Figure 4-3 shows the effects of the turbine heat number and the fraction of heat transfer before the turbine rotor on the ratio of the turbine heat efficiency to the turbine adiabatic efficiency. The turbine heat efficiency coincides with the turbine adiabatic efficiency at zero turbine heat number and/or zero heat transfer before the turbine rotor. However, these conditions cannot be achieved for the turbine.

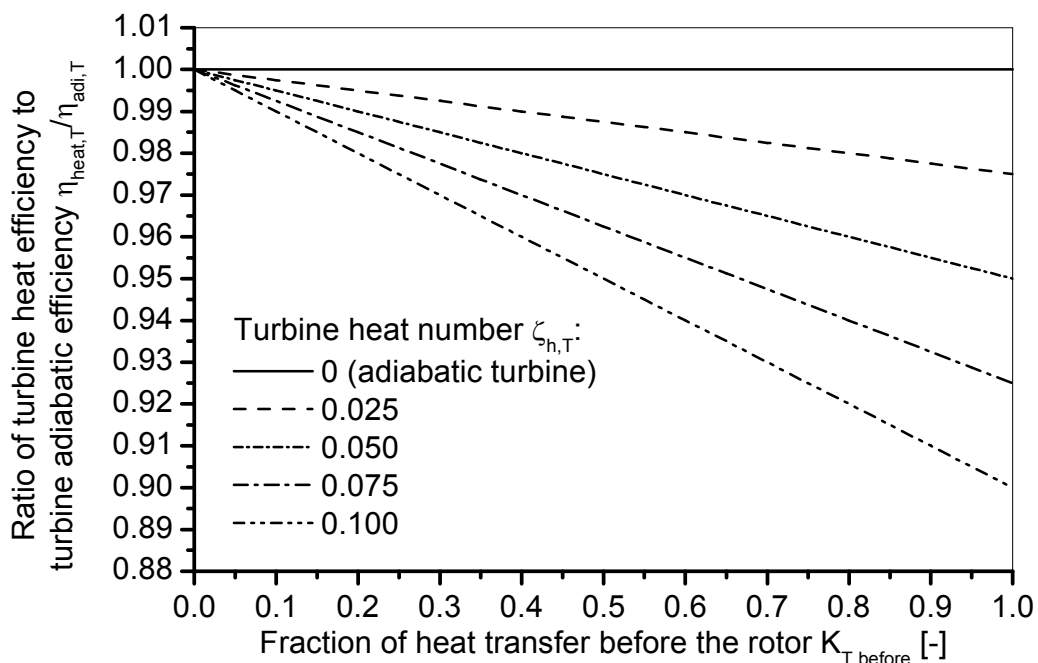


Figure 4-3 Ratio of turbine heat efficiency to turbine adiabatic efficiency as a function of turbine heat number and fraction of heat transfer before the turbine rotor

The amount of heat transfer from the turbine cannot be zero during normal operation of the turbocharger even with insulating the turbine surface area. This is because of the amount of heat transfer from the turbine to the bearing housing and then to the compressor. The fraction of heat transfer before the turbine also cannot be zero. This is because of the very large surface area of the turbine volute in comparison with the surface area of the rotor shroud. Therefore, the turbine heat efficiency is less than the adiabatic turbine efficiency. Increasing the amount of heat transfer from the turbine may cause significant decrease in the turbine heat efficiency and hence in the power delivered by the turbine. Figure 4-3 shows that the decrease in the turbine heat efficiency can be as high as 9% of the adiabatic turbine efficiency at a heat number of 0.09 and $K_{T,before} = 1$.

4.4 Effect of heat transfer on the measured compressor and turbine efficiencies

The compressor non-adiabatic efficiency can be expressed as

$$\eta_{dia,C} = \frac{\Delta h_{is,C}}{\Delta h_{adi,C^*} + q_C} \quad (4.20)$$

Rearranging equation (4.20)

$$\frac{1}{\eta_{dia,C}} = \frac{\Delta h_{adi^*}}{\Delta h_{is,C}} + \frac{q_C}{\Delta h_{is,C}} \quad (4.21)$$

The first term in the right hand side of equation (4.21) is the reciprocal of the compressor heat efficiency, equation (4.8). Therefore

$$\frac{1}{\eta_{dia,C}} = \frac{1}{\eta_{heat,C}} + \frac{q_C}{\Delta h_{is,C}} \quad (4.22)$$

Multiplying equation (4.22) by the adiabatic compressor efficiency

$$\frac{\eta_{adi,C}}{\eta_{dia,C}} = \frac{\eta_{adi,C}}{\eta_{heat,C}} + \frac{q_C}{\Delta h_{is,C}} \eta_{adi,C} \quad (4.23)$$

Equation (4.23) can be rewritten in the form

$$\frac{\eta_{adi,C}}{\eta_{dia,C}} = \frac{\eta_{adi,C}}{\eta_{heat,C}} + \frac{q_C}{\Delta h_{is,C}} \frac{\Delta h_{is,C^*}}{\Delta h_{is,C^*}} \eta_{adi,C} \quad (4.24)$$

It is evident from equation (4.1) that

$$\frac{\eta_{adi,C}}{\Delta h_{is,C^*}} = \frac{1}{\Delta h_{adi,C^*}} \quad (4.25)$$

Therefore, equation (4.24) can be rewritten as

$$\frac{\eta_{adi,C}}{\eta_{dia,C}} = \frac{\eta_{adi,C}}{\eta_{heat,C}} + \frac{q_C}{\Delta h_{adi,C^*}} \frac{\Delta h_{is,C^*}}{\Delta h_{is,C}} \quad (4.26)$$

Equation (4.26) can be rewritten as

$$\frac{\eta_{adi,C}}{\eta_{dia,C}} = \frac{\eta_{adi,C}}{\eta_{heat,C}} + \frac{q_C}{\Delta h_{adi,C^*}} \frac{T_{1t^*}}{T_{1t}} \frac{c_{p,air} T_{1t}}{c_{p,air} T_{1t}} \quad (4.27)$$

Substituting from equations (4.15), (4.16), and (4.17) in equation (4.27) and rearranging

$$\frac{\eta_{adi,C}}{\eta_{dia,C}} = \left(1 + K_{C,before} \zeta_{h,C}\right) \left(1 + \zeta_{h,C} \frac{c_{p,air} T_{1t}}{\Delta h_{adi,C^*}}\right) \quad (4.28)$$

Equation (4.28) can be further developed by applying Euler's equation for turbomachinery to the compressor

$$\Delta h_{adi,C^*} = u_2 c_{2u} - u_1 c_{1u} \quad (4.29)$$

The swirl velocity at the compressor inlet equals zero in the absence of compressor inlet guide vanes. Therefore

$$\Delta h_{adi,C^*} = u_2 c_{2u} \quad (4.30)$$

The swirl velocity at the impeller outlet is given by

$$c_{2u} = \mu \left(u_2 - c_{2m} / \tan \beta_{2,b}\right) \quad (4.31)$$

Substituting for c_{2u} in equation (4.30) and rearranging

$$\Delta h_{adi,C^*} = \mu u_2^2 \left(1 - \phi_2 / \tan \beta_{2,b}\right) \quad (4.32)$$

where ϕ_2 is the impeller flow coefficient, equation (1.16). Substituting for $\Delta h_{adi,C^*}$ from equation (4.32) in equation (4.28)

$$\frac{\eta_{adi,C}}{\eta_{dia,C}} = (1 + K_{C,before} \zeta_{h,C}) \left(1 + \zeta_{h,C} \frac{c_{p,air} T_{1t}}{\mu u_2^2 (1 - \phi_2 / \tan \beta_{2,b})} \right) \quad (4.33)$$

Since

$$c_{p,air} = \frac{\kappa_{air} R_{air}}{\kappa_{air} - 1} \quad (4.34)$$

Equation (4.33) can be rewritten as

$$\frac{\eta_{adi,C}}{\eta_{dia,C}} = (1 + K_{C,before} \zeta_{h,C}) \left(1 + \frac{\zeta_{h,C}}{\kappa_{air} - 1} \cdot \frac{1}{Mu_2^2} \cdot \frac{1}{\mu (1 - \phi_2 / \tan \beta_{2,b})} \right) \quad (4.35)$$

or

$$\frac{\eta_{dia,C}}{\eta_{adi,C}} = (1 + K_{C,before} \zeta_{h,C})^{-1} \cdot \left(1 + \frac{\zeta_{h,C}}{\kappa_{air} - 1} \cdot \frac{1}{Mu_2^2} \cdot \frac{1}{\mu (1 - \phi_2 / \tan \beta_{2,b})} \right)^{-1} \quad (4.36)$$

where Mu_2 is the compressor peripheral Mach number, equation (1.17). Equation (4.36) shows clearly that the deviation of the measured compressor non-adiabatic efficiency from the compressor adiabatic efficiency depends on many geometrical and operating parameters. These parameters are

1. Compressor heat number $\zeta_{h,C}$
2. Fraction of heat transfer before the impeller $K_{C,before}$
3. Impeller peripheral Mach number Mu_2
4. Impeller flow coefficient ϕ_2
5. slip factor μ
6. Blade angle at the impeller outlet $\beta_{2,b}$

It is very important to note that these parameters are also affecting the measured product of the turbine total-to-static efficiency and the mechanical efficiency. This is because the product of the turbine efficiency and the mechanical efficiency is estimated according to equation (1.12) from the turbocharger overall efficiency and the measured compressor efficiency. The measured compressor efficiency according to the new definitions is the non-adiabatic compressor efficiency. Therefore

$$(\eta_{6t8s,T} \eta_m)_{\text{measured}} = \frac{\eta_{\text{Turbo}}}{\eta_{\text{dia,C}}} \quad (4.37)$$

However, the actual product of the turbine efficiency and the mechanical efficiency should be estimated from the equation

$$(\eta_{6t8s,T} \eta_m)_{\text{ac}} = \frac{\eta_{\text{Turbo}}}{\eta_{\text{heat,C}}} \quad (4.38)$$

Therefore

$$(\eta_{6t8s,T} \eta_m)_{\text{ac}} = (\eta_{6t8s,T} \eta_m)_{\text{measured}} \cdot \frac{\eta_{\text{dia,C}}}{\eta_{\text{heat,C}}} \quad (4.39)$$

This means that the relative systematic error in the measured product of the turbine efficiency and the mechanical efficiency due to the amount of heat transfer to the compressor is

$$\frac{\Delta \eta_{6t8s,T}}{(\eta_{6t8s,T})_{\text{ac}}} = \frac{(\eta_{6t8s,T} \eta_m)_{\text{measured}} - (\eta_{6t8s,T} \eta_m)_{\text{ac}}}{(\eta_{6t8s,T} \eta_m)_{\text{ac}}} = \frac{\eta_{\text{heat,C}}}{\eta_{\text{dia,C}}} - 1 \quad (4.40)$$

The ratio of the compressor heat efficiency to the compressor non-adiabatic efficiency can be obtained by dividing equation (4.16) by equation (4.36)

$$\frac{\eta_{\text{heat,C}}}{\eta_{\text{dia,C}}} = 1 + \zeta_{h,C} \frac{1}{\kappa_{\text{air}} - 1} \cdot \frac{1}{\text{Mu}_2^2} \cdot \frac{1}{\mu (1 - \phi_2 / \tan \beta_{2,b})} \quad (4.41)$$

Substituting equation (4.41) in equation (4.40)

$$\frac{\Delta \eta_{6t8s,T}}{(\eta_{6t8s,T})_{\text{ac}}} = \zeta_{h,C} \frac{1}{\kappa_{\text{air}} - 1} \cdot \frac{1}{\text{Mu}_2^2} \cdot \frac{1}{\mu (1 - \phi_2 / \tan \beta_{2,b})} \quad (4.42)$$

It is therefore evident that the measured turbocharger performance is affected by the heat transfer between the turbocharger components. The measured compressor efficiency is less than the compressor heat efficiency and the measured turbine efficiency is higher than the turbine heat efficiency. This means that the estimated compressor power and turbine power from the measured performance maps are overestimated.

The above analysis defines the main parameters affecting the measured compressor and turbine efficiencies. The effect of each parameter on the measured compressor non-adiabatic efficiency and the error in the estimated product of the turbine

efficiency and the mechanical efficiency is discussed in the flowing sections.

4.4.1 Compressor heat number

The compressor heat number is a number that presents the amount of heat transfer to the compressor in non-dimensional form. Increasing the heat number causes an increase in the compressor power demand and a decrease in the compressor non-adiabatic efficiency. Figure 4-4 shows the variation of the ratio of the compressor non-adiabatic efficiency to the compressor adiabatic efficiency with the compressor heat number. This figure is obtained by varying the value of the compressor heat number in equation (4.36) and setting all other geometrical and operating parameters at typical values of the GT1749V 70 Trim turbocharger. The compressor non-adiabatic efficiency coincides with the compressor adiabatic efficiency at zero

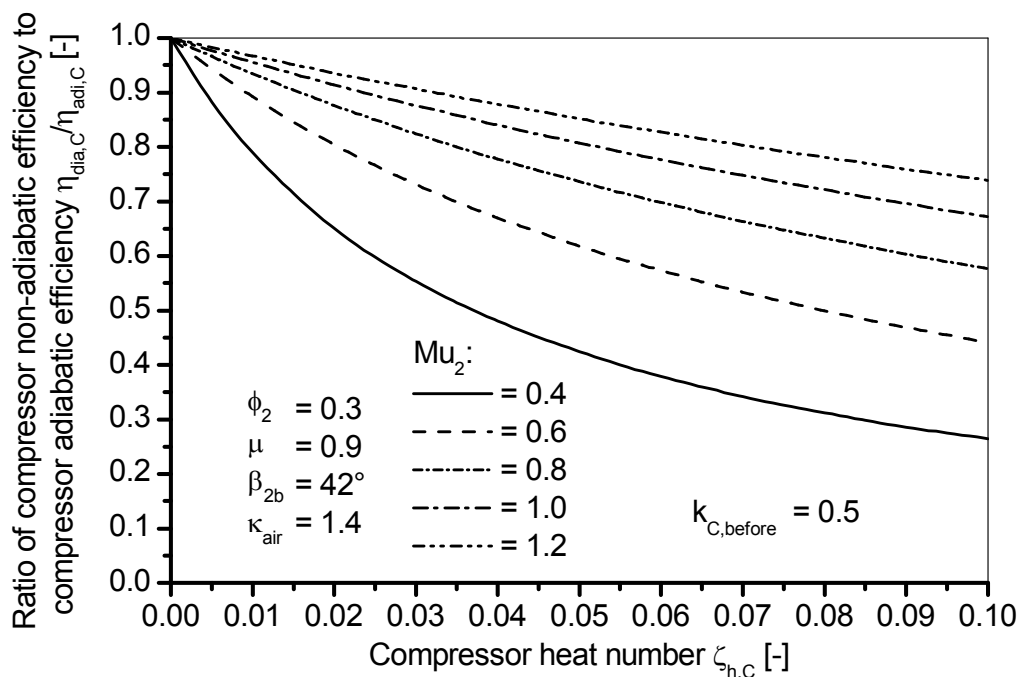


Figure 4-4 Variation of the ratio of compressor non-adiabatic efficiency to compressor adiabatic efficiency with the compressor heat number

compressor heat number. Increasing the amount of heat transfer to the compressor increases the compressor heat number and hence decreases the compressor non-adiabatic efficiency. This effect is very significant at low compressor peripheral Mach number Mu_2 (low rotational speeds). This is because the compressor aerodynamic work decreases with decreasing the compressor peripheral Mach number. Therefore, increasing the compressor heat number at low peripheral Mach number causes a significant increase of the ratio between the specific amount of heat transfer to the compressor and the compressor aerodynamic work. This makes the

effect of heat transfer to the compressor very significant at low rotational speeds. The measured product of the turbine efficiency and the mechanical efficiency is therefore significantly affected by the amount of heat transfer to the compressor at low rotational speeds. Figure 4-5 shows the percentage error of the measured product of the turbine efficiency and the mechanical efficiency as a function of the compressor heat number. This systematic percentage error can be as high as 100% at low compressor peripheral Mach number and sufficiently high compressor heat number. Decreasing the compressor heat number results in a decrease of the error in the product of the turbine efficiency and the mechanical efficiency. The effect of the compressor heat number on the error in the product of the turbine efficiency and the mechanical efficiency decreases with increasing the compressor peripheral Mach number. This is because the ratio of the compressor non-adiabatic efficiency to the compressor heat efficiency tends to be unity with increasing the compressor peripheral Mach number. This causes a decrease of the error in the product of the turbine efficiency and the mechanical efficiency according to equation (4.40).

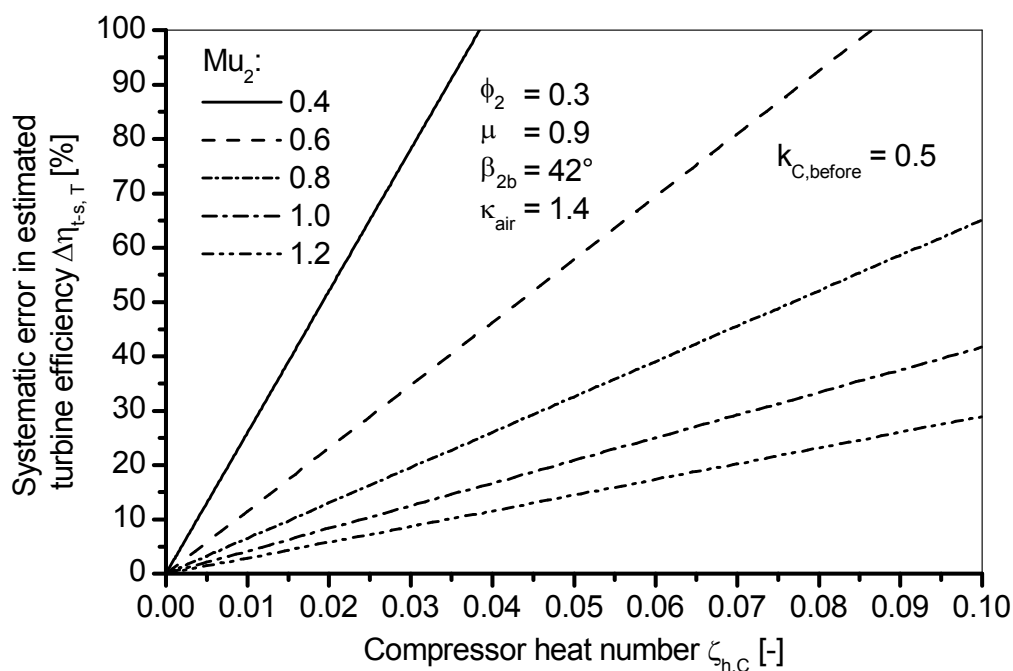


Figure 4-5 Percentage error of the measured product of the turbine efficiency and the mechanical efficiency as a function of the compressor heat number

4.4.2 Fraction of heat transfer before the compressor impeller

Figure 4-6 shows the variation of the ratio of the compressor non-adiabatic efficiency to the compressor adiabatic efficiency with the fraction of heat transfer before the compressor impeller. The fraction of heat transfer before the impeller has a very small effect on the compressor non-adiabatic efficiency. This small effect is mainly

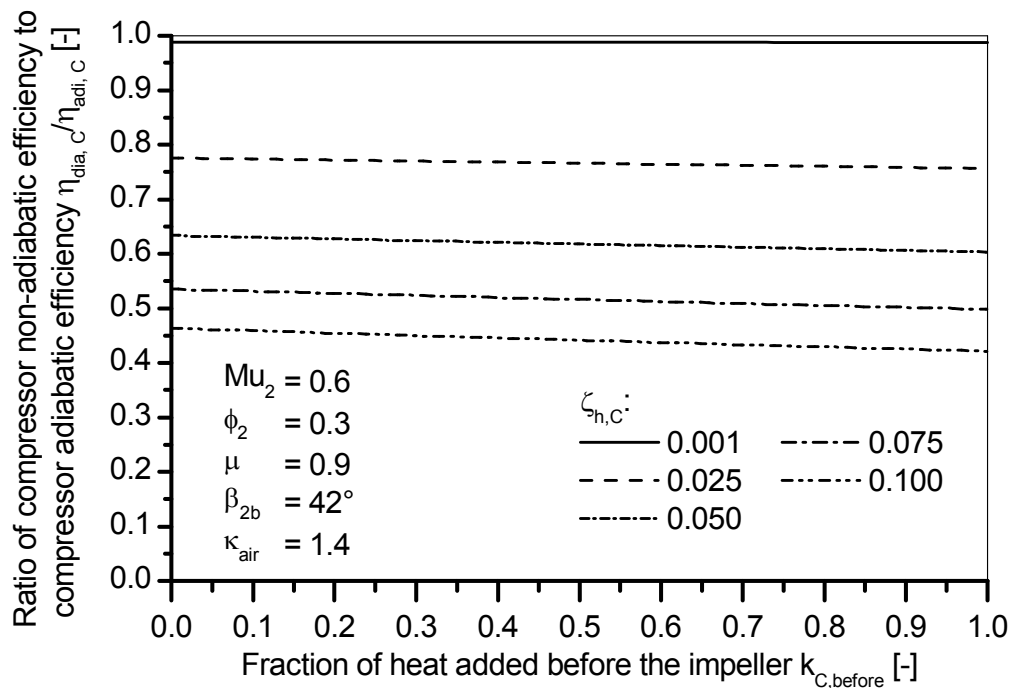


Figure 4-6 Variation of the ratio of compressor non-adiabatic efficiency to compressor adiabatic efficiency with the fraction of heat transfer before the compressor impeller

due to the increase in the compressor aerodynamic work with increasing the fraction of heat transfer to the compressor before the impeller. This is because the overall total temperature difference across the compressor results from the amount of heat transfer to the compressor and the compressor aerodynamic work. The increase in the total temperature due to the amount of heat transfer to the compressor is independent of the fraction of heat added before the impeller. The increase in compressor aerodynamic work depends on the fraction of heat transfer before the impeller. Therefore, the effect of the fraction of heat added to the compressor before the impeller is mainly due to the increase in the compressor aerodynamic work. This means that the fraction of heat transfer before the impeller affects both the compressor non-adiabatic efficiency and the compressor heat efficiency in the same way. Therefore, it has no effect on the percentage error of the measured product of the turbine efficiency and the mechanical efficiency as shown in equation (4.42).

4.4.3 Compressor peripheral Mach number

Compressor peripheral Mach number is one of the most important parameters affecting the non-adiabatic turbocharger performance. This can be clearly observed in equation (4.36) where the ratio of the compressor non-adiabatic efficiency to the compressor adiabatic efficiency depends on the square of the compressor peripheral

Mach number. This also applies to the percentage error in the product of the turbine efficiency and the mechanical efficiency as shown in equation (4.42). Figure 4-7 shows the variation of the ratio of the compressor non-adiabatic efficiency to the compressor adiabatic efficiency with the compressor peripheral Mach number. This ratio tends to be unity with increasing the compressor peripheral Mach number.

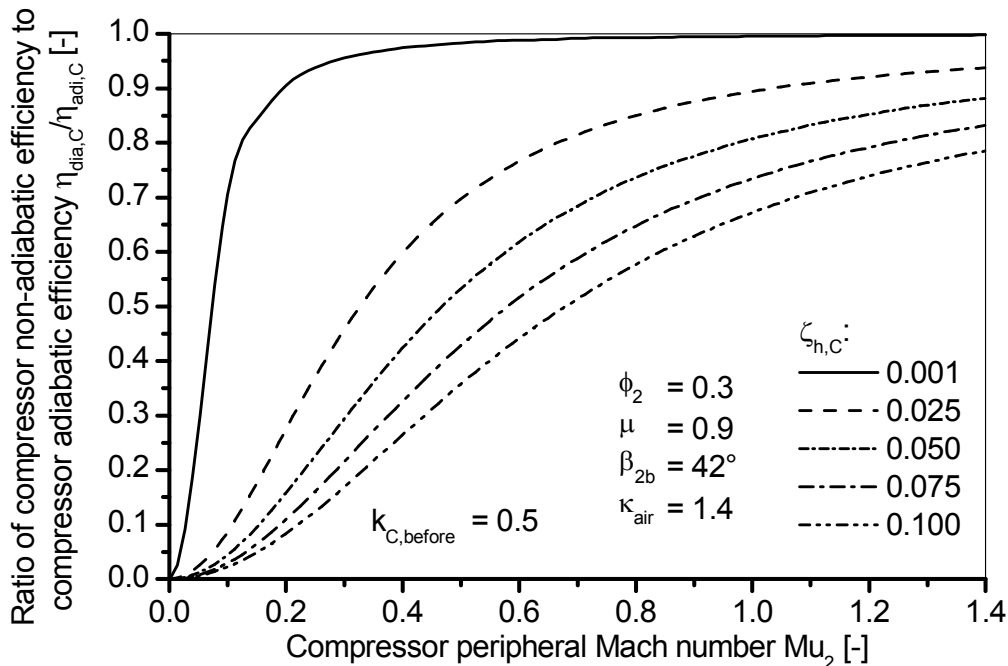


Figure 4-7 Variation of the ratio of compressor non-adiabatic efficiency to compressor adiabatic efficiency with the compressor peripheral Mach number

This is because the compressor aerodynamic work increases with increasing the rotational speed. Therefore, the ratio between the specific amount of heat transfer to the compressor and the compressor aerodynamic work decreases with increasing the rotational speed. This causes the deviation of the compressor non-adiabatic efficiency from the compressor adiabatic efficiency to decrease with increasing the rotational speed. It is also evident in Figure 4-7 that the compressor can be assumed to work adiabatically at high compressor peripheral Mach number and low compressor heat number. The deviation of the compressor non-adiabatic efficiency from the compressor adiabatic efficiency increases significantly with decreasing the rotational speed even at small heat numbers. This causes high error in the estimated product of the turbine efficiency and the mechanical efficiency at low rotational speeds, Figure 4-8. This error decreases with increasing the turbocharger rotational speed as a result of decreasing the ratio between the specific amount of heat transfer to the compressor and the compressor aerodynamic work.

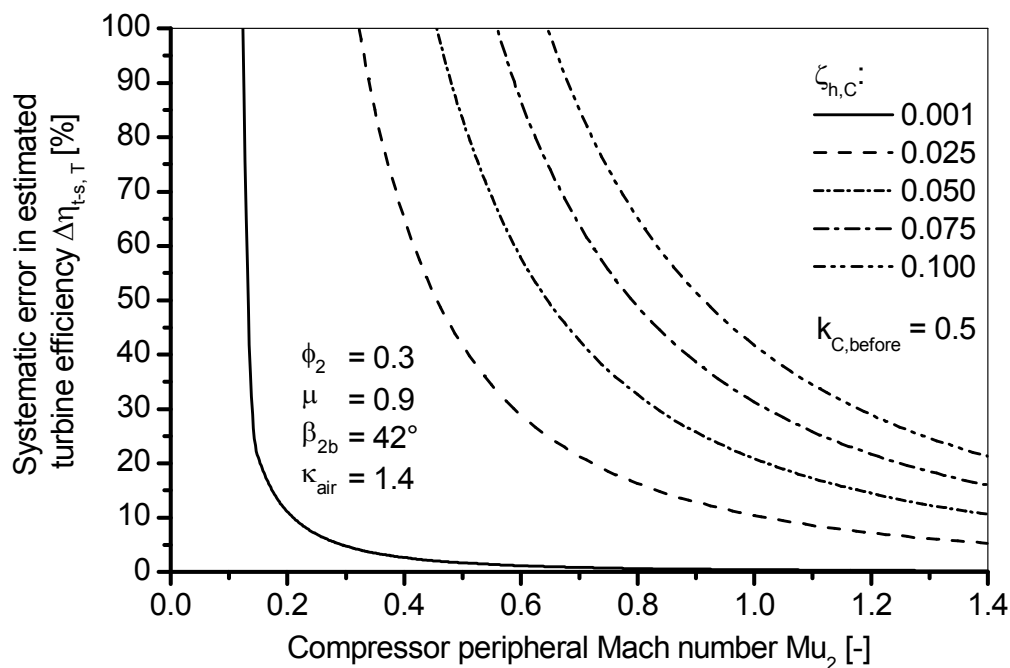


Figure 4-8 Percentage error of the measured product of the turbine efficiency and the mechanical efficiency as a function of the compressor peripheral Mach number

4.4.4 Impeller flow coefficient

Impeller flow coefficient affects the turbocharger non-adiabatic performance in the same way as the compressor peripheral Mach number. Increasing the impeller flow coefficient is always associated with decreasing the compressor aerodynamic work, equation (4.32). This causes an increase in the specific amount of heat transfer to the compressor in comparison with the compressor aerodynamic work. Therefore, the effect of heat transfer on the compressor non-adiabatic efficiency increases with increasing the impeller flow coefficient as shown in Figure 4-9. The error in the product of the turbine efficiency and the mechanical efficiency likewise increases with increasing the impeller flow coefficient as shown in Figure 4-10.

4.4.5 Impeller slip factor

The compressor slip factor directly affects the compressor aerodynamic work. High values of the slip factor at the same peripheral Mach number and impeller flow coefficient mean higher compressor aerodynamic work. Therefore, the ratio between the specific amount of heat transfer to the compressor and the compressor aerodynamic work decreases with increasing the compressor slip factor. This causes less deviation of the compressor non-adiabatic efficiency from the compressor adiabatic efficiency with increasing the value of the slip factor. This behavior can be

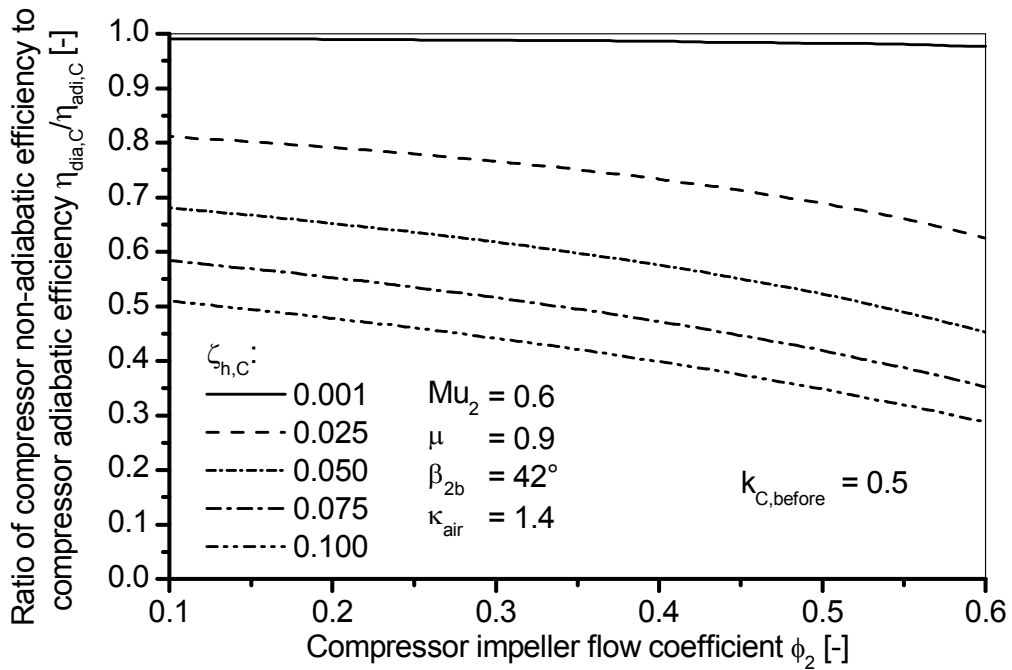


Figure 4-9 Variation of the ratio of compressor non-adiabatic efficiency to compressor adiabatic efficiency with the compressor impeller flow coefficient

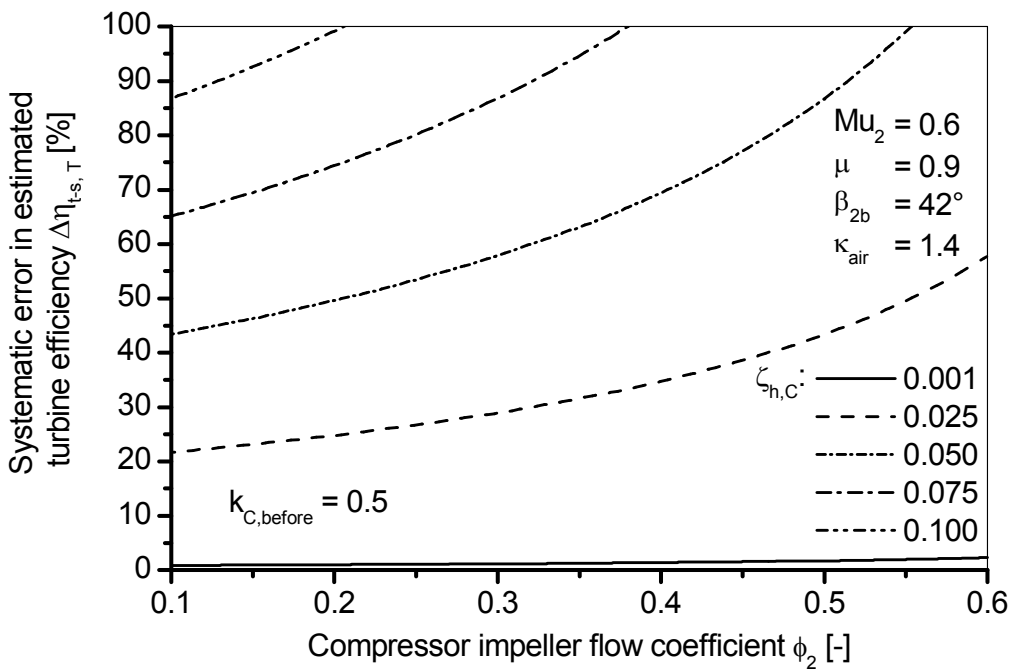


Figure 4-10 Percentage error of the measured product of the turbine efficiency and the mechanical efficiency as a function of the compressor impeller flow coefficient

clearly shown in Figure 4-11 where the ratio of the compressor non-adiabatic efficiency to the compressor adiabatic efficiency tends to be unity with increasing the slip factor. It is also evident in Figure 4-11 that the slip factor significantly affects the compressor non-adiabatic efficiency at values of the compressor heat number ≥ 0.025 .

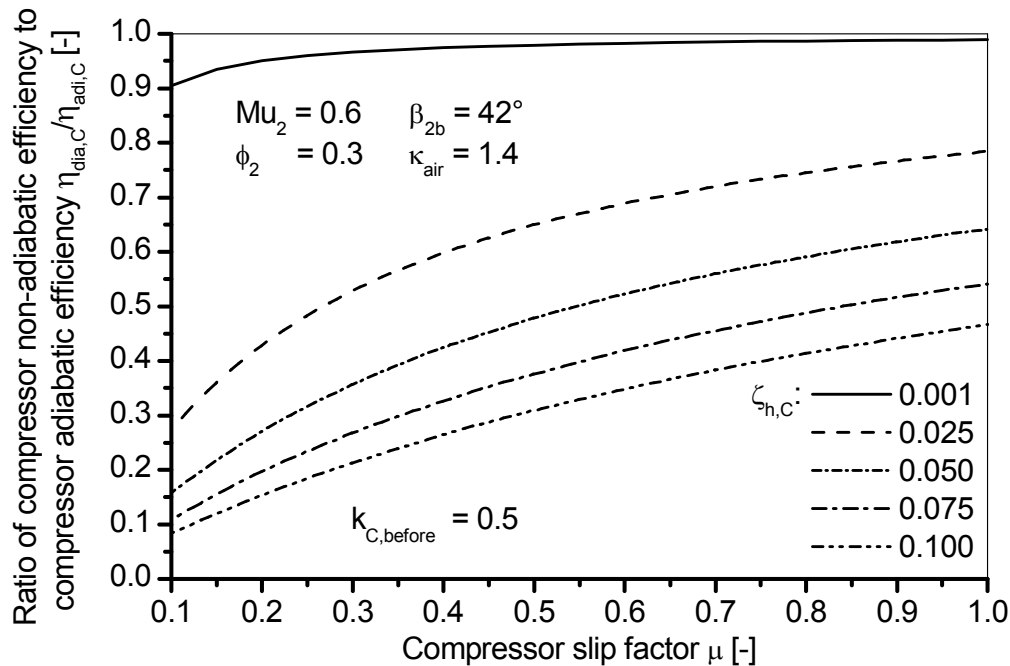


Figure 4-11 Variation of the ratio of compressor non-adiabatic efficiency to compressor adiabatic efficiency with the compressor slip factor

Figure 4-12 shows the systematic percentage error of the measured product of the turbine efficiency and the mechanical efficiency as a function of the compressor slip factor. The increase in the slip factor results in a decrease of the error in the product of the turbine efficiency and the mechanical efficiency. This is due to the decreasing effect of the amount of heat transfer to the compressor on the compressor non-adiabatic efficiency with increasing the value of the slip factor.

4.4.6 Blade angle at the impeller outlet

It is well known that impellers with large blade angle at outlet deliver higher aerodynamic work to the fluid. This can also be seen in equation (4.32). This makes compressors with large blade angle at impeller outlet less affected by the amount of heat transfer to the compressor. Figure 4-13 shows the variation of the ratio of the compressor non-adiabatic efficiency to the compressor adiabatic efficiency with the blade angle at the impeller outlet. The effect of blade angle at the impeller outlet is very small at low heat numbers and increases with increasing the compressor heat

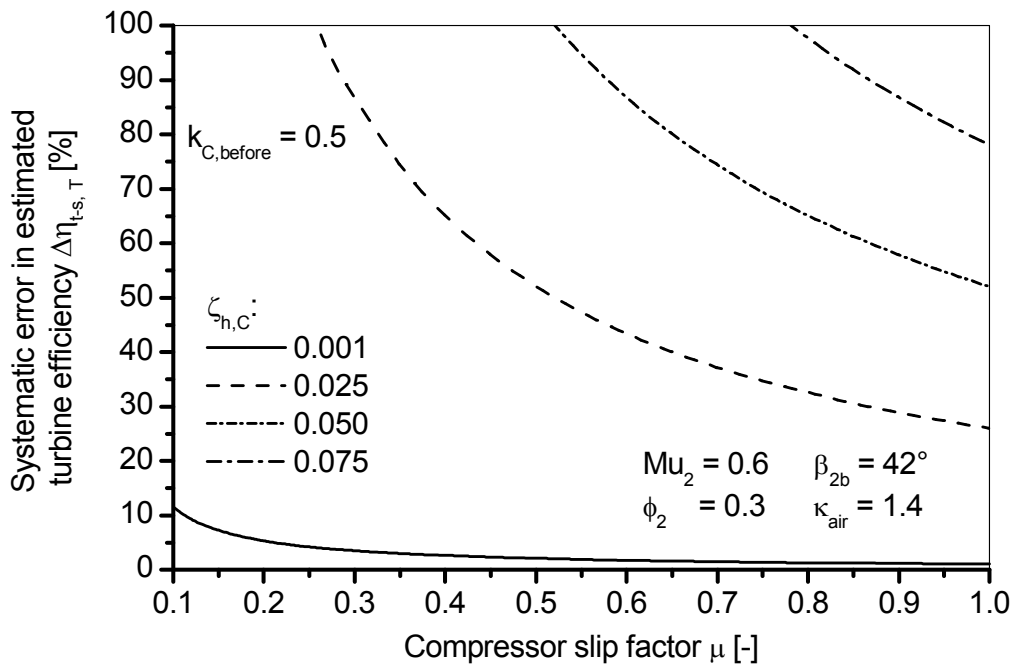


Figure 4-12 Percentage error of the measured product of the turbine efficiency and the mechanical efficiency as a function of the compressor slip factor

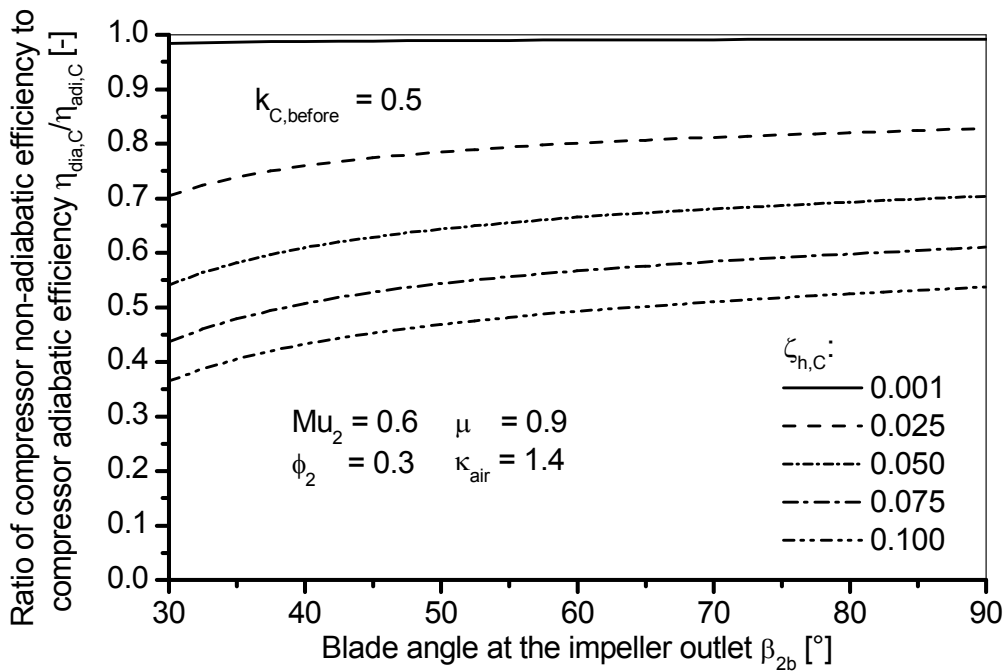


Figure 4-13 Variation of the ratio of compressor non-adiabatic efficiency to compressor adiabatic efficiency with the blade angle at impeller outlet

number. This effect is generally less significant than the effect of compressor peripheral Mach number, impeller flow coefficient, and slip factor. However, it should be noted that increasing the blade angle at impeller outlet also improves the compressor slip factor (*Wiesner, 1967; Stodola, 1945*). Therefore, the blade angle at the impeller outlet actually affects the compressor non-adiabatic efficiency in two ways. First, increasing the blade angles provides higher aerodynamic compressor work and hence a smaller ratio between the specific amount of heat transfer to the compressor and the compressor aerodynamic work. Second, increasing the blade angle at the impeller outlet improves the compressor slip factor and hence reduces the effect of heat transfer to the compressor on the non-adiabatic compressor efficiency. Thus, it can be generally said that a compressor with a large blade angle at the impeller outlet is less affected by the amount of heat transfer to the compressor. Consequently, the error in the product of the turbine efficiency and the mechanical efficiency decreases with increasing the blade angle at the impeller outlet as shown in Figure 4-14.

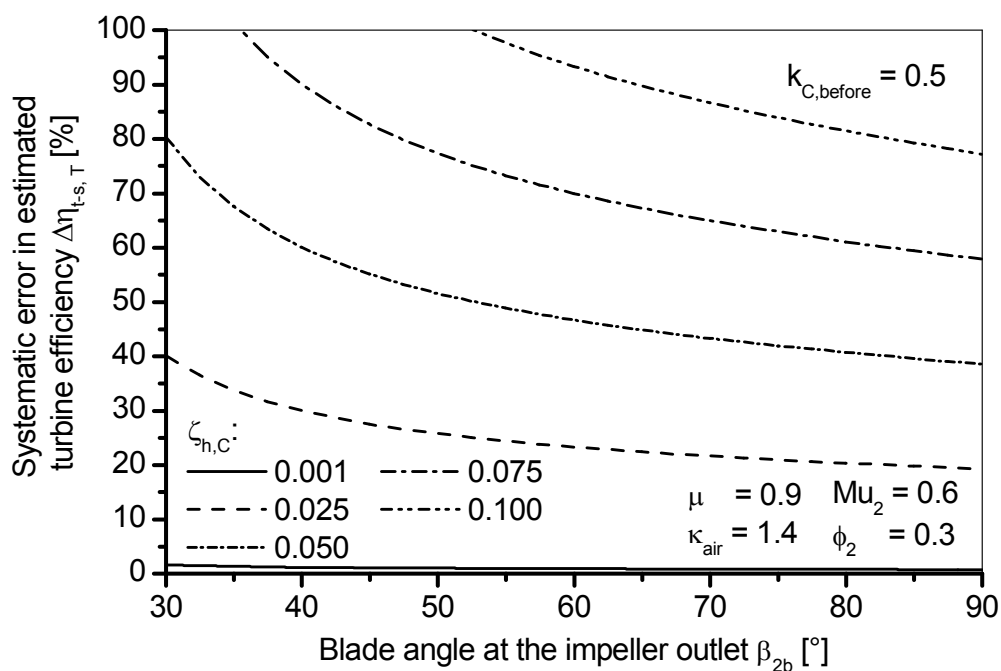


Figure 4-14 Percentage error of the measured product of the turbine efficiency and the mechanical efficiency as a function of the blade angle at impeller outlet

5. EXPERIMENTAL RESULTS AND ANALYSIS

5.1 Compressor non-adiabatic performance

Compressor non-adiabatic performance is investigated by comparing the results of the cold measurements with that of the hot measurements. Cold measurements are conducted by supplying the turbine with compressed air instead of the hot exhaust gases. The oil inlet temperature is kept lower than the total temperature at the compressor outlet to avoid any possible heat transfer from the oil to the compressor. Therefore, the compressor can be assumed to work adiabatically during the cold measurements and the measured compressor performance can be considered to be the adiabatic compressor performance. The turbine is supplied with hot exhaust gases in the hot measurements and the turbocharger performance maps are measured at constant total temperature at the turbine entry. These measurements are repeated at different exhaust gas total temperatures at the turbine entry. The hot measurements are then compared with the cold measurements. Any deviation of the measured compressor performance in the hot measurements from the adiabatic compressor performance is considered to be due to the amount of heat transfer to the compressor.

Two turbochargers are investigated at different exhaust gas total temperatures at the turbine entry. These turbochargers are the GT1749V 55 Trim turbocharger and the K29 turbocharger. The GT1749V 55 Trim turbocharger is also investigated at different turbine inlet guide-vane positions. The K29 turbocharger has a twin entry turbine without turbine inlet guide vanes. The performance of this turbocharger is also investigated under partial admission conditions.

5.1.1 Single entry turbocharger compressor

5.1.1.1 Effect of exhaust gas temperature at the turbine entry

Figure 5-1 shows the variation of the compressor total pressure ratio with the compressor reduced mass flow rate at different compressor reduced rotational speeds and total temperatures at the turbine entry for the GT1749V 55 Trim compressor. The measured performance lines of the compressor are not affected by the total temperature of the exhaust gas at the turbine entry. This means that the amount of heat transfer to the compressor has a negligible effect on the aerodynamic losses of the compressor and hence on the compressor total pressure ratio. This behaviour is also recorded during the measurements of a wide variety of turbochargers. However, these results are not available for publication in the present research work.

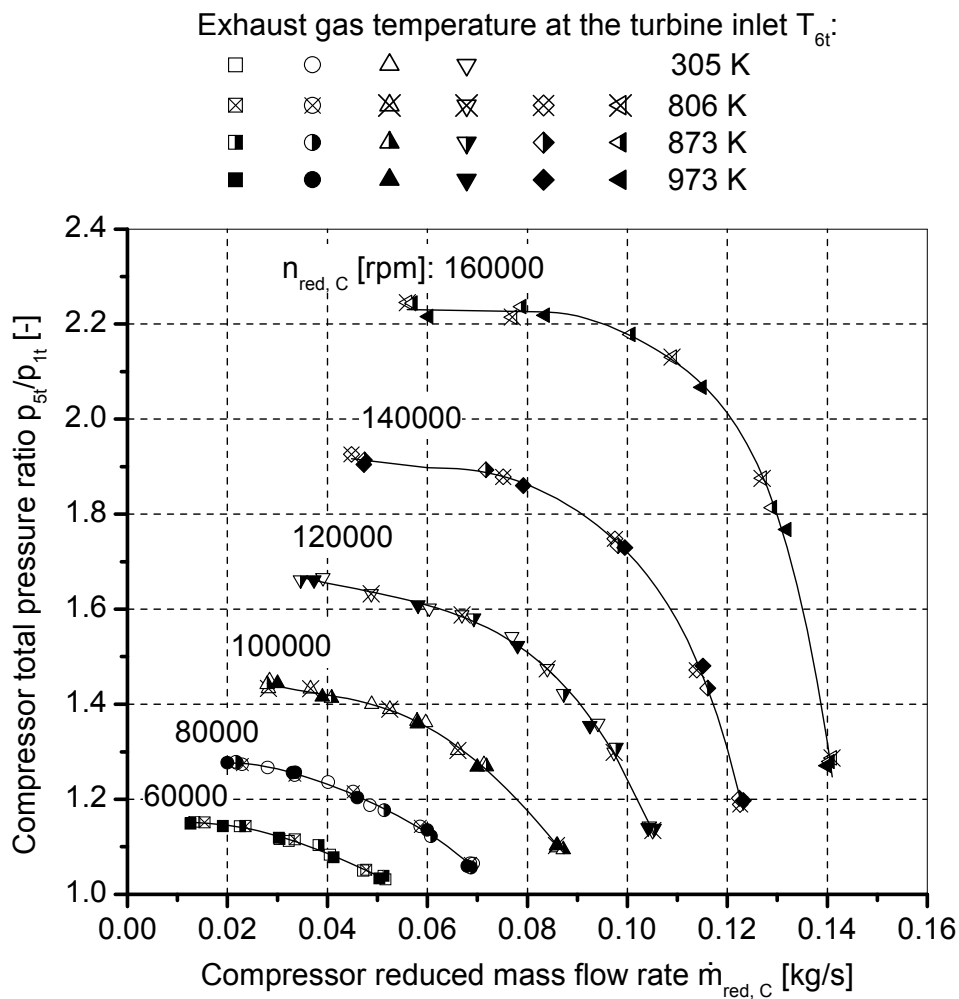


Figure 5-1 Variation of the compressor total pressure ratio with the compressor reduced mass flow rate at different compressor reduced rotational speeds and total temperatures at the turbine entry for the GT1749V 55 Trim compressor

Figure 5-2 shows the variation of the measured compressor efficiency with the compressor reduced mass flow rate at different compressor reduced rotational speeds and total temperatures at the turbine entry for the GT1749V 55 Trim compressor. The measured compressor efficiency at $T_{6t} = 305$ K represents the compressor adiabatic efficiency (cold measurements). The adiabatic efficiency is measured only in the operating range extending from 60000 rpm to 120000 rpm. This is because the fluid power supplied to the turbine in the cold measurements is not sufficient to drive the compressor at higher rotational speeds. Therefore, the adiabatic compressor performance is measured only for rotational speeds 60000-120000 rpm. The parameters extracted from the comparison of the cold and the hot measurements are therefore presented only in the operating range extending from 60000 rpm to 120000 rpm.

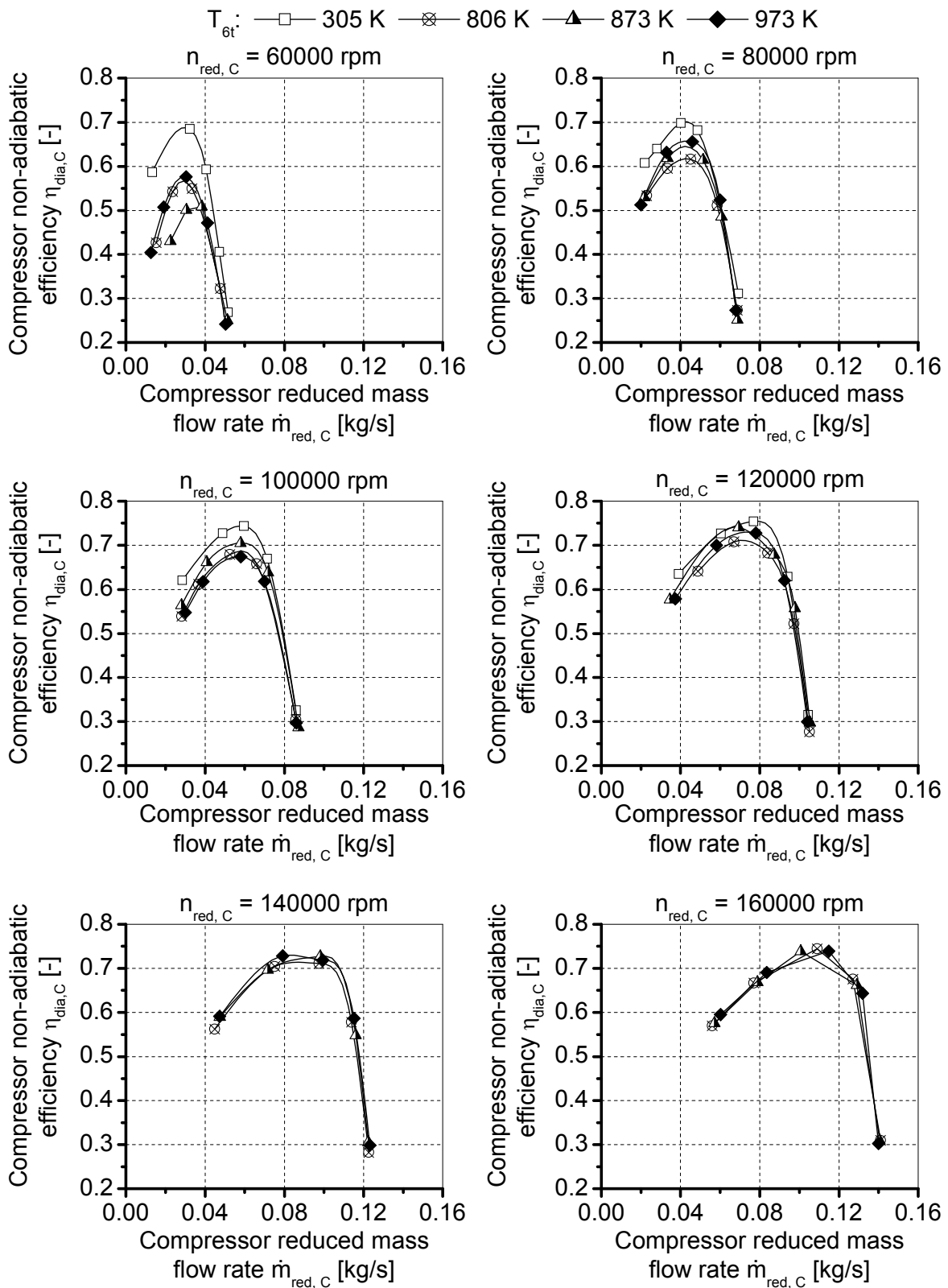


Figure 5-2 Variation of the compressor non-adiabatic efficiency with the compressor reduced mass flow rate at different compressor reduced rotational speeds and total temperatures at the turbine entry for the GT1749V 55 Trim compressor

The measured compressor efficiency in the hot measurements represents the non-adiabatic compressor efficiency. Figure 5-2 shows a clear effect of the total temperature at the turbine entry on the compressor non-adiabatic efficiency. The measured compressor non-adiabatic efficiency is lower than the compressor adiabatic efficiency due to the amount of heat transfer from the turbine to the compressor. The deterioration of the compressor non-adiabatic efficiency is very significant at low rotational speed (low compressor peripheral Mach number). The effect of heat transfer from the turbine to the compressor decreases with increasing the compressor rotational speed (increasing the compressor peripheral Mach number). Therefore, the deterioration of the compressor non-adiabatic efficiency decreases with increasing the turbocharger rotational speed. The measured compressor non-adiabatic efficiency at 140000 rpm and 160000 rpm is almost independent of the exhaust gas temperature at the turbine entry. This behavior coincides very well with the results of the parameter analysis of the turbocharger non-adiabatic performance presented in Chapter 4.

It is also evident in Figure 5-2 that the deviation of the compressor non-adiabatic efficiency from the compressor adiabatic efficiency is higher near the compressor surge line. This behavior depends on the specific amount of heat transfer to the compressor

$$q_C = Q_C / \dot{m}_C \quad (5.1)$$

The amount of heat transfer to the compressor Q_C depends on the temperature difference between the turbine and the compressor as well as the thermal resistance of the bearing housing. Figure A-10 shows that the temperature difference between the compressor casing and the turbine casing increases with increasing the compressor flow rate. This is mainly due to the decrease in the compressor casing temperature with increasing the flow rate through the compressor as shown in Figure A-11. The variation in the turbine casing temperature at certain constant rotational speed is small compared with that of the compressor casing as shown in Figure A-12. Increasing the temperature difference between the turbine and the compressor increases the amount of heat transfer to the compressor. Therefore, the amount of heat transfer to the compressor increases with increasing the compressor flow rate at certain constant rotational speed and vice versa. However, the rate of change of the temperature difference between the turbine casing and the compressor casing with the compressor flow rate at constant rotational speed is small as shown in Figure A-10. This means small rate of increase in the amount of heat transfer to the compressor with increasing the compressor mass flow rate at constant rotational speed. Therefore, the specific amount of heat transfer to the compressor decreases with increasing the compressor flow rate and this causes less deviation of the compressor non-adiabatic efficiency from the compressor adiabatic efficiency at high

compressor flow rate. The specific amount of heat transfer to the compressor increases significantly near the compressor surge line because of the low compressor flow rate and this causes the higher deterioration of the compressor non-adiabatic efficiency at low flow rate.

Figure 5-3 shows the variation of the compressor heat number with the compressor stage flow coefficient at different compressor reduced rotational speeds and total temperatures at the turbine entry for the GT1749V 55 Trim compressor. The compressor heat number is estimated by comparing the compressor non-adiabatic efficiency (hot measurements) with the compressor adiabatic efficiency (cold measurements). Figure 5-3 shows that the compressor heat number increases with decreasing the compressor flow rate. The rate of change of the compressor heat

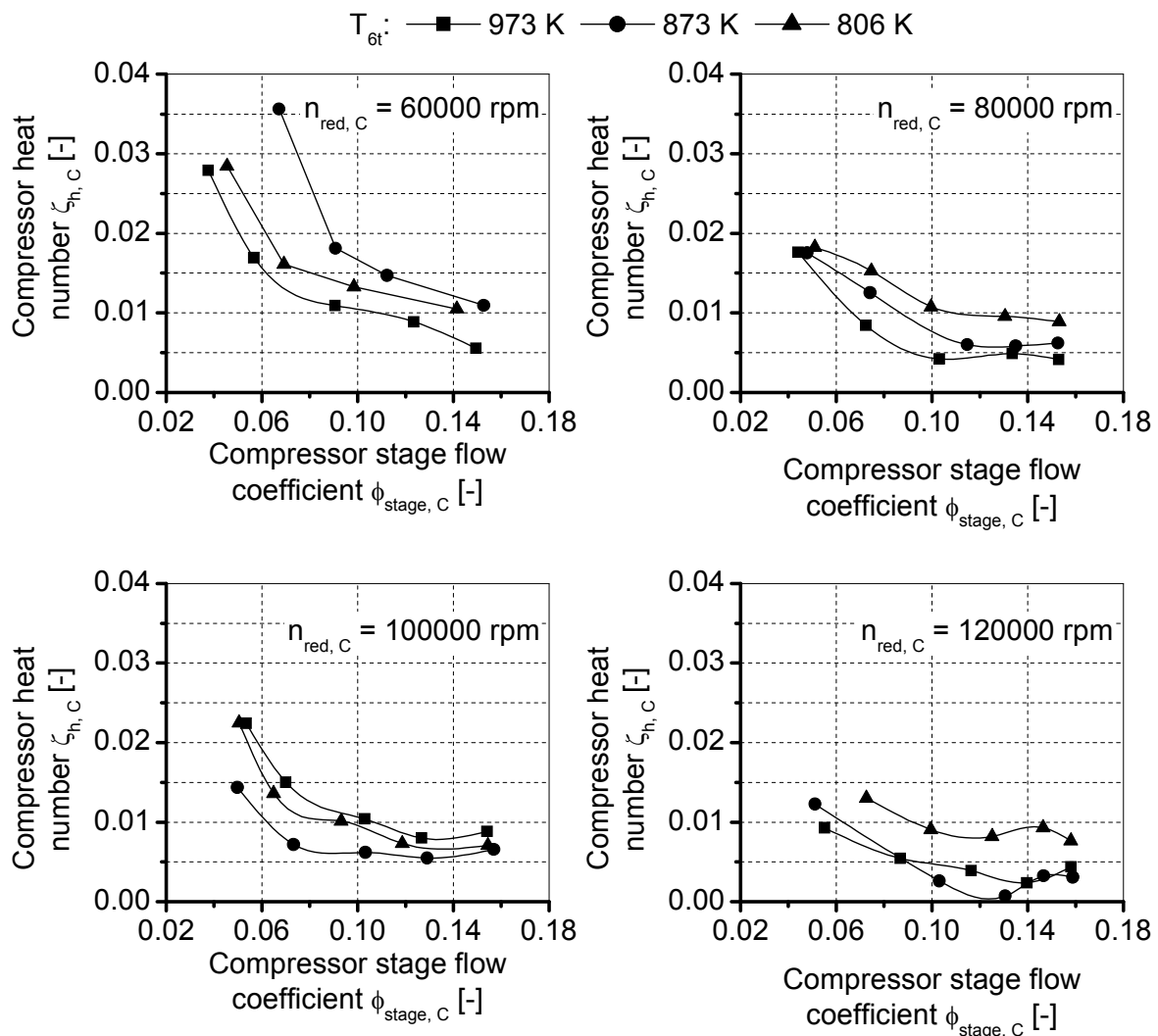


Figure 5-3 Variation of the compressor heat number with the compressor stage flow coefficient at different compressor reduced rotational speeds and total temperatures at the turbine entry for the GT1749V 55 Trim compressor

number with the compressor flow rate is high at low flow rates and decreases with increasing the flow rate. The compressor heat number decreases with increasing the compressor flow rate due to the decrease of the specific amount of heat transfer to the compressor with increasing the compressor flow rate. It significantly increases at the compressor surge line due to the significant increase of the specific amount of heat transfer to the compressor at low flow rates. This means that the deterioration of the compressor non-adiabatic efficiency increases with increasing the compressor heat number. This measured behavior also matches very well the results of the parameter analysis of the turbocharger non-adiabatic performance (Section 4.4.1).

Figure 5-4 shows the ratio of the compressor non-adiabatic efficiency to the compressor adiabatic efficiency at different compressor reduced rotational speeds and total temperatures at the turbine entry for the GT1749V 55 Trim compressor. The ratio of the compressor non-adiabatic efficiency to the compressor adiabatic efficiency tends to be unity with increasing turbocharger rotational speed. The significant effect of the heat transfer to the compressor on the compressor non-adiabatic efficiency at low rotational speeds is due to the small compressor aerodynamic work in this operating range. The ratio of the specific amount of heat transfer to the compressor to the compressor aerodynamic work is therefore very significant at low compressor rotational speeds even at relatively small compressor heat number. Consequently, the amount of heat transfer to the compressor significantly affects the compressor non-adiabatic efficiency at low rotational speeds.

Figure 5-5 shows the percentage difference between the compressor non-adiabatic efficiency and the adiabatic efficiency as a function of the compressor stage flow coefficient for the GT1749V 55 Trim turbocharger at the exhaust gas temperature $T_{6t} = 973$ K. The difference between the compressor efficiencies decreases significantly with increasing compressor rotational speed. This is due to the decrease in the ratio of the specific amount of heat transfer to the compressor to the compressor aerodynamic work. The difference of the compressor efficiencies also decreases with increasing flow rate from the surge flow rate as a result of decreasing compressor heat number. With further increase of the flow rate, the compressor reaches an operating point where the decrease in the compressor aerodynamic work is more significant than the decrease in the specific amount of heat transfer to the compressor. The difference of the compressor efficiencies starts to increase once again with increasing the compressor flow rate after this point.

It is also very important to note that the behavior of the compressor non-adiabatic efficiency as well as the compressor heat number with the exhaust gas temperature at the turbine entry is non-intuitive. It was expected that the amount of heat transfer to the compressor increases with increasing the exhaust gas temperature at the

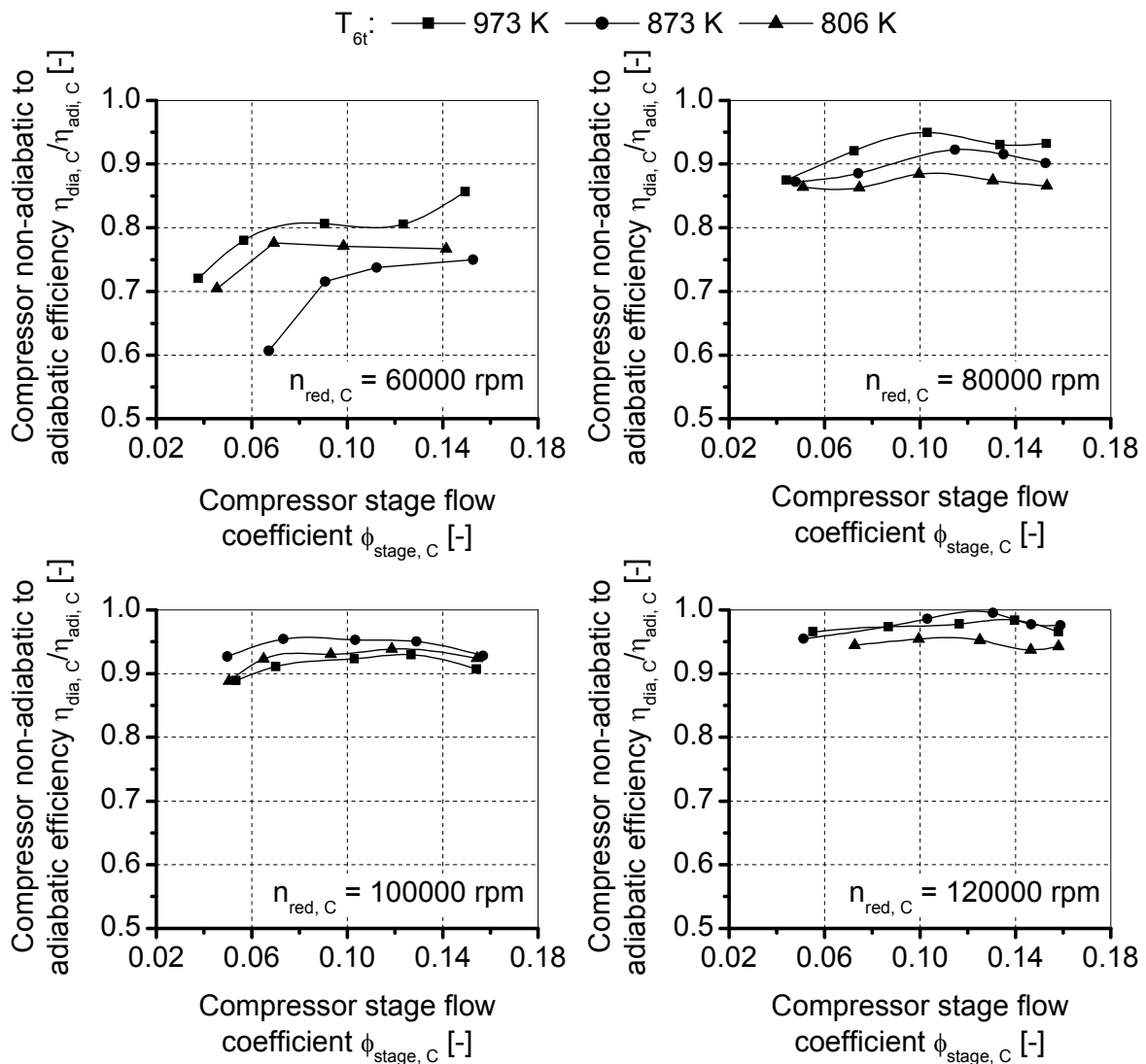


Figure 5-4 Ratio of the compressor non-adiabatic efficiency to the compressor adiabatic efficiency at different compressor reduced rotational speeds and total temperatures at the turbine entry for the GT1749V 55 Trim compressor

turbine entry. However, Figure 5-2 and Figure 5-3 show that the measured compressor non-adiabatic efficiency and the estimated compressor heat number are not directly dependent on the exhaust gas temperature at the turbine entry. The highest deterioration of the compressor non-adiabatic efficiency and the highest compressor heat number for the 60000 rpm compressor performance line take place at $T_{6t} = 873$ K. For the 100000 rpm compressor performance line, this occurs at $T_{6t} = 973$ K for example. This behavior means that the exhaust gas temperature at the turbine entry is not the only parameter affecting the compressor heat number. This is because heat transfers first by conduction from the turbine casing to the bearing housing. The lubrication oil removes part of this conduction heat transfer and

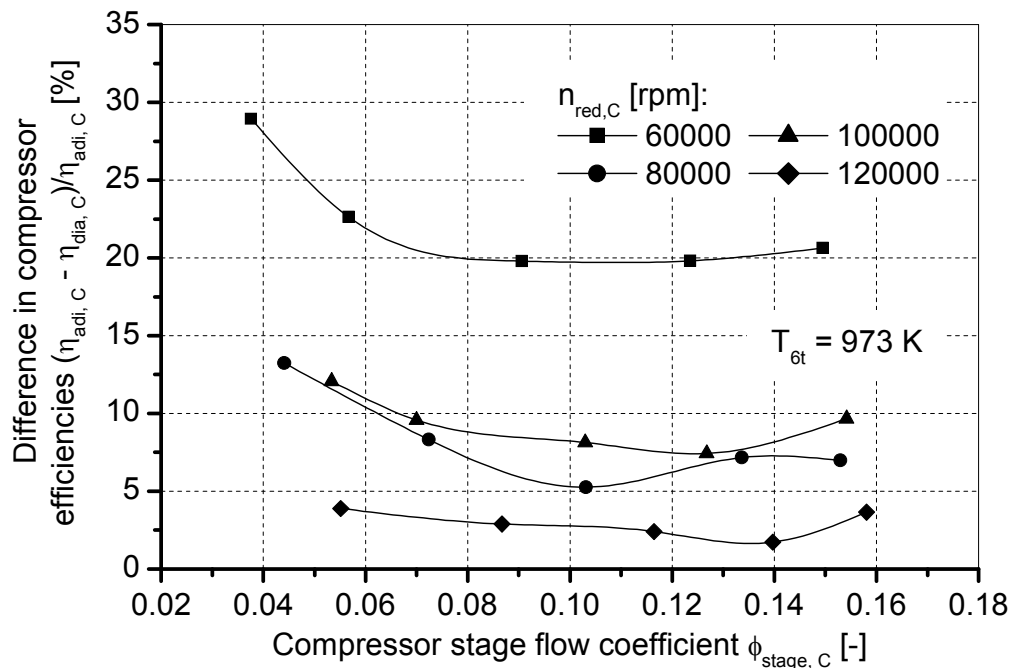


Figure 5-5 Difference between the compressor non-adiabatic efficiency and the adiabatic efficiency of the GT1749V 55 Trim turbocharger at exhaust gas temperature $T_{6t} = 973$ K

the rest flows to the compressor. Thus, the lubrication oil also works as a cooling fluid for the bearing housing. It has therefore a significant effect on the amount of heat transfer to the compressor and hence on the compressor heat number. It is therefore very important to estimate the amount of heat transfer to the oil.

It is also important to estimate the effect of heat transfer to the compressor on the compressor heat efficiency. Figure 5-6 shows the ratio of the compressor heat efficiency to the compressor adiabatic efficiency of the GT1749V 55 Trim turbocharger at different rotational speeds and exhaust gas temperatures at the turbine entry. This figure is estimated from the measured data with the assumption that 50% of the heat transfer to the compressor takes place before the impeller. It is shown in Section 4.3 that this assumption can be made for the compressor at low compressor heat numbers without a significant error in the estimated heat efficiency. Figure 5-6 shows that the amount of heat transfer to the compressor causes 0.5-1.5% deterioration of the compressor heat efficiency at low rotational speeds. The deterioration of the compressor heat efficiency increases with decreasing the compressor flow rate because of the increase in the compressor heat number with decreasing the flow rate.

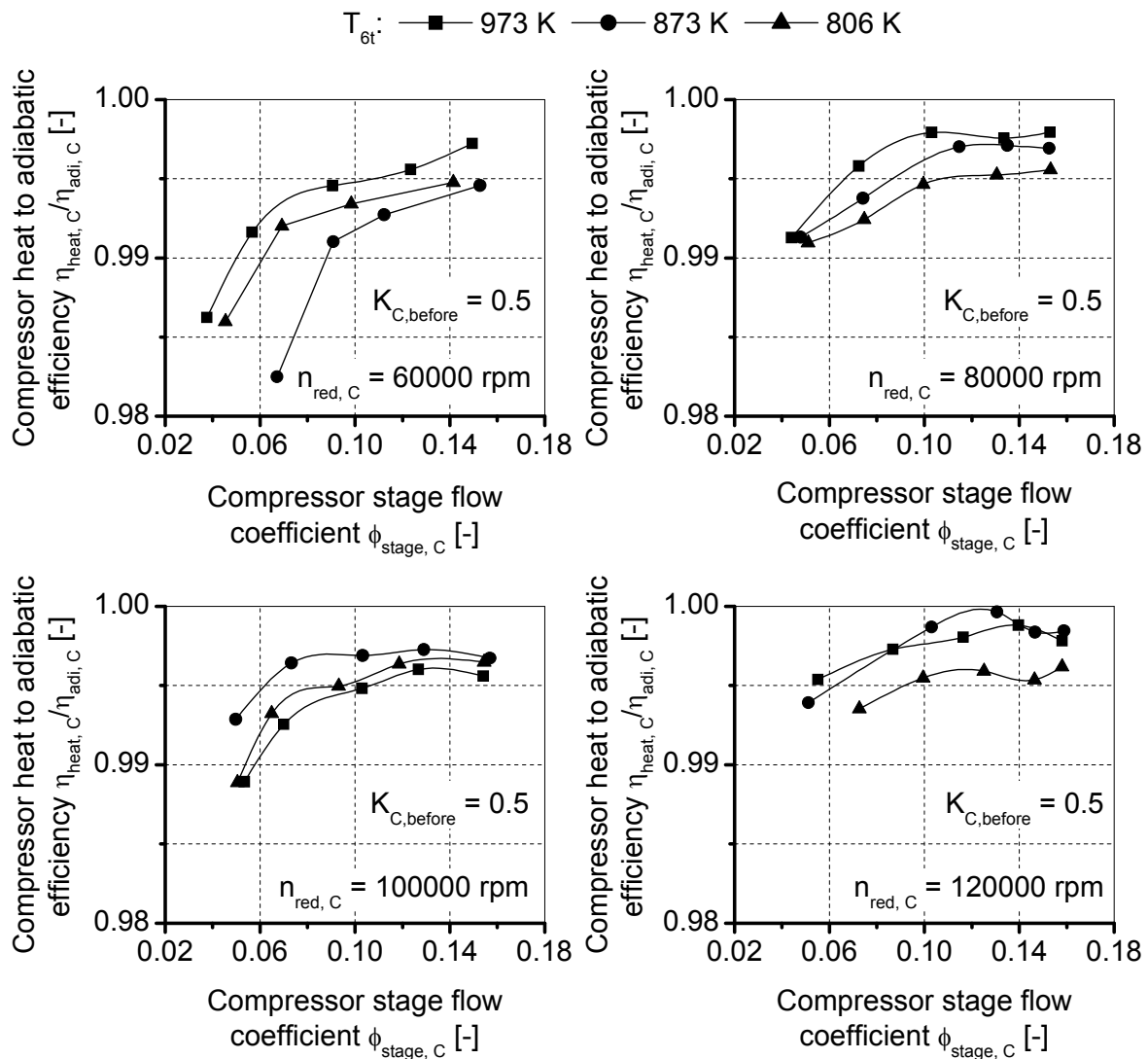


Figure 5-6 Ratio of the compressor heat efficiency to the compressor adiabatic efficiency of the GT1749V 55 Trim turbocharger at different rotational speeds and exhaust gas temperatures at the turbine entry

5.1.1.2 Effect of lubrication oil

The amount of heat transfer to the oil can be estimated from the total power added to the oil and the bearing frictional power. The total power added to the oil is estimated from the oil flow rate and the oil temperature difference across the bearing housing. The frictional power of the bearing can be estimated from the cold measurements of the turbocharger. An empirical formula is obtained for the bearing frictional power as a fraction of the compressor power. This formula is applied because the amount of heat transfer to the oil during hot measurement causes further increase in the oil temperature and hence further decrease of the oil viscosity. The formula is obtained by fitting the test data of the GT1749V 55 Trim turbocharger using the subroutine

“Ifit.for” (*Press et al., 1992*). The test data of the turbocharger at rotational speeds 60000 – 100000 rpm are used as input to the subroutine. The formula is then selected to match very well the test data at 120000 rpm. This enhances the ability of this empirical formula to extrapolate the bearing frictional power at higher rotational speeds. This empirical formula was not tested with bearing geometries and bearing types different than that of the GT1749V 55 Trim turbocharger. It takes the form

$$\frac{Q_{B, \text{fri}}}{\dot{W}_C} = 491627.1 \exp\left(-7.87 \text{Re}_{\text{oil,u}}^{-0.12} \text{Sr}^{0.14}\right) \quad (5.2)$$

The oil Reynolds number based on shaft speed is given by

$$\text{Re}_{\text{oil,u}} = \frac{u_{\text{shaft}} (2cl_B)}{\nu_{\text{oil}}} \quad (5.3)$$

The oil viscosity is estimated at the oil mean temperature. The shaft speed is estimated from the turbocharger rotational speed n and the shaft mean diameter D_{shaft}

$$u_{\text{shaft}} = \frac{\pi n D_{\text{shaft}}}{60} \quad (5.4)$$

The Strouhal number is defined as the ratio of the shaft speed to the oil mean velocity c_{oil}

$$\text{Sr} = u_{\text{shaft}} / c_{\text{oil}} \quad (5.5)$$

The oil mean velocity is estimated by applying continuity equation to the oil flow inside the bearing housing

$$c_{\text{oil}} = \dot{m}_{\text{oil}} / \left(\rho_{\text{oil}} \frac{\pi}{4} (D_{B,i}^2 - D_{\text{shaft}}^2) \right) \quad (5.6)$$

Figure A-13 shows that equation (5.2) can be used to estimate the frictional power of the bearing with a good accuracy based on the test results. Therefore, the amount of heat transfer to the oil during the hot measurements can also be estimated.

Figure 5-7 shows the ratio of the amount of heat transfer to the oil to the compressor power at different turbocharger normalized rotational speeds and exhaust gas temperatures at the turbine entry. This figure is estimated from the measurements along the compressor surge line to ensure comparison under identical turbocharger operating conditions. The turbocharger normalized rotational speed is defined as the ratio of the turbocharger rotational speed to the compressor design rotational speed. The amount of heat transfer to the oil increases with increasing the exhaust gas

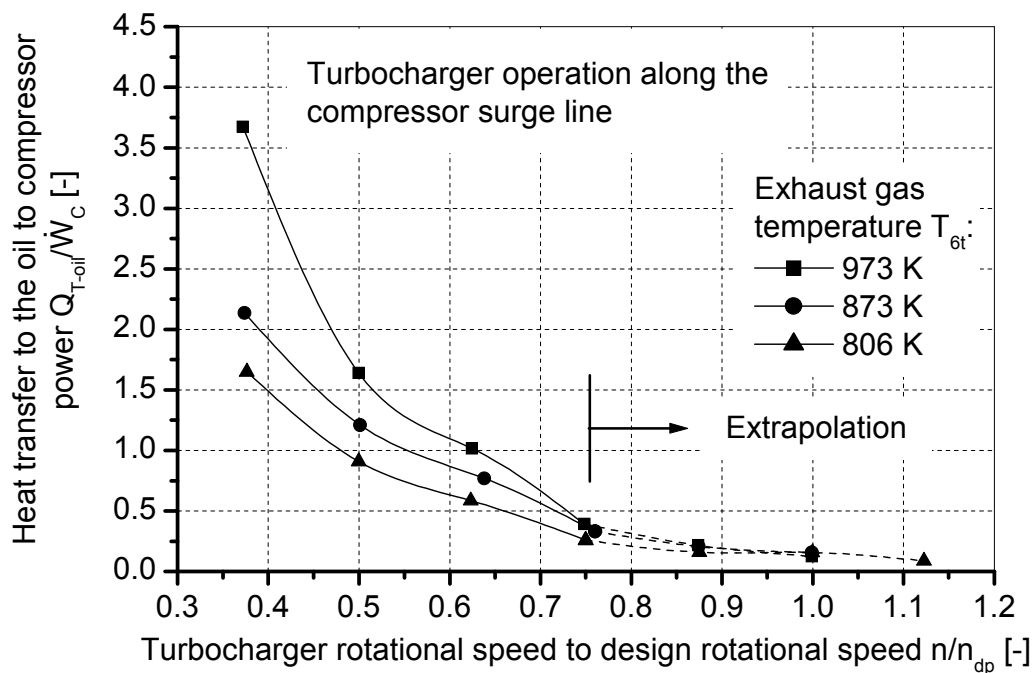


Figure 5-7 Ratio of the amount of heat transfer to the oil to the compressor power at different turbocharger normalized rotational speeds and exhaust gas temperatures at the turbine entry

temperature at the turbine entry. It can be as high as 1.5-3.5 times the compressor power at low rotational speed. The ratio of the amount of heat transfer to the oil to the compressor power decreases with increasing the turbocharger rotational speed. This is due to the increase in the compressor power with increasing the rotational speed. Figure 5-8 shows the amount of heat transfer to the oil as a fraction of the total power added to the oil at different turbocharger normalized rotational speeds. This figure is also extracted from the test data along the compressor surge line. The amount of heat transfer to the oil represents 90-95% of the total power added to the oil at low rotational speeds. This fraction decreases with increasing the turbocharger rotational speed as a result of increasing the bearing frictional power.

Figure 5-7 and Figure 5-8 illustrate clearly the significant effect of the lubrication oil on the turbocharger non-adiabatic performance. The lubrication oil causes complex heat transfer mechanisms inside the turbocharger. This is because the amount of heat transfer from the turbine to the oil increases with increasing the exhaust gas temperature at the turbine entry. This increases the oil temperature in the bearing housing and hence decreases the oil viscosity. Decreasing the oil viscosity decreases the bearing frictional power and increases the oil Reynolds number. Increasing the oil Reynolds number increases the amount of heat transfer to the oil. Therefore, increasing the amount of heat transfer from the turbine to the bearing housing is associated with increasing the ability of the oil to cool the bearing housing.

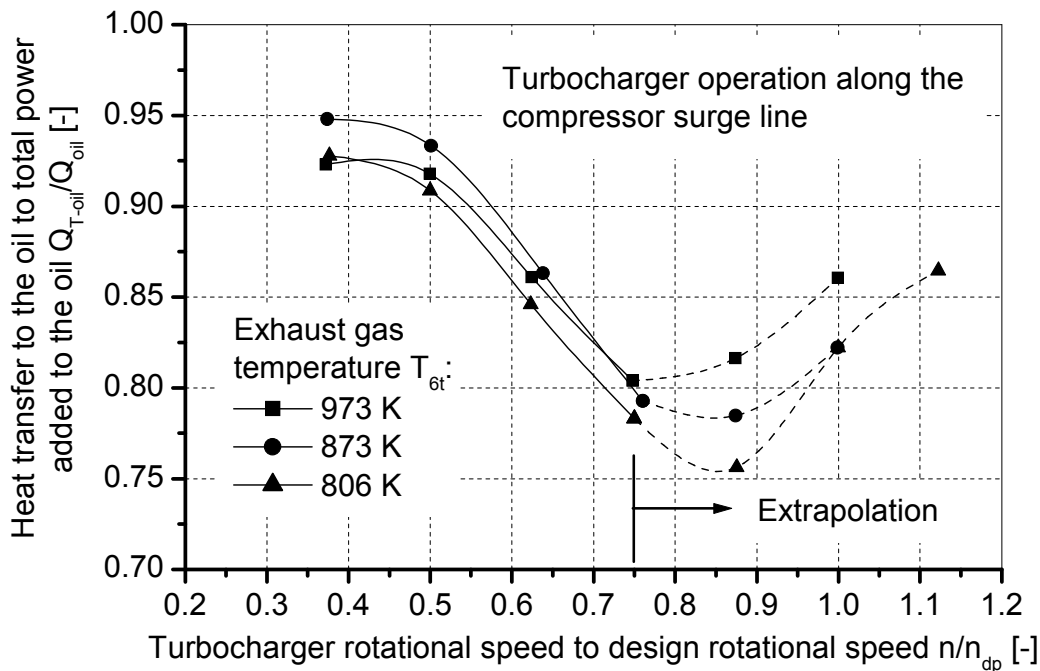


Figure 5-8 Amount of heat transfer to the oil as a fraction of the total power added to the oil at different turbocharger normalized rotational speeds

The amount of heat transfer to the compressor depends on the amount of heat transfer from the turbine to the bearing housing and the amount of heat transfer to the oil. Therefore, the compressor heat number and the deterioration of the compressor non-adiabatic efficiency are affected not only by the exhaust gas temperature at the turbine entry but also by the flow rate and the physical properties of the lubrication oil.

Figure 5-8 also shows that the fraction of heat transfer to the oil increases with increasing the rotational speed above 120000 rpm. These data are estimated from the extrapolation of equation (5.2). This means that heat may also transfer from the compressor to the oil at high rotational speeds. This behavior unfortunately cannot be directly estimated from the available measurements. This is because heat transfer from the compressor to the oil may take place during the cold as well the hot measurements. Comparison of the hot and the cold measurements therefore cannot help in the direct estimation of this behavior. This makes this heat transfer mode hypothetical for the time being. However, this hypothesis can be proven with the help of the available test data. Figure 5-2 shows that the measured compressor non-adiabatic efficiencies at rotational speeds 140000 rpm and 160000 rpm are independent of the exhaust gas temperature at the turbine entry. This means that either the amount of heat transfer to the compressor is very small or heat transfers from the compressor. Figure 5-9 shows the ratio of the compressor casing temperature to the total temperature at the compressor outlet. The compressor

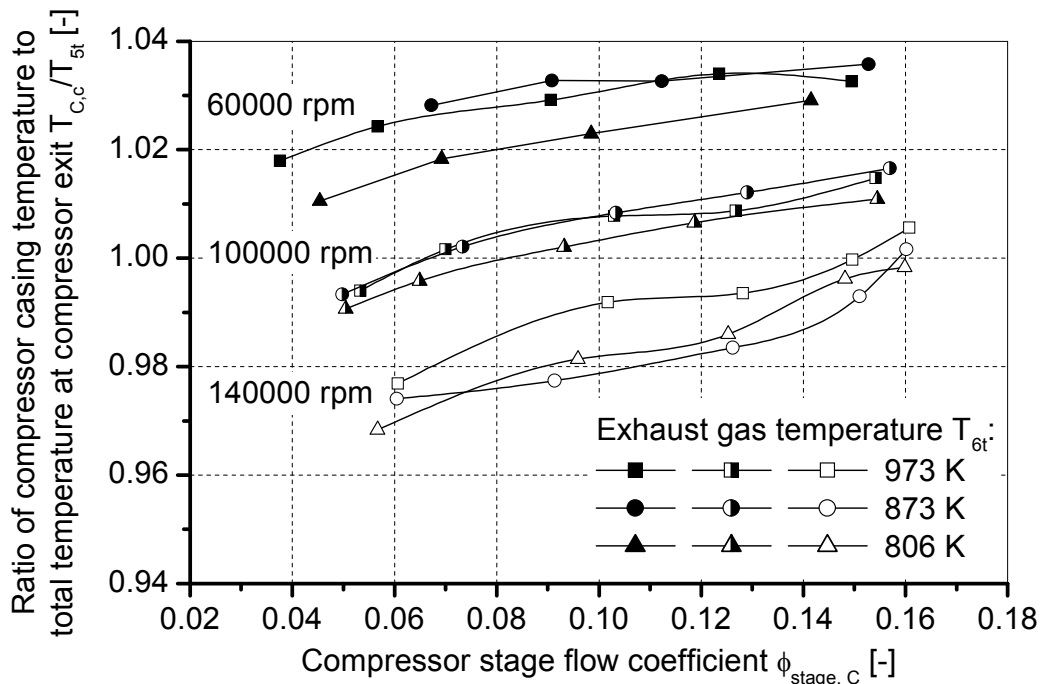


Figure 5-9 Ratio of the compressor casing temperature to the total air temperature at the compressor outlet

casing temperature is measured at a point located on the back side of the compressor at a radius that corresponds to the diffuser outlet and the volute inlet. The casing temperature is higher than the total temperature at the compressor outlet at low rotational speeds. This means that heat transfers to the compressor after the impeller at low rotational speeds. The ratio of the casing temperature to the total temperature at the compressor outlet decreases with decreasing the flow rate and increasing the rotational speed. This indicates that the amount of heat transfer to the compressor decreases with increasing the rotational speed. The compressor casing temperature is lower than the total temperature at the compressor outlet by about 12.6 °C at the surge point of the 140000 rpm performance line. This indicates that heat transfers from the air to the compressor casing at high rotational speeds.

A special experiment is made to prove whether this heat transfers to the ambient by free convection and radiation or to the bearing housing. This experiment is made using the GT1749V 70 Trim turbocharger because the GT1749V 55 Trim was damaged at the end of the experimental work and was no longer available. The GT1749V 70 Trim compressor also shows a non-adiabatic compressor efficiency that is independent of the exhaust gas temperature at high rotational speeds. The GT1749V 70 Trim compressor non-adiabatic efficiency is measured at rotational speed 180000 rpm and exhaust gas temperature 873 K with insulation around the compressor and without insulation. Figure A-14 shows the measured compressor non-adiabatic efficiency with insulation and without insulation. The amount of heat

transfer from the compressor by free convection and radiation has almost no effect on the measured compressor non-adiabatic efficiency. This means that heat can transfer from the compressor to the oil at high turbocharger rotational speeds. This also means that heat transfer by free convection and radiation from the turbine to the compressor has a negligible effect on the compressor non-adiabatic performance. This is because the common surface area available for convection and radiation heat exchange between the turbine and the compressor is small compared with that available for conduction heat transfer in the bearing housing. The low absorptivity of the bright compressor casing also reduces the effect of radiation heat transfer from the turbine to the compressor furthermore. Therefore, it can be assumed that the amount of heat transfer by conduction in the bearing housing is the main source of heat transfer to the compressor.

5.1.1.3 Effect of turbine guide-vane position

The performance of the GT1749V 55 Trim turbocharger is also investigated at different turbine inlet guide-vane positions. Figure A-15 shows a comparison of the measured compressor non-adiabatic efficiency at turbine inlet guide-vane positions 100% open and 0% open and exhaust gas temperature at the turbine entry of 973 K. The turbine inlet guide-vane position has a negligible effect on the compressor non-adiabatic efficiency. This behavior is also observed for many other measured turbochargers. However, these latter results are not available for publication in the present research work. This behavior may be due to the ability of the lubrication oil to overcome any slight variation in the amount of heat transfer from the turbine to the bearing housing with varying turbine inlet guide-vane position.

5.1.2 Twin entry turbocharger compressor

The K29 turbocharger is a twin entry turbocharger without turbine inlet guide vanes. The two turbine entries are called “entry A” and “entry B” in the present research work. Entry A is located in the front half of the turbine while entry B is located in the rear half of the turbine as shown in Figure A-16. The non-adiabatic performance of the K29 compressor is also investigated by comparing the hot and the cold measurements of the K29 turbocharger performance. The K29 compressor non-adiabatic performance is also investigated at different entry total pressure ratios. The entry total pressure ratio is defined as the ratio of the total pressure of turbine entry A to that of turbine entry B

$$\pi_{\text{entry}} = p_{6t,A} / p_{6t,B} \quad (5.7)$$

Figure 5-10 shows the measured compressor total pressure ratio at different

compressor reduced mass flow rates, rotational speeds, and exhaust gas total temperatures at the turbine entry. The exhaust gas temperature at the turbine entry does not affect the measured compressor total pressure ratio. This behavior is similar to the one recorded for the GT1749V 55 Trim turbocharger.

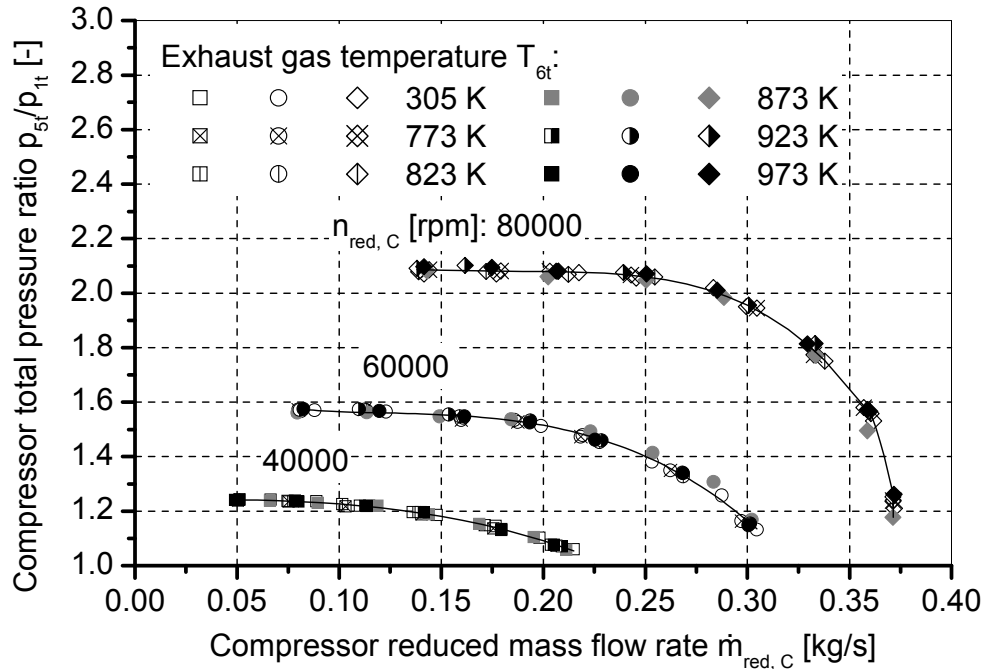


Figure 5-10 Variation of the compressor total pressure ratio with the compressor reduced mass flow rate at different compressor reduced rotational speeds and total temperatures at the turbine entry for the K29 compressor

The measured compressor non-adiabatic efficiency of the K29 turbocharger shows a different behavior than that of the GT1749V 55 Trim turbocharger. Figure 5-11 shows the measured compressor non-adiabatic efficiency of the K29 turbocharger at different rotational speeds and exhaust gas temperatures at the turbine entry. The measured compressor efficiency of the K29 turbocharger is independent of the exhaust gas temperature in the measured range of operation. This means that the amount of heat transfer to the compressor is very small and has a negligible effect on the compressor efficiency. This behavior of the K29 turbocharger is due to the relatively large turbine surface area and the high oil flow rate of the K29 turbocharger. The large turbine surface area causes an increase of the amount of heat transfer from the turbine to the ambient by free convection and radiation. This causes the amount of heat transfer from the turbine to the bearing housing to decrease. The high oil flow rate removes most of the heat transferred to the bearing housing. The high compressor aerodynamic work also results in high air temperature at the impeller outlet. These factors together cause the compressor efficiency of the

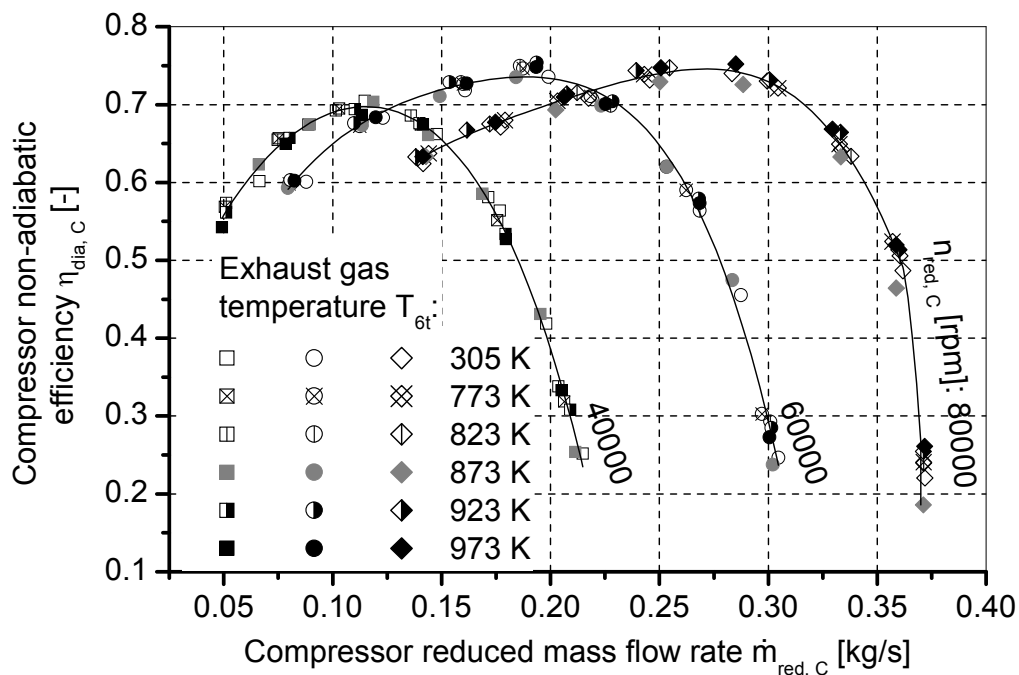


Figure 5-11 Variation of the compressor non-adiabatic efficiency with the compressor reduced mass flow rate at different compressor reduced rotational speeds and total temperatures at the turbine entry for the K29 compressor

K29 turbocharger to be independent of the exhaust gas temperature at the turbine entry. This also applies to the effect of the turbine entry pressure ratio on the measured compressor efficiency as shown in Figure A-17.

5.2 Turbine non-adiabatic performance

Turbine performance is normally presented in terms of the turbine reduced mass flow rate and the product of the turbine efficiency and the turbocharger mechanical efficiency. This product is estimated from the turbocharger efficiency and the compressor efficiency. In the absence of heat transfer to the compressor, the measured compressor efficiency represents the compressor adiabatic efficiency as well as the compressor heat efficiency. The measured turbine heat efficiency in this case represents the actual turbine heat efficiency. The amount of heat transfer to the compressor causes deterioration of the measured compressor non-adiabatic efficiency. Therefore, the measured turbine heat efficiency in this case is greater than the actual turbine heat efficiency. The difference between the measured turbine heat efficiency and the actual turbine heat efficiency is the systematic error due to the amount of heat transfer to the compressor. The amount of heat transfer from the turbine also affects the actual turbine heat efficiency.

5.2.1 Single entry turbine

The performance of the GT1749V 55 Trim turbine is investigated at different inlet guide-vane positions and different exhaust gas temperatures at the turbine entry.

5.2.1.1 Effect of turbine guide-vane position

Figure 5-12 shows the variation of the turbine reduced mass flow rate with the turbine total-to-static pressure ratio at different values of the turbine rotational speed parameter and inlet guide-vane positions. The turbine reduced mass flow rate increases with increasing the turbine total-to-static pressure ratio due to the increase of the expansion ratio through the turbine. It also increases with opening the inlet guide vanes. This is due to the increase of the flow area between the inlet guide vanes with opening the guide vanes. Increasing the turbine flow rate at high turbine rotational speeds increases the centrifugal force on the fluid particles. This centrifugal force acts in the direction opposite to the inward flow direction. It causes a reduction of the flow rate through the turbine at high flow rates and high rotational speeds. This behavior can be observed in Figure 5-12 at inlet guide-vane positions 50% open and 100% open. The effect of the centrifugal force on the turbine reduced mass flow rate at guide-vane position 0% open is very small. This is because of the relatively low turbine flow rate at this inlet guide-vane position.

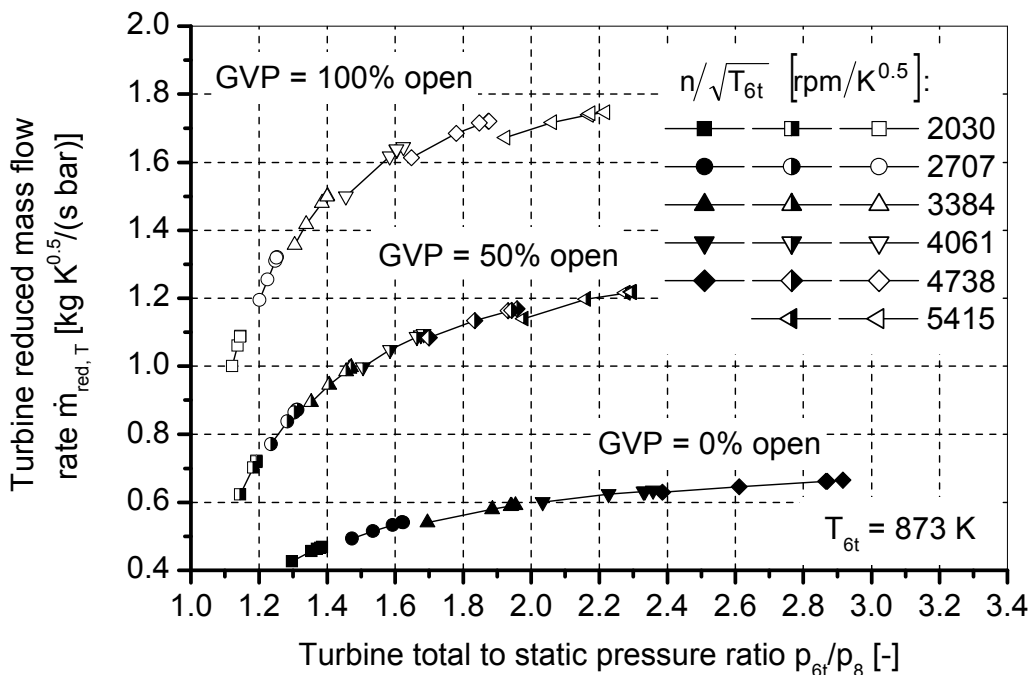


Figure 5-12 Variation of the turbine reduced mass flow rate with the turbine total-to-static pressure ratio at different values of the turbine rotational speed parameter and inlet guide-vane positions

Figure 5-13 shows the variation of the product of the turbine efficiency and the mechanical efficiency with the turbine total-to-static pressure ratio at different values of the turbine rotational speed parameter and inlet guide-vane positions. The highest turbine efficiency is reached at the inlet guide-vane position 50% open. This guide-vane position is therefore assumed to be the design guide-vane position of the GT1749V 55 Trim turbine. The highest turbine efficiency takes place at this position because the flow angle at the guide vanes outlet matches very well with the blade angle at the rotor inlet. The other guide-vane positions represent off-design conditions. Therefore, they have lower turbine efficiency compared with the turbine efficiency at the inlet guide-vane position 50% open.

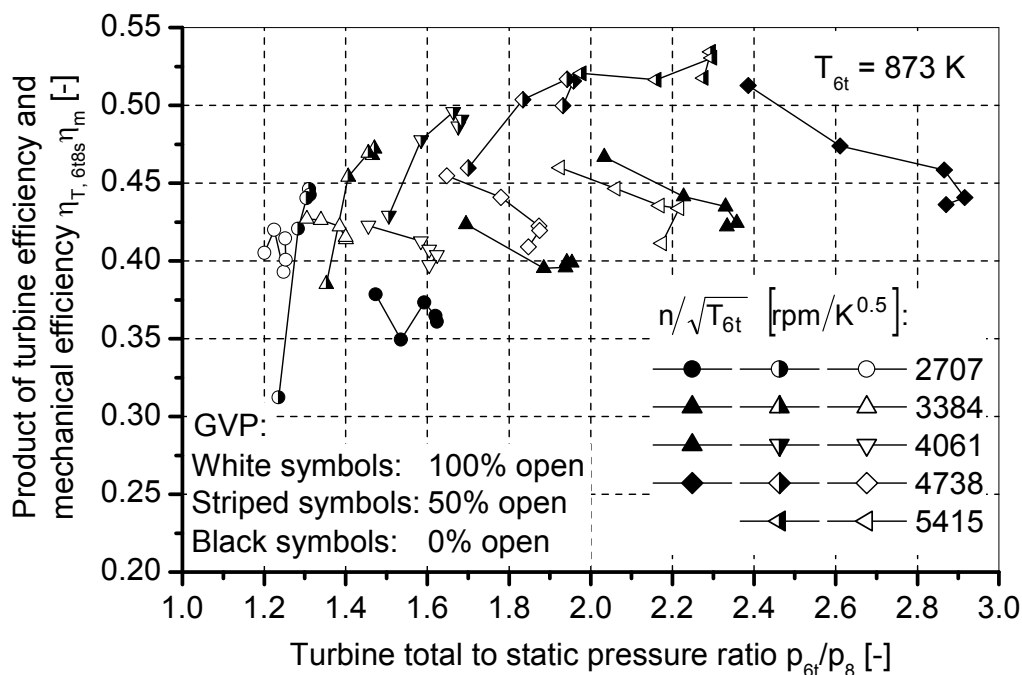


Figure 5-13 Variation of the product of the turbine efficiency and the mechanical efficiency with the turbine total-to-static pressure ratio at different values of the turbine rotational speed parameter and inlet guide-vane positions of the GT1749V 55 Trim turbocharger

5.2.1.2 Effect of exhaust gas temperature at the turbine inlet

Figure 5-14 shows the effect of the exhaust gas temperature at the turbine entry on the turbine reduced mass flow rate. The turbine reduced mass flow rate at different exhaust gas temperatures at the turbine entry depends on the turbine rotational speed parameter and the total-to-static pressure ratio. The effect of the centrifugal force on the turbine reduced mass flow rate can also be observed for the different exhaust gas temperatures at the turbine entry.

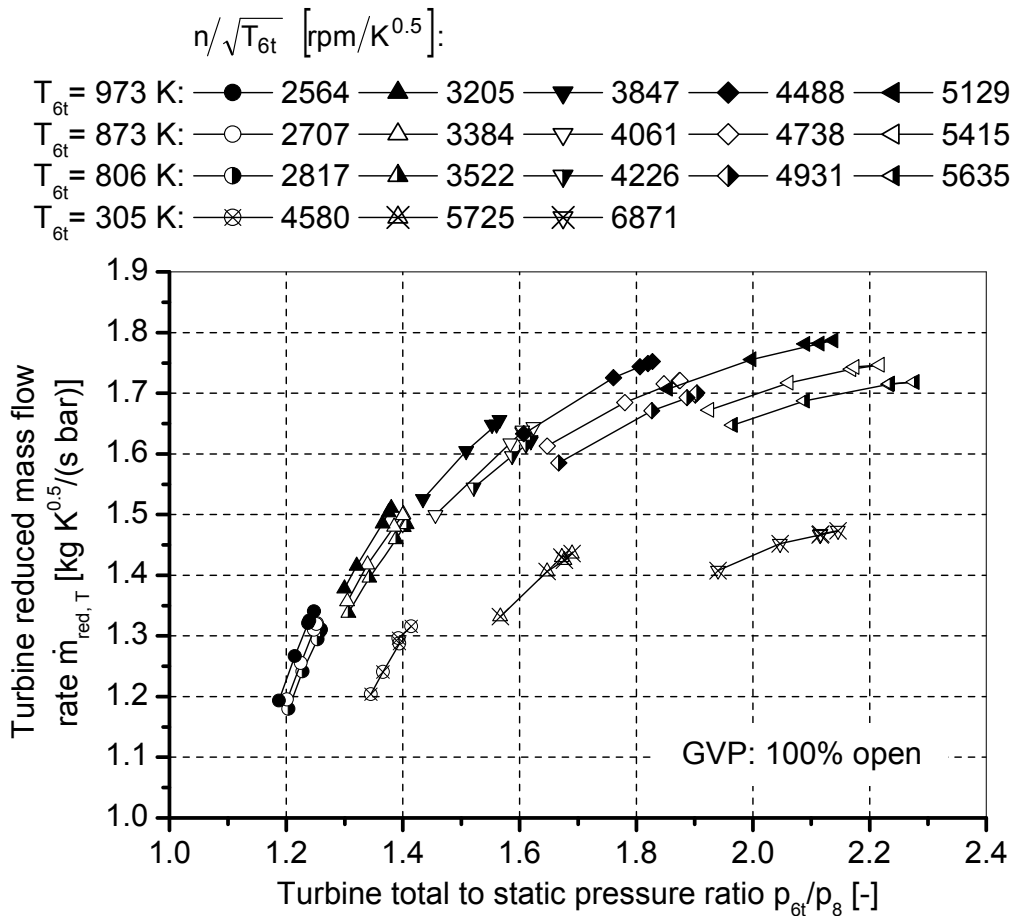


Figure 5-14 Variation of the turbine reduced mass flow rate with the turbine total-to-static pressure ratio at different values of the turbine rotational speed parameter and exhaust gas temperatures at the turbine entry of the GT1749V 55 Trim turbocharger

Figure 5-15 shows the effect of the exhaust gas temperature at the turbine entry on the product of the turbine efficiency and the mechanical efficiency. The measured product of the turbine efficiency and the mechanical efficiency increases with decreasing the total temperature at the turbine entry at the same pressure ratio and turbine rotational speed. This is due to the increase in the amount of heat transfer from the turbine with increasing the exhaust gas temperature at the turbine entry. This increases the turbine heat number with increasing the exhaust gas temperature at the turbine entry as shown in Figure A-18. The effect of the exhaust gas temperature on the product of the turbine efficiency and the mechanical efficiency decreases with increasing the turbine rotational speed. This is due to the decrease of the turbine heat number with increasing the turbine rotational speed, Figure A-18. The decrease in the turbine heat number with increasing the turbine rotational speed is due to the increase of the turbine mass flow rate with increasing the rotational speed. This causes the specific amount of heat transfer from the turbine to decrease with increasing the turbine rotational speed.

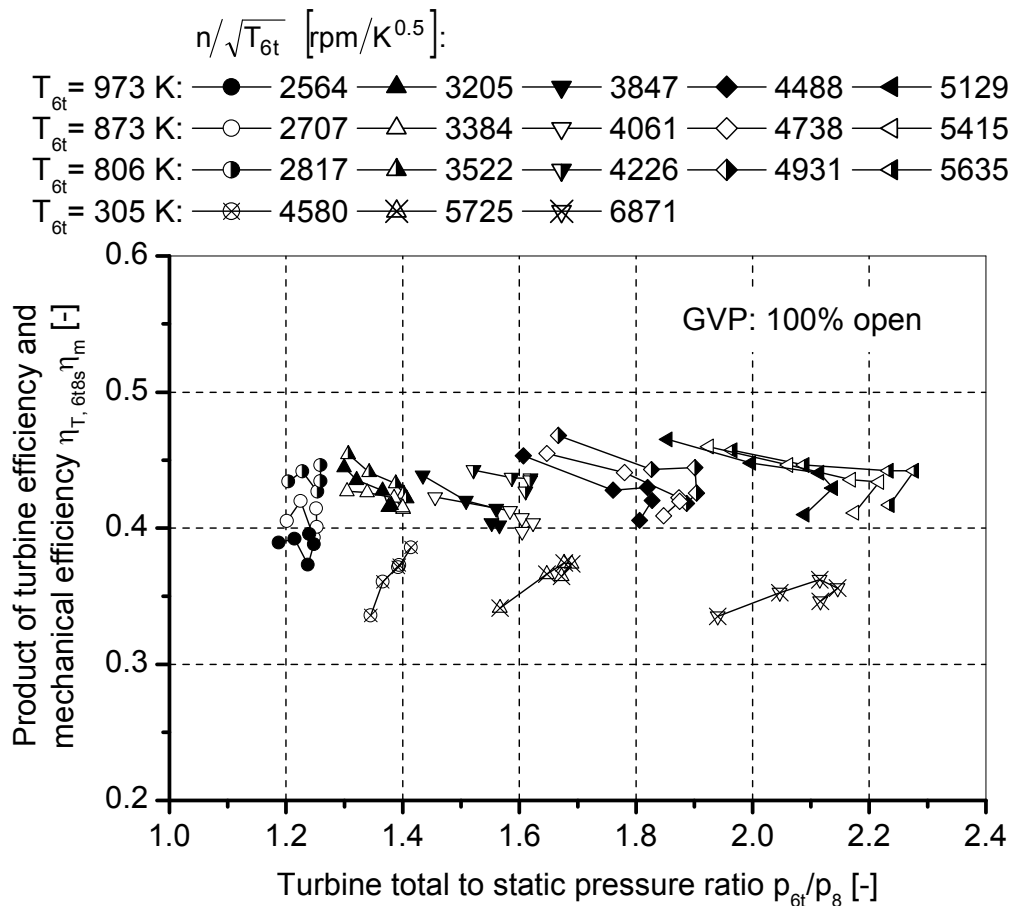


Figure 5-15 Effect of the exhaust gas temperature at the turbine entry on the product of the turbine efficiency and the mechanical efficiency of the GT1749V 55 Trim turbocharger

5.2.1.3 Effect of heat transfer to the compressor

The measured product of the turbine efficiency and the mechanical efficiency is affected by the amount of heat transfer to the compressor at rotational speeds less than or equal to 120000 rpm. This is due to the effect of heat transfer to the compressor on the compressor non-adiabatic efficiency. Therefore, the measured turbine efficiency at low rotational speeds must be corrected to account for the effect of heat transfer to the compressor on the measured compressor non-adiabatic efficiency. The systematic error in the measured product of the turbine efficiency and the mechanical efficiency can be estimated with the help of equations (4.39) and (4.40).

Figure 5-16 shows the systematic percentage error in the estimated turbine heat efficiency due to the amount of heat transfer to the compressor. The systematic error in the turbine heat efficiency increases hyperbolically with decreasing the

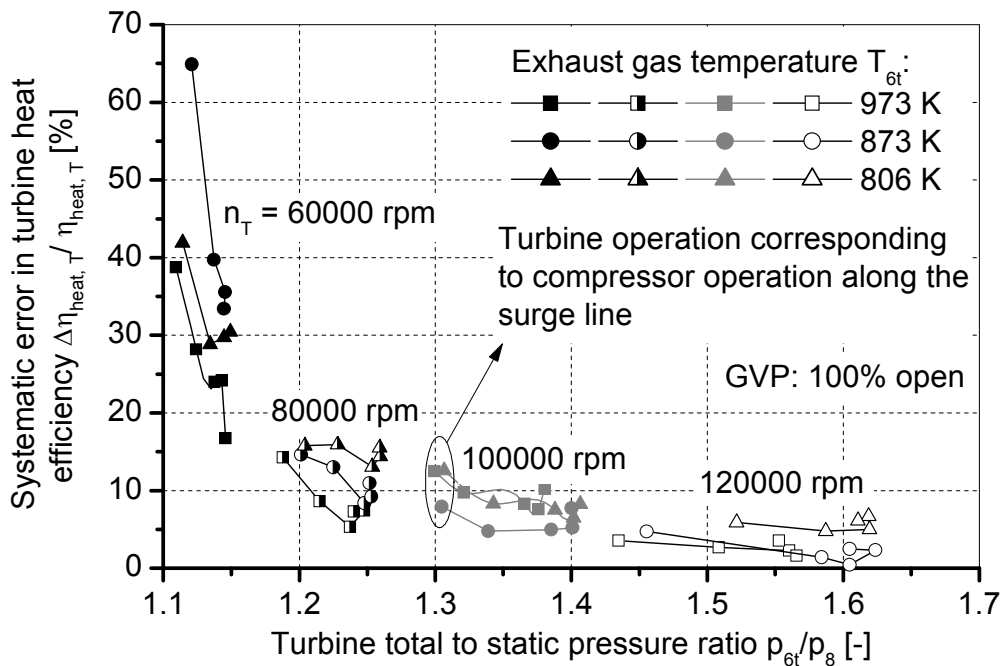


Figure 5-16 Percentage error in the estimated turbine efficiency due to the amount of heat transfer to the compressor of the GT1749V 55 Trim turbocharger

turbocharger rotational speed. It can be as high as 70% at turbocharger rotational speed 60000 rpm. Furthermore, the probable measuring error of the product of the turbine efficiency and the mechanical efficiency is relatively high at low turbocharger rotational speeds (Chapter 3). This may be the reason why the low rotational speed range is not normally included in the manufacturer performance maps. It can also be noted that the systematic error of the turbine heat efficiency due to the amount of heat transfer to the compressor at low rotational speeds is higher than the measuring error. It is therefore very important to correct the measured product of the turbine efficiency and the mechanical efficiency at low rotational speeds using equations (4.39) and (4.40) in order to estimate the actual turbine heat efficiency.

Figure 5-17 shows a comparison between the turbine non-adiabatic efficiency, measured turbine heat efficiency, and the actual turbine heat efficiency. The actual turbine heat efficiency is estimated from the measured turbine heat efficiency using equation (4.39). The turbine non-adiabatic efficiency is estimated from the equation

$$\eta_{\text{dia},T} = \frac{c_{p,\text{exh}}(T_{6t} - T_{8t})}{c_{p,\text{exh}} T_{6t} \left(1 - \pi_{6t8s}^{\frac{\kappa_{\text{exh}}}{\kappa_{\text{exh}} - 1}} \right)} \quad (5.8)$$

The turbine non-adiabatic efficiency increases hyperbolically with decreasing the

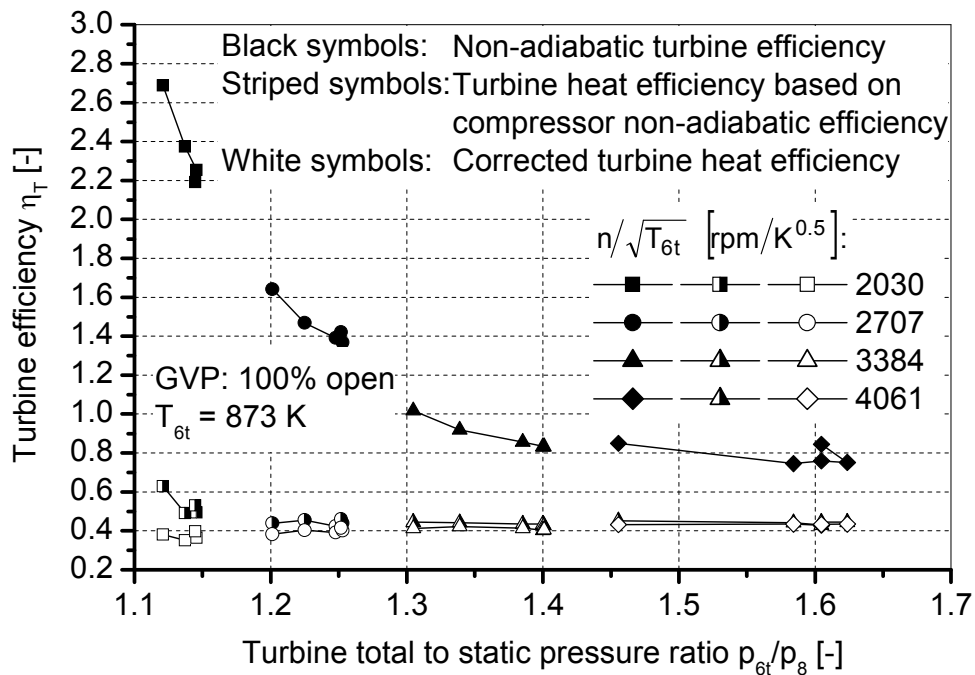


Figure 5-17 Comparison between the turbine non-adiabatic efficiency, the measured turbine heat efficiency, and the actual turbine heat efficiency of the GT1749V 55 Trim turbocharger

turbine rotational speed. The estimated turbine non-adiabatic efficiency exceeds 100% at low rotational speeds and can be as high as 270% at 60000 rpm. This behavior is also recorded by Malobabic (1989). It is of course clear that turbine efficiency higher than 100% has no physical meaning. This happens because the definition of the turbine non-adiabatic efficiency assumes the amount of heat transfer from the turbine to be useful work, equation (5.8). The amount of heat transfer from the turbine is very large compared with the turbine power at low rotational speeds. Therefore, the estimated turbine non-adiabatic efficiency exceeds 100% at low rotational speeds.

The total amount of heat transfer from the turbine is the sum of the amount of heat transfer from the turbine to the ambient and the amount of heat transfer from the turbine to the bearing housing. The latter is further divided into heat transfer to the oil and heat transfer to the compressor. The amount of heat transfer to the compressor is included in the definition of the compressor non-adiabatic efficiency as a compressor power. The compressor non-adiabatic efficiency is used to estimate the product of the turbine efficiency and the mechanical efficiency. Therefore, the systematic error in the measured turbine heat efficiency results from the erroneous consideration of the amount of heat transfer to the compressor divided by the turbocharger mechanical efficiency as a useful turbine power. The amount of heat transfer to the compressor is very small compared with the total amount of heat

transfer from the turbine. Therefore, the measured turbine heat efficiency does not exceed 100%. However, it contains an error that can be as high as 70% at low rotational speeds.

The corrected turbine heat efficiency provides the actual performance of the turbine. Figure 5-17 shows that the turbine non-adiabatic efficiency and the measured heat efficiency increase with decreasing the rotational speed due to the amount of heat transfer between the components of the turbocharger as well as between the turbocharger and the ambient. The corrected turbine heat efficiency decreases with decreasing the turbine rotational speed. This is because of the increase in the aerodynamic losses of the turbine at part load operation.

5.2.2 Twin entry turbine

The performance of the K29 turbine is investigated at entry pressure ratios extending from 0.6 to 1.4 and at a mean exhaust gas temperature at the turbine entry of 873K. The mean total temperature at the turbine entry is estimated from the equation

$$T_{6t} = \frac{\dot{m}_A T_{6t,A} + \dot{m}_B T_{6t,B}}{\dot{m}_A + \dot{m}_B} \quad (5.9)$$

The investigated rotational speeds are 40000, 60000, 80000, and 100000 rpm. However, low rotational speeds are not measured at some entry pressure ratios. This is because one of the two turbine entries was completely closed before reaching the required rotational speed at the required entry pressure ratio. The highest measured turbocharger rotational speed, 100000 rpm, is measured only at entry pressure ratios 0.9, 1.0, and 1.1. This is because the turbine power under test conditions was not sufficient to drive the compressor at 100000 rpm for the other entry pressure ratios. The performance of the turbine is measured at all entry pressure ratios at 80000 rpm and a mean exhaust gas temperature of 873K. The performance of the turbine is also investigated at different mean exhaust gas temperatures at the turbine entry for entry pressure ratio of 1.0.

5.2.2.1 Turbine reduced mass flow rate

Figure A-19 to Figure A-27 show the variation of the reduced mass flow rate with the turbine total-to-static pressure ratio at different entry pressure ratios. The reduced mass flow rate of the K29 turbocharger is presented separately for each turbine entry. The entry reduced mass flow rate is defined on the basis of the corresponding entry total pressure and total temperature

$$\dot{m}_{\text{red},T,A} = \frac{\dot{m}_{T,A} \sqrt{T_{6t,A}}}{p_{6t,A}} \quad (5.10)$$

$$\dot{m}_{\text{red},T,B} = \frac{\dot{m}_{T,B} \sqrt{T_{6t,B}}}{p_{6t,B}} \quad (5.11)$$

The reduced mass flow rate of each entry is also presented in the figures as a function of the corresponding total-to-static pressure ratio

$$\pi_{6t8s,A} = p_{6t,A} / p_8 \quad (5.12)$$

$$\pi_{6t8s,B} = p_{6t,B} / p_8 \quad (5.13)$$

Figure A-19 to Figure A-27 show that the entry reduced mass flow rate depends on the corresponding total-to-static pressure ratio. The reduced mass flow rate of entry A is less than that of entry B at entry total pressure ratio less than 1.0. The reduced mass flow rate of entry A is greater than that of entry B at entry total pressure ratio greater than 1.0. However, the two reduced mass flow rates are not equal at entry pressure ratio of 1.0. The flow rate through entry A is higher than that through entry B at entry pressure ratio of 1.0. This behavior was also recorded by Pischinger and Wuensche (1978) for twin entry turbines. This behavior may be explained with the variation of the rotor passage losses with the passage width as follows. The passage width can be divided into two halves. The first half extends from the rotor wall to the mid plane of the rotor. This half is facing entry B as shown in Figure 5-18 and is therefore called half B. The second half extends from the rotor mid plane to the rotor shroud. This half is facing entry A of the turbine and it is therefore called half A. The comparison between the two halves shows that half A has a shorter mean passage length than half B, Figure 5-18. This means that friction losses and passage losses of half A are lower than that of half B. The rotor wall in half B also causes higher development of the boundary layers in this half. Furthermore, the higher radius of curvature of half B results in higher fluid velocity in this half. The high fluid velocity and the high radius of curvature impose higher centrifugal force on the fluid particles in half B. This higher centrifugal force presses the faster fluid particles toward the rotor wall and deflects the slower particles from the wall. Thus the process of turbulent mixing is accentuated and the intensity of turbulence increases (*Schlichting, 1968*). This enhances the development of the boundary layers on the rotor wall in half B. The relatively long passage length of half B enhances the boundary layer development on the rotor wall further. The curvature of half A also imposes centrifugal force on the fluid particles. However, it forces the faster particles away from the wall and therefore impedes the turbulent mixing (*Schlichting, 1968*).

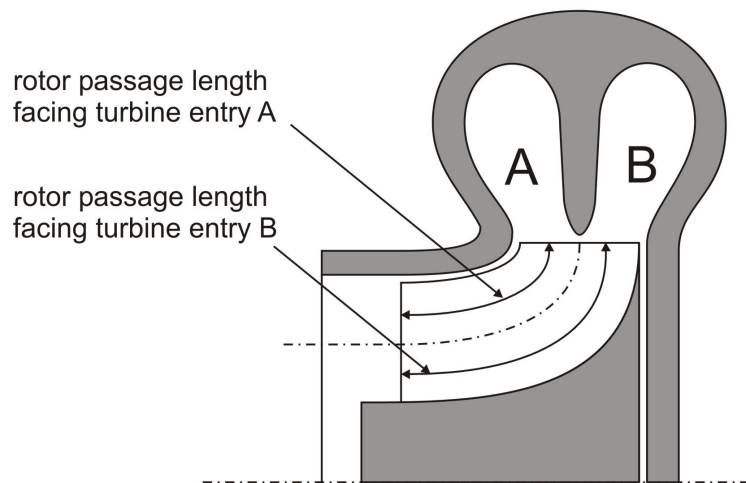


Figure 5-18 Declaration of the effect of the rotor passage aerodynamic losses on the entry mass flow rate of the K29 turbine

This causes a reduction of the boundary layer thickness in half A. the rotation of the blades relative to the shroud causes a further decrease in the boundary layer thickness. Therefore, half B is characterized by higher aerodynamic losses compared with that of half A. This introduces higher aerodynamic resistance against the flow in half B. Therefore, the flow rate through entry A is higher than that through entry B even at entry pressure ratio of 1.0.

The effect of the turbine rotor on the entry flow rate can be further investigated with the help of Figure 5-19. This figure shows the ratio of the entry flow rate to the total turbine mass flow rate as a function of the entry isentropic pressure ratio ψ_{AB} at a turbocharger rotational speed 81404 rpm. The entry isentropic enthalpy ratio ψ_{AB} is defined as

$$\psi_{AB} = \frac{\Delta h_{6t8s,is,A}}{\Delta h_{6t8s,is,B}} \quad (5.14)$$

At entry isentropic enthalpy ratio of 1.0, the flow rate through entry A is higher than that through entry B as discussed above. For an entry isentropic enthalpy ratio of 0.6, the mass flow rate through entry A represents 30% of the turbine mass flow rate and that of entry B represents 70% of the turbine flow rate. For an entry isentropic enthalpy ratio of 1/0.6, the mass flow rate through entry A represents 72.5% of the turbine mass flow rate and that of entry B represents 27.5% of the turbine flow rate. This means that the rotor aerodynamic resistance introduces asymmetry in the flow rate through entries A and B. The flow rate through entry A at a certain entry isentropic enthalpy ratio is always higher than that through entry B which operates at

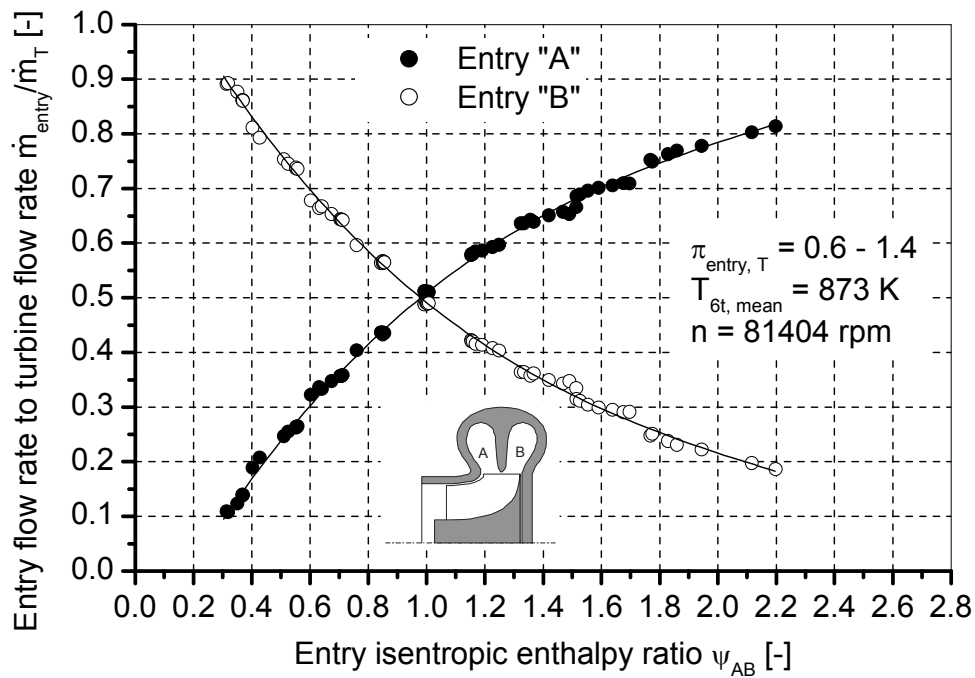


Figure 5-19 Ratio of the entry flow rate to the total turbine mass flow rate of the K29 turbine as a function of the entry isentropic pressure ratio at turbocharger rotational speed 81404 rpm

the reciprocal of the same isentropic enthalpy ratio. This applies to all investigated isentropic enthalpy ratios and rotational speeds, Figure A-28 to Figure A-30.

5.2.2.2 Turbine efficiency

The product of the turbine efficiency and the mechanical efficiency of the K29 turbocharger is estimated from (Section 1.5.2)

$$\eta_{heat,T} \eta_m = \frac{\dot{m}_C \Delta h_{t,is,C}}{\dot{m}_T \Delta h_{6t8s,is}} \cdot \frac{1}{\eta_{heat,C}} \quad (5.15)$$

The isentropic total-to-static enthalpy difference of the K29 turbine is estimated from

$$\Delta h_{6t8s,is} = \frac{\dot{m}_{T,A} c_{p,exh} T_{6t,A} \left(1 - \pi_{6t8s,A}^{\frac{\kappa_{exh}-1}{\kappa_{exh}}} \right) + \dot{m}_{T,B} c_{p,exh} T_{6t,B} \left(1 - \pi_{6t8s,B}^{\frac{\kappa_{exh}-1}{\kappa_{exh}}} \right)}{\dot{m}_{T,A} + \dot{m}_{T,B}} \quad (5.16)$$

Figure A-31 shows the variation of the product of the turbine efficiency and the mechanical efficiency of the K29 turbocharger with the mean total-to-static pressure ratio at different values of the turbine rotational speed parameter and entry pressure ratio of 1.0. The mean total-to-static pressure ratio is defined as the ratio of the mean

total pressure at the turbine entry to the static pressure at the turbine outlet. The mean total pressure at the turbine entry is given by

$$p_{6t} = 0.5 (p_{6t,A} + p_{6t,B}) \quad (5.17)$$

The estimated product of the turbine efficiency and the mechanical efficiency of the K29 turbocharger represents the actual turbine performance. This is because the compressor of the K29 turbocharger works almost adiabatically as mentioned before. The product of the turbine efficiency and the mechanical efficiency is therefore not affected by the amount of heat transfer to the compressor. However, the amount of heat transfer from the turbine does affect the heat efficiency of the K29 turbine. Figure A-32 shows the product of the turbine efficiency and the mechanical efficiency of the K29 turbine at different exhaust gas temperatures at the turbine entry. The K29 turbine efficiency increases with decreasing the exhaust gas temperature at the turbine entry. This behavior is also observed for the GT1749V 55 Trim turbocharger within the investigated range of exhaust gas temperatures at the turbine entry. This behavior occurs because decreasing the exhaust gas temperature at the turbine entry results in decreasing the overall heat losses of the turbine.

It is also of special importance to investigate the effect of partial admission ($\pi_{\text{entry}} \neq 1.0$) on the efficiency of the K29 turbine. Figure 5-20 shows the heat efficiency of the K29 turbine as a function of the blade speed parameter u/c_s at different entry pressure ratios. The turbine heat efficiency is estimated from the measured product of the turbine efficiency and the mechanical efficiency. The mechanical efficiency is estimated from the frictional power of the K29 turbocharger. The turbine spouting velocity [equation (1.20)] is estimated for the K29 turbine from

$$c_s = \sqrt{2\Delta h_{6t-8s, \text{is}}} \quad (5.18)$$

The isentropic total-to-static enthalpy difference $\Delta h_{6t-8s, \text{is}}$ is estimated under partial admission conditions ($\pi_{\text{entry}} \neq 1.0$) from equation (5.16). The line drawn in Figure 5-20 represents a parabolic best fit of the turbine heat efficiency at an entry pressure ratio of 1.0. The turbine efficiency under full admission condition as well as under partial admission condition depends mainly on the turbine blade speed parameter. A function representing the turbine efficiency in terms of the blade speed parameter at full admission condition can also be used to estimate the turbine efficiency under partial admission conditions. This supports the statement that the blade speed parameter u/c_s is the main parameter affecting the efficiency of radial turbines (*Rodgers, 2003*). This statement also applies to a partial admission condition of the K29 twin entry turbine provided that the isentropic total-to-static enthalpy difference is estimated under partial admission condition from equation (5.16).

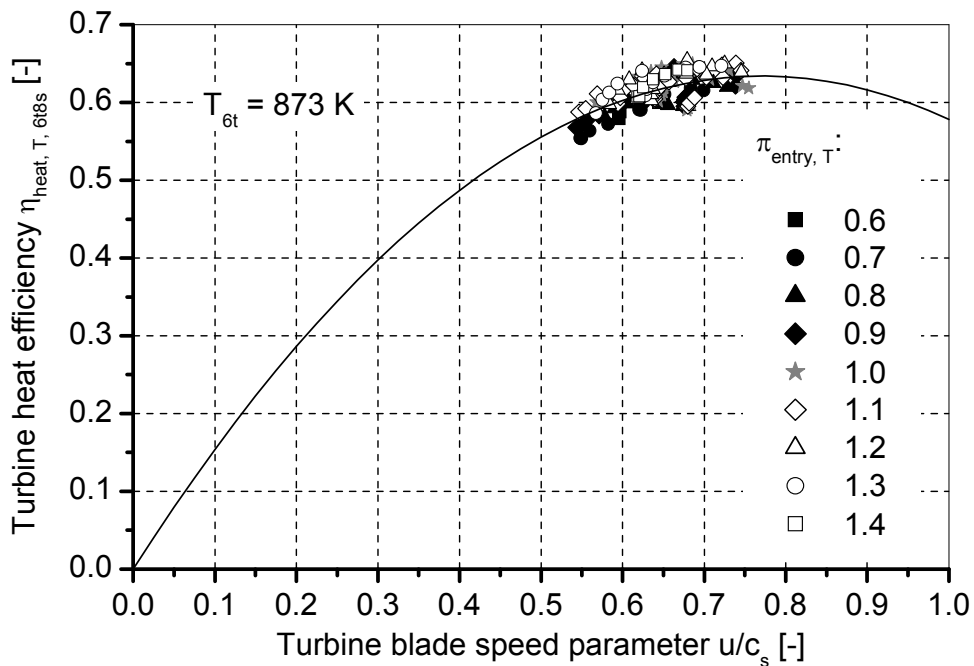


Figure 5-20 Heat efficiency of the K29 turbine as a function of the blade speed parameter at different entry pressure ratios

5.3 Amount of heat transfer in/from the single entry turbocharger

The amount of heat transfer from the turbocharger to the ambient can be estimated by applying a heat balance to the turbocharger. Figure 5-21 shows the turbocharger as a thermodynamic system. The amount of heat transfer by convection and radiation from the turbine to the ambient can be estimated from

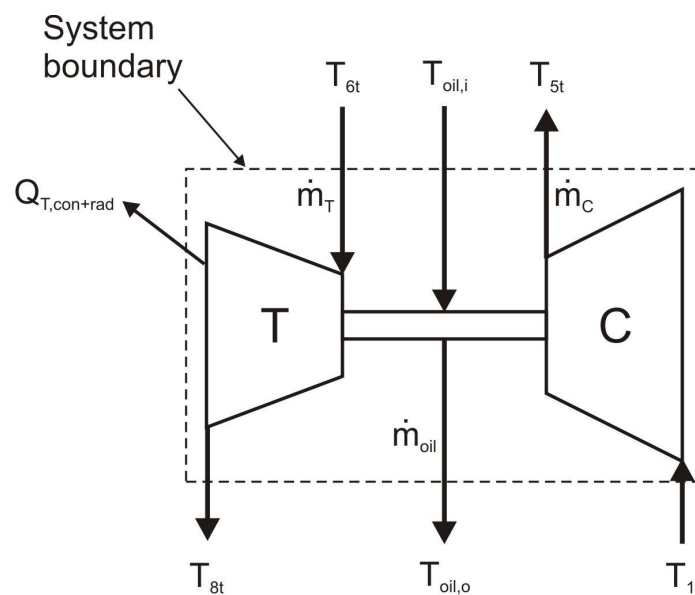


Figure 5-21 Turbocharger as a thermodynamic system

$$Q_{\text{con+rad,T}} = \dot{m}_T c_{p,\text{exh}} (T_{6t} - T_{8t}) - \dot{m}_C c_{p,\text{air}} (T_{5t} - T_{1t}) - Q_{\text{oil}} \quad (5.19)$$

The total power added to the oil can be estimated from

$$Q_{\text{oil}} = \dot{m}_{\text{oil}} (c_{p,\text{oil,o}} T_{\text{oil,o}} - c_{p,\text{oil,i}} T_{\text{oil,i}}) \quad (5.20)$$

The subscripts i and o in equation (5.20) denote inlet and outlet of the bearing housing, respectively. The amount of heat transfer from the turbine to the oil can be estimated from the total power added to the oil and the bearing frictional power

$$Q_{T-\text{oil}} = Q_{\text{oil}} - Q_{B,\text{fri}} \quad (5.21)$$

The bearing frictional power can be estimated for the GT1749V 55 Trim turbocharger from equation (5.2). The amount of heat transfer from the turbine to the compressor through the bearing housing can be estimated from the equation

$$Q_{T-C} = \dot{m}_C c_{p,\text{air}} (T_{5t} - T_{1t}) - \dot{W}_C \quad (5.22)$$

The compressor aerodynamic work and hence the compressor power can be estimated from the cold measurements.

The overall turbine heat loss is the summation of the amount of heat transfer from the turbine to the ambient, the amount of heat transfer from the turbine to the oil, and the amount of heat transfer from the turbine to the compressor through the bearing housing

$$Q_T = Q_{\text{con+rad,T}} + Q_{T-\text{oil}} + Q_{T-C} \quad (5.23)$$

Figure 5-22 shows the amount of heat transfer by convection and radiation from the turbine to the ambient as a fraction of the total amount of heat transfer from the turbine. Convection and radiation heat transfer from the turbine are the main mechanisms of heat transfer from the turbine. They represent 60-70% of the total amount of heat transfer from the turbine at low rotational speeds. This percentage increases with increasing the turbocharger rotational speed and can be as high as 90% of the total amount of heat transfer from the turbine. This is because the amount of heat transfer from the turbine to the oil as well as the amount of heat transfer from the turbine to the compressor decrease with increasing the turbocharger rotational speed.

The amount of heat transfer from the turbine to the oil represents 10-49% of the total amount of heat transfer from the turbine as shown in Figure 5-23. This means that the oil acts as a heat barrier that removes most of the heat transfer from the turbine

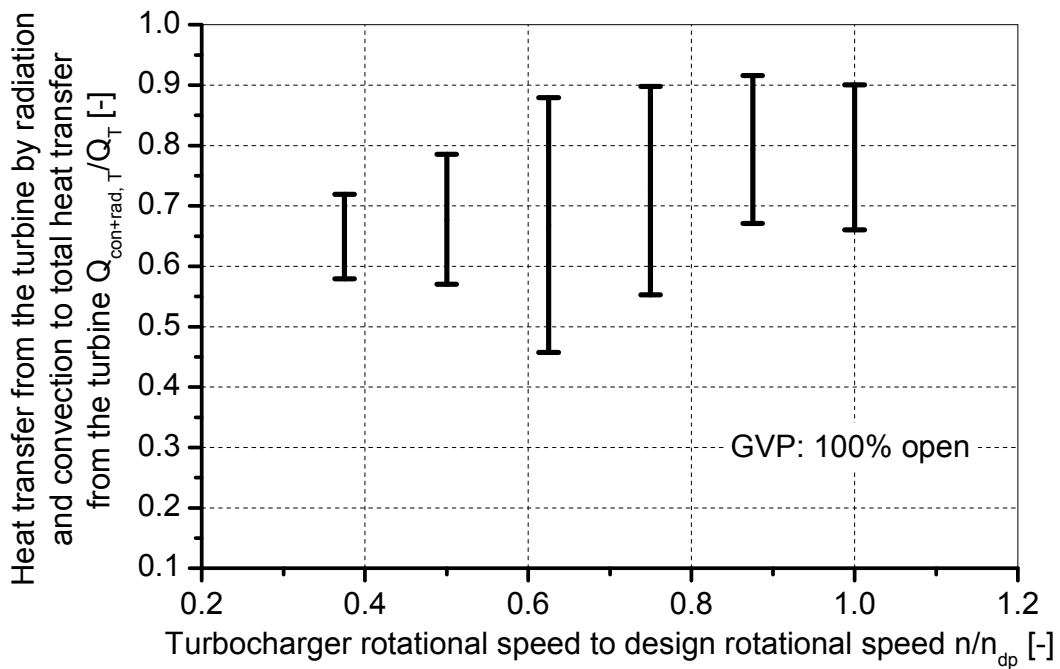


Figure 5-22 Range of heat transfer by convection and radiation from the turbine to the ambient as a fraction of the total amount of heat transfer from the turbine of the GT1749V 55 Trim turbocharger

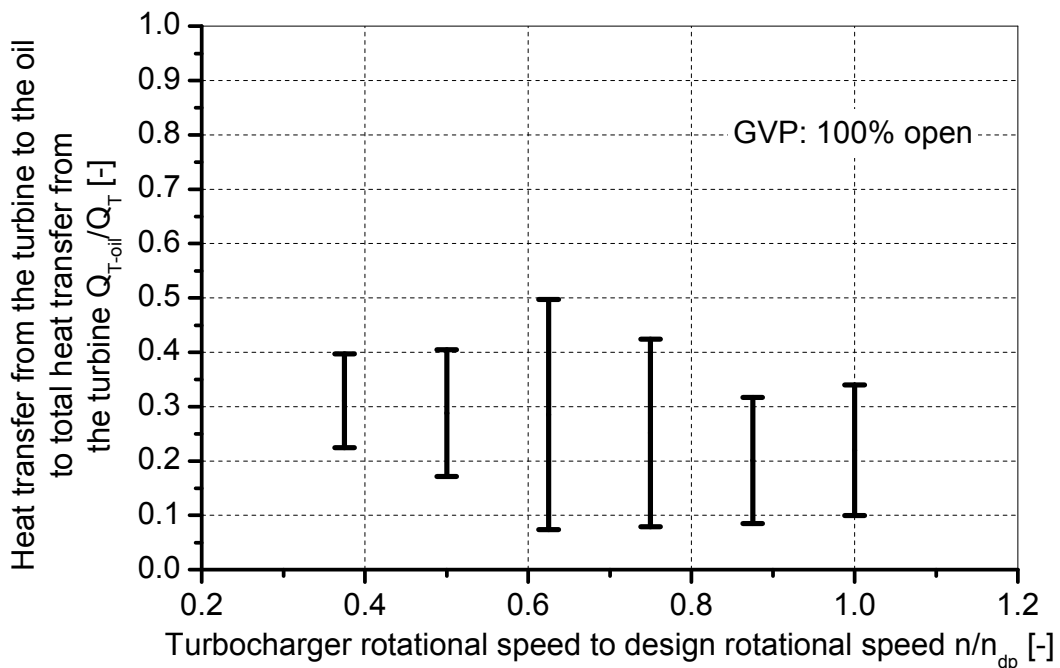


Figure 5-23 Range of heat transfer from the turbine to the oil as a fraction of the total amount of heat transfer from the turbine of the GT1749V 55 Trim turbocharger

to the compressor through the bearing housing.

The amount of heat transfer from the turbine to the compressor through the bearing housing is less than 10% of the total amount of heat transfer from the turbine as shown in Figure 5-24. This small percentage causes significant deterioration of the compressor non-adiabatic performance at very low rotational speeds because of the very small compressor aerodynamic work at this operating range.

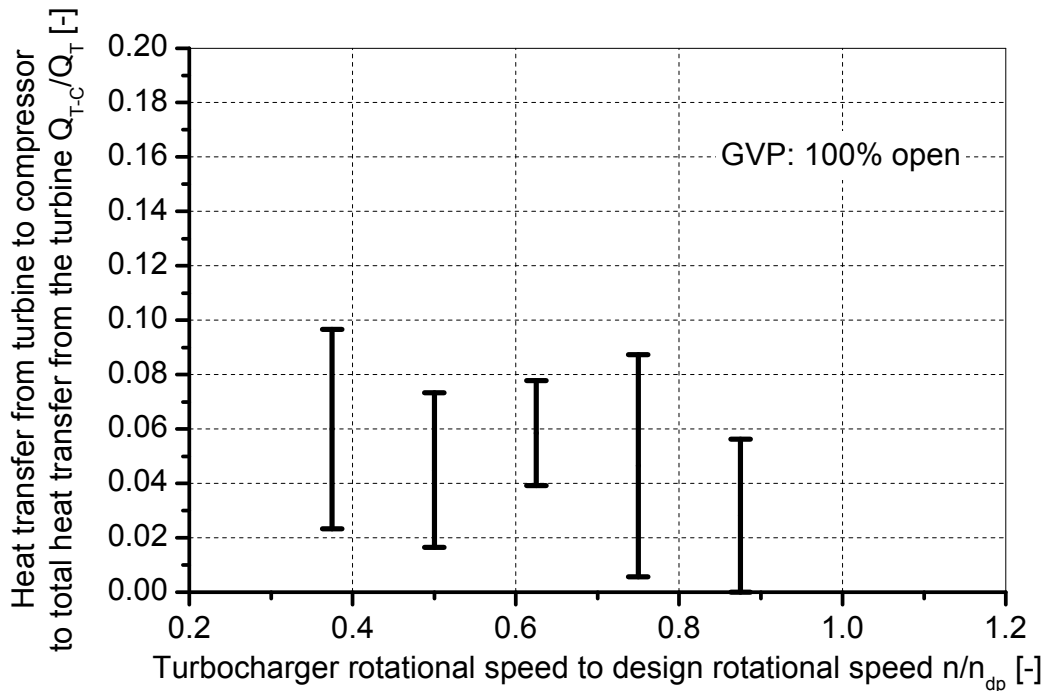


Figure 5-24 Range of heat transfer from the turbine to the compressor as a fraction of the total amount of heat transfer from the turbine of the GT1749V 55 Trim turbocharger

The total amount of heat transfer from the turbine itself represents a very small fraction of the fluid power supplied to the turbine. Figure 5-25 shows the total amount of heat transfer from the turbine as a fraction of the fluid power supplied to the turbine. The total amount of heat transfer from the turbine represents about 6-8% of the fluid power supplied to the turbine at 60000 rpm. This percentage decreases with increasing the turbocharger rotational speed and reaches about 4% of the fluid power supplied to the turbine at the rotational speed of 120000 rpm. This is because the increase in the fluid power supplied to the turbine with increasing the turbocharger rotational speed is more significant than the increase of the turbine casing temperature, Figure A-12. Therefore, it can be said that the amount of heat transfer from the turbine to the compressor represents about 0.4% of the fluid power supplied to the turbine.

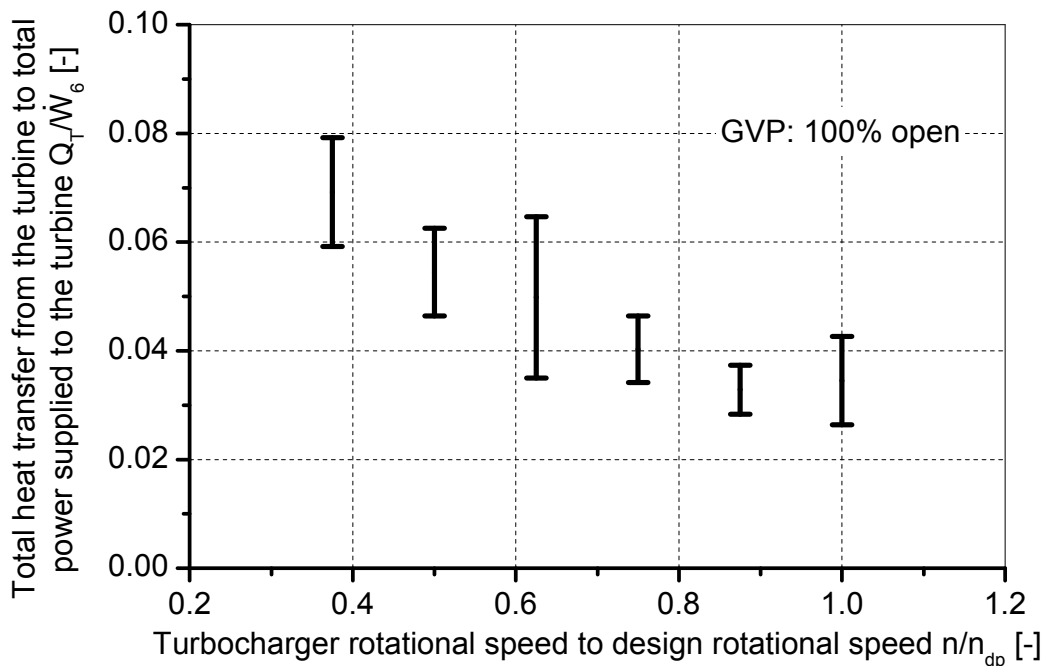


Figure 5-25 Range of total amount of heat transfer from the turbine as a fraction of the fluid power supplied to the turbine of the GT1749V 55 Trim turbocharger

The power delivered by the turbine also represents a small fraction of the supplied fluid power to the turbine as shown in Figure 5-26. The turbine power represents only 1-1.5% of the fluid power supplied to the turbine at a rotational speed of 60000 rpm. This percentage increases with increasing the turbocharger rotational speed and reaches about 4-5% of the fluid power supplied to the turbine at a rotational speed of 120000 rpm. This means that the total amount of heat transfer from the turbine is higher than the turbine power at low rotational speeds.

Figure 5-27 shows the ratio of the total amount of heat transfer from the turbine to the turbine power. The total amount of heat transfer from the turbine can be as high as 8 times the turbine power at low rotational speed. This causes the turbine non-adiabatic efficiency to exceed 100% at low rotational speeds. The turbine power increases with increasing the turbocharger rotational speed. The increase in the turbine power with increasing the turbocharger rotational speed is faster than the increase of the total amount of heat transfer from the turbine. This causes the ratio of the total amount of heat transfer from the turbine to the turbine power to decrease with increasing the turbocharger rotational speed. The sum of the total amount of heat transfer from the turbine and the turbine power also represents a small fraction of the fluid power supplied to the turbine. This means that the major fraction of the fluid power supplied to the turbine is lost at the turbine outlet.

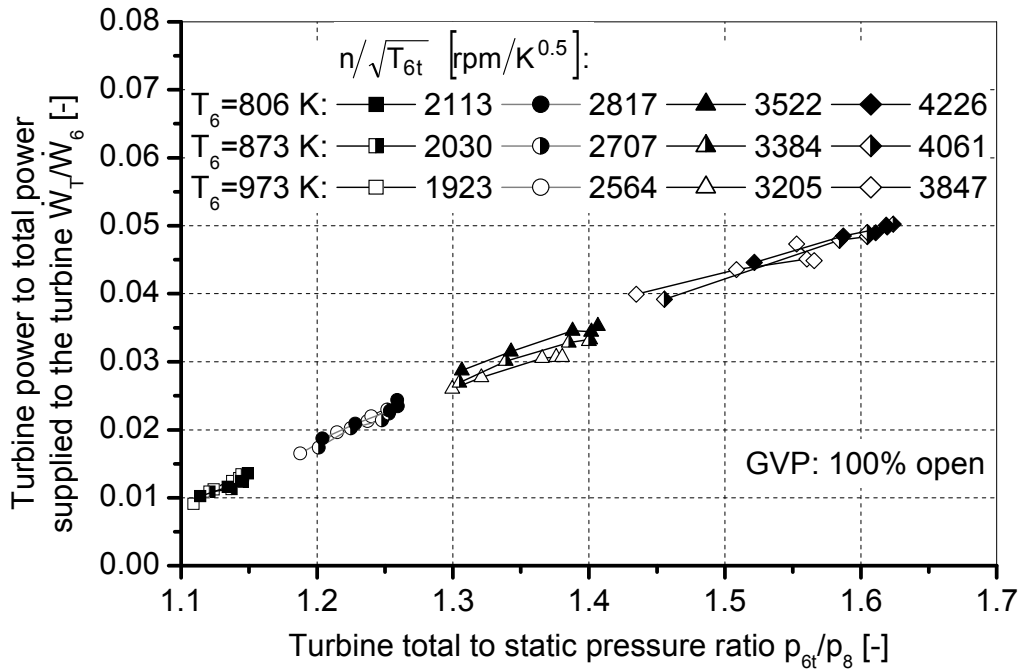


Figure 5-26 Turbine power as a fraction of the fluid power supplied to the turbine of the GT1749V 55 Trim turbocharger

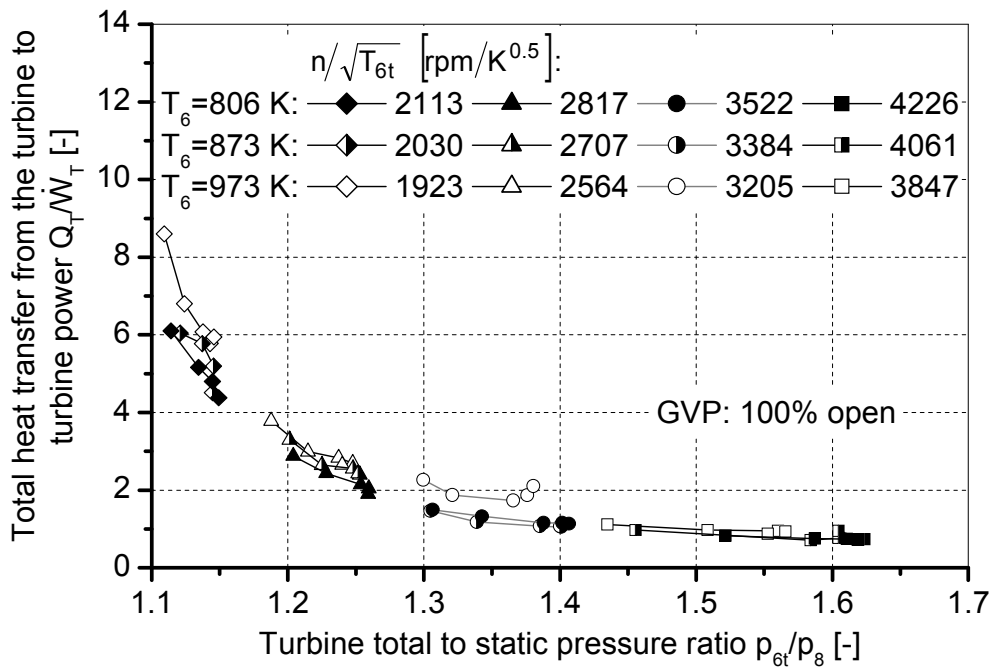


Figure 5-27 Ratio of the total amount of heat transfer from the turbine to the turbine power of the GT1749V 55 Trim turbocharger

Figure 5-28 shows the power lost at the turbine outlet as a fraction of the fluid power supplied to the turbine. The power lost at the turbine outlet represents about 92% of the fluid power supplied to the turbine. This means that the fluid power at the turbine outlet could be further used in other applications to achieve the maximum use of the exhaust gas power. This reduces the loss of power at the turbine outlet and improves the overall engine efficiency.

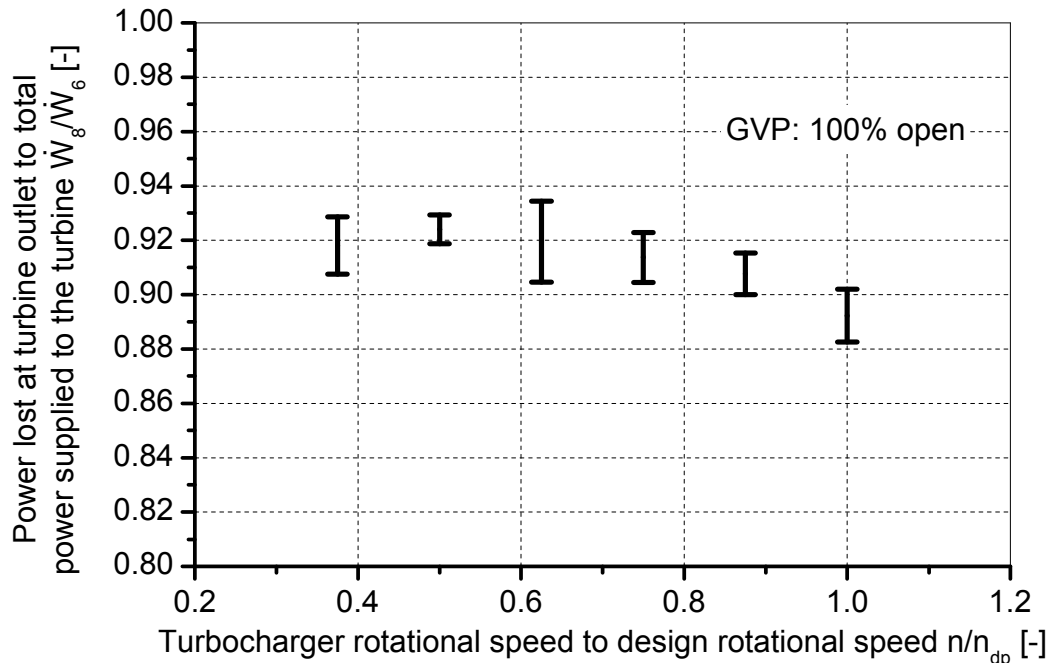


Figure 5-28 Range of power lost at the turbine outlet as a fraction of the fluid power supplied to the turbine of the GT1749V 55 Trim turbocharger

5.4 Aerodynamic performance of micro compressors

Small turbocharger compressors are characterized by very small dimensions as shown in Table A-1. The outer diameter of the GT1749V 55 Trim and GT1749V 70 Trim turbochargers is only 49 mm. The width of the impeller at outlet is only 3.35 mm and the width of the vaneless diffuser at outlet is only 2.66 mm. These very small dimensions make detailed measurements of the flow field inside the compressor almost impossible. However, it is very important to investigate the aerodynamic performance of these micro turbomachines. This investigation helps in understanding the aerodynamic performance of these machines and therefore enhances the ability to improve their performance. It also helps in the simulation of the compressor performance down to very low rotational speeds.

The compressor of the GT1749V 70 Trim turbocharger is used here for the investigation of the aerodynamic performance of micro compressors. Static pressure

tabs are located in the back side of the vaneless diffuser at diameter ratios $\lambda=1.26$ and 1.6, respectively. The performance of the compressor is measured in cold as well as hot experiments. The exhaust gas temperature at the turbine entry during the hot measurements is kept at 873K. The compressor surface area is insulated during the cold measurements to minimize any possible heat transfer from or to the compressor during the measurements. The oil inlet temperature is also kept lower than the total temperature at the compressor outlet to avoid heat transfer from the oil to the compressor at low rotational speeds. Therefore, the measured compressor performance during cold measurements can be considered to be the adiabatic compressor performance. Figure A-33 and Figure A-34 show the measured compressor performance maps during the cold and the hot measurements. The comparison between the compressor adiabatic efficiency and the compressor non-adiabatic efficiency also shows deterioration of the compressor non-adiabatic efficiency at low rotational speeds. This is due to the amount of heat transfer to the compressor through the bearing housing as mentioned before.

The static pressure distribution inside the diffuser at diameter ratios $\lambda = 1.26$ and 1.6 is measured at every compressor operating point. Figure A-35 to Figure A-40 show the measured static pressure distribution at every operating point during the cold measurements. These figures show a clear effect of the volute tongue (located at peripheral angle 119°) on the flow field inside the diffuser. This effect extends from the diffuser outlet down to the diffuser inlet. This means that the volute tongue also affects the flow field at the impeller outlet and hence the impeller aerodynamic performance. The measured static pressure distribution also shows a static pressure gradient in the circumferential direction inside the diffuser. This static pressure gradient in the circumferential direction depends on the flow rate through the compressor. The diffuser exhibits a negative pressure gradient in the circumferential direction at flow rates higher than the design flow rate. The static pressure distribution inside the diffuser is almost uniform in the circumferential direction at the design flow rate. A positive static pressure gradient in the circumferential direction is present inside the diffuser at flow rates lower than the design flow rate. This behavior depends directly on the performance of the volute at different flow rates. The geometry of the volute matches very well with the design flow rate. Therefore, neither acceleration nor deceleration takes place inside the volute at the design flow rate. This causes a uniform static pressure distribution in the circumferential direction at the diffuser outlet. This uniform static pressure distribution also extends upstream to the diffuser inlet. Flow acceleration takes place inside the volute at flow rates higher than the design flow rate. This means that the volute operates as a nozzle at flow rates higher than the design flow rate. This causes a negative static pressure gradient inside the volute at high flow rates. The negative pressure gradient inside the volute causes a negative pressure gradient in the circumferential direction at the

diffuser outlet. This effect also extends upstream in the diffuser to the diffuser inlet. The volute operates as a diffuser at flow rates lower than the design flow rate. This causes a positive pressure gradient in the circumferential direction inside the diffuser. This static pressure gradient in the circumferential direction extends from the diffuser outlet upstream to the diffuser inlet. It therefore affects the flow field at the impeller outlet and hence the impeller aerodynamic performance. It can therefore be said that the aerodynamic performance of the compressor depends not only on the performance of the individual components but also on the interaction between these components.

Figure A-41 to Figure A-46 show a comparison between the static pressure distribution at $\lambda = 1.6$ and that at $\lambda = 1.26$ for different compressor operating points. Of particular importance in these figures is the measured static pressure at a peripheral angle of 315° . This angle is located at 180° from the volute tongue in the circumferential direction. The radial pressure gradient at this angle decreases with decreasing the flow rate through the compressor. It becomes almost zero along the compressor surge line. This means that flow separation takes place at this peripheral angle along the compressor surge line. The flow field at the diffuser inlet where separation takes place can be divided circumferentially into two main parts as shown in Figure A-47. The first part extends from the volute tongue to 180° after the volute tongue. This part is characterized by high positive pressure gradient in the circumferential direction. This positive pressure gradient reaches the critical condition at the end of this part (peripheral angle 315°) and therefore flow separation takes place at the diffuser inlet. The second part extends from the point of the flow separation to the peripheral angle corresponding to the inlet of the volute exit cone. This part is characterized by slight flow acceleration with small negative pressure gradient in the circumferential direction. This flow acceleration takes place as a result of the flow separation and the existence of the volute exit cone in this part. It can also be observed in Figure A-41 to Figure A-46 that the non-uniformity of the static pressure distribution at the diffuser inlet is higher than that at the diffuser outlet along the compressor surge line because of the flow separation at the diffuser inlet. This non-uniformity increases significantly with increasing the rotational speed due to the increased interaction between the impeller and the diffuser.

The investigation of the compressor performance during the hot measurements shows the same behavior concerning the static pressure distribution inside the diffuser and the flow separation at the peripheral angle 315° .

The above experimental results are further used in estimating the aerodynamic losses and the slip factor of micro compressors. This estimation is very important for the prediction of the compressor performance at very low rotational speeds. The

estimation of the compressor aerodynamic losses and the slip factor is presented in Chapter 6.

6. EXTENSION OF THE TURBOCHARGER PERFORMANCE MAPS

6.1 Introduction

The extension of the turbocharger performance maps is very important for engine simulation programs. This is because the turbocharger provides the boundary conditions required for the estimation of the engine performance. Figure 1-9 (*Pucher et al., 2001*) shows clearly that the measured compressor performance map covers very few compressor operating points in comparison with the engine operating range. This is also true for the turbine performance map. Therefore, an extension of the turbocharger performance maps is very important for the simulation of engine performance. Models for extending the turbocharger performance maps down to very low turbocharger rotational speeds are presented in this chapter. The simulation of the compressor performance in the fourth quadrant of the map is also considered in the extension of the compressor performance maps.

6.2 Modeling of the heat transfer inside the turbocharger

Heat transfer takes place inside the turbocharger from the turbine to the bearing housing as well as from the bearing housing to the compressor. Heat is also transferred from the turbine to the compressor by radiation and convection. However, test results show that the amount of heat transfer from the turbine to the compressor by radiation and convection is very small and can be neglected. This also applies to the amount of heat transfer from the compressor to the ambient. Therefore, heat transfer by conduction through the bearing housing is assumed to be the main source of heat transfer to the compressor. Figure 6-1 shows a schematic diagram of the different heat transfer mechanisms that take place in the bearing housing in the absence of turbocharger cooling water. Heat is transferred first from the turbine to the bearing housing. Part of this heat transfer is removed by the lubrication oil. Another part is transferred to the ambient by convection. The rest of the heat from the turbine to the bearing housing flows into the compressor. The following assumptions are made to simplify the modeling of the heat transfer inside the turbocharger

- a. The temperature distribution in the radial and the circumferential directions inside the bearing housing is uniform. This reduces the model to a simple one dimensional model.
- b. The thermal conductivity of the bearing housing is constant.
- c. Cavitation does not take place in the clearance between the shaft and the bearing housing. Thus, oil completely fills the clearance between the bearing housing and the shaft.

d. The oil temperature in the bearing clearance is uniform and equals the oil mean temperature. The oil mean temperature is given by

$$T_{oil,mean} = 0.5(T_{oil,i} + T_{oil,o}) \tag{6.1}$$

e. Heat transfer from the bearing housing to the oil takes place at a uniform coefficient of heat transfer by forced convection.

f. Heat transfer by conduction through the shaft is negligible. This is because of the small cross section area and the relatively long length of the shaft.

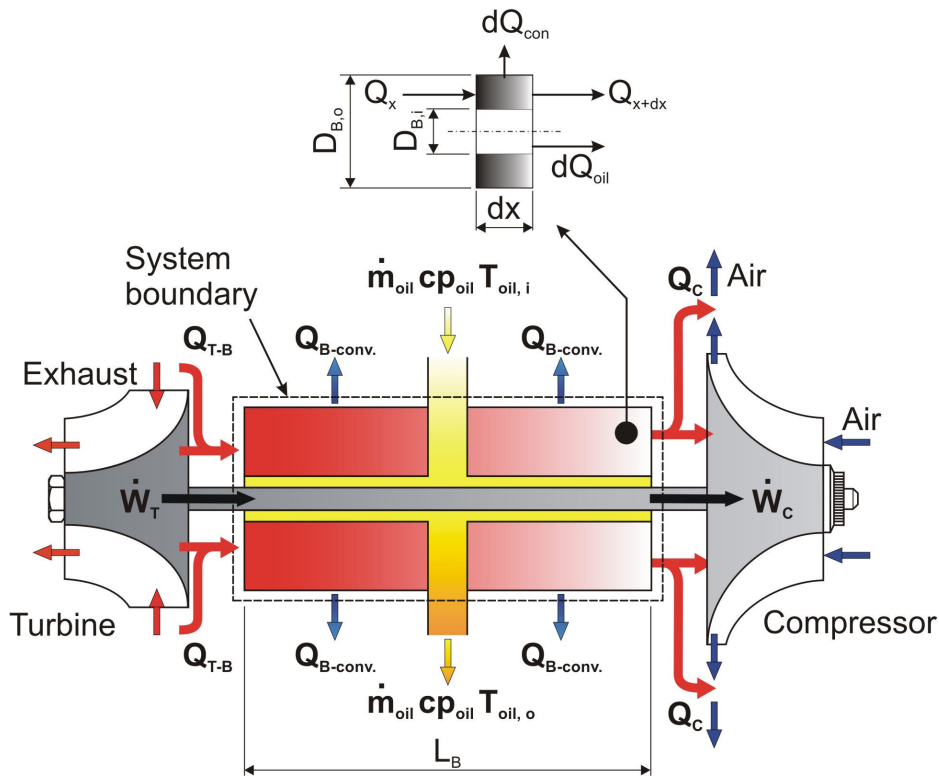


Figure 6-1 Schematic diagram of the different heat transfer mechanisms in the bearing housing

The differential equation of heat transfer through the bearing housing is obtained by applying heat balance to an element of length dx as shown in Figure 6-1

$$Q_x = Q_{x+dx} + dQ_{oil}(x) + dQ_{con}(x) \tag{6.2}$$

The amount of heat transfer to the element is given by Fourier's law as

$$Q_x = -k_B A_B \frac{\partial T}{\partial x} \tag{6.3}$$

The bearing cross sectional area is given by

$$A_B = \frac{\pi}{4} (D_{B,o}^2 - D_{B,i}^2) \quad (6.4)$$

The amount of heat transfer by conduction at the exit from the element is given by

$$Q_{x+dx} = Q_x + \frac{\partial}{\partial x} (Q_x) dx \quad (6.5)$$

The amount of heat transfer to the oil is given by

$$dQ_{oil} = h_{oil} \cdot dA_i(x) \cdot (T - T_{oil,mean}) \quad (6.6)$$

The inner surface area of the element is given by

$$dA_i(x) = P_{B,i} dx \quad (6.7)$$

The amount of heat transfer by convection from the bearing housing to the ambient is given by

$$dQ_{con}(x) = h_{con} \cdot dA_o(x) \cdot (T - T_{atm}) \quad (6.8)$$

The outer surface area of the element is given by

$$dA_o(x) = P_{B,o} dx \quad (6.9)$$

Substituting in equation (6.2) and rearranging

$$-\frac{\partial}{\partial x} \left(-k_B A_B \frac{\partial T}{\partial x} \right) dx = h_{oil} \cdot P_{B,i} \cdot dx \cdot (T - T_{oil,mean}) + h_{con} \cdot P_{B,o} \cdot dx \cdot (T - T_{atm}) \quad (6.10)$$

With the assumption that the thermal conductivity of the bearing housing is constant, equation (6.10) reduces to

$$k_B A_B \frac{\partial^2 T}{\partial x^2} - h_{oil} \cdot P_{B,i} \cdot (T - T_{oil,mean}) - h_{con} \cdot P_{B,o} \cdot (T - T_{atm}) = 0 \quad (6.11)$$

Since

$$(T - T_{atm}) = T - T_{oil,mean} + (T_{oil,mean} - T_{atm}) \quad (6.12)$$

Equation (6.11) can be rewritten as

$$k_B A_B \frac{\partial^2 T}{\partial x^2} - h_{oil} \cdot P_{B,i} \cdot (T - T_{oil,mean}) - h_{con} \cdot P_{B,o} \cdot (T - T_{oil,mean}) = h_{con} \cdot P_{B,o} \cdot (T_{oil,mean} - T_{atm}) \quad (6.13)$$

Equation (6.13) can be normalized by introducing non-dimensional expressions for the temperature T and the distance x . These expressions take the form

$$\theta_h = (T - T_{oil,mean}) / (T_{B,mean} - T_{oil,mean}) \quad (6.14)$$

$$\chi_h = x / L_B \quad (6.15)$$

The bearing housing mean temperature is defined as

$$T_{B,mean} = (T_{6t} + T_{atm} + T_{5t}) / 3 \quad (6.16)$$

Substituting for θ_h and χ_h in equation (6.13) and rearranging

$$\frac{\partial^2 \theta_h}{\partial \chi_h^2} - \frac{h_{oil} P_{B,i} + h_{con} P_{B,o}}{k_B A_B} L_B^2 \theta_h = \frac{h_{con} P_{B,o}}{k_B A_B} L_B^2 \frac{T_{oil,mean} - T_{atm}}{T_{B,mean} - T_{oil,mean}} \quad (6.17)$$

By considering that

$$m_h^2 = \frac{h_{oil} P_{B,i} + h_{con} P_{B,o}}{k_B A_B} \quad (6.18)$$

$$O_h = \frac{h_{con} P_{B,o}}{k_B A_B} L_B^2 \frac{T_{oil,mean} - T_{atm}}{T_{B,mean} - T_{oil,mean}} \quad (6.19)$$

Equation (6.17) can be rewritten as

$$\frac{\partial^2 \theta_h}{\partial \chi_h^2} - (m_h L_B)^2 \theta_h = O_h \quad (6.20)$$

Equation (6.20) is a second order non-homogeneous partial differential equation. The general solution of this equation is the summation of the homogeneous solution and the non-homogeneous solution. The homogeneous solution of equation (6.20) is known as

$$\theta_{h,hom} = C_{1h} \exp(m_h L_B \chi_h) + C_{2h} \exp(-m_h L_B \chi_h) \quad (6.21)$$

where C_{1h} and C_{2h} are constants. The non-homogeneous solution of equation (6.20) can be obtained by assuming a general solution for the non-dimensional temperature distribution and applying this solution to equation (6.20). This is achieved by assuming that

$$\theta_{h,non-hom} = C_{3h} + C_{4h} \chi_h \quad (6.22)$$

where C_{3h} and C_{4h} are constants. Substituting equation (6.22) in equation (6.20)

$$0 - (m_h L_B)^2 (C_{3h} + C_{4h} \chi_h) = O_h \quad (6.23)$$

Equating the terms of both sides in equation (6.23)

$$\chi_h^0 \Rightarrow C_{3h} = -O_h / (m_h L_B)^2 \quad (6.24)$$

$$\chi_h^1 \Rightarrow C_{4h} = 0 \quad (6.25)$$

So that, the non-homogeneous solution of equation (6.20) takes the form

$$\theta_{h, \text{non-hom}} = -O_h / (m_h L_B)^2 = -\frac{h_{\text{con}} P_{B,o}}{h_{\text{oil}} P_{B,i} + h_{\text{con}} P_{B,o}} \frac{T_{\text{oil,mean}} - T_{\text{atm}}}{T_{B,\text{mean}} - T_{\text{oil,mean}}} \quad (6.26)$$

The general solution of equation (6.20) is therefore

$$\theta_h = C_{1h} \exp(m_h L_B \chi_h) + C_{2h} \exp(-m_h L_B \chi_h) - \frac{h_{\text{con}} P_{B,o}}{h_{\text{oil}} P_{B,i} + h_{\text{con}} P_{B,o}} \frac{T_{\text{oil,mean}} - T_{\text{atm}}}{T_{B,\text{mean}} - T_{\text{oil,mean}}} \quad (6.27)$$

The third term in the right hand side of equation (6.27) represents the non-homogeneous solution of equation (6.20). Equation (6.27) presents the temperature distribution in the bearing housing. This equation can be further used in estimating the amount of heat transfer from the turbine to the bearing housing as well as from the bearing housing to the compressor

$$Q_{T-B} = -k_B A_B \left. \frac{\partial T}{\partial x} \right|_{x=0} = -\frac{k_B A_B}{L_B} (T_{B,\text{mean}} - T_{\text{oil,mean}}) \left. \frac{\partial \theta_h}{\partial \chi_h} \right|_{\chi_h=0} \quad (6.28)$$

$$Q_{B-C} = -k_B A_B \left. \frac{\partial T}{\partial x} \right|_{x=L_B} = -\frac{k_B A_B}{L_B} (T_{B,\text{mean}} - T_{\text{oil,mean}}) \left. \frac{\partial \theta_h}{\partial \chi_h} \right|_{\chi_h=1} \quad (6.29)$$

Therefore, the amount of heat transfer from the bearing housing to the compressor is given by

$$Q_{B-C} = \sqrt{k_B A_B (h_{\text{oil}} P_{B,i} + h_{\text{con}} P_{B,o})} \cdot (C_{2h} \exp(-m_B L_B) - C_{1h} \exp(m_B L_B)) \cdot (T_{B,\text{mean}} - T_{\text{oil,mean}}) \quad (6.30)$$

Empirical expressions for the coefficients C_{1h} and C_{2h} are obtained by fitting the experimental data using the subroutine "lfit.for" (Press et al., 1992). The first temperature distribution coefficient can be estimated from the equation

$$C_{1h} = 0.5 \text{Re}_{\text{oil}}^{0.1} \left(\frac{726.5 \text{Re}_{\text{oil,u}}^{0.05}}{\text{Pr}_{\text{oil}}^{0.19} \text{Re}_{\text{oil}}^{0.17}} F_{B1} - 1 \right) \quad (6.31)$$

where

$$F_{B1} = f_1(T_{6t}/T_{5t}) \cdot f_1(m_B L_B) \cdot f_1(T_{oil,i}/T_{atm}) \quad (6.32)$$

$$f_1(T_{6t}/T_{5t}) = \frac{(T_{6t}/T_{5t})^{1.2} - 1}{(T_{6t}/T_{5t})^{4.16}} \quad (6.33)$$

$$f_1(m_B L_B) = (m_B L_B)^{0.72} \exp[-1.63((m_B L_B)^{0.6} + 1)] \quad (6.34)$$

$$f_1(T_{oil,i}/T_{atm}) = [1.1 - (T_{oil,i}/T_{atm})^{-0.55}]^{-0.21} \quad (6.35)$$

The oil Reynolds number is estimated from the equation

$$Re_{oil} = \frac{c_{oil} D_{h,B}}{\nu_{oil}} \quad (6.36)$$

The bearing hydraulic diameter is estimated from the equation

$$D_{h,B} = 2cl_B \quad (6.37)$$

The oil mean flow velocity is given by

$$c_{oil} = \dot{m}_{oil} / (\rho_{oil} A_{oil, flow}) \quad (6.38)$$

where

$$A_{oil, flow} = \frac{\pi}{4} (D_{B,i}^2 - D_{shaft}^2) \quad (6.39)$$

The oil Reynolds number based on peripheral speed is estimated from equation (5.3). The oil Prandtl number is given by

$$Pr_{oil} = \frac{\rho_{oil} \nu_{oil} c_{p,oil}}{k_{oil}} \quad (6.40)$$

The oil thermal conductivity is calculated from the equation (*Shell documentation*)

$$k_{oil} = \frac{0.423 - 0.000226 t_{oil}}{\sqrt{\rho_{oil, 15^\circ C} / 1000}} \quad \frac{kJ}{m \cdot h \cdot K} \quad (6.41)$$

where

t_{oil}	oil temperature in °C
$\rho_{oil, 15^\circ C}$	oil density at 15°C in kg/m ³

This equation can be applied to mineral oils that have a density in the range 740-

1000 kg/m³ at a temperature of 15 °C with accuracy of ±10%. The oil properties are estimated at the mean oil temperature. The coefficient of heat transfer by natural convection is calculated from the natural convection correlations available in the literature. The coefficient of heat transfer by forced convection from the bearing housing to the oil is estimated from the experimental results

$$h_{oil} = \frac{Q_{T-oil}}{\pi L_B D_{B,i} \left(\frac{T_{6t} + T_{5t}}{2} - T_{oil,mean} \right)} \quad (6.42)$$

Figure A-48 shows a comparison between the estimated first temperature distribution coefficient C_{1h} and the predicted one.

The second temperature distribution coefficient C_{2h} can be estimated from the equation

$$C_{2h} = \frac{15.5 F_{B2}}{Pr_{oil}^{0.06} Re_{oil,u}^{0.066} Re_{oil}^{0.04}} \quad (6.43)$$

$$F_{B2} = f_2(T_{6t}/T_{5t}) \cdot f_2(m_B L_B) \cdot f_2(T_{oil,i}/T_{atm}) \quad (6.44)$$

$$f_2(T_{6t}/T_{5t}) = \frac{(T_{6t}/T_{5t})^{4.86}}{\left[(T_{6t}/T_{5t})^{1.2} - 1 \right]^{2.95}} \quad (6.45)$$

$$f_2(m_B L_B) = (m_B L_B)^{-0.29} \exp\left[0.38 (m_B L_B)^{1.2}\right] \quad (6.46)$$

$$f_2(T_{oil,i}/T_{atm}) = \left[1.1 - (T_{oil,i}/T_{atm})^{-0.1} \right]^{1.89} \quad (6.47)$$

Equations (6.31) and (6.43) are obtained by fitting the test results. They can be used within the operation range:

$$Re_{oil} = 38.5 - 150$$

$$Re_{oil,u} = 1735 - 8087$$

$$Pr_{oil} = 205 - 544$$

Figure A-49 shows a comparison between the estimated second temperature distribution coefficient C_{2h} and the predicted one.

Figure A-50 shows a comparison between the measured compressor adiabatic efficiency and the calculated compressor adiabatic efficiency. The calculated

adiabatic efficiency is extracted from the hot measurements of the compressor using the model described above. The model can estimate the compressor adiabatic efficiency within the range of the experimental error.

6.3 Heat transfer to the oil

The amount of heat transfer to the oil can be estimated with the help of the coefficient of convective heat transfer to the oil. The coefficient of heat transfer by forced convection from the bearing housing to the oil can be estimated using an empirical correlation for the oil Nusselt number. This correlation is found from the experimental results of the GTI749V 55 Trim in the form

$$Nu_{oil} = 0.795 \frac{Re_{oil}^{3.62} Re_{oil,u}^{1.82}}{Pr_{oil}^{2.1}} \cdot F_{oil} \quad (6.48)$$

where

$$F_{oil} = \text{Exp} \left(-0.61 \left(Re_{oil,u}^{0.077} Re_{oil}^{0.32} Pr_{oil}^{0.237} - \frac{57.4}{(Re_{oil} + 1)^{0.46}} \right) \right) \quad (6.49)$$

This equation is obtained by fitting the test results and can be used within the operation range:

$$\begin{aligned} Re_{oil} &= 38.5 - 150 \\ Re_{oil,u} &= 1735 - 8087 \\ Pr_{oil} &= 205 - 544 \end{aligned}$$

The oil Reynolds number Re_{oil} and the oil Reynolds number based on shaft speed $Re_{oil,u}$ in equation (6.48) account for the flow characteristics in both the axial and the peripheral directions inside the bearing clearance.

Figure A-51 shows a comparison between the predicted oil Nusselt number and the estimated oil Nusselt number. Equation (6.49) can be used to predict the oil Nusselt number within the investigated operating range with an acceptable accuracy in comparison with the very complex flow mechanism and heat transfer mechanism of the oil in the bearing clearance.

6.4 Turbine heat transfer

The total amount of heat transfer from the turbine is the sum of the amount of heat

transfer by radiation and convection from the turbine to the ambient and the amount of heat transfer from the turbine to the bearing housing. The amount of heat transfer from the turbine to the bearing housing can be estimated from equation (6.28). The amount of heat transfer by radiation from the turbine is estimated from the simplified equation

$$Q_{T, \text{Rad}} = A_{\text{surface}, T} \sigma \varepsilon_T (T_{6t}^4 - T_{\text{atm}}^4) \quad (6.50)$$

The emissivity of the turbine casing is assumed to be 0.93 (experiments by *Bohn et al., 2003a*). The amount of heat transfer by natural convection from the turbine to the ambient is calculated from the simplified equation

$$Q_{T, \text{con}} = A_{\text{surface}, T} h_{\text{con}, T} (T_{6t} - T_{\text{atm}}) \quad (6.51)$$

The coefficient of heat transfer by natural convection is estimated from the available natural convection correlations for a slender cylinder. However, a comparison with test results shows that the actual coefficient of heat transfer is about 3.4 times that calculated from free convection correlations. Therefore, it is recommended to multiply the estimated value of the natural convection coefficient by 3.4 to account for the high surface temperature and the complex geometry of the turbine casing. This improves the prediction accuracy of the total temperature at the turbine outlet. Figure A-52 shows a comparison between the measured total temperature at the turbine outlet and the predicted one. The model described above can predict the total temperature at the turbine outlet within a maximum error of $\pm 1.98\%$.

6.5 Compressor aerodynamic performance

The measured static pressure distribution in the vaneless diffuser of the GT1749V 70 Trim compressor provides information regarding the aerodynamic performance of the small compressors. It also highlights the importance of the interaction between the components of the compressor. The measured static pressure distribution is further used in estimating the aerodynamic losses and the slip factor of the small compressors. This is achieved by solving the conservation equations of the flow inside the diffuser at the measured static pressure distribution, the total temperature at the impeller outlet, and the mass flow rate. The present model is based on the conservation equations presented by Traupel (1977) for vaneless diffusers. These equations assume that the losses in the diffuser are due to fluid friction and energy dissipation only. The following assumptions are made

- a. The flow inside the diffuser is one-dimensional.

- b. The compressor is adiabatic. This is because only the cold measurements of the compressor are used in this model.
- c. The swirl velocity at the impeller outlet is uniform around the impeller circumference (*Sideris and Van den Braembussche, 1987*).

The conservation equations for the flow inside the diffuser are:

1. Conservation of mass

$$c_m(br)d\rho + \rho(br)dc_m + \rho c_m d(br) = 0 \quad (6.52)$$

2. Conservation of momentum (*Traupel, 1977*)

$$d(rc_u) = -\frac{c_f \rho c_u \sqrt{c_u^2 + c_m^2}}{\rho_2 c_{2m} b_2 r_2} r^2 dr \quad (6.53)$$

3. Conservation of energy (*Traupel, 1977*)

$$\frac{dp}{\rho} = -d\left(\frac{c_u^2 + c_m^2}{2}\right) - \frac{c_{dis} \rho (c_u^2 + c_m^2)^{3/2}}{\rho_2 c_{2m} b_2 r_2} r dr \quad (6.54)$$

where c_{dis} is the dissipation coefficient.

4. The equation of state

$$p/\rho = R_{air} T \quad (6.55)$$

Equation (6.55) can be rewritten for adiabatic flow as

$$\frac{p}{\rho} = R_{air} \left(T_{2t} - \frac{c^2}{2c_{p,air}} \right) \quad (6.56)$$

By differentiating equation (6.56), where T_{2t} is constant for the adiabatic compressor

$$d\left(\frac{p}{\rho}\right) = -\frac{R_{air}}{c_{p,air}} \left(\frac{c^2}{2}\right) \quad (6.57)$$

where

$$c^2 = c_u^2 + c_m^2 \quad (6.58)$$

and

$$\frac{R_{air}}{c_{p,air}} = \frac{\kappa_{air} - 1}{\kappa_{air}} \quad (6.59)$$

Therefore, equation (6.57) can be rewritten as

$$\frac{\kappa_{\text{air}}}{\kappa_{\text{air}} - 1} d\left(\frac{p}{\rho}\right) = -\left(\frac{c_u^2 + c_m^2}{2}\right) \quad (6.60)$$

Equations (6.52), (6.53), (6.54), and (6.60) are the conservation equations governing the flow in the vaneless diffuser of the compressor. These equations are further normalized and solved in the non-dimensional form. Dividing equation (6.52) by $\rho c_m (br)$ and rearranging

$$\frac{d\rho}{\rho} = -\left(\frac{dc_m}{c_m} + \frac{d(br)}{br}\right) \quad (6.61)$$

Equation (6.53) can also be rewritten as

$$r dc_u + c_u dr = -\frac{c_f \rho c_u \sqrt{c_u^2 + c_m^2}}{\rho_2 c_{2m} b_2 r_2} r^2 dr \quad (6.62)$$

Dividing equation (6.62) by $r c_u$ and rearranging

$$\frac{dc_u}{c_u} = -\left(\frac{dr}{r} + \frac{c_f \rho \sqrt{c_u^2 + c_m^2}}{\rho_2 c_{2m} b_2 r_2} r dr\right) \quad (6.63)$$

Similarly, equations (6.54) and (6.60) can be solved together and normalized to give an expression for the change in the meridional velocity through the diffuser

$$\frac{dc_m}{c_m} = \frac{\frac{\rho}{\kappa_{\text{air}} \rho} \left(c_u dc_u + \frac{\kappa_{\text{air}} c_{\text{dis}} \rho (c_u^2 + c_m^2)^{3/2}}{\rho_2 c_{2m} b_2 r_2} r dr \right) - \frac{d(br)}{br}}{1 - c_m^2 / (\kappa_{\text{air}} \rho / \rho)} \quad (6.64)$$

Equations (6.61), (6.63), and (6.64) are the non-dimensional equations governing the flow through the diffuser. These equations are solved numerically by dividing the diffuser into large number of radius segments Δr and peripheral angle segments $\Delta\theta$. The governing equations are solved in each segment along the streamline. The friction coefficient is estimated from the available correlations for the flow between two parallel plates. The solution procedure is programmed in a Fortran 77 program called "V-Diffuser". Figure 6-2 shows the flow chart of the program "V-Diffuser". The calculation starts by estimating the swirl velocity at the impeller outlet from the measured total temperature at the compressor outlet. The program assumes a value

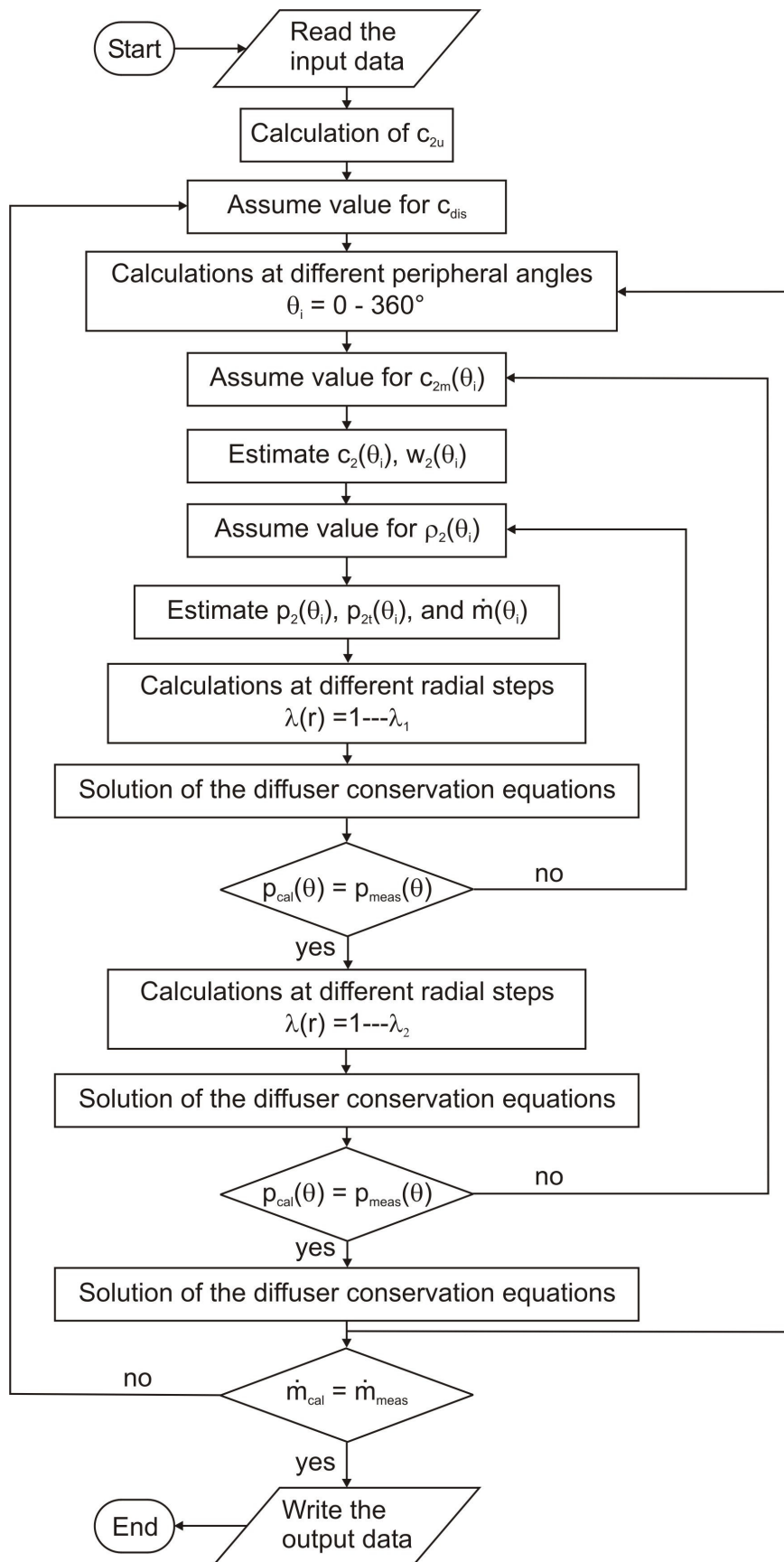


Figure 6-2 Flow chart for the program "V-Diffuser"

for the dissipation coefficient c_{dis} as a ratio of the friction coefficient. The calculations at different peripheral angles starts with the peripheral angle $\theta_i = 0$. The number of peripheral angle segments as well as the radial segments can be controlled in the input file of the program. The program also assumes a value for the local meridional velocity at the impeller outlet for the calculated peripheral angle. The local flow velocity at the impeller outlet can therefore be estimated from the equation

$$c_2(\theta_i) = \sqrt{c_{2u}^2 + [c_{2m}(\theta_i)]^2} \quad (6.65)$$

The program assumes then a value for the local density at the impeller outlet for the calculated peripheral angle. Therefore, the mass flow rate through the calculated segment can be estimated from

$$\dot{m}(\theta_i) = \rho_2(\theta_i) A_2(\theta_i) c_{2m}(\theta_i) \quad (6.66)$$

Equations (6.61), (6.63), and (6.64) are then solved at different radius steps. The calculations are divided into three different stages. The first stage takes place from the impeller outlet up to the diameter ratio of the first measured static pressure distribution, $\lambda=1.26$ for the GT1749V 70 Trim. At this point, the program compares the calculated static pressure with the measured one. If the calculated static pressure does not equal the measured one, the program assumes a new value for the local density at the impeller outlet and repeats the calculations once again. The calculations are repeated until the deviation between the estimated and the measured static pressure becomes within an acceptable percentage error. The acceptable deviation of the calculated pressure from the measured pressure is specified in the input file of the program. The program performs spline interpolation of the measured data to find the value of the static pressure if the calculated peripheral angle is located between two measured peripheral angles. Once the calculated static pressure coincides with the measured one, the program performs the second stage of the calculations. The conservation equations are solved along the same streamline until the diameter ratio of the second measured pressure distribution is reached, $\lambda=1.6$ for the GT1749V 70 Trim. The program compares the value of the calculated static pressure with the measured one. If both values do not agree with each other, the program assumes new value for the local meridional velocity at the impeller outlet and repeats the calculations. Once the value of the calculated static pressure agrees with the measured one, the program performs the third stage of calculations. The calculations are also performed along the same streamline until the diffuser outlet is reached. This calculation procedure is repeated at the different peripheral angles. The flow rate through the compressor is estimated at the end of the calculations at the different peripheral angles from the equation

$$\dot{m}_{\text{cal}} = \sum_{i=1}^{n_{\theta}} \rho_2(\theta_i) A_2(\theta_i) c_{2m}(\theta_i) \quad (6.67)$$

where n_{θ} is the number of the calculation segments in the circumferential direction. The estimated flow rate is compared with the measured one. If the estimated flow rate does not agree with the measured one, a new value for the dissipation coefficient is assumed and the calculations are repeated. The diffuser of the GT1749V 70 Trim is divided into 1500 radial segments and 360 peripheral segments. This requires about 11 hr calculation time for the complete measured performance map of the GT1749V 70 Trim compressor on a Pentium 4 processor.

The experimental data of Rautenberg et al. (1998) are used to validate the model described above. These data represent the aerodynamic performance of a large centrifugal compressor with a vaneless diffuser and an external volute. Figure A-53 shows a comparison between the measured volute loss coefficient and the calculated one for the data of Rautenberg et al. (1998). The volute loss coefficient is defined as

$$\xi_{\text{vol}} = \frac{p_{3t} - p_{5t}}{0.5 \rho_3 c_3^2} \quad (6.68)$$

It is evident in Figure A-53 that the model described above can predict the flow field inside the diffuser with a good accuracy. This is not only true for the loss coefficient but also for the flow angle at the diffuser outlet as shown in Figure A-54.

6.6 Compressor aerodynamic losses

6.6.1 Overall aerodynamic losses

Compressor aerodynamic losses are divided into impeller, diffuser, and volute losses. The impeller loss coefficient in the present work is defined as

$$\xi_{\text{imp}} = \frac{c_{p,\text{air}} (T_{2t,\text{adi}} - T_{2t,\text{is}})}{u_2^2} \quad (6.69)$$

The diffuser loss coefficient is defined as

$$\xi_{\text{dif}} = \frac{p_{2t} - p_{3t}}{0.5 \rho_2 c_2^2} \quad (6.70)$$

The volute loss coefficient is defined in equation (6.68). Figure 6-3 shows the overall loss coefficient of the GT1749V 70 Trim compressor as a function of the impeller flow coefficient. The overall compressor loss coefficient is estimated from the equation

$$\xi_C = \frac{c_{p,air}(T_{5t,adi} - T_{5t,is})}{u_2^2} \quad (6.71)$$

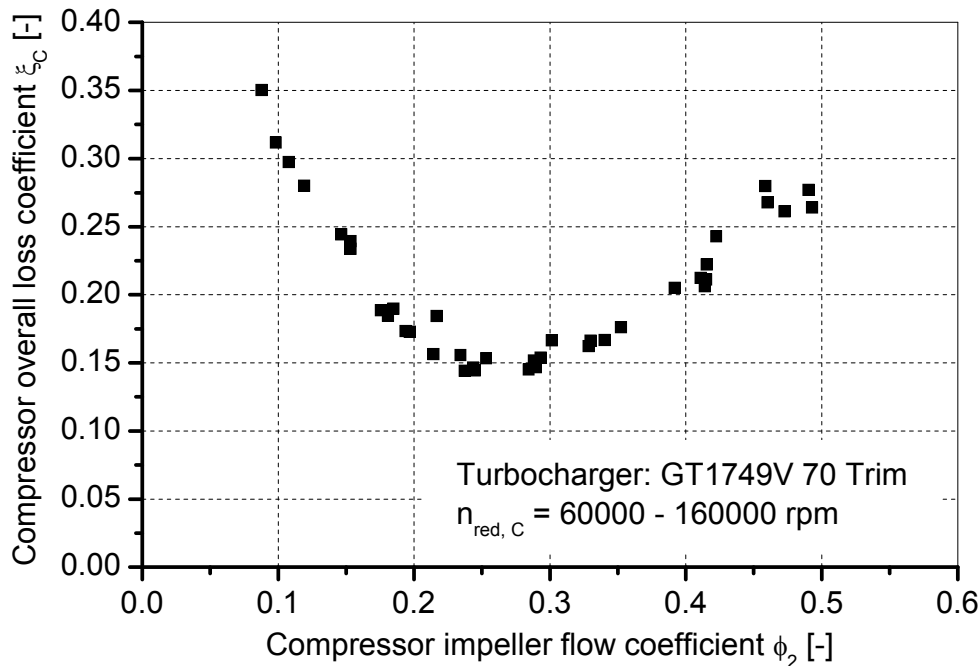


Figure 6-3 Overall loss coefficient of the GT1749V 70 Trim compressor

The minimum compressor overall losses take place at the compressor design point. The losses increase with decreasing the flow rate from the design flow rate. This is because of the increase in the diffusion losses, incidence losses, and the diffuser losses. Flow rates greater than the design flow rate cause a further increase in the compressor aerodynamic losses. This increase is due to the increased incidence losses, passage losses, and volute losses. The aerodynamic losses of the individual components of the compressor are discussed in details in the following sections.

6.6.2 Impeller aerodynamic losses

The impeller loss coefficient is estimated using the program “V-Diffuser”. Figure 6-4 shows the estimated impeller loss coefficient as a function of the impeller flow coefficient. The impeller loss coefficient is about 1/3 the overall loss coefficient of the GT1749V 70 Trim compressor. It reaches a minimum value at the compressor design point. This is because the flow angle at the impeller inlet matches very well the blade angle at the impeller inlet. The compressor design point also represents an

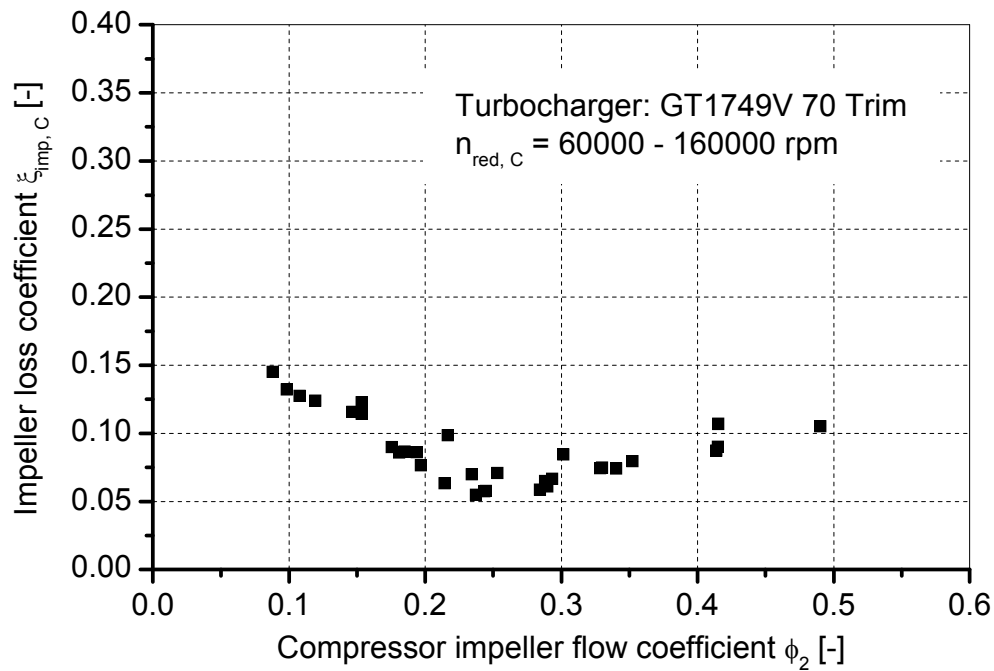


Figure 6-4 Impeller loss coefficient of the GT1749V 70 Trim compressor

optimum point for diffusion, blade loading, passage, and friction losses. The losses increase at low flow rates due to the increased incidence, diffusion, and blade loading losses. They also increase with increasing the flow rate due to the increased incidence, passage, and friction losses.

The impeller loss coefficient can be modeled by considering the main loss mechanisms of the impeller. These loss mechanisms can be classified into

1. Incidence losses
2. Friction losses
3. Disk friction losses
4. Diffusion losses
5. Passage losses
6. Clearance losses
7. Blade loading losses

Incidence losses take place at the impeller inlet during compressor off-design operation due to the mismatch between the flow angle and the blade angle. Figure 6-5 shows a schematic diagram of the velocity triangle at the impeller inlet during off-design operation. The incidence losses are considered to be proportional to the kinetic energy based on the normal component of the relative velocity at the rotor inlet (*Whitfield and Baines, 1990*)

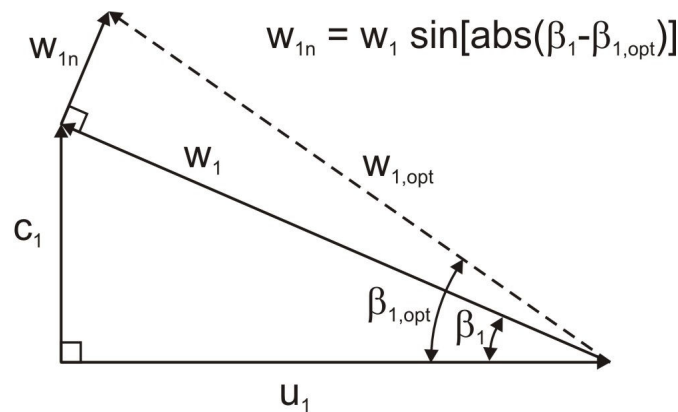


Figure 6-5 Schematic diagram of the velocity triangle at the impeller inlet during off-design operation

$$W_{\text{inc,loss}} = K_{\text{inc}} \cdot 0.5w_1^2 \sin^2[\text{abs}(\beta_{1b} - \beta_{1,\text{opt}})] \quad (6.72)$$

The value of the correction factor K_{inc} is to be determined from the experimental data. The optimum flow angle at the impeller inlet $\beta_{1,\text{opt}}$ can be estimated by applying the continuity equation to the flow at the impeller inlet (*Whitfield and Baines, 1990*). It can also be estimated from the measured performance map. This is done by considering the compressor best efficiency point as the design point. The flow angle at the impeller inlet is estimated for the design flow rate. This angle is considered the optimum flow angle at the impeller inlet.

Impeller friction losses are estimated from the analogous pipe friction model

$$W_{\text{fri,loss}} = \frac{4c_f L_{\text{imp}}}{D_{h,\text{imp}}} \frac{w_2^2 + w_1^2}{2} \quad (6.73)$$

The impeller passage length L_{imp} is considered to be the mean of two quarter circles representing the blade contour (*Baines, 1998*). The impeller hydraulic diameter $D_{h,\text{imp}}$ is the mean of the hydraulic diameters at the impeller inlet and the impeller outlet. The friction coefficient of the impeller is estimated from the available pipe flow models at the impeller Reynolds number

$$\text{Re}_{\text{imp}} = \frac{0.5(w_2 + w_1)D_{h,\text{imp}}}{v_{\text{air}}} \quad (6.74)$$

Disk friction losses are estimated from the correlation of Daily and Nece (1960). Impeller diffusion losses are considered to be proportional to the difference between the kinetic energy at the impeller inlet and that at the impeller outlet

$$W_{\text{diff,loss}} = K_{\text{diff}} \frac{(w_1^2 - w_2^2)}{2} \quad (6.75)$$

Passage losses are considered to be proportional to the mean kinetic energy of the impeller

$$W_{\text{pass,loss}} = K_{\text{pass}} \frac{w_2^2 + w_1^2}{2} \quad (6.76)$$

Clearance losses are considered to be proportional to the energy carried by the flow through the impeller clearance

$$W_{\text{cl,loss}} = K_{\text{cl}} \frac{\dot{m}_{\text{cl}}}{\dot{m}} u_2 c_{2u} \quad (6.77)$$

The flow rate through the clearance is estimated from the model of Aungier (*Aungier, 2000*). Blade loading losses are considered to be proportional to the square of the impeller blade loading

$$W_{\text{bl,loss}} = K_{\text{bl}} (w_{\text{suc}} - w_{\text{pre}})^2 \quad (6.78)$$

The impeller blade loading is estimated from the equation (*Aungier, 2000*)

$$w_{\text{suc}} - w_{\text{pre}} = \frac{2 \pi D_2}{z L_{\text{imp}}} c_{2u} \quad (6.79)$$

The impeller loss coefficient can therefore be expressed as

$$\xi_{\text{imp}} = \frac{\sum W_{\text{imp,loss}}}{u_2^2} \quad (6.80)$$

Expressions for the unknown empirical coefficients are obtained by fitting the estimated impeller aerodynamic losses with equation (6.80). The data used to obtain these expressions are those of the large centrifugal compressor (1998) and the very small GT1749V 70 Trim compressor. The unknown empirical coefficients can be estimated from the following equations

$$K_{\text{inc}} \approx 1.0 \quad (6.81)$$

$$K_{\text{diff}} = 0.367 (w_1/w_2)^{0.5} \quad (6.82)$$

$$K_{\text{pass}} = \frac{9.327}{\text{Re}_{\text{imp}}^{0.9} (D_1/D_2)^{1.2}} + 0.005 \quad (6.83)$$

$$K_{cl} = 0.0524 \quad (6.84)$$

$$K_{bl} = 0.002 \quad (6.85)$$

Figure A-55 shows a comparison between the estimated impeller loss coefficient using the program “V-Diffuser” and the calculated one using the above loss model.

6.6.3 Diffuser aerodynamic losses

Diffuser losses are also estimated from the measured static pressure distribution in the vaneless diffuser using the program “V-Diffuser”. Figure 6-6 shows the variation of the diffuser loss coefficient with the impeller flow coefficient for the GT1749V 70 Trim compressor. The diffuser loss coefficient increases with decreasing the compressor flow rate. This is mainly because of the increase in the pressure gradient through the diffuser with decreasing flow rate. This increases the diffusion losses and the development of the boundary layers inside the diffuser. The diffuser aerodynamic losses also affect the diffuser pressure coefficient

$$C_{p,dif} = \frac{p_3 - p_2}{0.5 \rho_2 c_2^2} \quad (6.86)$$

Figure 6-7 shows the variation of the diffuser pressure coefficient with the impeller flow coefficient for the GT1749V 70 Trim compressor. The diffuser pressure

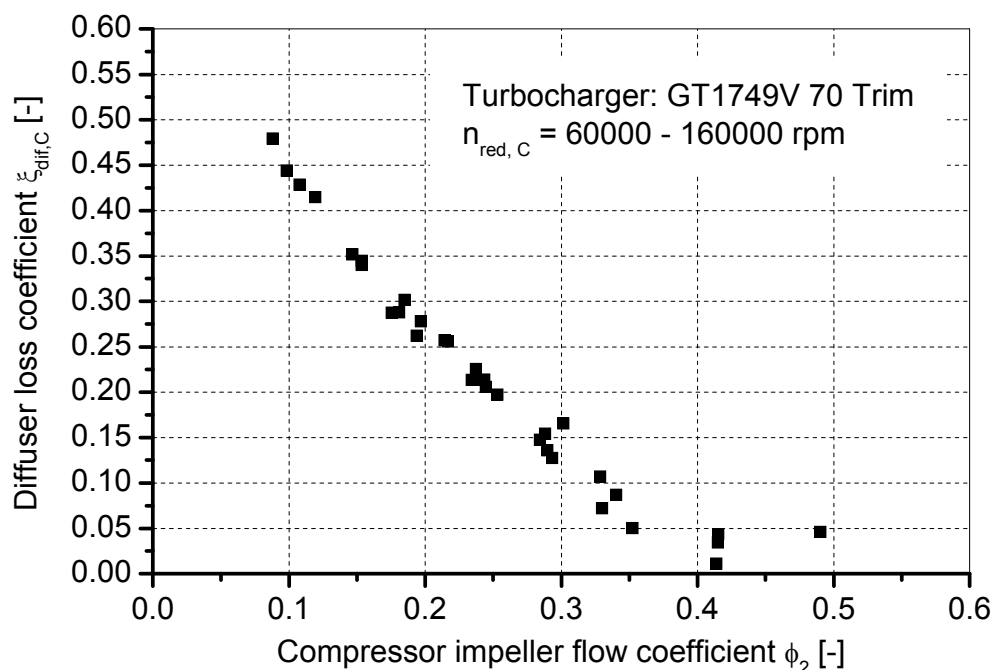


Figure 6-6 Diffuser loss coefficient of the GT1749V 70 Trim compressor

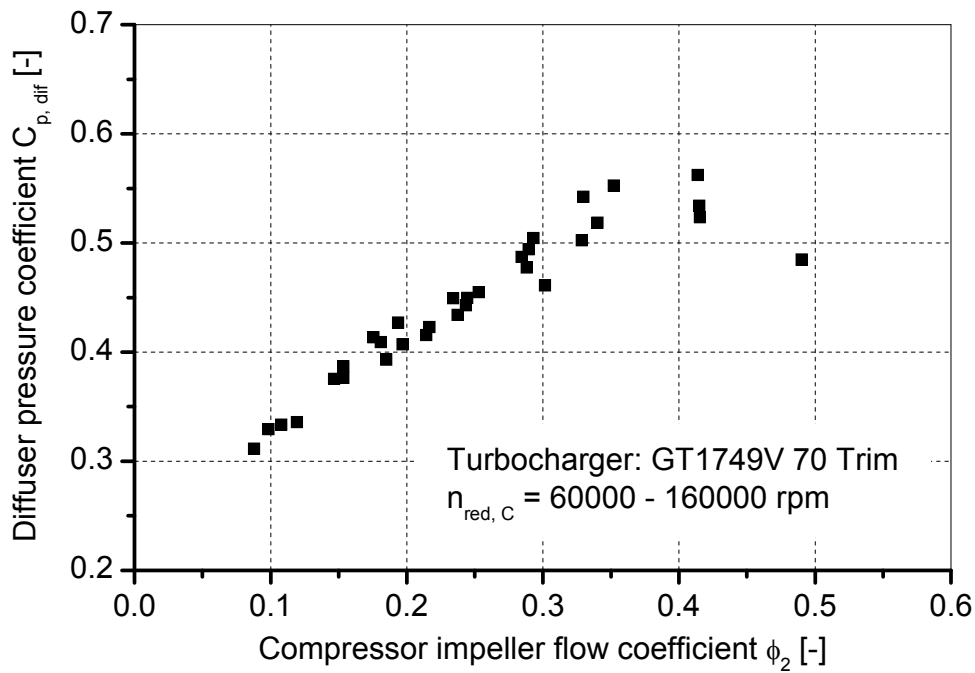


Figure 6-7 Diffuser pressure coefficient of the GT1749V 70 Trim compressor

coefficient increases with decreasing the diffuser losses. This is because the diffuser loss coefficient and the diffuser pressure coefficient are actually related to each other. This can be clarified with the help of equation (6.86). This equation can be rewritten as

$$C_{p,dif} = \frac{(p_{3t} - 0.5 \rho_3 c_3^2) - (p_{2t} - 0.5 \rho_2 c_2^2)}{0.5 \rho_2 c_2^2} \quad (6.87)$$

Rearranging equation (6.87)

$$C_{p,dif} = 1 - \left(\frac{\rho_3}{\rho_2} \right) \left(\frac{c_3}{c_2} \right)^2 - \frac{p_{2t} - p_{3t}}{0.5 \rho_2 c_2^2} \quad (6.88)$$

The third term in the right hand side of equation (6.88) is the diffuser loss coefficient. The ideal diffuser pressure coefficient is achieved at zero losses inside the diffuser

$$C_{p,dif,ideal} = 1 - \left(\frac{\rho_3}{\rho_2} \right) \left(\frac{c_3}{c_2} \right)^2 \quad (6.89)$$

Therefore, the diffuser pressure coefficient is related to the diffuser loss coefficient by the relation

$$C_{p,dif} = C_{p,dif,ideal} - \xi_{dif} \quad (6.90)$$

The ideal diffuser pressure coefficient depends on the geometry of the diffuser as well as the flow angle at the diffuser inlet. If the flow in the diffuser is incompressible and the swirl velocity at the diffuser outlet can be estimated from the free vortex flow relation

$$c_{3u} = r_2 c_{2u} / r_3 \quad (6.91)$$

then the ideal diffuser pressure coefficient can be estimated from

$$C_{p,dif,ideal} = 1 - \left(\frac{D_2}{D_3} \right)^2 \frac{1 + (b_2/b_3)^2 \tan^2 \alpha_2}{1 + \tan^2 \alpha_2} \quad (6.92)$$

Equation (6.92) shows clearly that the diffuser pressure coefficient depends on the geometry of the diffuser as well as the flow angle at the diffuser inlet. The diffuser loss coefficient also depends greatly on the diffuser geometry and the flow angle at the diffuser inlet.

Two additional vaneless diffusers are computed with the program "V-Diffuser" to obtain a general correlation for the diffuser loss coefficient. These diffusers have a width to diameter ratio $b_2/D_2 = 0.065$ and diameter ratios $\lambda = D_3/D_2 = 1.5$ and 1.9 . The impeller outer diameter of these two compressors is 0.4m . The vaneless diffuser of the GT1749V 70 Trim has a width to diameter ratio $b_2/D_2 = 0.068$ and a diameter ratio $\lambda = 1.67$. Therefore, the analysis covers a wide variety of diffuser geometries.

An expression for the vaneless diffuser loss coefficient is obtained from the estimated performance of the three different diffusers in the form

$$\xi_{dif} = \left(\frac{c_f + c_{dis}}{2} \right)^{0.63} \left(\frac{b_2}{D_2} \right)^{-1} \left(\frac{b_3 D_3}{b_2 D_2} \right)^{0.71} (\lambda - 1)^{0.65} \exp(-3.1 \sin \alpha_2) \quad (6.93)$$

Figure A-56 shows a comparison between the diffuser loss coefficient and the loss coefficient estimated from equation (6.93). The diffuser loss coefficient of the small GT1749 70 Trim compressor is higher than that of the large centrifugal compressors. This is because of the very small diffuser width of the GT1749V 70 Trim compressor. This amplifies the effect of the boundary layer on the diffuser performance. It also causes an increase in the dissipation and the friction losses of the GT1749V 70 Trim compressor diffuser in comparison with the vaneless diffusers of the large centrifugal compressors.

The friction coefficient and the dissipation coefficient in equation (6.93) are estimated

at the diffuser mean diameter. An expression for the dissipation coefficient is obtained from the data of the three different diffusers. This expression provides the mean value of the dissipation coefficient and not the local value in the boundary layers. The expression takes the form

$$C_{dis} = 90.7 \frac{Re_{dif,mean}^{0.379 - 6.2b_{dif,mean}/D_2}}{(0.009 Re_{dif,mean}^{0.81} + 390)} \exp(-1.225 \cos \alpha_2) \quad (6.94)$$

The mean diffuser Reynolds number is estimated from the equation

$$Re_{dif,mean} = \frac{0.5 (c_2 + c_3) (2b_{dif,mean})}{0.5 (v_2 + v_3)} \quad (6.95)$$

Figure A-57 shows a comparison between the estimated values of the dissipation coefficient and calculated values from equation (5.96) for the three investigated vaneless diffusers.

6.6.4 Volute aerodynamic losses

The experimental investigation of the GT1749V 70 Trim compressor shows that the volute can act as a diffuser at low mass flow rates or as a nozzle at high mass flow rates. The flow inside the volute neither accelerates nor decelerates at the design flow rate of the volute. Figure 6-8 shows the variation of the volute loss coefficient of the GT1749V 70 Trim compressor with the impeller flow coefficient. The volute loss coefficient increases with increasing the flow rate through the compressor. This is because of the increase in the meridional velocity at the volute inlet. This meridional velocity generates a vortex inside the volute. The vortex may be completely dissipated in the volute and this causes an increase in the volute loss coefficient. The vortex also increases the friction losses and the exit cone losses of the volute. Increasing the flow rate also causes a high acceleration in the volute. This increases the losses in the volute further. Figure 6-8 shows also that the volute loss coefficient for the GT1749V 70 Trim compressor exceeds unity at high flow rates. This means that the total pressure loss in the volute exceeds the dynamic pressure at the diffuser outlet. This behavior takes place at high negative pressure gradient inside the volute where the dynamic pressure at the volute outlet is greater than that at the inlet. The accelerating flow in the volute is characterized by negative volute pressure coefficient

$$C_{p,vol} = \frac{p_5 - p_3}{0.5 \rho_3 c_3^2} \quad (6.96)$$

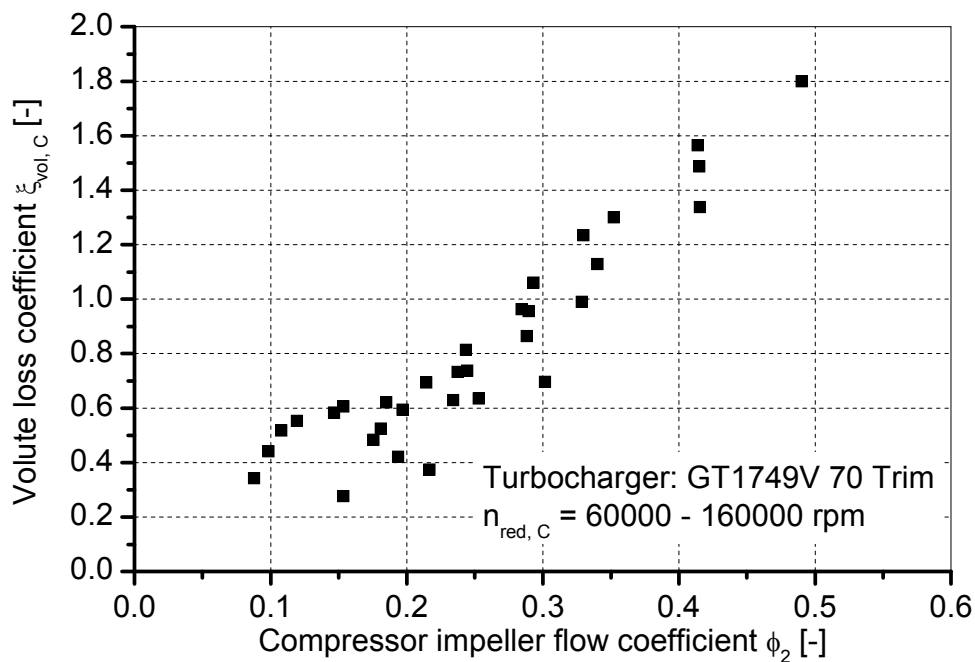


Figure 6-8 Volute loss coefficient of the GT1749V 70 Trim compressor

Figure 6-9 shows the volute pressure coefficient as a function of the impeller flow coefficient. Acceleration takes place at high mass flow rate and this causes a negative volute pressure coefficient. The volute acts as a diffuser at low mass flow rate with a positive pressure coefficient. Zero pressure coefficient of the volute means neither acceleration nor deceleration of the flow in the volute. This takes place at the design point of the compressor. This behavior can be observed in Figure 6-9 and Figure 6-3 where the volute pressure coefficient is shown to be zero at the point of the minimum measured compressor losses. This zero pressure coefficient at the design point means that the estimated performance using the program “V-Diffuser” matches very well the experimental results of the GT1749V 70 Trim compressor.

Figure 6-10 shows the combined pressure coefficient for the volute and the diffuser

$$C_{p, \text{dif+vol}} = \frac{p_5 - p_2}{0.5 \rho_2 c_2^2} \quad (6.97)$$

The combined pressure coefficient is higher than the diffuser pressure coefficient at flow rates less than the compressor design flow rate. This is because of the additional positive pressure gradient in the volute at low flow rates. The combined pressure coefficient coincides with that of the diffuser at the design point where the volute pressure coefficient equals zero. The combined pressure coefficient is lower than that of the diffuser at high flow rates due to the negative pressure gradient of the volute. At very high flow rates, the high negative pressure gradient in the volute

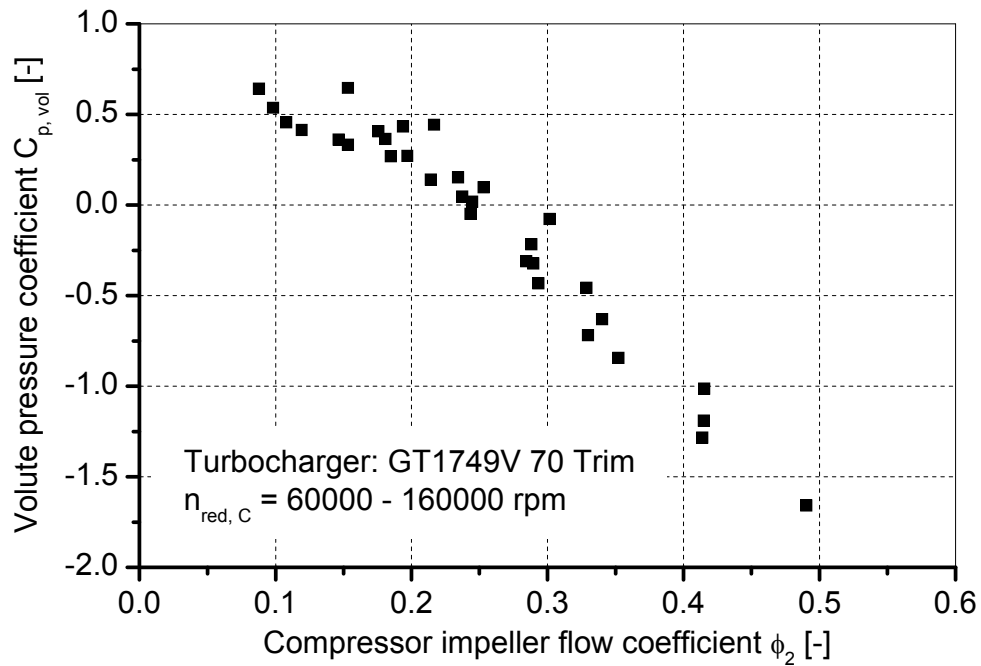


Figure 6-9 Volute pressure coefficient of the GT1749V 70 Trim compressor

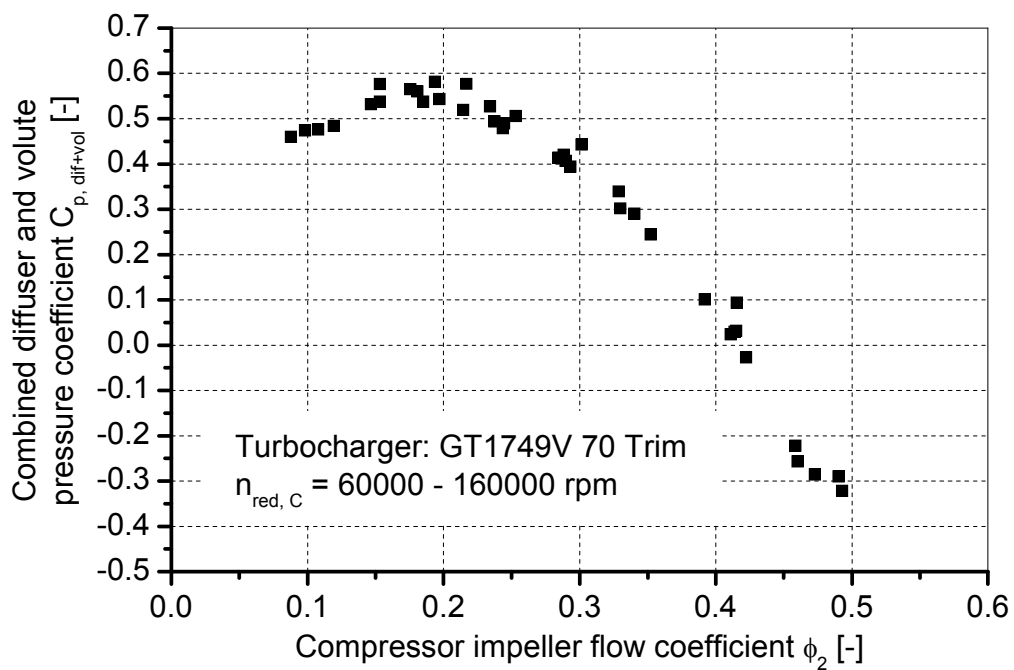


Figure 6-10 Combined pressure coefficient of the volute and the diffuser of the GT1749V 70 Trim compressor

overcomes the positive pressure gradient of the diffuser and the combined pressure coefficient is negative.

The volute loss coefficient can be expressed in terms of the main loss mechanisms inside the volute. These losses can be divided into

1. Friction losses
2. Exit cone losses
3. Loss of meridional velocity
4. Diffusion losses

Figure A-58 shows a schematic diagram for the volute. The friction losses of the volute are estimated from the equivalent pipe flow models

$$\xi_{\text{fri,vol}} = \frac{4 c_f L_{\text{vol,mean}}}{D_{h,4}} \frac{\rho_5}{\rho_3} \left(\frac{c_4}{c_3} \right)^2 \quad (6.98)$$

The mean volute length is estimated from the equation

$$L_{\text{vol,mean}} = \pi(r_3 + r_{\text{cone}}) \quad (6.99)$$

The friction coefficient is estimated at a mean volute Reynolds number

$$\text{Re}_{\text{vol,mean}} = \frac{0.5 (c_4 + c_{u,\text{vol,mean}}) D_{h,4}}{v_4} \quad (6.100)$$

The mean velocity in the circumferential direction is estimated from the equation

$$c_{u,\text{vol,mean}} = \frac{r_3 c_{u3}}{0.5(r_3 + r_{\text{cone}})} \quad (6.101)$$

The exit cone loss can be estimated from (*Aungier, 2000*)

$$\xi_{\text{vol,cone}} = \frac{(c_4 - c_5)^2}{c_3^2} \quad (6.102)$$

This equation is modified to account for the density change along the volute

$$\xi_{\text{vol,cone}} = \frac{\rho_5}{\rho_3} \frac{(c_4 - c_5)^2}{c_3^2} \quad (6.103)$$

The meridional flow at the volute inlet is directed into a vortex. This vortex is normally

assumed to be completely dissipated in the volute (*Aungier, 2000; Whitfield and Baines, 1990*). However, this vortex may not be completely dissipated. It is also possible that part of the meridional velocity at the volute inlet is recovered in the exit cone (*Japikse, 1996*). Therefore, the effect of the meridional velocity at the volute inlet is modeled in two ways. First, a fraction of the meridional velocity is considered to be dissipated in the volute

$$\xi_{vol,m} = K_{vol,m} \left(\frac{C_{3m}}{C_3} \right)^2 \quad (6.104)$$

Secondly, the vortex generated by the meridional velocity is assumed to increase friction and exit cone losses of the volute. A correction factor is inserted to account for the effect of the meridional velocity on friction and exit cone losses. It also accounts for the effect of the boundary layer on friction and exit cone losses.

The volute diffusion losses are considered to take place when the mean dynamic pressure of the volute is greater than the dynamic pressure at the inlet of the volute exit cone. The volute diffusion loss coefficient is expressed as

$$\xi_{vol,diff} = K_{vol,diff} \left(\frac{\rho_3 C_{u,vol,mean}^2 - \rho_4 C_4^2}{\rho_3 C_3^2} \right) \quad (6.105)$$

Therefore, the volute loss coefficient is presented in the form

$$\xi_{vol} = (\xi_{vol,fri} + \xi_{vol,cone}) F_{vol} + \xi_{vol,m} + \xi_{vol,diff} \quad (6.106)$$

Values for the unknown coefficients can be estimated from the experimental data. This model is applied to the data of the GT1749V 70 Trim compressor as well as to the experimental data of Rautenberg et al. (1998). Figure A-59 shows a comparison between the volute loss coefficient of the large centrifugal compressor with an external volute (*Rautenberg et al., 1998*) and the loss coefficient estimated by fitting the experimental data with equation (6.106). Similar results for the GT1749V 70 Trim compressor with a central volute are shown in Figure A-60. Figure A-59 and Figure A-60 show clearly that equation (6.106) can correctly represent the loss mechanisms inside the volute. However, it is difficult to find recommended values for the unknown empirical coefficients that match the whole operating range of both compressors. This is because of the wide variety of designs available for the volute. However, recommended values for the empirical coefficients of equation (6.106) are obtained for the low rotational speed operating range of the small and the large compressor. This is because of the relatively weak vortex inside the volute at low rotational

speeds. These values are

$$K_{\text{vol,m}} = 0.43 \quad (6.107)$$

$$K_{\text{vol,diff}} = 0.54 \quad (6.108)$$

$$F_{\text{vol}} = \frac{3.28}{\text{Re}_{\text{vol}}^{0.05}} \left(\frac{c_{3m}}{0.5(c_{\text{u,vol,mean}} + c_4)} \right)^{0.04} \quad (6.109)$$

6.6.5 Effect of aerodynamic losses on the overall compressor performance

The overall compressor performance results from the performance of the individual compressor components. The contribution of each component to the overall performance depends on the compressor operating point. The diffuser aerodynamic losses are very significant at low mass flow rates while the volute aerodynamic losses are very significant at high flow rates. Figure A-61 and Figure A-62 show the total pressure loss of each compressor component as a fraction of the compressor overall total pressure loss of the GT1749V 55 Trim compressor. The measured compressor adiabatic efficiency is also presented in the same figures. It can be observed that the best measured efficiency at each rotational speed is located at the point of interaction between the volute total pressure loss and the diffuser total pressure loss. This means that the best efficiency point represents an optimum point for these two components. This behavior is also shown by the data of Rautenberg et al. (1974) as shown in Figure A-63. However, the best efficiency point for the data of Rautenberg et al. (1998) is located at the point of intersection between the volute total pressure loss and the impeller total pressure loss, Figure A-64. This is because the diffuser total pressure loss is very small compared with the total pressure loss of the impeller and the volute. Therefore, it can be generally said that the compressor best efficiency point represents an optimum point for the aerodynamic losses of the individual compressor components.

6.7 Slip factor

The slip factor of centrifugal compressors accounts for the deviation of the actual swirl velocity at the impeller outlet from the ideal one. This deviation depends on many geometrical and operating parameters of the compressor. The slip factor is estimated from the computation of the flow field inside the diffuser using the program "V-Diffuser". This is because the direct estimation of the slip factor from the measured data requires information regarding the density at the impeller outlet. This requires detailed measurements at the impeller outlet. These detailed measurements

are almost impossible for small centrifugal compressors. The actual swirl velocity at the impeller outlet is estimated by applying the energy equation and Euler's equation for turbomachinery to the impeller in the absence of compressor inlet guide vanes

$$c_{2u} = [c_{p,air}(T_{2t,adi} - T_{1t}) - w_{imp,diskf}] / u_2 \quad (6.110)$$

Most of the authors (*Aungier, 2000; Aungier, 1995; Whitfield and Baines, 1990*) neglect the disk friction losses in the estimation of the slip coefficient. This is because disk friction losses are very small compared with the compressor aerodynamic work during the normal operation of the compressor. However, the aerodynamic work of the compressor decreases with decreasing the compressor rotational speed. Therefore, disk friction losses may be important at low rotational speeds in comparison with the compressor aerodynamic work. Therefore, the disk friction losses are included in the estimation of the compressor slip factor. Figure 6-11 shows the variation of the slip factor with the impeller flow coefficient for three different impellers.

The slip factor of the centrifugal compressors increases with increasing the impeller blade angle at outlet. It also increases with decreasing the flow rate through the impeller. This is because of the jet-weak flow inside the impeller and the flow separation on the pressure side of the blade with decreasing the flow rate. These cause an increase in the relative velocity near and at the suction side of the blades. The relative flow angle gets closer to the blade angle at the impeller outlet and the slip factor is improved. The slip factor of the radial impeller and the back-swept impeller decreases with increasing the flow rate within the investigated range of operation. The slip factor of the GT1749V 55 Trim impeller decreases first with increasing the flow rate and then starts to increase once again with increasing the flow rate. The increase of the slip factor at high flow rates is due to the increase in the fluid inertia with increasing the flow rate. This is because the high inertia fluid has less ability to follow the change in the back-sweep angle near the impeller outlet. Therefore, the fluid flows closer to the blade suction side at the impeller outlet and this causes an increase of the slip factor.

The classical explanation for the slip phenomena (*Balje, 1981; Whitfield and Baines, 1990*) uses the concept of relative eddy. As the flow into the impeller is normally irrotational and a frictionless fluid will remain irrotational, then the flow at the impeller outlet must rotate relative to the impeller with an angular velocity equal and opposite to that of the impeller (*Balje, 1981; Whitfield and Baines, 1990*). The slip velocity at the impeller outlet can be estimated from

$$c_{slip} = r_{eddy} \omega \quad (6.111)$$

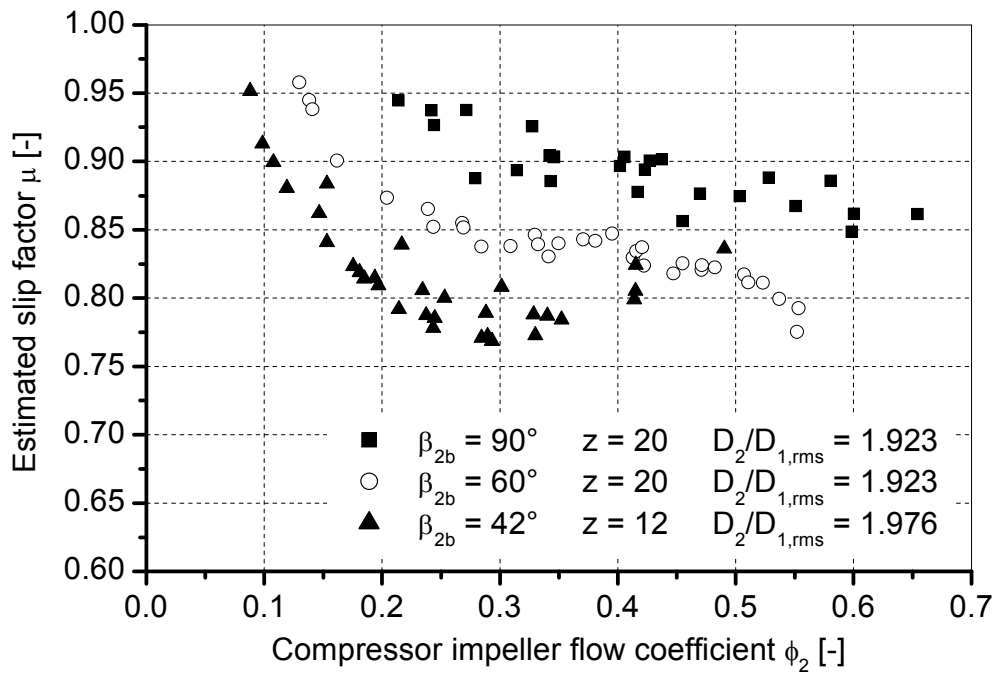


Figure 6-11 Variation of the slip factor with the impeller flow coefficient for three different impellers

The eddy radius at the impeller outlet in the absence of flow separation and aerodynamic blockage of the impeller area at outlet can be estimated from the equation

$$r_{\text{eddy}} = \frac{\pi D_2}{2z} \sin \beta_{2b} \quad (6.112)$$

However, aerodynamic blockage and flow separation take place inside the impeller. Therefore, the eddy radius at the impeller outlet is expressed as

$$r_{\text{eddy}} = \frac{\pi D_2}{2z} \sin \beta_{2b} F_{\text{eddy}} \quad (6.113)$$

The empirical coefficient F_{eddy} accounts for the effect of the geometrical and operating conditions of the impeller on the eddy radius. Substituting equation (6.113) in equation (6.111) and rearranging

$$c_{\text{slip}} = u_2 \frac{\pi}{z} \sin \beta_{2b} F_{\text{eddy}} \quad (6.114)$$

Therefore, the slip factor of the compressor can be expressed as

$$\mu = 1 - \frac{u_2}{c_{2u,b}} \frac{\pi}{z} \sin \beta_{2b} F_{\text{eddy}} \quad (6.115)$$

The slip factor formula of Stanitz (1952b) for radial impellers can be obtained from equation (6.115) by substituting for the empirical coefficient F_{eddy} by 0.63. An expression for the empirical coefficient F_{eddy} is obtained by fitting the estimated values of the slip coefficient for the three different impellers using the subroutine "lfit.for" (Press *et al.*, 1992)

$$F_{\text{eddy}} = \frac{0.0294 (w_2/w_1)^{0.697+0.054\Delta\beta}}{(D_2/D_{1,\text{rms}} - 1)^{0.945}} \text{Re}_{\text{imp}}^{0.252} \left(\frac{C_{2m}}{C_{2u,b}} \right)^{-0.924 (w_2/w_1)^{1.1} \cos \beta_{2b}} \quad (6.116)$$

The blade camber parameter is defined as

$$\Delta\beta = (\beta_{2b} - \beta_{1b,\text{mean}}) / \beta_{1b,\text{mean}} \quad (6.117)$$

The ratio of the relative velocity at the impeller outlet to that at the impeller inlet is the de Haller number. The de Haller number and the impeller passage Reynolds number account for the effect of flow separation and the development of the boundary layers inside the impeller on the slip factor. The blade camber parameter and the impeller diameter ratio account for the effect of passage geometry on the slip factor. The ratio of the flow velocity at the impeller outlet to the ideal swirl velocity accounts for the effect of fluid inertia on the slip factor. The effect of fluid inertia is more significant for impellers with small blade angles at the impeller outlet. This is because small blade angle at the impeller outlet implies higher change in the peripheral direction near the impeller outlet. Therefore, impellers with small back-sweep angle are more affected by the fluid inertia.

Combining equations (6.115) and (6.116), the slip factor can therefore be estimated from the equation

$$\mu = 1 - \frac{u_2}{C_{2u,b}} \frac{\pi}{Z} \sin \beta_{2b} \cdot \frac{0.0294 (w_2/w_1)^{0.697+0.054\Delta\beta}}{(D_2/D_{1,\text{rms}} - 1)^{0.945}} \text{Re}_{\text{imp}}^{0.252} \left(\frac{C_{2m}}{C_{2u,b}} \right)^{-0.924 (w_2/w_1)^{1.1} \cos \beta_{2b}} \quad (6.118)$$

A mean value for the eddy parameter based on the data of the three different impellers is found to be 0.76. Therefore, a simplified formula for the quick estimation of the slip factor takes the form

$$\mu = 1 - 0.76 \frac{u_2}{C_{2u,b}} \frac{\pi}{Z} \sin \beta_{2b} \quad (6.119)$$

This formula can be applied for both the backswept as well as the radial impellers.

Figure A-65 to Figure A-67 show a comparison between the estimated values of the slip factor and the calculated values for the three different impellers. Equation (6.118) estimates the slip coefficient of the three different impellers with a good accuracy. It can also simulate the effect of the fluid inertia on the slip factor. The Wiesner correlation (1967) intersects with the estimated slip factor at some operating point. However, this operating point is not the compressor design point as it should be. The simplified formula, equation (6.119), can also be used to estimate the slip factor. For the three investigated impellers, it has generally a better accuracy than the Wiesner correlation. It also has a better accuracy than the Stanitz correlation for the radial impellers at the compressor design point. Table 6-1 shows the percentage error in estimating the slip factor at the compressor design point using equation (6.118), equation (6.119), Stanitz's correlation [equation (2.11)], and Wiesner's correlation [equation (2.12)].

Table 6-1 Percentage error in estimating the slip factor at the compressor design point

Impeller geometry	% Error in the estimated slip coefficient			
	Equation (6.118)	Equation (6.119)	Wiesner correlation	Stanitz correlation
$\beta_{2b}=60^\circ$ $D_2= 0.4$ m	1.08%	4.9%	6.65%	-----
$\beta_{2b}=42^\circ$ $D_2= 0.049$ m	0.327%	4.01%	8.72%	-----
$\beta_{2b}=90^\circ$ $D_2= 0.4$ m	2.6%	0.55%	0.94%	1.75%

6.8 Part load performance prediction of small turbocharger compressors

The present performance prediction model is based on the mean streamline prediction technique. The model uses empirical loss correlations along the mean streamline to predict the performance of the compressor. The compressor aerodynamic work is estimated from the application of Euler's equation for turbomachinery to the impeller. This also requires the prediction of the impeller slip factor under different geometrical and operating conditions.

The above empirical loss correlations as well as the slip factor correlation are used to predict the compressor performance at part load operation. A Fortran 77 program, called "CPLP-Prediction", is written to predict the compressor performance at part load operation. Figure 6-12 shows a flow chart for the program. The calculations start with the assumption that the flow in the impeller is incompressible. This assumption can be applied at low rotational speeds. However, the program performs iterating calculations to estimate the actual density at the impeller outlet. The initial

assumption of the density at the impeller outlet permits the estimation of the ideal swirl velocity at the impeller outlet. The slip factor is also estimated from iterating calculations. A value is initially assumed for the slip factor. This provides the estimate of an initial value for the actual swirl velocity at the impeller outlet. The velocity triangle at the impeller outlet can therefore be initially estimated. The relative velocity at the impeller outlet as well as the total temperature and the total pressure at the impeller outlet can also be estimated. The initial estimation of the velocity triangle at the impeller outlet permits the estimation of a new value for the slip factor using equation (6.118). The new value of the slip factor is compared with the initial value. The previous calculations are iterated until the value of the slip factor is converged. This means that the actual velocity triangle at the compressor outlet as well as the total pressure and the total temperature are known. However, these parameters are known for the initial assumption of the density at the impeller outlet.

The impeller aerodynamic losses are estimated from equations (6.72) to (6.80). The estimation of the impeller aerodynamic losses enables the estimation of a new value for the total pressure at the impeller outlet. Therefore, a new value for the density at the impeller outlet can also be estimated. This new value is compared with the initial one and the calculations are iterated until the density at the impeller outlet is converged. This means that the impeller aerodynamic work as well as the flow field at the impeller outlet has been now predicted.

The conservation equations of the flow inside the diffuser are then solved. The solution of these equations is similar to the one used in the program "V-Diffuser". However, these equations are solved only in the radial direction using the mean values of the flow at the impeller outlet. The dissipation coefficient is estimated from equation (6.94). The compressor performance is predicted for the adiabatic condition only. This means that the total temperature at the diffuser outlet equals the total temperature at the impeller outlet. The solution of the flow field inside the vaneless diffuser allows the prediction of the diffuser loss coefficient as well as the total pressure and the velocities at the diffuser outlet.

The aerodynamic losses of the volute are estimated from equations (6.98) to (6.106). This also requires iterative calculations for the density at the compressor outlet. The prediction of the volute performance enables the estimation of the total pressure at the compressor outlet. The compressor total pressure ratio is estimated from the total pressure at the compressor outlet and the total pressure at the compressor inlet. The compressor adiabatic efficiency is estimated from the total pressure ratio and the total temperatures at the compressor inlet and outlet.

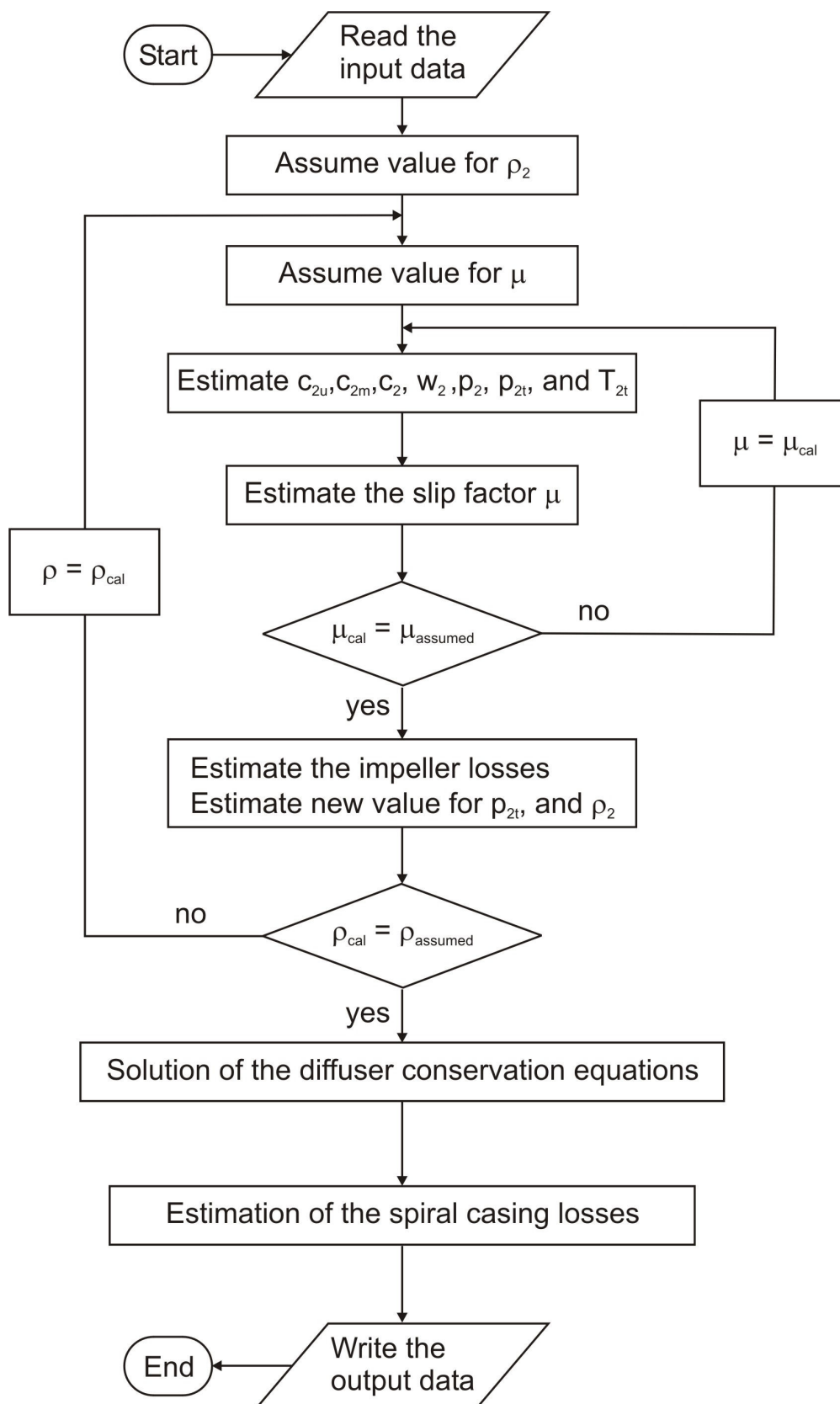


Figure 6-12 Flow chart for the program "CPLP-Prediction"

Five different compressors are predicted using the program “CPLP-Prediction”. These compressors are the GT1749V 55 Trim, the GT1749V 70 Trim, the K29, the VNT12, and the K03 compressor. These compressors provide a wide variety of small turbocharger compressor geometries. The main dimensions of the GT1749V 55 Trim, the GT1749V 70 Trim, and the K29 compressor are listed in Table A-1 while the main dimension of the VNT12 compressor and the K03 compressor are listed in Table A-2.

Figure A-68 to Figure A-72 show a comparison between the predicted compressor performance and the measured compressor performance at low rotational speeds for the five different compressors. The program “CPLP-Prediction” can predict the measured total pressure ratio of the compressors at low rotational speeds with a good accuracy. The smallest measured mass flow rate through the compressor in each figure represents the surge point of the corresponding compressor. This means that the predicted performance at flow rates lower than this flow rate represents only a theoretical extrapolation of the performance map. The program “CPLP-Prediction” can also predict the adiabatic efficiency of the compressor with a good accuracy in comparison with the very poor measuring accuracy in the low rotational speed operating range. The data presented in Figure A-69 were measured by the technical university of Berlin for the GT1749V 55 Trim compressor at extremely low rotational speeds as well as compressor operation in the fourth quadrant of the map. The program can also predict the compressor pressure ratio in the fourth quadrant of the map with a maximum error of $\pm 5.03\%$ based on the experimental results. This error takes place at extremely high compressor flow rate and during compressor operation as an abnormal turbine. The program can also predict the compressor performance at zero compressor rotational speed with a good accuracy up to a compressor reduced mass flow rate of 0.0407 kg/sec. This flow rate is very high for the compressor at zero rotational speed. The error increases with increasing compressor flow rate and it reaches 6.87% at a compressor reduced flow rate of 0.0544 kg/sec and zero compressor rotational speed. The total pressure at the compressor inlet was adjusted to 1.5 bar during the measurements to achieve a compressor reduced flow rate of 0.0544 kg/sec. Therefore, such high reduced mass flow rate is not likely to occur during actual operation of the turbocharger at zero rotational speed.

The measured compressor efficiency of the GT1749V 55 Trim compressor is significantly lower than the predicted compressor efficiency. This high deviation is mainly due to the amount of heat transfer from the oil to the compressor. This is because the oil temperature at the bearing housing inlet was 358 K during the measurements of the compressor performance. This temperature was higher than the total temperature at the compressor outlet. Therefore, heat was transferred from the bearing housing to the compressor and this caused high deterioration of the measured compressor efficiency at extremely low rotational speeds. The deviation of

the predicted compressor efficiency from the measured one is also shown for the VNT12 and the K03 compressors. This is also because the performance of these compressors was measured with an exhaust gas temperature at the turbine inlet of 873 K. The predicted compressor efficiency of the K03 compressor is also overestimated at low compressor flow rates. This is because the predicted compressor pressure ratio is higher than the measured one at low flow rates. The percentage error of the estimated pressure ratio of the K03 compressor at the surge point is +2.257%. This error results however in a high percentage error in the estimated compressor efficiency due to the very small temperature difference across the compressor in this operating range. Therefore, it is recommended to use the estimated compressor power to judge the compressor performance in the low rotational speed operating range. This is because it is less subjected to calculating errors than the compressor efficiency. The program therefore also offers the predicted compressor power as an output parameter in the output list.

6.9 Turbine performance simulation

Turbine performance simulation aims at estimating the turbine performance at every turbine operating point. The method described in this section is based on the measured turbine performance map. It requires knowledge of the turbine main dimensions as well as the frictional power of the turbocharger bearing. Information regarding the geometry of the turbine inlet guide vanes is also required for the turbines with inlet guide vanes.

6.9.1 Turbine mass flow rate

The turbine mass flow rate is estimated by modeling the expansion through the turbine as an expansion through a nozzle with an effective total-to-static pressure ratio. The effective total-to-static pressure ratio takes the effect of the centrifugal force on the turbine mass flow rate into account. This effect is modelled by considering each turbine rotor passage as a rotating channel. A rotating channel exerts a radial outward pressure that causes lower effective pressure ratio than the applied pressure ratio. The radial outward pressure is estimated from the equation

$$p_{r,T} = 0.5 \rho_6 (r_{rot} \omega)^2 \quad (6.120)$$

The radius of rotation is estimated from the equation

$$r_{rot} = 0.5 (r_7 + r_{8i}) \quad (6.121)$$

The effective total pressure at the turbine inlet can therefore be estimated from the equation

$$p_{6t,eff} = p_{6t} - 0.5 \rho_6 (r_{rot} \omega)^2 \quad (6.122)$$

The effective pressure ratio is defined as the ratio of the effective total pressure at the turbine inlet to the static pressure at the turbine outlet

$$\pi_{6t8s,eff} = p_{6t,eff} / p_8 \quad (6.123)$$

The mass flow rate through the turbine is estimated from equations (2.2) to (2.4) but with the effective total pressure and the effective total-to-static pressure ratio

$$\dot{m}_T = C_{d,T} A_{7,T} \frac{p_{6t,eff}}{\sqrt{R_{exh} T_{6t}}} \Phi_{T,eff} \quad (6.124)$$

The turbine effective flow function $\Phi_{T,eff}$ in equation (6.124) is estimated from equations (2.3) and (2.4) using the effective total-to-static pressure ratio

$$\text{for } 1 \leq \pi_{6t8s,eff} < \left(\frac{\kappa_{exh} + 1}{2} \right)^{\frac{\kappa_{exh}}{\kappa_{exh} - 1}} : \quad (6.125)$$

$$\Phi_{T,eff} = \sqrt{\frac{2 \kappa_{exh}}{\kappa_{exh} - 1} \left(\pi_{6t8s,eff}^{-2/\kappa_{exh}} - \pi_{6t8s,eff}^{-(\kappa_{exh} + 1)/\kappa_{exh}} \right)}$$

$$\text{for } \pi_{6t8s,eff} \geq \left(\frac{\kappa_{exh} + 1}{2} \right)^{\frac{\kappa_{exh}}{\kappa_{exh} - 1}} :$$

$$\Phi_{T,eff} = \sqrt{\kappa_{exh} \left(\frac{2}{\kappa_{exh} + 1} \right)^{\frac{\kappa_{exh} + 1}{\kappa_{exh} - 1}}} \quad (6.126)$$

The turbine discharge coefficient is estimated first from the test data. Figure 6-13 shows the variation of the turbine discharge coefficient with the Reynolds number at the turbine inlet for different guide-vane positions of the GT1749V 55 Trim turbine.

The Reynolds number at the turbine inlet is estimated from the equation

$$Re_6 = (c_6 D_6) / \nu_6 \quad (6.127)$$

The exhaust gas viscosity is estimated at the exhaust gas pressure and temperature according to the method described by Poling et al. (2001). Figure 6-13 is estimated from the manufacturer performance map of the turbine. It shows that the turbine discharge coefficient of the GT1749V 55 Trim turbocharger depends on the Reynolds number and the turbine area ratio. The turbine area ratio is defined as the ratio of the

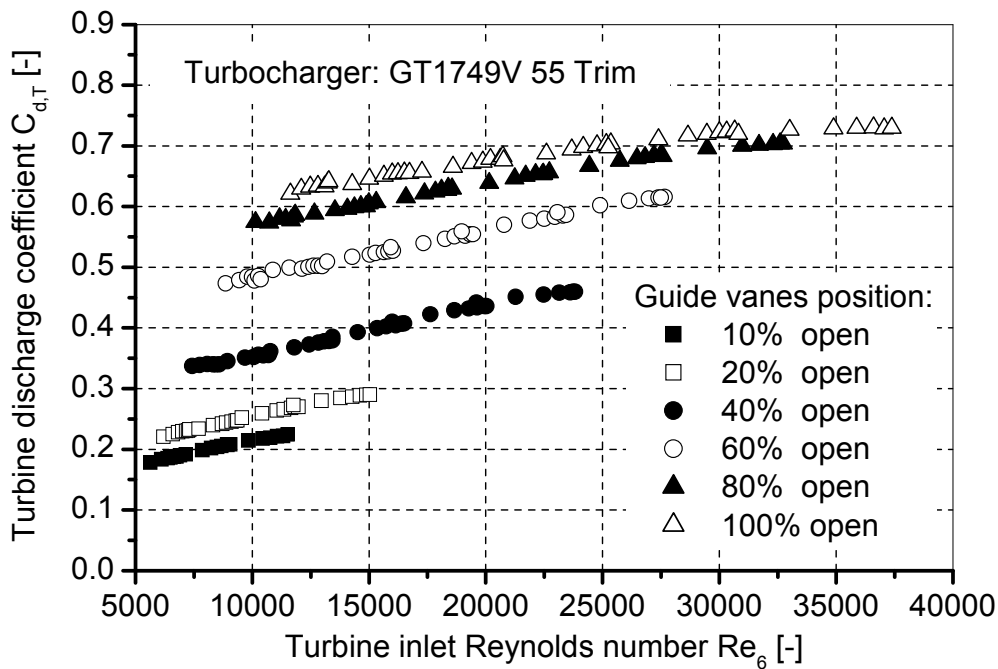


Figure 6-13 Variation of the turbine discharge coefficient with the Reynolds number at the turbine inlet for different guide-vane positions of the GT1749V 55 Trim turbine

throat area of the inlet guide vanes to the inlet area of the rotor. The turbine discharge coefficient increases with increasing the Reynolds number at the turbine inlet and increasing the turbine area ratio. The dependence of the turbine discharge coefficient on the Reynolds number decreases with increasing the Reynolds number. Based on the test results, the turbine discharge coefficient of the GT1749V 55 Trim turbocharger can be expressed as

$$C_{d,T} = 0.3886 AR_T^{2.9083} Re_6^{f(AR_T)} \quad (6.128)$$

The exponent of the Reynolds number in equation (6.128) also depends on the turbine area ratio. Figure A-73 shows the variation of the Reynolds number exponent with the turbine area ratio. This exponent varies between 0.325-0.144 for the GT1749V 55 Trim turbocharger. It decreases with increasing the turbine area ratio. This means less influence of the Reynolds number on the turbine discharge coefficient with opening the inlet guide vanes. This is because increasing the area between the guide vanes means less aerodynamic blockage due to the boundary layers and hence less effect of the Reynolds number on the turbine discharge coefficient.

Equation (6.128) can be used to estimate the turbine discharge coefficient and hence the turbine mass flow rate. This implies iterating calculations for the estimation of the

mass flow rate. The value of the discharge coefficient is initially assumed. The mass flow rate is estimated from equation (6.124) with the initial value of the turbine discharge coefficient. The Reynolds number is estimated from the calculated mass flow rate. A new value for the turbine discharge coefficient is estimated from equation (6.128). The iterations continue until the value of the turbine discharge coefficient is converged. Figure A-74 shows a comparison between the measured turbine mass flow rate and the estimated turbine mass flow rate. The method described above can be used to estimate the turbine mass flow rate with a good accuracy in the whole turbine operating range.

The method described above is also applied for the K29 twin entry turbine. In this case, the turbine discharge coefficient is estimated for each turbine entry separately. The mass flow rate through each turbine entry is estimated from the equations

$$\dot{m}_{T,A} = C_{d,T,A} \left(0.5 A_{7,T}\right) \frac{P_{6t,eff,A}}{\sqrt{R_{exh} T_{6t,A}}} \Phi_{T,A,eff} \quad (6.129)$$

$$\dot{m}_{T,B} = C_{d,T,B} \left(0.5 A_{7,T}\right) \frac{P_{6t,eff,B}}{\sqrt{R_{exh} T_{6t,B}}} \Phi_{T,B,eff} \quad (6.130)$$

Figure 6-14 shows the variation of the turbine discharge coefficient for each turbine entry with the corresponding Reynolds number for an entry pressure ratio $\pi_{entry} = 1$. The K29 turbine discharge coefficient also depends on the entry Reynolds number. It increases with increasing the entry Reynolds number. The results also show that the turbine discharge coefficient of the K29 turbocharger depends on the total-to-static pressure ratio of each turbine entry. It increases with increasing the effective total-to-static pressure ratio of the turbine entry. This behaviour is due to the wall separating the two entries of the turbine. This wall extends from the turbine entry down to the inlet of the turbine rotor. It causes significant development of the boundary layers inside the turbine casing. Increasing the total-to-static pressure ratio of the turbine means increasing the flow rate through the turbine and hence increasing the Reynolds number. It also means higher expansion ratio through the turbine with a favourable pressure gradient. This reduces the viscous effects and therefore improves the turbine discharge coefficient. The discharge coefficient of each turbine entry of the K29 turbine at an entry pressure ratio $\pi_{entry}=1$ can be estimated from the equations

$$C_{d,T,A} = 0.3188 Re_{6,A}^{0.038} \pi_{6t8s,eff,A}^{0.3043} \quad (6.131)$$

$$C_{d,T,B} = 0.2119 Re_{6,B}^{0.073} \pi_{6t8s,eff,B}^{0.249} \quad (6.132)$$

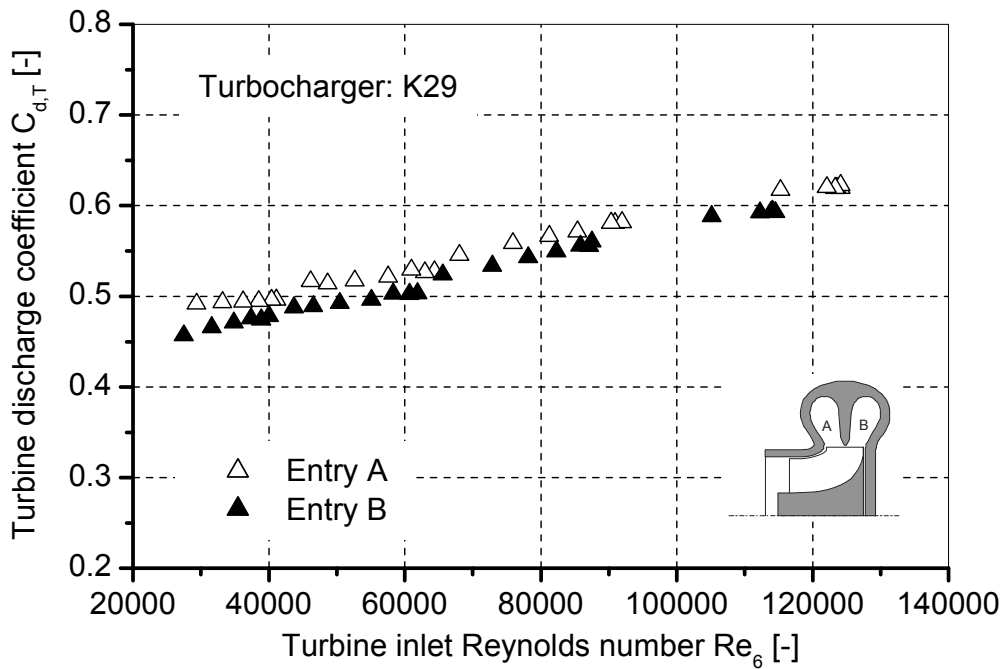


Figure 6-14 Variation of the turbine discharge coefficient with the Reynolds number for the K29 turbine at entry pressure ratio 1.0

It is evident that the discharge coefficient of entry A is higher than that of entry B due to the effect of the rotor aerodynamic losses as discussed in Chapter 5. Equations (6.131) and (6.132) can be used for the estimation of the turbine mass flow rate at an entry pressure ratio $\pi_{\text{entry}} = 1$. Figure A-75 and Figure A-76 show a comparison between the measured turbine entry mass flow rate and the estimated turbine entry flow rate. The method can also be used to estimate the mass flow rate of the turbine with a good accuracy in the whole operating range under full admission conditions.

The estimation of the entry flow rate under partial admission condition ($\pi_{\text{entry}} \neq 1$) using equations (6.129) and (6.130) requires another correction factor. This correction factor accounts for the effect of the entry with higher total pressure on the other entry with lower total pressure. This is because the exhaust gas with higher total pressure tends to flow back into the entry with lower total pressure. Therefore, it partially blocks the flow area of the entry with lower total pressure and causes its flow rate to decrease. The partial admission correction factor φ_{AB} is found from the test results of the K29 turbine

$$\varphi_{AB} = 0.947 \left(\frac{p_{6t,\text{eff},j}}{p_{6t,\text{eff},\text{mean}}} \right)^{1.27} \quad (6.133)$$

The index j in equation (6.133) accounts for the entry with higher total pressure.

Figure A-77 and Figure A-78 show a comparison between the measured flow rate and the estimated flow rate under partial admission conditions of the K29 turbine. The model described above can be used to extrapolate the turbine performance under partial admission conditions with a good accuracy for a considerable portion of the operating range. However, a deviation of the measured mass flow rate from the estimated mass flow rate is found at some operating points. These points are located at low rotational speed and extreme entry pressure ratios. This is because one of the two entries is almost closed at these operating points. This increases the back flow from one entry to the other and causes significant reduction of the entry flow rate. So that, the model described above has less accuracy at the operating points with one entry almost closed.

6.9.2 Turbine heat efficiency

The simulation of the turbine heat efficiency takes place in two steps. The first step is the extraction of the actual turbine heat efficiency from the measured product of the turbine efficiency and the mechanical efficiency. This is achieved by correcting the measured product of the turbine efficiency and the mechanical efficiency using equation (4.39). The bearing frictional power is used to estimate the mechanical efficiency of the turbocharger. The actual turbine heat efficiency is estimated from the corrected product of the turbine efficiency and the mechanical efficiency. The second step in the simulation procedure is the modeling of the estimated actual turbine heat efficiency. The actual heat efficiency is assumed to be mainly a function of the blade speed parameter. This assumption is confirmed by test data of the radial inward flow turbines. It is further assumed that the ratio of the turbine actual heat efficiency to the maximum actual heat efficiency is symmetric around the best efficiency point of the turbine. The ratio of the turbine actual heat efficiency to the maximum actual heat efficiency is called the relative heat efficiency of the turbine

$$\eta_{rel,T} = \eta_{heat,T} / \eta_{heat,T,max} \quad (6.134)$$

The ratio of the blade speed parameter to the blade speed parameter at the turbine best efficiency point is called the relative blade speed parameter

$$(u/c_s)_{rel} = (u/c_s) / (u/c_s)_{\eta_{heat,T,max}} \quad (6.135)$$

The turbine blade speed parameter is estimated on the basis of the effective total-to-static pressure ratio. This applies to both the GT1749V 55 Trim turbocharger and to the K29 turbocharger.

According to the above assumptions, the relative heat efficiency of the turbine is related to the relative blade speed parameter with the equation

$$\eta_{rel,T} = 2(u/c_s)_{rel} - (u/c_s)_{rel}^2 \quad (6.136)$$

Substituting equations (6.134) and (6.135) in equation (6.136) and rearranging

$$\frac{\eta_{heat,T}}{(u/c_s)^2} = \frac{\eta_{heat,T,max}}{(u/c_s)_{\eta_{heat,T,max}}^2} \left(\frac{2}{(u/c_s)_{rel}} - 1 \right) \quad (6.137)$$

The first term in the right hand side of equation (6.137) is assumed to be constant at each guide-vane position and each turbine rotational speed parameter. The value of this term can be estimated from the best efficiency point of the measured turbine performance map. An expression for the optimum blade speed parameter at each guide vane position and turbine rotational speed parameter is also obtained from the test data. Therefore, equation (6.137) can be used to estimate the actual turbine heat efficiency at each turbine blade speed parameter and inlet guide-vane position.

Figure A-79 to Figure A-84 show a comparison between the actual heat efficiency of the GT1749V 55 Trim turbine and the calculated turbine heat efficiency using equation (6.137). The method described above can be used to estimate the actual turbine heat efficiency at different operating points as well as at different guide-vane positions with a good accuracy. Some experimental points at low rotational speeds show a high deviation from the calculated turbine heat efficiency. This is because of the high measuring uncertainty in the low rotational speeds operating range. The method described above can also be applied successfully to the K29 turbine as shown in Figure A-85.

6.10 Turbocharger performance simulation program

The methods described in the previous sections can be used to estimate the turbocharger performance at each operating point. However, they require some details about the turbocharger geometry in order to provide a physically meaningful simulation of the turbocharger performance. These details may not be available to the users of the engine simulation programs. The iterations implied in the calculations also cause an increase of the calculation time. Therefore, a turbocharger simulation program (called TC_2003) is written especially for the engine simulation programs.

6.10.1 Description of the “TC_2003” program

The program is based on the measured turbocharger performance maps. It is designed to simulate the turbocharger performance with a minimum amount of data regarding the turbocharger geometry. This requires the use of regression equations

to simulate the turbocharger performance. However, the regression equations used are based on physically meaningful equations representing the turbocharger performance. This is necessary for the extension of the turbocharger performance maps towards very low rotational speeds. The “TC_2003” stand-alone program consists of two main subroutines, Figure 6-15. The first subroutine estimates the performance of the compressor while the second one estimates the performance of the turbine. Both subroutines can be implemented in the engine simulation programs to estimate the turbocharger performance at each operating point. The two subroutines are also designed to simulate the performance of several turbochargers at the same time. This is very important for the simulation of engines supplied with multistage turbocharging.

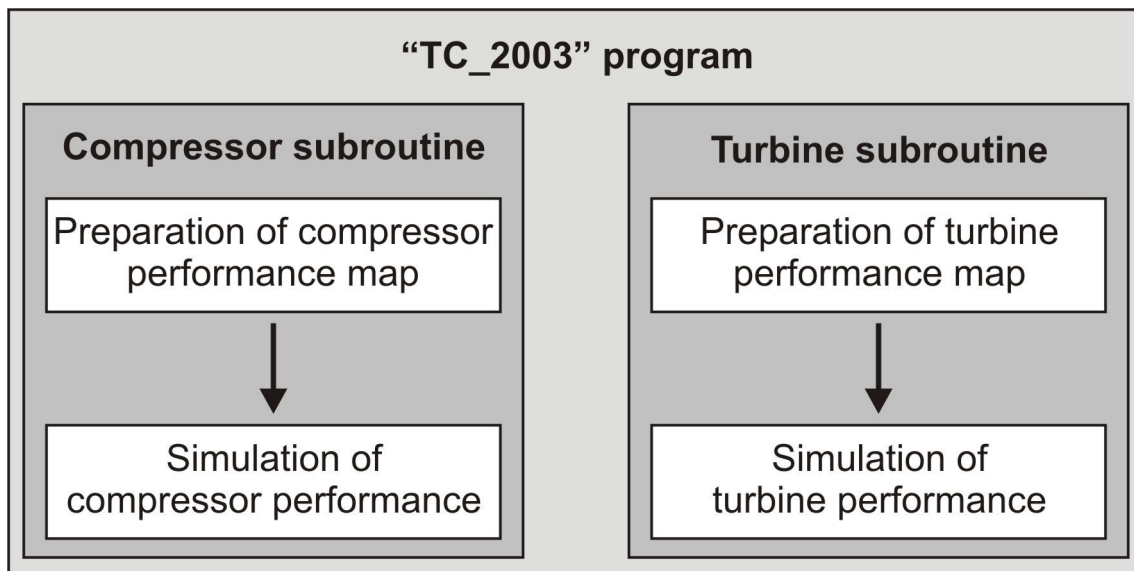


Figure 6-15 Schematic of the “TC_2003” program

Each subroutine consists of two main parts. The first part, the preparation part, converts the measured performance map into a non-dimensional form and obtains regression equations for the non-dimensional map. The second part uses the estimated regression equations to estimate the turbocharger performance at each operating point. The preparation part is used only one time per turbocharger. The engine simulation program decides whether the preparation part is to be executed or not. This is achieved with the help of control parameters in the parameter list of each subroutine. The compressor subroutine is designed to operate flexibly with the engine simulation program. This means that the engine simulation program can use either the reduced compressor mass flow rate or the compressor total pressure ratio as an input to the subroutine.

The variables used in the parameter list of the compressor subroutine are:

(← = output data, → = input data)

→ (←) PIVER	compressor total pressure ratio
→ NREDV	Compressor reduced rotational speed [rpm]
→ T3TTUR	total temperature at the turbine entry (entry A of twin entry turbines) [K]
→ T1TVER	total temperature at the compressor inlet [K]
→ P1TVER	total pressure at the compressor inlet [Pa]
← (→) MREDV	compressor reduced mass flow rate [kg/s]
← ETAVD	non-adiabatic compressor efficiency
← PV	compressor power [W]
← T2TOUT	total temperature at the compressor outlet [K]
→ KAPVER	specific heat ratio of the air
→ RVER	gas constant of the air [J/ (kg . K)]
→ COUNT	=0 by first call of the subroutine to execute the preparation part
← CONTR	control parameter for the modifications performed by the program for the input parameters. This occurs, for example, when the input mass flow rate is higher than the choking flow rate of the compressor at the input rotational speed
→ CONTRM	=0: → PIVER and ← MREDV, =1: ← PIVER and → MREDV
→ VDATEINAME	name of the file that contains the measured compressor performance map, =0: name of the file is the same as in the TC_2003 input file
→ TCEIN	name of the program input data file (for the calculations of several turbochargers), =0 : file =“TC2003_Eing.dat”
→ TURBON	turbocharger number (for the calculations of several turbochargers)
→ TURBJ	=0: no output file, =1: the subroutine establish an output file like that of the stand alone program
← BBERICHT	provides a report on the calculated point
→ SALONE	=0 : the subroutine works as the stand alone program >0 : the subroutine uses the data of the engine simulation program in the calculations

The variables used in the parameter list of the turbine subroutine are:

(← = output data, → = input data)

→ NREDT turbine rotational speed parameter [rpm/K^{0.5}]

→ P3TP4S	turbine total-to-static pressure ratio
→ LSR	inlet guide-vane position
→ T3AT	total temperature at the turbine entry (entry A of twin entry turbines) [K]
→ T3BT	total temperature at entry B (for twin entry turbines only) [K]
→ P3T	total pressure at the turbine inlet [Pa]
← ETAHEATT	turbine heat efficiency
← ETADIAT	non-adiabatic turbine efficiency
→ ETAMM	turbocharger mechanical efficiency
← MREDTA	turbine reduced mass flow rate (entry A of twin entry turbines) [kg .K ^{0.5} /(s . bar)]
← MREDTB	turbine reduced mass flow rate of entry B (for twin entry turbines only) [kg .K ^{0.5} /(s . bar)]
← T4T	total temperature at the turbine outlet [K]
→ COUNT	=0 by first call of the subroutine to execute the preparation part
→ TURBJ	=0: no output file, =1: the subroutine establish an output file like that of the stand alone program
→ KAPTUR	specific heat ratio of the exhaust gases
→ RTUR	gas constant of the exhaust gases [J/ (kg . K)]
→ CPTUR	specific heat at constant pressure of the exhaust gases [J/(kg . K)]
→ TDATEINAME	name of the file that contains the measured turbine performance map, =0: name of the file is the same as in the TC_2003 input file
→ VDATEINAME	name of the file that contains the measured compressor performance map, =0: name of the file is the same as in the TC_2003 input file
→ TCEIN	name of the program input data file (for the calculations of several turbochargers), =0 : file =“TC2003_Eing.dat”
→ TURBON	turbocharger number (for the calculations of several turbochargers)
→ SALONE	=0 : the subroutine works as the stand alone program >0 : the subroutine uses the data of the engine simulation program in the calculations

6.10.2 Compressor subroutine

The compressor subroutine reads at first the measured compressor performance map. The first step in the calculation is the estimation of the actual compressor work

from the measured data. The energy equation of the compressor under non-adiabatic operating conditions and in the absence of compressor inlet guide vanes takes the form

$$c_{p,\text{air}}(T_{5t} - T_{1t}) = \mu u_2 c_{2u,b} + q_C \quad (6.138)$$

Substituting for the ideal swirl velocity at the impeller outlet $c_{2u,b}$ from equation (2.8) in equation (6.138) and rearranging

$$\frac{c_{p,\text{air}}(T_{5t} - T_{1t})}{u_2^2} = \mu \left(1 - \frac{\phi_2}{\tan \beta_{2,b}} \right) + \frac{q_C}{u_2^2} \quad (6.139)$$

The amount of heat transfer to the compressor is represented by a simplified one-dimensional conduction equation

$$Q_C = \varepsilon_{\text{oil}} \frac{k_B A_B}{L_B} (T_{6t} - T_{5t}) \quad (6.140)$$

The heat reduction parameter ε_{oil} accounts for the fraction of heat removed by the oil. Equation (6.139) can therefore be rewritten as

$$\frac{c_{p,\text{air}}(T_{5t} - T_{1t})}{u_2^2} = \mu \left(1 - \frac{\phi_2}{\tan \beta_{2,b}} \right) + \varepsilon_{\text{oil}} \frac{k_B A_B}{L_B \dot{m}_C u_2^2} (T_{6t} - T_{5t}) \quad (6.141)$$

The left hand side of equation (6.141) is defined as the compressor non-adiabatic work coefficient. The non-adiabatic work coefficient is greater than the actual compressor work coefficient due to the amount of heat transfer to the compressor. The compressor subroutine calculates the non-adiabatic work coefficient from the measured data. It then obtains regression equations for the non-adiabatic compressor work coefficient as a function of the impeller flow coefficient at each constant peripheral Mach number. So that the non-adiabatic work coefficient is presented as a two dimensional matrix as shown schematically in Figure 6-16. The i-components of this matrix represent the values of the non-adiabatic work coefficient at constant peripheral Mach number. The j-components of this matrix represent the values of the non-adiabatic work coefficient at constant impeller flow coefficient. The compressor slip factor is assumed to be constant for all operating points with the same impeller flow coefficient. Thus the application of equation (6.141) to the operating points with the same impeller flow coefficient results in

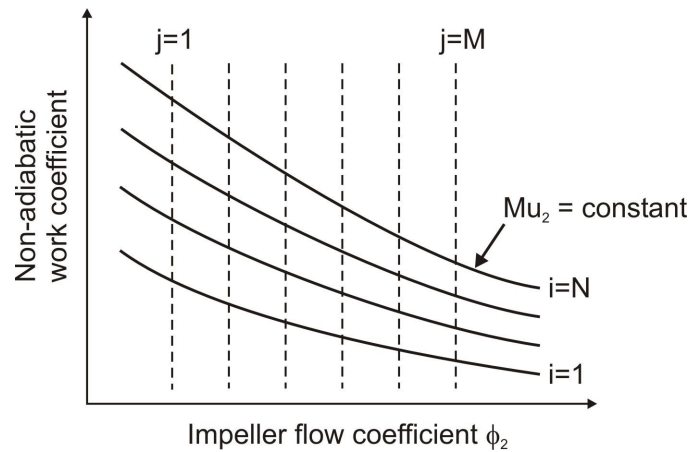


Figure 6-16 Schematic diagram for the modeling of the non-adiabatic work coefficient in the “TC_2003” program

$$\frac{c_{p,air}(T_{5t} - T_{1t})}{u_2^2} \Big|_{j,i} - \frac{c_{p,air}(T_{5t} - T_{1t})}{u_2^2} \Big|_{j,i+1} = \frac{k_B A_B}{L_B} \left(\varepsilon_{oil} \frac{(T_{6t} - T_{5t})}{\dot{m}_C u_2^2} \Big|_{j,i} - \varepsilon_{oil} \frac{(T_{6t} - T_{5t})}{\dot{m}_C u_2^2} \Big|_{j,i+1} \right) \quad (6.142)$$

A regression equation is used for the heat reduction parameter ε_{oil} as a function of the compressor operating parameters. The coefficients of this regression equation are obtained by fitting the results of equation (6.142). Thus, the heat reduction parameter and hence the slip factor can be estimated at each compressor operating point. A mean value for the heat reduction parameter is also given to the program through the input file. This value is used for the estimation of the compressor non-adiabatic efficiency when the measured compressor map is obtained from cold measurements. The recommended mean value of the heat reduction parameter is 0.15. This value is obtained from the test data of the GT1749V 55 Trim turbocharger.

The compressor subroutine obtains a regression equation for the compressor slip factor. Thus, regression equations are obtained for both the heat reduction parameter and the compressor slip factor. These regression equations are used in the calculation part of the subroutine to estimate the compressor power and the compressor non-adiabatic efficiency.

The compressor aerodynamic loss coefficient is first estimated from the equation

$$\xi_C = \frac{c_{p,air}(T_{5t} - T_{5t,is}) - q_c}{u_2^2} \quad (6.143)$$

The isentropic total temperature at the compressor outlet is estimated from the total pressure ratio of the compressor and the total temperature at the compressor inlet

$$T_{5t, is} = T_{1t} \left(\frac{p_{5t}}{p_{1t}} \right)^{\frac{\kappa_{air} - 1}{\kappa_{air}}} \quad (6.144)$$

A regression equation is obtained for the compressor loss coefficient by fitting the estimated values of the compressor loss coefficient. This regression equation is based on the main loss mechanisms of the compressor. It includes terms that represent

1. Impeller friction losses
2. Impeller Passage losses
3. Impeller diffusion losses
4. Diffuser losses
5. Volute losses

The impeller friction losses are estimated from equation (6.73). The impeller passage losses are considered to be proportional to the mean kinetic energy of the air. The impeller diffusion losses are considered to be proportional to the diffusion coefficient. The diffuser losses are presented as a function of the diffuser friction coefficient, diffuser width to diameter ratio, diffuser diameter ratio, and the flow angle at the impeller outlet (*Rodgers, 1984*). The volute losses are considered to be due to friction loss, loss of meridional velocity, and exit cone losses. These loss mechanisms constitute the regression equation of the compressor loss coefficient. This regression equation is used in the calculation part of the compressor subroutine to estimate the compressor total pressure ratio.

The compressor total pressure ratio near the surge point is presented as a linear function of the compressor reduced mass flow rate. This is because the slope of the compressor performance line tends to be zero or negative near the surge point. Small performance line slope may cause convergence problems in engine simulation programs. This is because a small change in the total pressure ratio causes a significant change in the compressor mass flow rate and vice versa. Negative slope of the compressor performance line causes additional calculation errors. This is because a certain compressor total pressure ratio in this case has two corresponding compressor flow rates as shown schematically in Figure 6-17. Therefore, the compressor performance line is presented as a linear function of the reduced mass flow rate near the compressor surge line. The limiting value of the compressor performance line slope is given to the program through the input file. The program

uses the linear relation for the total pressure ratio once the slope of the performance line falls below the limiting slope. The linear relation is also used to extrapolate the compressor performance beyond the surge line. This extrapolation is necessary because some engine operating points may be located beyond the measured surge line using combustion chamber test rigs, Figure 1-9.

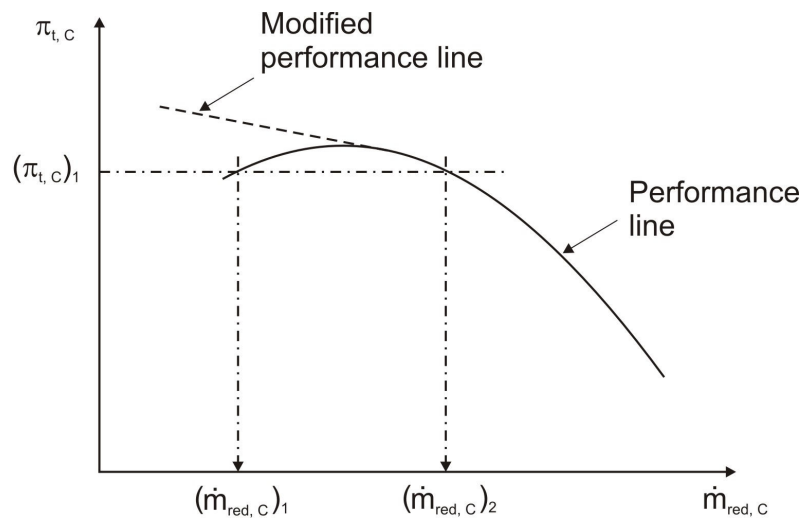


Figure 6-17 Schematic diagram of a compressor performance line with a negative slope near the surge point

The compressor subroutine estimates the absolute Mach number and the relative Mach number at the compressor inlet, the Mach number based on meridional velocity at the impeller outlet, and the Mach number at the inlet of the volute exit cone. It estimates additional shock losses if any of these Mach numbers exceed unity. These losses are estimated from the normal shock relations. Compressor choking takes place when the absolute Mach number at the compressor inlet, the Mach number based on meridional velocity at the impeller outlet, or the Mach number at the inlet of the volute exit cone reaches 1. The extension of the compressor performance using the "TC_2003" program is limited by compressor choking. This is because the estimation of the transonic compressor performance requires more detailed geometry and more calculation time. Therefore, the "TC_2003" program is designed to estimate the compressor performance up to the compressor choke limit. However, the compressor subroutine estimates the compressor performance after choking with the help of the input total pressure ratio. This total pressure ratio is given to the subroutine through the parameter list. If the given total pressure ratio is lower than the choking pressure ratio, an adiabatic shock wave is assumed to take place inside the compressor. The compressor subroutine performs the calculations using the choking mass flow rate of the compressor at the given reduced rotational speed. It estimates the compressor efficiency from the calculated total temperature at the

compressor outlet and the given total pressure ratio. The subroutine returns the estimated compressor efficiency and the given total pressure ratio at the choking mass flow rate.

6.10.3 Turbine subroutine

The turbine subroutine also reads the measured turbine map and then converts it into a non-dimensional form. Regression equations are obtained for the non-dimensional form of the turbine performance map. These equations are used later for the estimation of the turbine performance at each turbine operating point.

The turbine mass flow rate is estimated on the basis of equation (2.2). The turbine discharge coefficient is first estimated from the measured turbine mass flow rate. A regression equation is obtained for the turbine discharge coefficient by fitting the estimated values of the turbine discharge coefficient. This regression equation is a function of turbine rotational speed parameter, turbine total-to-static pressure ratio to the power 0.204, and inlet guide-vane position. The latter is used only for the turbines with inlet guide vanes. The exponent of the total-to-static pressure ratio in the regression equation is estimated by Pucher (*Pucher et al., 2003b*) based on the measurements of Zinner (1961). The turbine rotational speed parameter accounts for the effect of the centrifugal force on the turbine mass flow rate. The same principle is applied to the twin entry turbine at an entry pressure ratio $\pi_{\text{entry}} = 1$. The turbine mass flow rate under partial admission conditions are estimated using equation (2.2) and the regression equation of the turbine discharge coefficient. The mean total pressure at the turbine entry under partial admission conditions is estimated from the equation

$$p_{6t,\text{mean}} = 0.5(p_{6t,A} + p_{6t,B}) - \xi_{\text{mix},T} \cdot \text{abs}(p_{6t,A} - p_{6t,B}) \quad (6.145)$$

The value of the mixing losses coefficient based on the experimental results of the K29 turbine is found to be 0.1. The mean total pressure under partial admission conditions and the mean total temperature of the twin entry turbine are used in equation (2.2) to estimate the turbine flow rate. The mass flow rate of each turbine entry is also estimated from equation (2.2) and the regression equation of the turbine discharge coefficient. The total pressure and the total temperature of each turbine entry are used to estimate the corresponding turbine entry mass flow rate. The estimated flow rate of each turbine entry is corrected to account for the effect of the rotor aerodynamic losses on the mass flow rate of each turbine entry. A corrected flow rate through turbine entry A is obtained on the bases of the test results of the K29 turbine in the form

$$\dot{m}_{T,A} = \frac{\dot{m}_T}{1 + \left(\frac{c_{d,T,B} \rho_{6t,B} \Phi_{T,B} \sqrt{T_{6t,A}}}{c_{d,T,A} \rho_{6t,A} \Phi_{T,A} \sqrt{T_{6t,B}}} \right)^{1.7}} \quad (6.146)$$

The actual mass flow rate of entry B is estimated from the turbine mass flow rate and the mass flow rate through the turbine entry A

$$\dot{m}_{T,B} = \dot{m}_T - \dot{m}_{T,A} \quad (6.147)$$

The estimation of the actual heat efficiency requires first the correction of the measured turbine heat efficiency using equation (4.39). The amount of heat transfer from the turbine to the compressor is estimated from the equation

$$q_{C,rel} = \frac{q_C}{c_{p,exh} (T_{6t} - T_{1t})} \quad (6.148)$$

The value of the variable $q_{C,rel}$ is given to the program as input data. The value of $q_{C,rel}$ is found from the test results of the GT1749V 55 Trim turbocharger and the K29 turbocharger. It equals 0.0063 for the GT1749V 55 Trim and equals zero for the K29 turbocharger. This is because the test results of the K29 turbocharger show that the compressor works almost adiabatically. The value of $q_{C,rel}$ can also be set to zero for the GT1749V 55 Trim to ignore the effect of heat transfer from the turbine to the compressor on the turbine heat efficiency. The corrected turbine heat efficiency is used to obtain a regression equation for the turbine heat efficiency. This is achieved by applying Euler's equation for turbomachinery to the turbine rotor

$$W_T = u_7 c_{7u} + u_8 c_{8u} \quad (6.149)$$

The turbine heat efficiency can therefore be represented as

$$\eta_{heat,T} = \frac{u_7 c_{7u} + u_8 c_{8u}}{c_{p,exh} T_{6t} \left(1 - \left(\frac{p_{6t}}{p_8} \right)^{\frac{\kappa_{exh} - 1}{\kappa_{exh}}} \right)} \quad (6.150)$$

Equations for the swirl velocities at the turbine rotor inlet and outlet are obtained using the turbine velocity coefficients (*Balje, 1981*). The turbine velocity coefficient is defined as the ratio of the actual flow velocity to the ideal flow velocity. This applies for both the turbine stator and the turbine rotor. Thus

$$c_{7u} = \psi_{T,stator} \sqrt{1 - \mathfrak{R}_T} c_s \cos \alpha_7 \quad (6.151)$$

$$c_{8u} = \psi_{T,rotor} \cos \beta_8 \left[c_s^2 \mathfrak{R}_T + \psi_{T,stator}^2 c_s^2 (1 - \mathfrak{R}_T) - 2u_7 c_s \psi_{T,stator} \cos \alpha_7 \sqrt{1 - \mathfrak{R}_T} + u_8^2 \right]^{0.5} - u_8^2 \quad (6.152)$$

Substituting for c_{7u} and c_{8u} in equation (6.150) and rearranging

$$\frac{\eta_{heat,T}}{2(u_7/c_s)} + \delta_T^2 \left(\frac{u_7}{c_s} \right) = \psi_{T,stator} \cos \alpha_7 \sqrt{1 - \mathfrak{R}_T} + \psi_{T,rotor} \cdot \cos \beta_8 \delta_T \cdot \left[\mathfrak{R}_T + \psi_{T,stator} (1 - \mathfrak{R}_T) - 2 \psi_{T,stator} \cos \alpha_7 (u_7/c_s) \sqrt{1 - \mathfrak{R}_T} + \delta_T^2 (u_7/c_s)^2 \right]^{0.5} \quad (6.153)$$

where:

$$\delta_T = u_8/u_7 \quad (6.154)$$

Equation (6.154) can be rewritten as

$$\frac{\eta_{heat,T}}{2(u_7/c_s)} + \delta_T^2 \left(\frac{u_7}{c_s} \right) = f[(u/c_s), \pi_{6t8s}, \eta_{red,T}, GVP] \quad (6.155)$$

A regression equation is obtained for the left hand side of equation (6.153) as a function of turbine blade speed parameter, turbine rotational speed parameter, turbine total-to-static pressure ratio, and guide-vane position (only for turbines with inlet guide vanes). This regression equation is used in the calculation section of the program to estimate the turbine heat efficiency at each turbine operating point.

The estimation of the turbine non-adiabatic efficiency as well as the total temperature at the turbine outlet requires the estimation of the overall turbine heat losses. The overall heat transfer from the turbine is estimated in the "TC_2003" program using simplified equations. First, the amount of heat transfer from the turbine to the ambient by radiation is estimated from the equation

$$Q_{T,Rad} = A_{surface,T} \sigma \varepsilon_T (T_{T,c}^4 - T_{atm}^4) \quad (6.156)$$

The turbine casing temperature is estimated from the equation

$$T_{T,c,rel} = \frac{T_{T,c} - T_{atm}}{T_{6t} - T_{atm}} \quad (6.157)$$

The value of the variable $T_{T,c,rel}$ is given to the program using the input data file. A

value of $T_{T,c, rel} = 0.59$ is obtained from the test results of the GT1749V 55 Trim turbocharger. The amounts of heat transfer by convection from the turbine to the ambient and by conduction from the turbine to the bearing housing are given to the turbine subroutine as fractions of the turbine radiation heat transfer. The total temperature at the turbine outlet is estimated from the equation

$$T_{8t} = T_{6t} - \frac{q_T + W_T}{C_{p,exh}} \quad (6.158)$$

The turbine non-adiabatic efficiency is estimated according to equation (5.8).

6.10.4 Program results

The “TC_2003” program is used to simulate the compressor performance maps of five different compressors. These compressors are the GT1749V 55 Trim, the GT1749V 70 Trim, the K29, the K03, and the VNT12 compressor. The turbine performance map is simulated for the GT1749V 55 Trim, and the K29 turbine. This is because the turbine subroutine requires test data at different guide-vane positions. These data are available only for the GT1749V 55 Trim turbocharger. The GT1749V 55 Trim turbocharger and the GT1749V 70 Trim turbocharger also have the same turbine.

Figure A-86 shows the extended compressor performance map of the GT1749V 70 trim compressor. This extended performance map is estimated from the cold measurements of the turbocharger. Figure A-86 shows that program “TC_2003” can extend the performance map of the compressor with a good accuracy. The ability of the program to extrapolate and interpolate the performance map is examined by eliminating some performance lines from the input performance map. The new performance map is used as input to the program and the results of the program are compared with the original performance map. Figure A-87 shows a comparison between the calculated performance lines and the measured performance lines at three different compressor reduced rotational speeds. The performance line at 180000 rpm is calculated using the cold measurements of the compressor as an input performance map. This performance map is measured only up to 160000 rpm. The symbols represent the measured performance line at 180000 rpm during the hot measurements. The 60000 rpm performance line is calculated using the cold performance map without the data at 60000 rpm as an input to the program. It is also evident that the extrapolation towards low rotational speeds provides reasonable results in comparison with the poor measuring accuracy in this operating range. The 120000 rpm performance line is also calculated using the measured performance map without the data at 120000 rpm. This also shows that the program can

interpolate the measured performance map with a good accuracy.

Figure A-88 shows the extended compressor performance map of the GT1749V 70 Trim compressor using the measured compressor map at an exhaust gas temperature 873 K as an input to the program. It is evident in Figure A-88 that the "TC_2003" program can estimate the non-adiabatic compressor performance with acceptable accuracy. A deviation of the estimated compressor non-adiabatic efficiency from the measured non-adiabatic efficiency is shown at 60000 rpm. This deviation corresponds to a maximum error of $\pm 0.5\%$ in the estimated compressor total pressure ratio and ± 0.5 K in the estimated total temperature difference across the compressor. These values are within the range of the experimental error at this low compressor rotational speed.

Figure A-89 shows a comparison between the estimated compressor heat efficiency using the hot measurements as an input to the program and the measured heat efficiency of the compressor (cold measurements). The estimated heat efficiency of the compressor represents the measured one for most of the measured compressor operating points.

The ability of the subroutine to estimate the non-adiabatic compressor performance from the adiabatic one is also examined. This is achieved using the measured adiabatic compressor performance map as an input to the subroutine. The calculations are performed at a total temperature at the turbine inlet of 873K. This type of calculation can only be made using the compressor subroutine because the stand-alone program is designed to simulate the compressor performance at the measured turbine inlet temperature. Figure A-90 shows that the subroutine can also estimate the compressor non-adiabatic efficiency from the measured compressor adiabatic efficiency with an accuracy of $\pm 4\%$ -points at low rotational speeds.

Figure A-91 shows the extended compressor performance map for the GT1749V 55 Trim compressor. The ability of the program to interpolate the performance map is also examined for the GT1749V 55 Trim turbocharger. This is achieved by deleting the 140000 rpm compressor performance line from the input data of the compressor. Figure A-92 shows a comparison between the interpolated performance line and the measured performance line at 140000 rpm. The program can perform the interpolation of the GT1749V 55 Trim compressor map with an acceptable accuracy.

Figure A-93 shows a comparison between the estimated compressor performance at very low rotational speeds and compressor operation in the fourth quadrant of the map and the measured performance. The measured performance and the predicted

performance using the program “CPLP-Prediction” are also presented in the same figure. The results of the two programs are very similar. However, the program “CPLP-Prediction” estimates the performance in the fourth quadrant of the map with better accuracy. This is because it is based on physical models while the “TC_2003” program is based on physically meaningful regression equations. The deviation of the estimated compressor adiabatic efficiency from the measured one is very high. This is because of the high oil temperature at the bearing housing inlet during the measurements as mentioned before.

Figure A-94 shows a comparison between the estimated compressor heat efficiency and the measured one. The ability of the “TC_2003” program to simulate the non-adiabatic performance from the measured adiabatic performance is also examined as shown in Figure A-95. The extended compressor performance maps of the K29, the K03, and the VNT12 compressor are presented in Figure A-96 to Figure A-98.

Figure A-99 and Figure A-100 show a comparison of the measured turbine performance maps and the extended turbine performance maps using the program “TC_2003” for the GT1749V 55 Trim turbocharger and the K29 turbocharger. The extension of the GT1749V 55 Trim turbine performance map is performed at different inlet guide-vane positions and different values of the turbine rotational speed parameter. The extension of the K29 turbine performance map is performed at entry pressure ratio $\pi_{\text{entry}} = 1$ and different values of the turbine rotational speed parameter. Figure A-99 and Figure A-100 show that the “TC_2003” program can also estimate the measured turbine performance map with a good accuracy. The ability of the program to interpolate and extrapolate the measured turbine performance maps is examined in the same way as for the compressor. Some intermediate measured performance lines are deleted from the input file to the “TC_2003” program. The results of the program are compared with the measured performance map as shown in Figure A-101. This comparison shows that the “TC_2003” program interpolates the turbine performance map with a good accuracy. Likewise, some performance lines at high and low turbine rotational speed parameter are deleted from the input file to examine the ability of the program to extrapolate the turbine performance maps. Figure A-102 shows a comparison between the extrapolated performance lines and the measured performance lines of the GT1749V 55 Trim turbine. This comparison also shows that the extrapolation of the turbine performance map is performed with a good accuracy.

Figure A-103 shows the variation of the K29 turbine reduced mass flow rate with the entry pressure ratio at rotational speed 80000 rpm and a mean total-to-static pressure ratio of 1.8. The symbols in Figure A-103 represent the measured data and

the lines represent the extended turbine performance map. The reduced mass flow rate of each turbine entry is also presented in Figure A-103. The “TC_2003” program can extrapolate the performance map of the K29 turbine under partial admission conditions with a good accuracy.

The K29 turbine heat efficiency under partial admission conditions is estimated from the regression equation at an entry pressure ratio $\pi_{\text{entry}} = 1$. The turbine total-to-static enthalpy difference is estimated from equation (5.16). The blade speed parameter under partial admission conditions can therefore be used to estimate the turbine heat efficiency under partial admission conditions. This procedure provides acceptable estimation of the twin entry turbine heat efficiency under partial admission conditions as shown in Figure 5-20.

7. CONCLUSIONS AND RECOMMENDATIONS FOR FUTURE WORK

The present research work deals with the investigation of turbocharger non-adiabatic performance and the extension of turbocharger performance maps down to very low rotational speed. The extension of turbocharger performance maps also requires the simulation of the compressor performance in the fourth quadrant of the compressor map.

A parameter study of the turbocharger non-adiabatic performance is presented. This parameter study shows that the amount of heat transfer to the compressor causes a deviation of the compressor non-adiabatic efficiency from the adiabatic efficiency. This deviation depends mainly on the compressor peripheral Mach number and the compressor heat number, equation (4.17). The deviation increases with decreasing the compressor peripheral Mach number and increasing the compressor heat number. Therefore, the amount of heat transfer to the compressor introduces a significant systematic error in the measured product of the turbine efficiency and the mechanical efficiency at low rotational speeds. The measured non-adiabatic performance of the GT1749V 55 Trim turbocharger matches very well the results of the parameter analysis.

The measured compressor efficiency of the K29 turbocharger is independent of the exhaust gas temperature in the measured range of operation. This is due to the relatively large turbine surface area, the high oil flow rate of the K29 turbocharger, the high aerodynamic compressor work, and the high compressor peripheral Mach number.

The experimental results of the GT1749V 55 Trim turbine show that the measured product of the turbine efficiency and the turbocharger mechanical efficiency must be corrected using equations (4.39) and (4.40) to enable accurate estimation of the turbine power at low rotational speeds.

The amount of heat transfer from the turbine is estimated by applying energy balance to the GT1749V 55 Trim turbocharger. It is found that convection and radiation heat transfer represent 60-70% of the total amount of heat transfer from the turbine at low rotational speeds. This percentage increases with increasing the turbocharger rotational speed and can be as high as 90% of the total amount of heat transfer from the turbine at 120000 rpm. The amount of heat transfer from the turbine to the compressor through the bearing housing is less than 10% of the total amount of heat transfer from the turbine. The oil receives 10-49% of the total amount of heat transfer from the turbine. This means that the oil acts as a heat barrier that removes most of

the heat transfer from the turbine to the compressor through the bearing housing.

The performance of the twin entry K29 turbine under full admission as well as partial admission conditions is investigated. The variation of the rotor passage losses with the passage width introduces asymmetry in the flow rate through the turbine entries. The turbine efficiency under full admission condition as well as under partial admission condition mainly depends on the turbine blade speed parameter.

The aerodynamic performance of micro compressors is investigated by means of measuring the static pressure distribution in the vaneless diffuser of the GT1749V 70 Trim compressor. This investigation shows a clear effect of the volute tongue on the flow field inside the diffuser. This tongue effect extends from the diffuser outlet upstream to the diffuser inlet.

The static pressure distribution inside the diffuser is almost uniform in the circumferential direction at the design flow rate. At the compressor surge line, the non-uniformity of the static pressure distribution at the diffuser inlet is higher than that at the diffuser outlet. This behavior increases significantly with increasing the rotational speed due to the interaction between the diffuser and the impeller. Flow separation is detected at the diffuser inlet along the compressor surge line. It takes place at an angle located at 180° peripheral angle from the volute tongue.

Empirical correlations for the aerodynamic losses and the slip factor of centrifugal compressors are obtained. A part load performance prediction program is developed with the help of these correlations. This program can predict the aerodynamic compressor performance down to zero rotational speed as well as compressor operation in the fourth quadrant of the map with acceptable accuracy.

A turbocharger performance simulation program is developed. This program can operate either as a stand-alone program or as two subroutines in the engine simulation programs. The program can simulate the turbocharger performance down to zero rotational speed with acceptable accuracy.

For future work, it is recommended to perform cold as well as hot measurements for every turbocharger. This is of particular importance at low rotational speeds. It is also recommended to perform cold measurements at low oil inlet temperature to estimate the turbocharger adiabatic performance. The results of cold measurements are to be used in correcting the measured turbine performance using equations (4.39) and (4.40). Thereby, the actual turbocharger aerodynamic performance can be extracted from hot measurements.

It is also recommended to perform detailed experimental and theoretical investigation of the heat transfer mechanisms inside the bearing housing. This investigation should also include the mutual effects between the heat transfer to the oil and the bearing frictional power. The recommended investigation aims at optimizing the bearing housing design to reduce the amount of heat transfer to the compressor at low rotational speeds. It also aims at improving the turbocharger mechanical efficiency at low rotational speeds by improving the amount of heat transfer to the oil.

A. APPENDIX

Table A-1 Main dimensions of the investigated turbochargers

	GT1749V 55 Trim	GT1749 70 Trim	K29
1. Compressor:			
Inner diameter at compressor inlet [mm]	12.07	12.07	22
Outer diameter at compressor inlet [mm]	36.25	32.93	57
Impeller outer diameter [mm]	49	49	87
Blade angle at impeller exit [°]	42	42	62
Number of blades	12/6 splitter	12/6 splitter	14/7 splitter
Diffuser width [mm]	2.66	2.66	5
Diffuser exit diameter [mm]	82	82	120
2. Turbine:			
Diameter of turbine wheel at inlet [mm]	42.93	42.93	81.9
Width of turbine wheel at inlet [mm]	4.8	4.8	11.8
Blade angle at wheel inlet [°]	90	90	90
Outer diameter of turbine wheel at exit [mm]	36	36	74.4
Inner diameter of turbine wheel at exit [mm]	13	12.46	26.4
Casing geometry	Single entry-VTG	Single entry-VTG	Twin entry

Table A-2 Main dimensions of the VNT12 and K03 compressors

	VNT12	K03
Inner diameter at compressor inlet [mm]	10.75	9.05
Outer diameter at compressor inlet [mm]	26.00	31.40
impeller outer diameter [mm]	44	45
Blade angle at impeller outlet [°]	50	48
Number of blades	12/6 splitter	8/4 splitter
Diffuser width [mm]	2.25	3.30
Diffuser outlet diameter [mm]	76.5	71.8

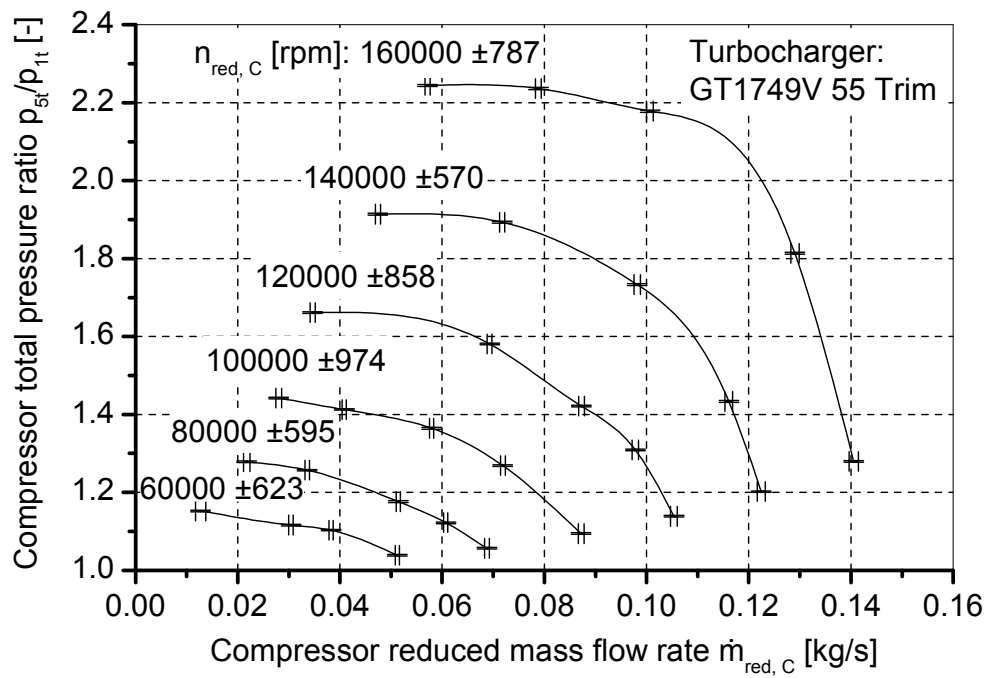


Figure A-1 Error analysis of the measured total pressure ratio, reduced rotational speed, and reduced mass flow rate of the GT1749V 55 Trim compressor

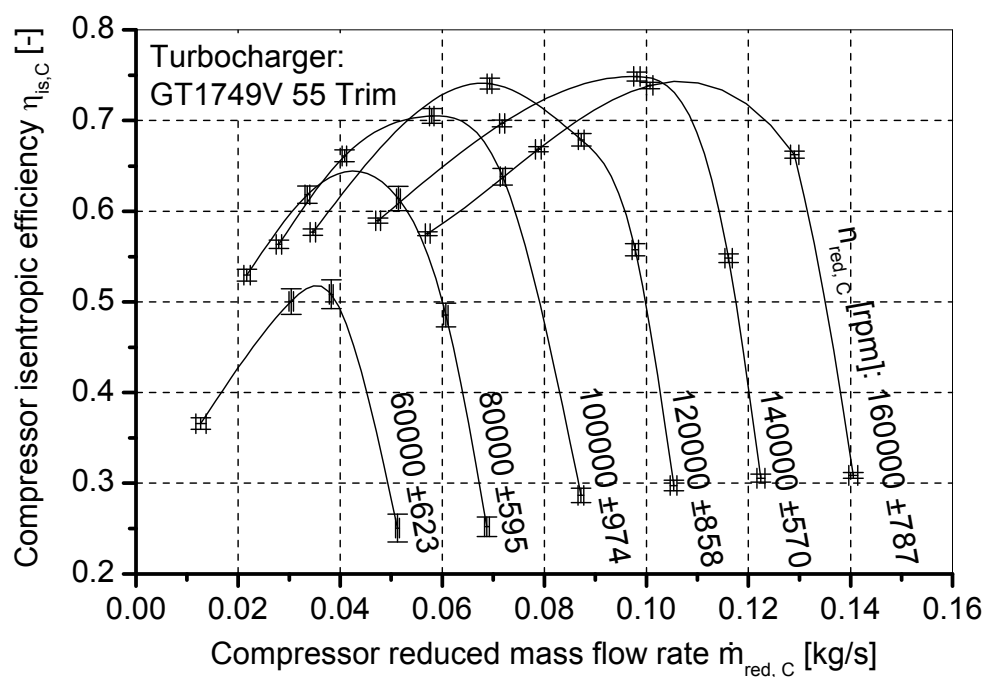


Figure A-2 Error analysis of the measured isentropic efficiency of the GT1749V 55 Trim compressor

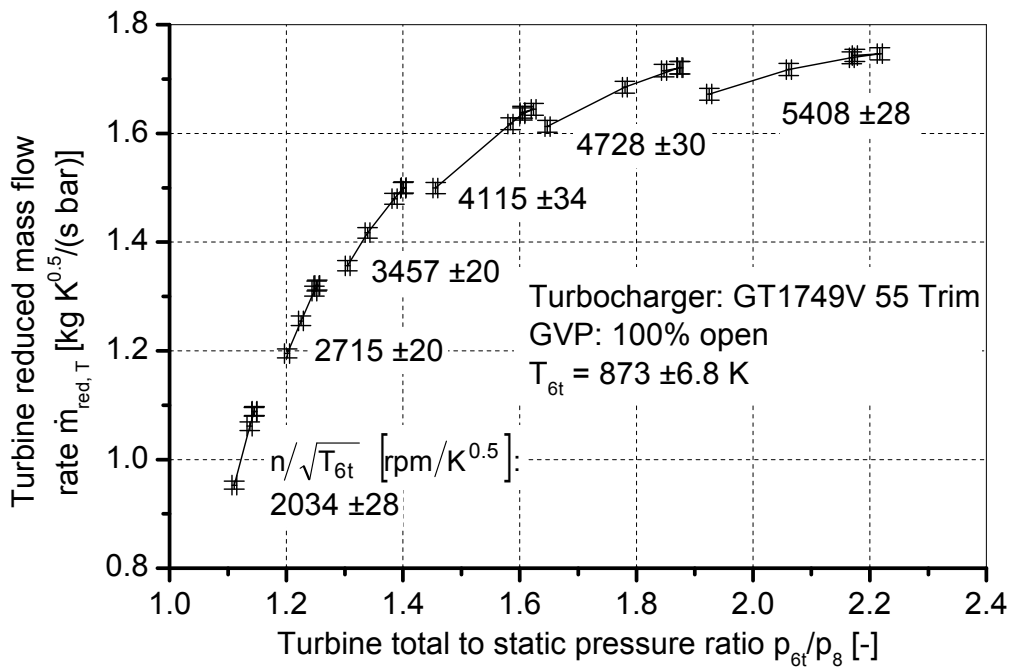


Figure A-3 Error analysis of the measured total-to-static pressure ratio, reduced rotational speed, and reduced mass flow rate of the GT1749V 55 Trim turbine

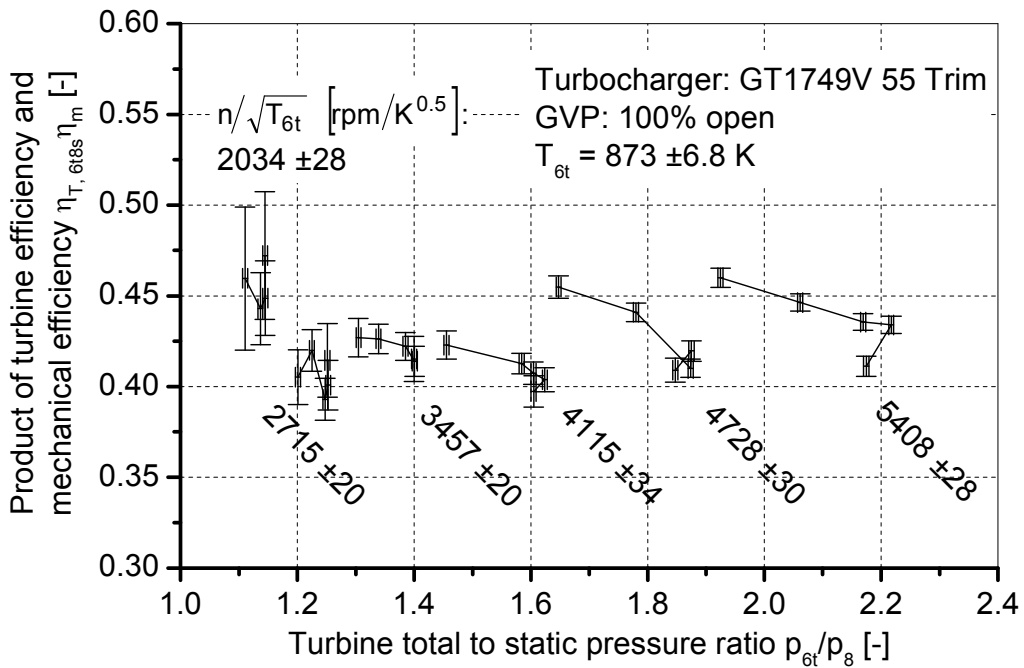


Figure A-4 Error analysis of the estimated product of total-to-static turbine efficiency and mechanical efficiency of the GT1749V 55 Trim turbocharger

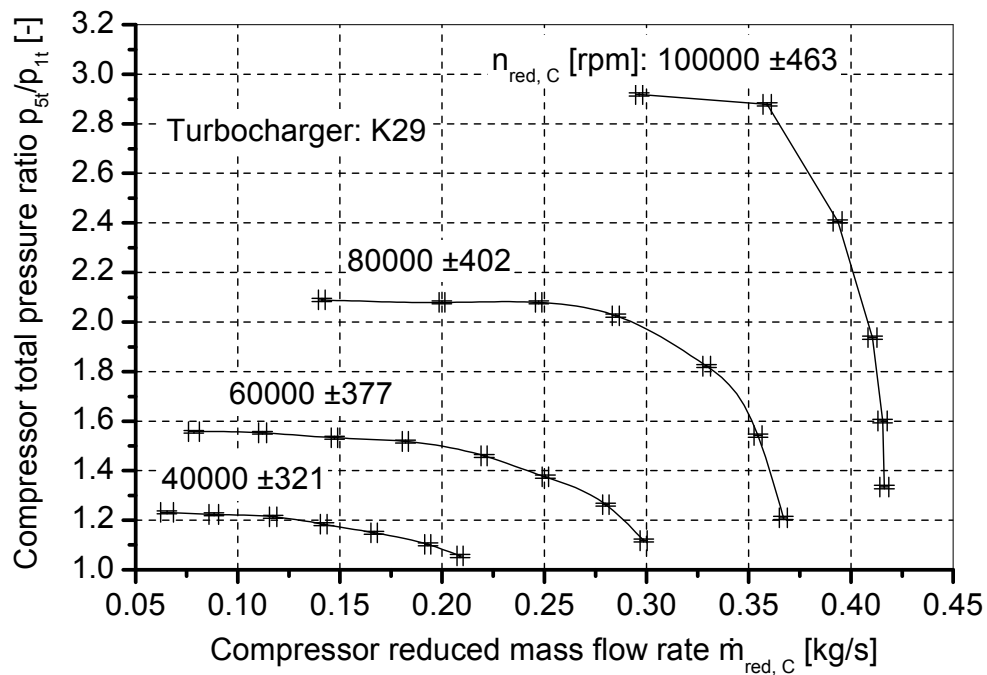


Figure A-5 Error analysis of the measured total pressure ratio, reduced rotational speed, and reduced mass flow rate of the K29 compressor

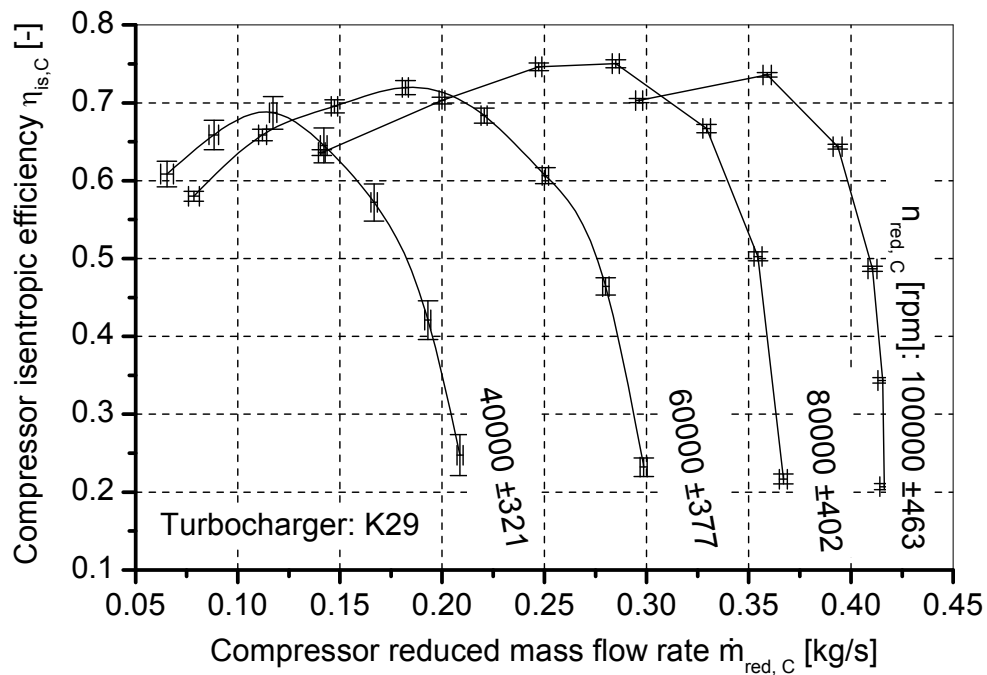


Figure A-6 Error analysis of the measured isentropic efficiency of the K29 compressor

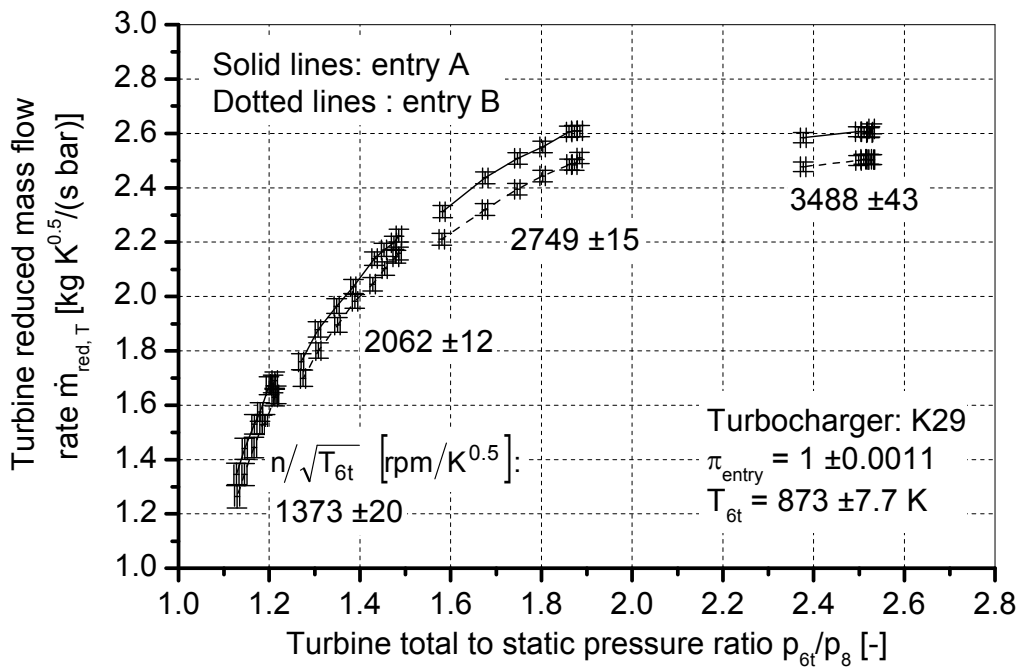


Figure A-7 Error analysis of the measured total-to-static pressure ratio, reduced rotational speed, and reduced mass flow rate of the K29 turbine

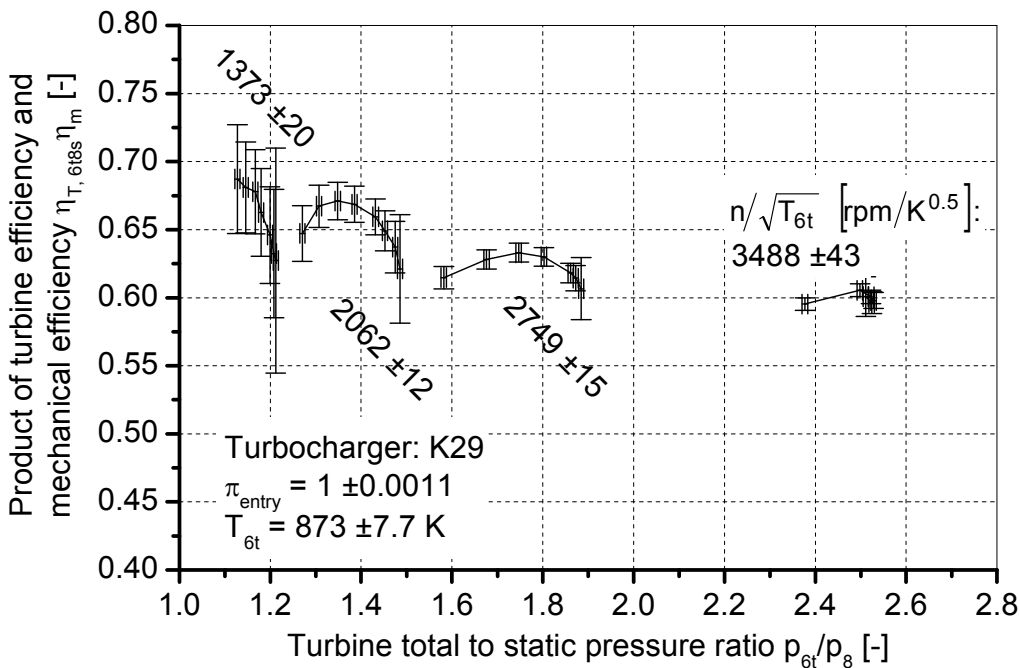


Figure A-8 Error analysis of the estimated product of total-to-static turbine efficiency and mechanical efficiency of the K29 turbocharger

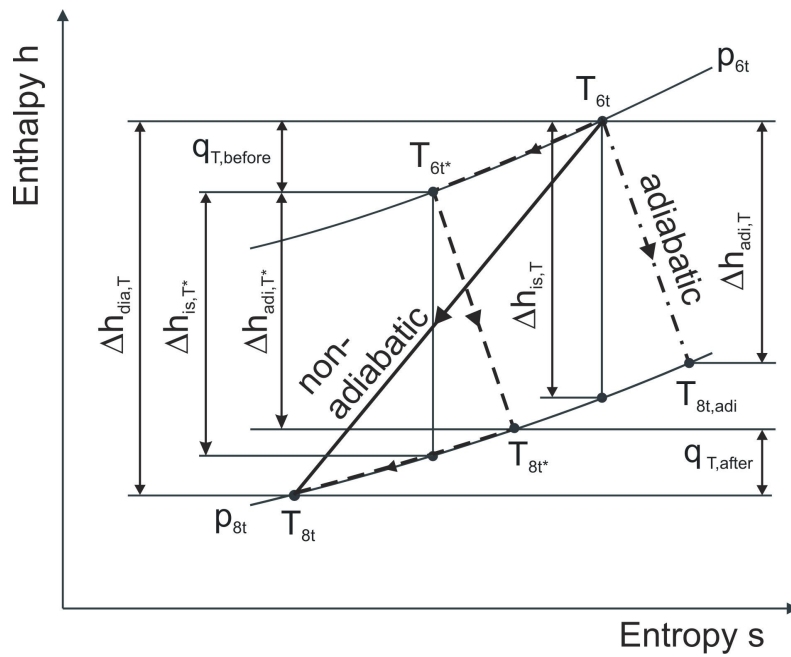


Figure A-9 Schematic h-s diagram of the expansion process in a non-adiabatic turbine

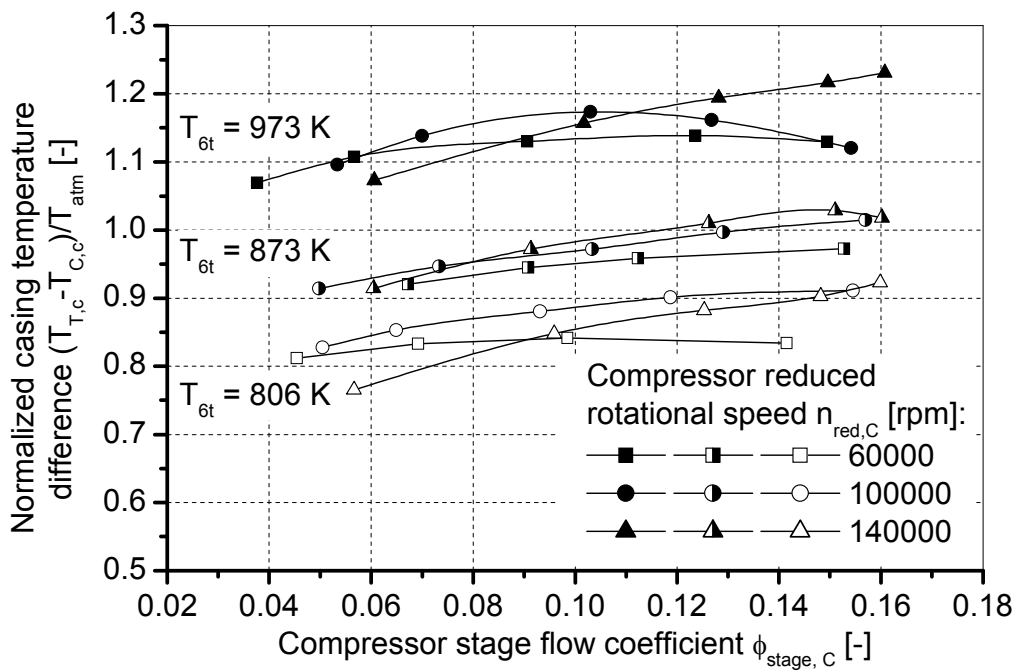


Figure A-10 Temperature difference between the turbine casing and the compressor casing of the GT1749V 55 Trim compressor

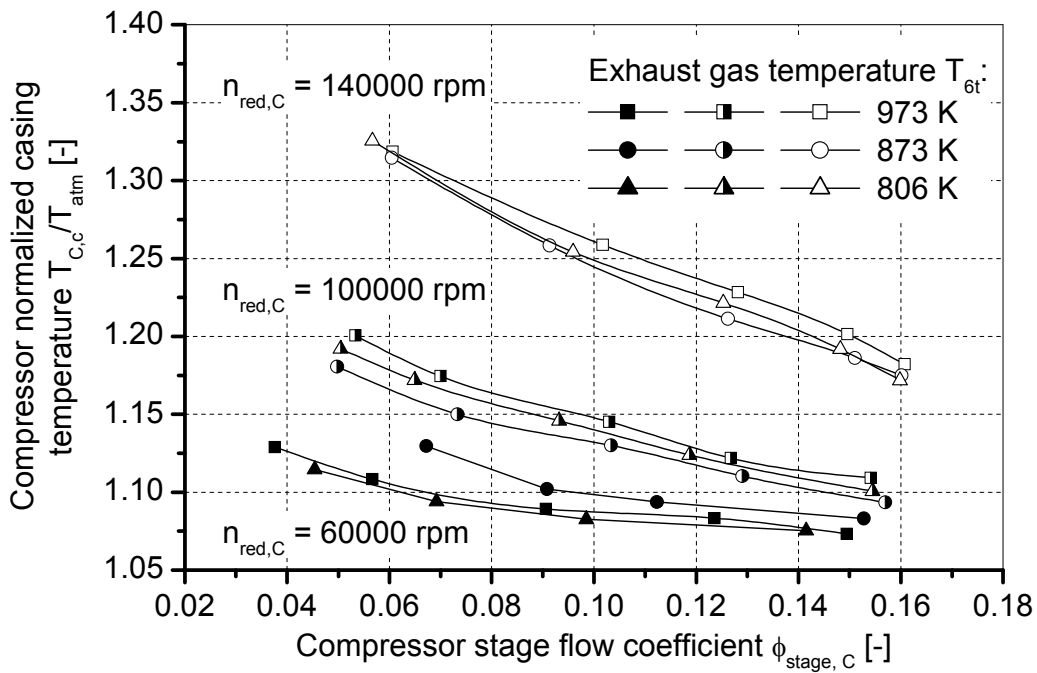


Figure A-11 Normalized compressor casing temperature of the GT1749V 55 Trim compressor

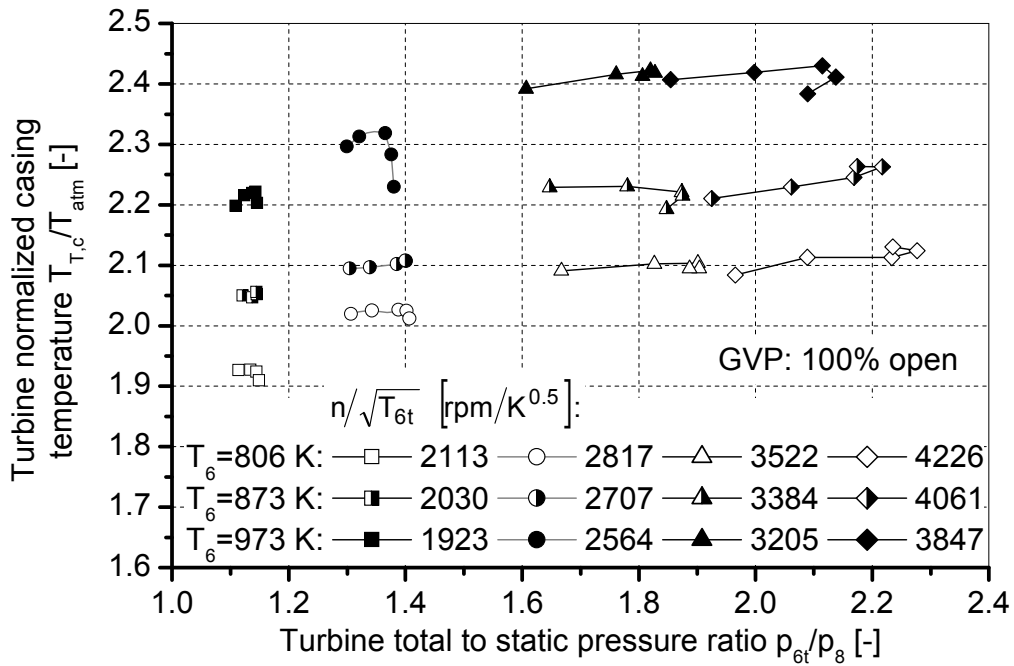


Figure A-12 Normalized turbine casing temperature of the GT1749V 55 Trim turbocharger

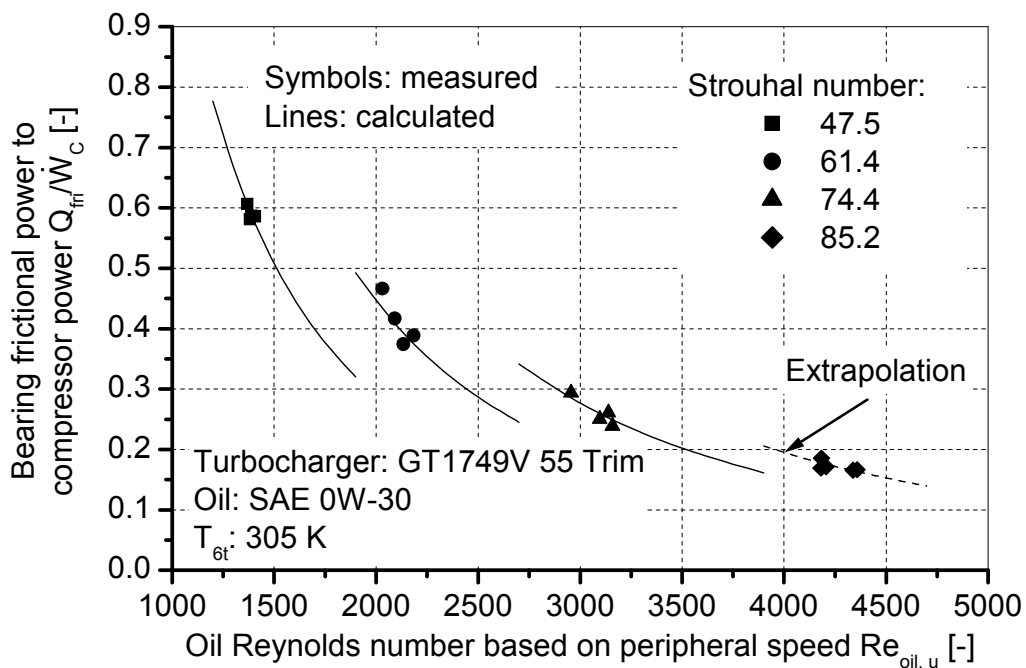


Figure A-13 Comparison between the measured and the calculated ratio of the bearing frictional power to the compressor power of the GT1749V 55 Trim turbocharger

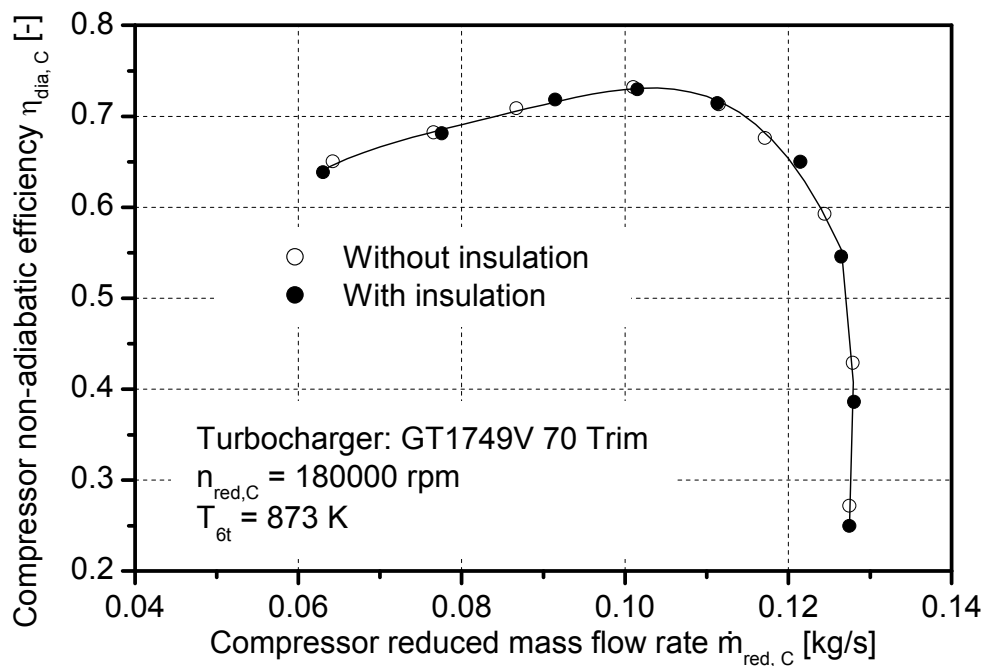


Figure A-14 Non-adiabatic Compressor efficiency of the GT1749V 70 Trim turbocharger with insulation and without insulation

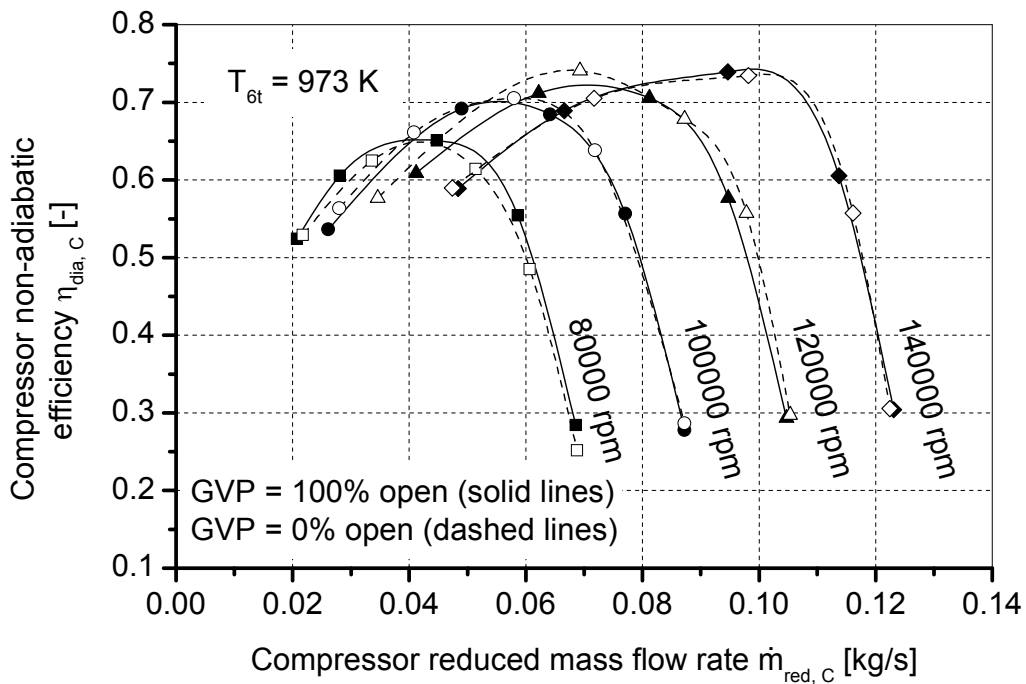


Figure A-15 comparison of the measured compressor non-adiabatic efficiency at turbine inlet guide-vane positions 100% open and 0% open and exhaust gas temperature at the turbine entry of 973 K

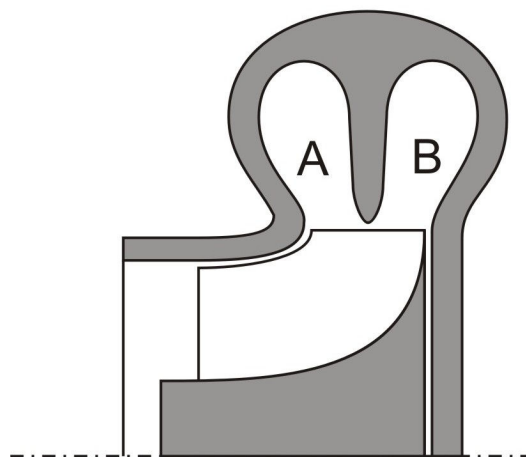


Figure A-16 Schematic diagram of the K29 twin entry turbine

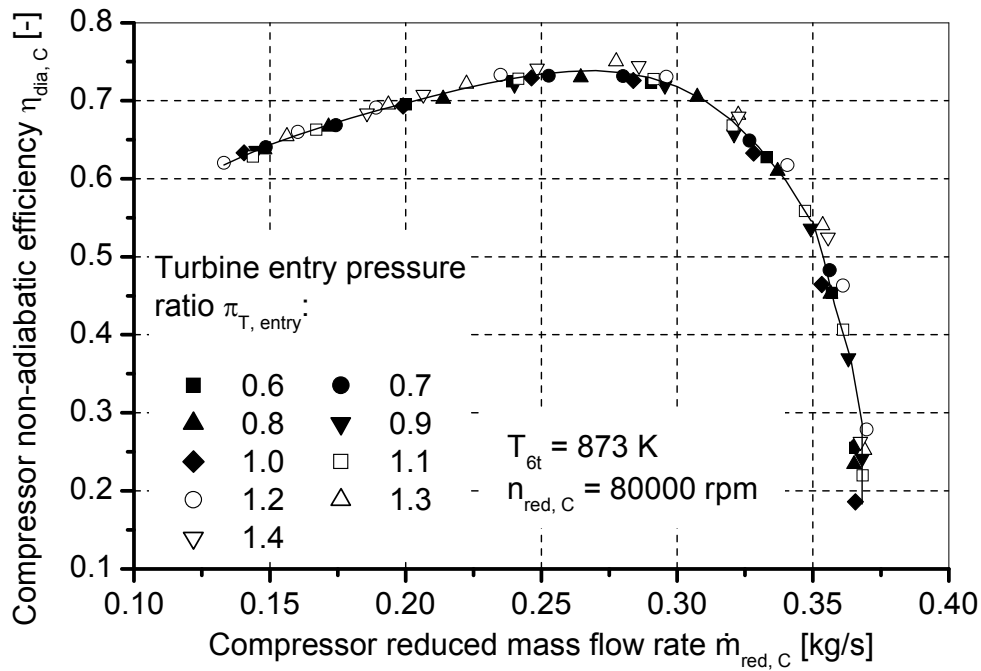


Figure A-17 Effect of the turbine entry pressure ratio on the measured compressor efficiency of the K29 turbocharger

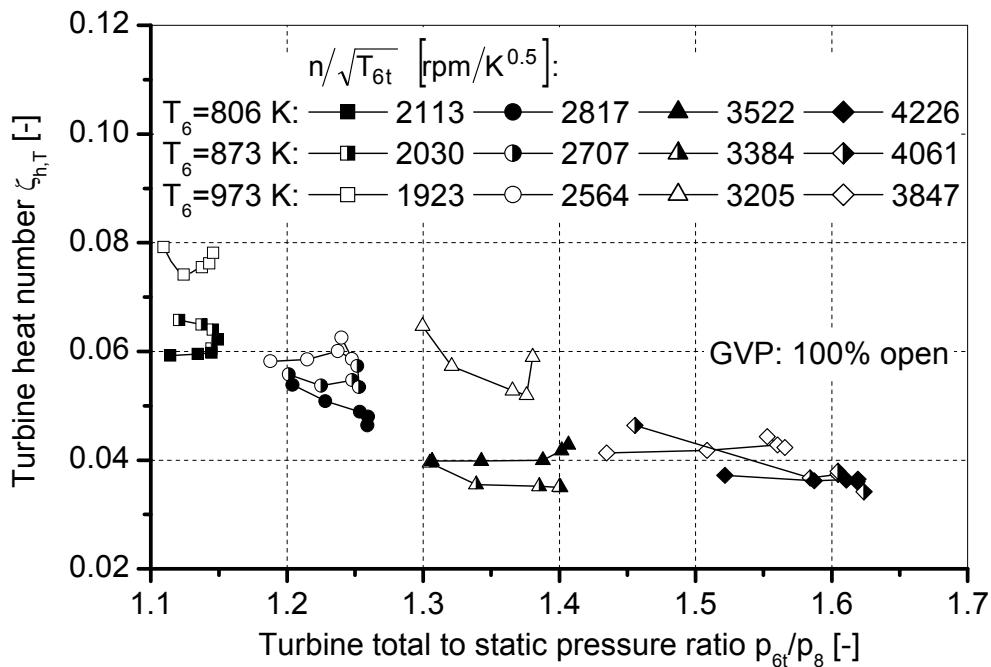


Figure A-18 Variation of the turbine heat number with the turbine total-to-static pressure ratio at different values of the turbine rotational speed parameter and exhaust gas temperatures at the turbine entry of the GT1749V 55 Trim turbine

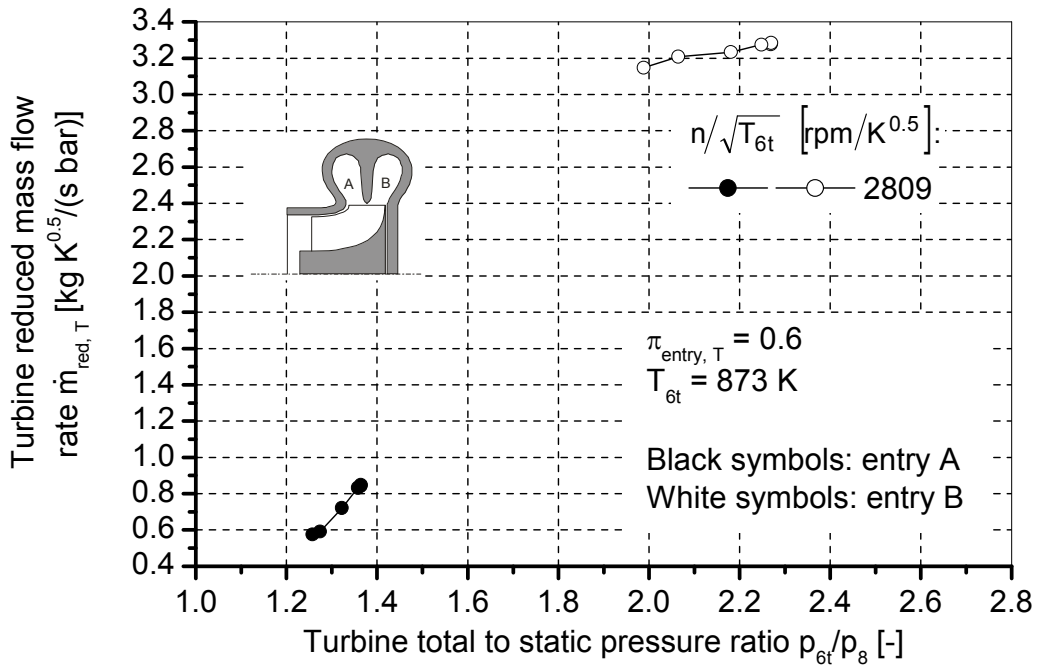


Figure A-19 Variation of the reduced mass flow rate with the turbine total-to-static pressure ratio of the K29 turbine at entry pressure ratio 0.6

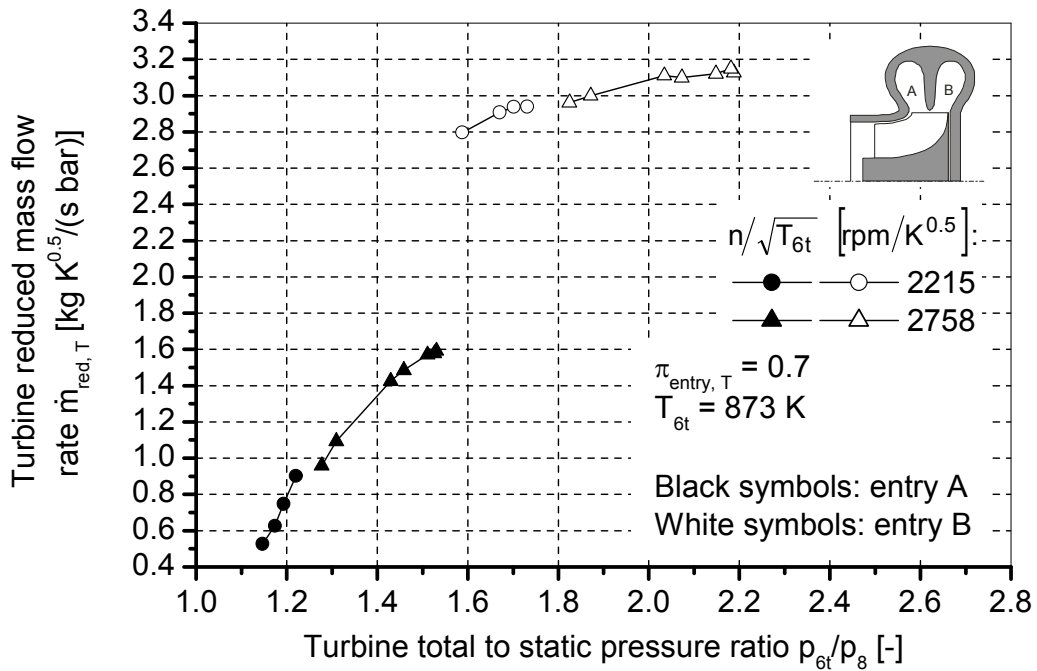


Figure A-20 Variation of the reduced mass flow rate with the turbine total-to-static pressure ratio of the K29 turbine at entry pressure ratio 0.7

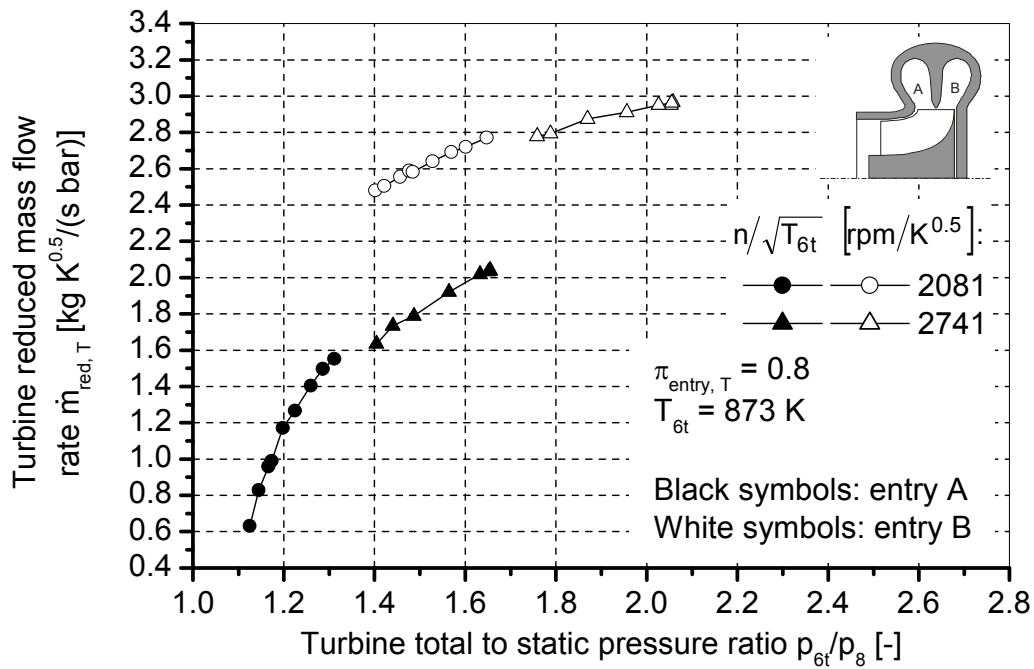


Figure A-21 Variation of the reduced mass flow rate with the turbine total-to-static pressure ratio of the K29 turbine at entry pressure ratio 0.8

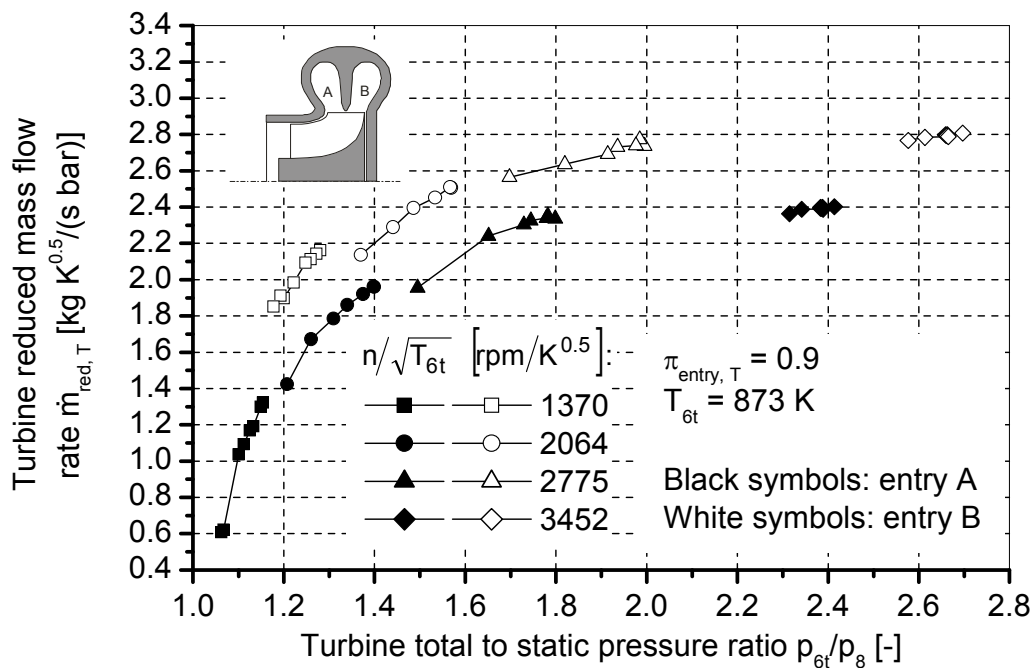


Figure A-22 Variation of the reduced mass flow rate with the turbine total-to-static pressure ratio of the K29 turbine at entry pressure ratio 0.9

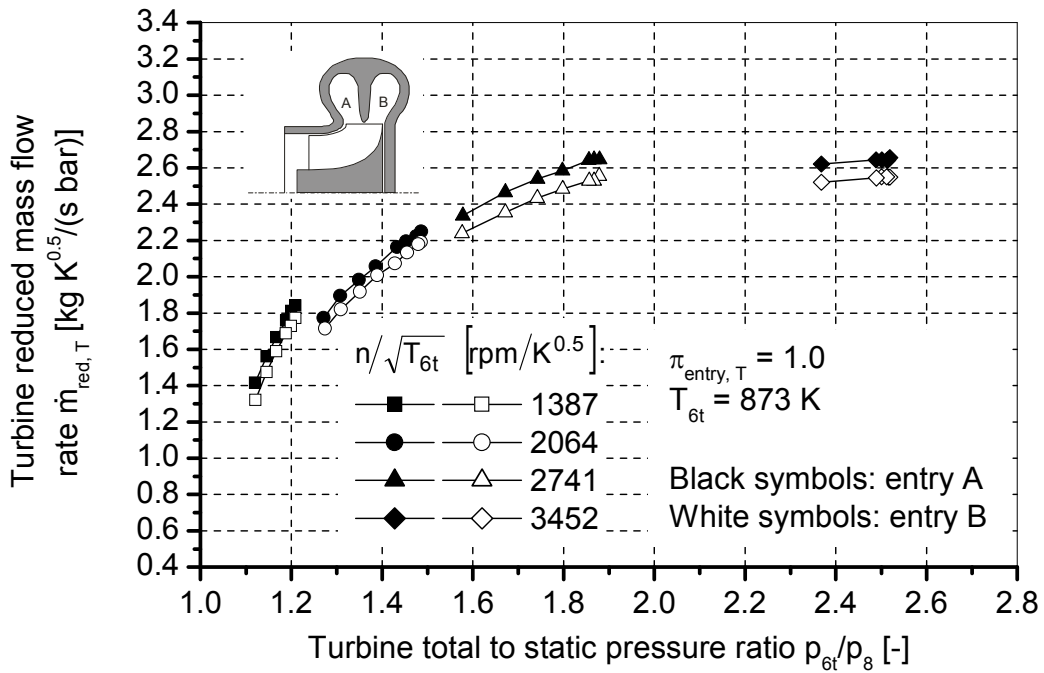


Figure A-23 Variation of the reduced mass flow rate with the turbine total-to-static pressure ratio of the K29 turbine at entry pressure ratio 1.0

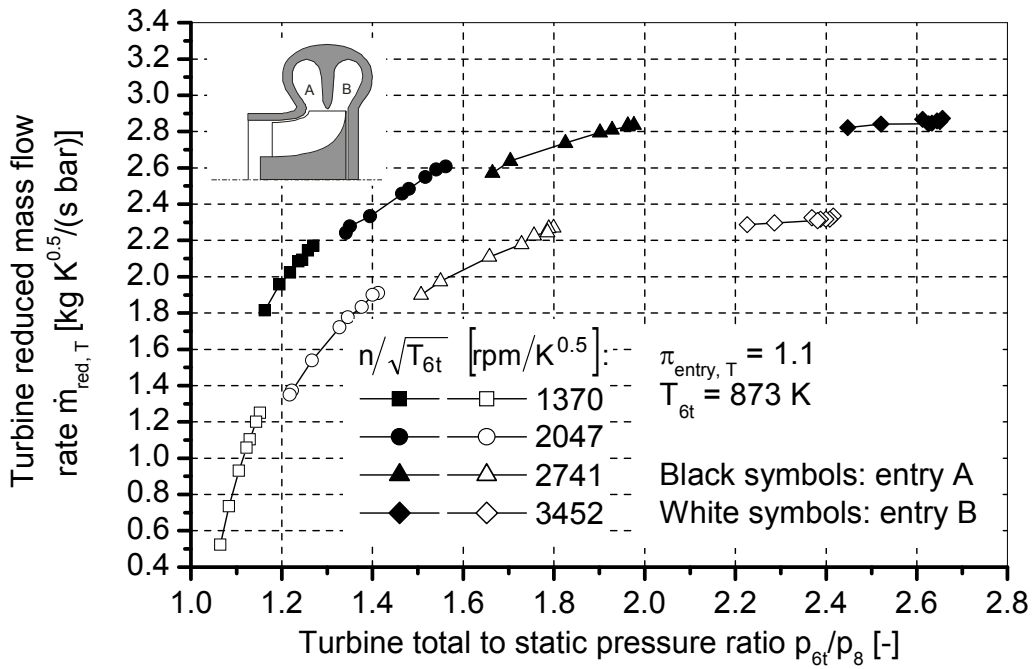


Figure A-24 Variation of the reduced mass flow rate with the turbine total-to-static pressure ratio of the K29 turbine at entry pressure ratio 1.1

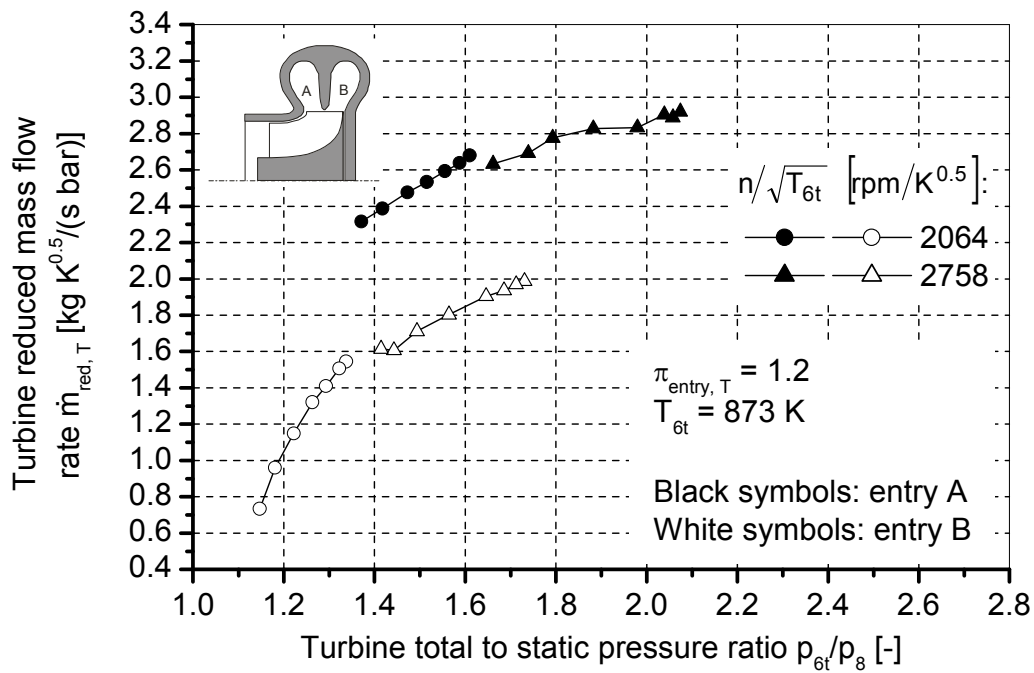


Figure A-25 Variation of the reduced mass flow rate with the turbine total-to-static pressure ratio of the K29 turbine at entry pressure ratio 1.2

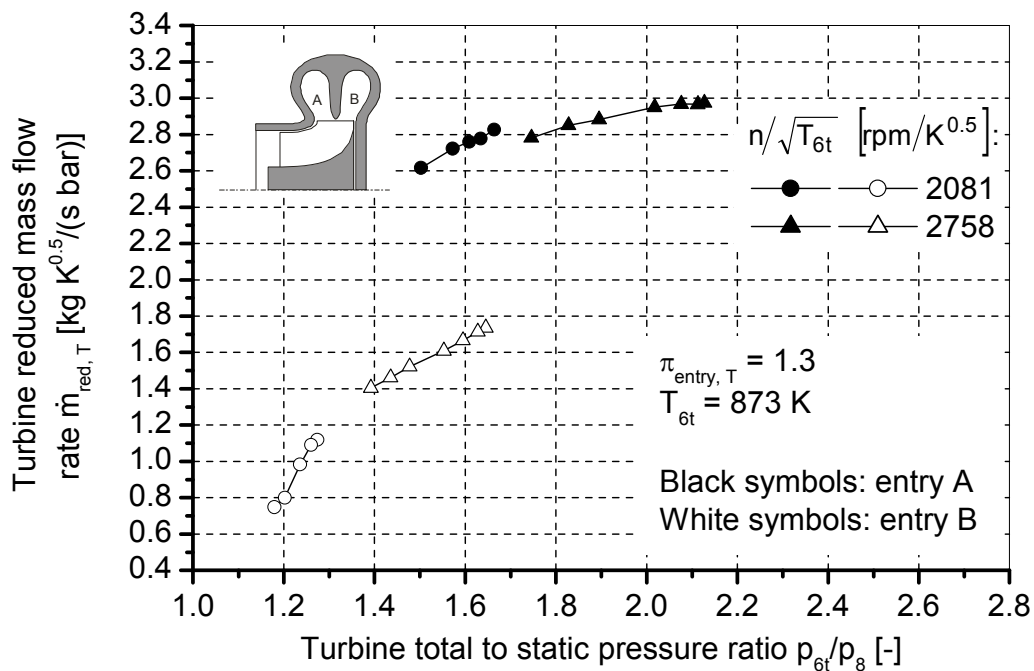


Figure A-26 Variation of the reduced mass flow rate with the turbine total-to-static pressure ratio of the K29 turbine at entry pressure ratio 1.3

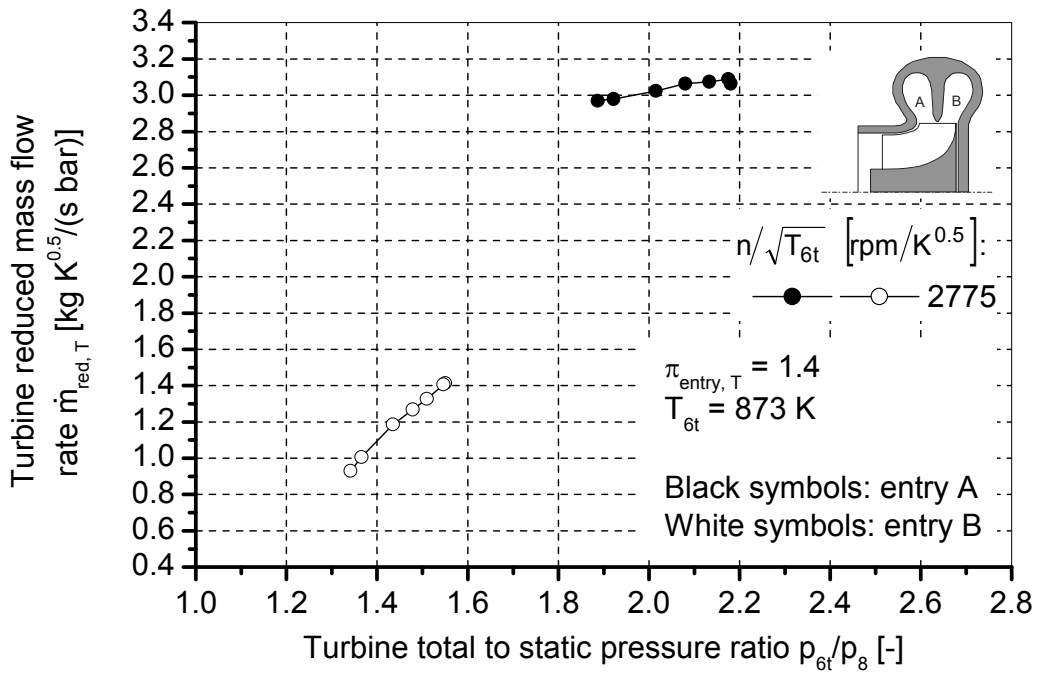


Figure A-27 Variation of the reduced mass flow rate with the turbine total-to-static pressure ratio of the K29 turbine at entry pressure ratio 1.4

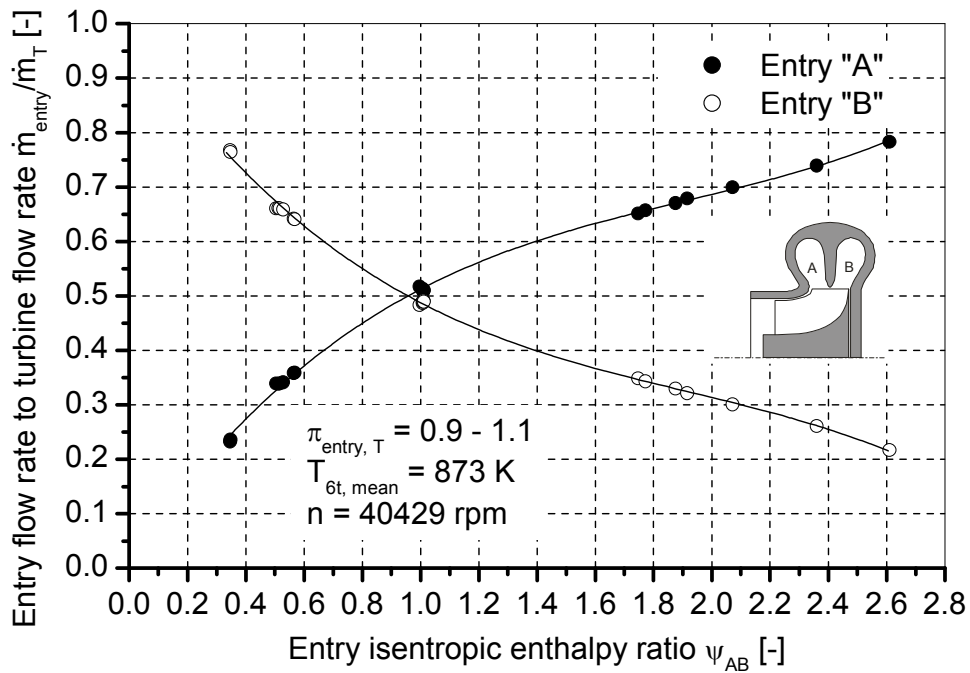


Figure A-28 Ratio of the entry flow rate to the total turbine mass flow rate of the K29 turbine as a function of the entry isentropic pressure ratio at turbocharger rotational speed 40429 rpm

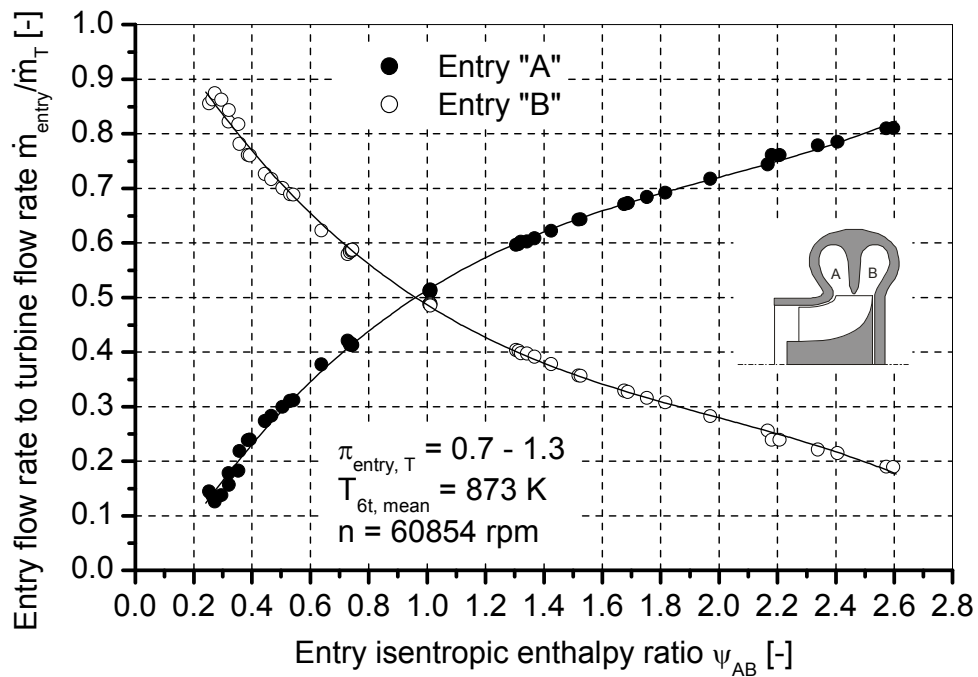


Figure A-29 Ratio of the entry flow rate to the total turbine mass flow rate of the K29 turbine as a function of the entry isentropic pressure ratio at turbocharger rotational speed 60854 rpm

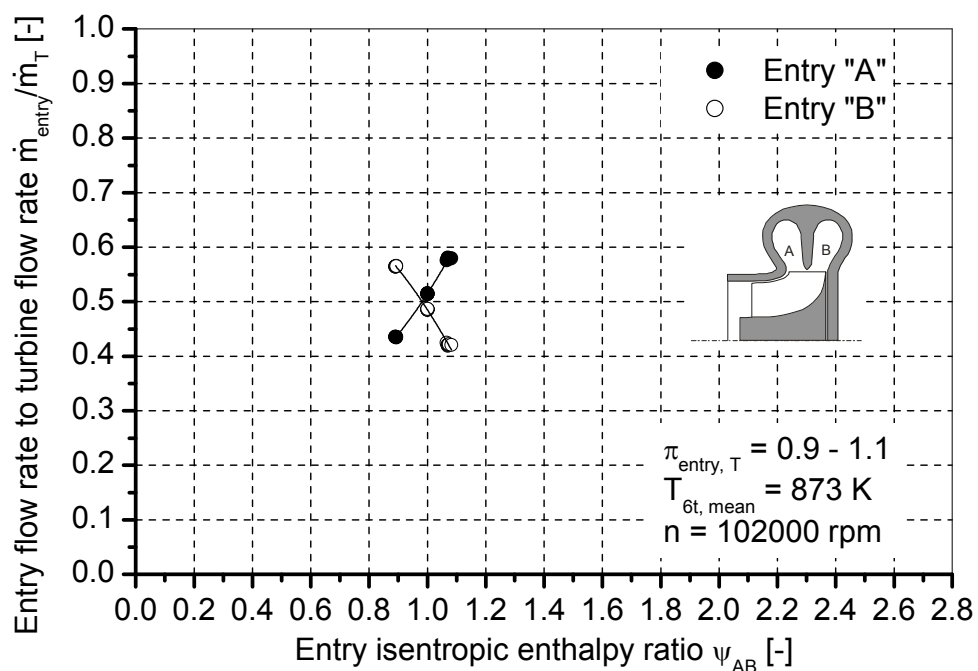


Figure A-30 Ratio of the entry flow rate to the total turbine mass flow rate of the K29 turbine as a function of the entry isentropic pressure ratio at turbocharger rotational speed 102000 rpm

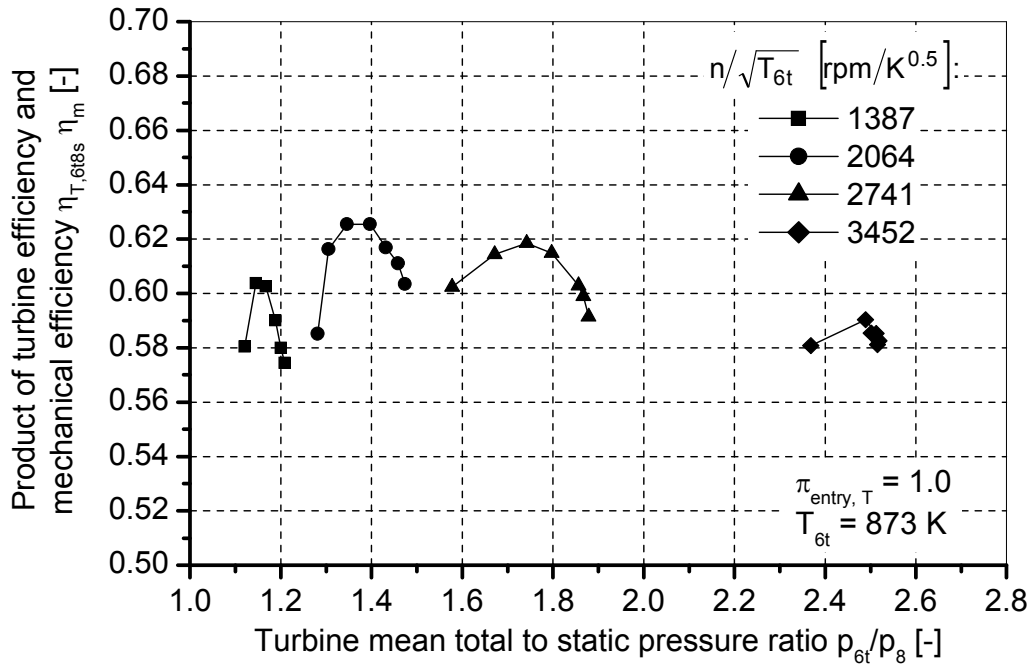


Figure A-31 Variation of the product of the turbine efficiency and the mechanical efficiency of the K29 turbocharger with the mean total-to-static pressure ratio at different values of the turbine rotational speed parameter and entry pressure ratio 1.0

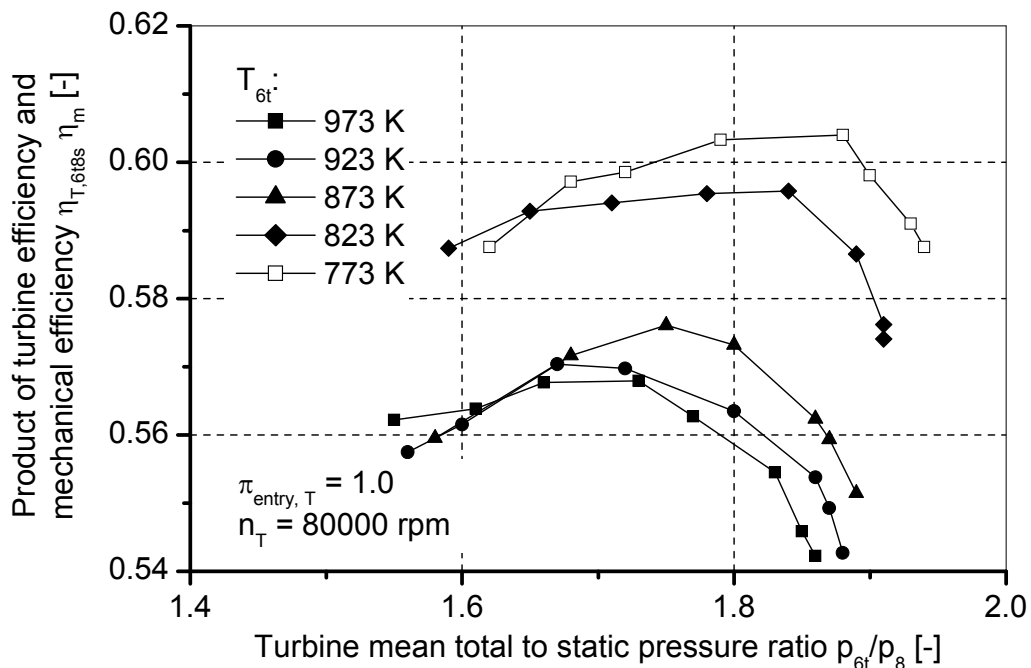


Figure A-32 Product of the turbine efficiency and the mechanical efficiency of the K29 turbine at different exhaust gas temperatures at the turbine entry

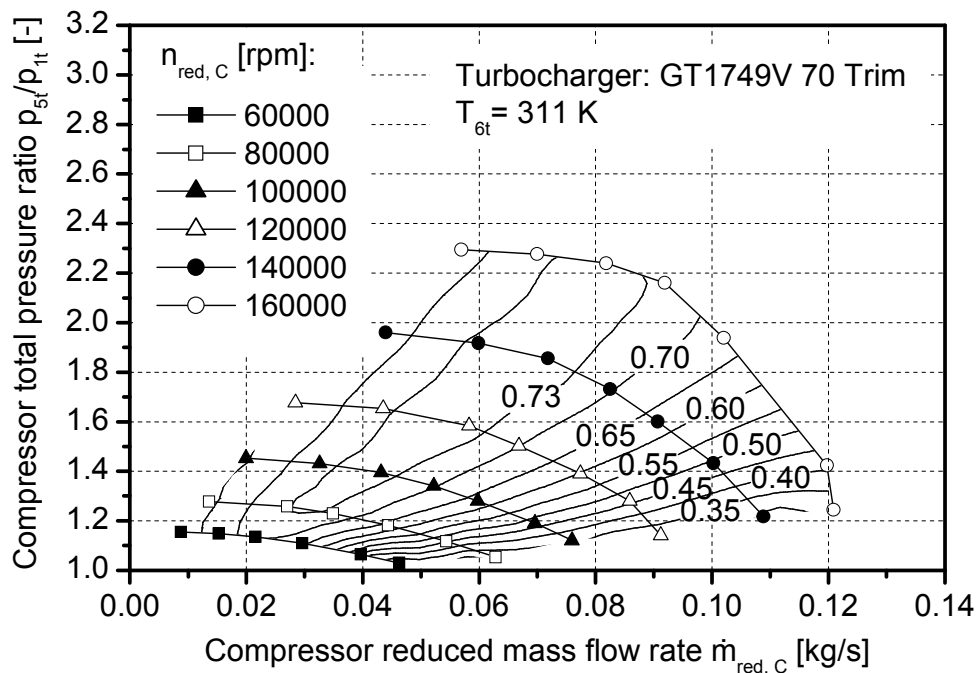


Figure A-33 Measured performance map of the GT1749V 70 Trim compressor at exhaust gas temperature at the turbine entry $T_{6t} = 311$ K

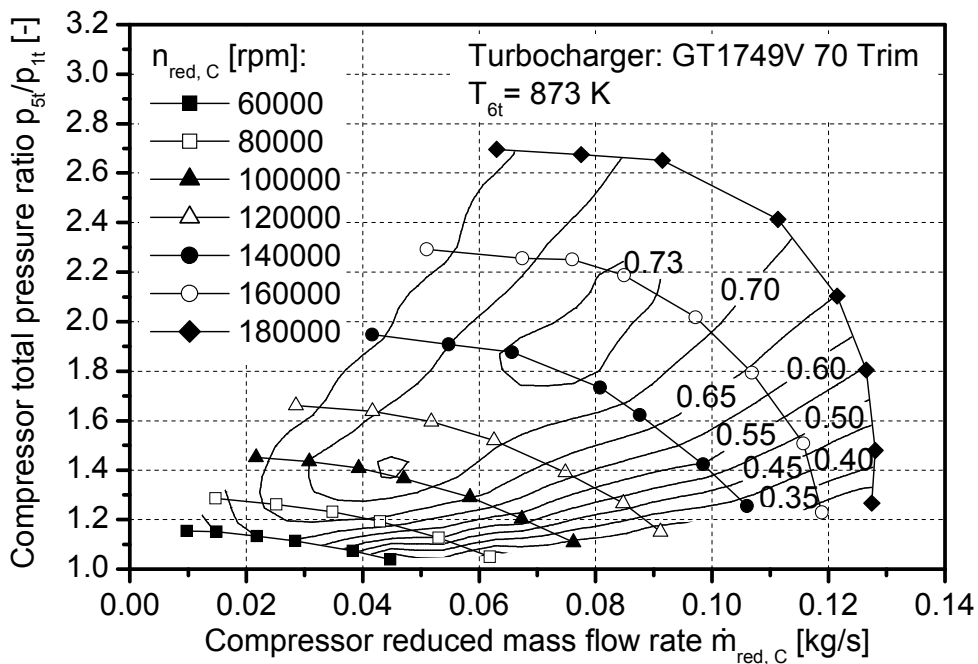


Figure A-34 Measured performance map of the GT1749V 70 Trim compressor at exhaust gas temperature at the turbine entry $T_{6t} = 873$ K

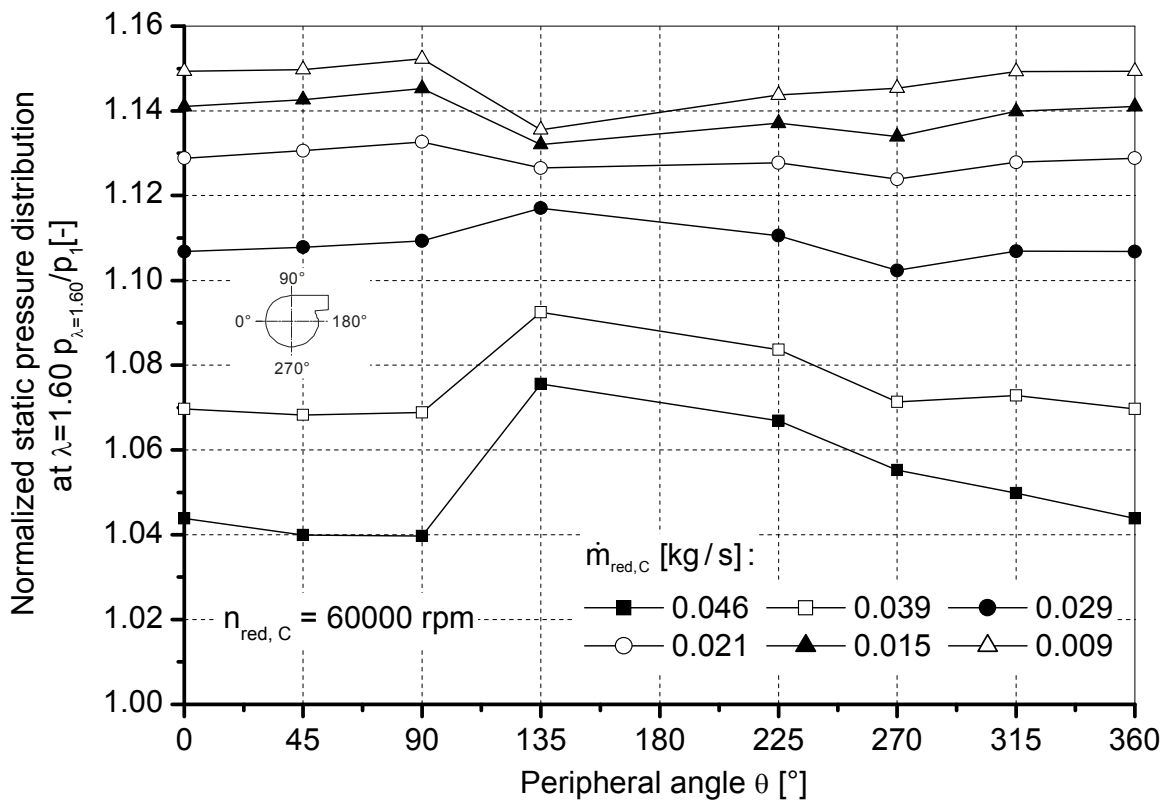
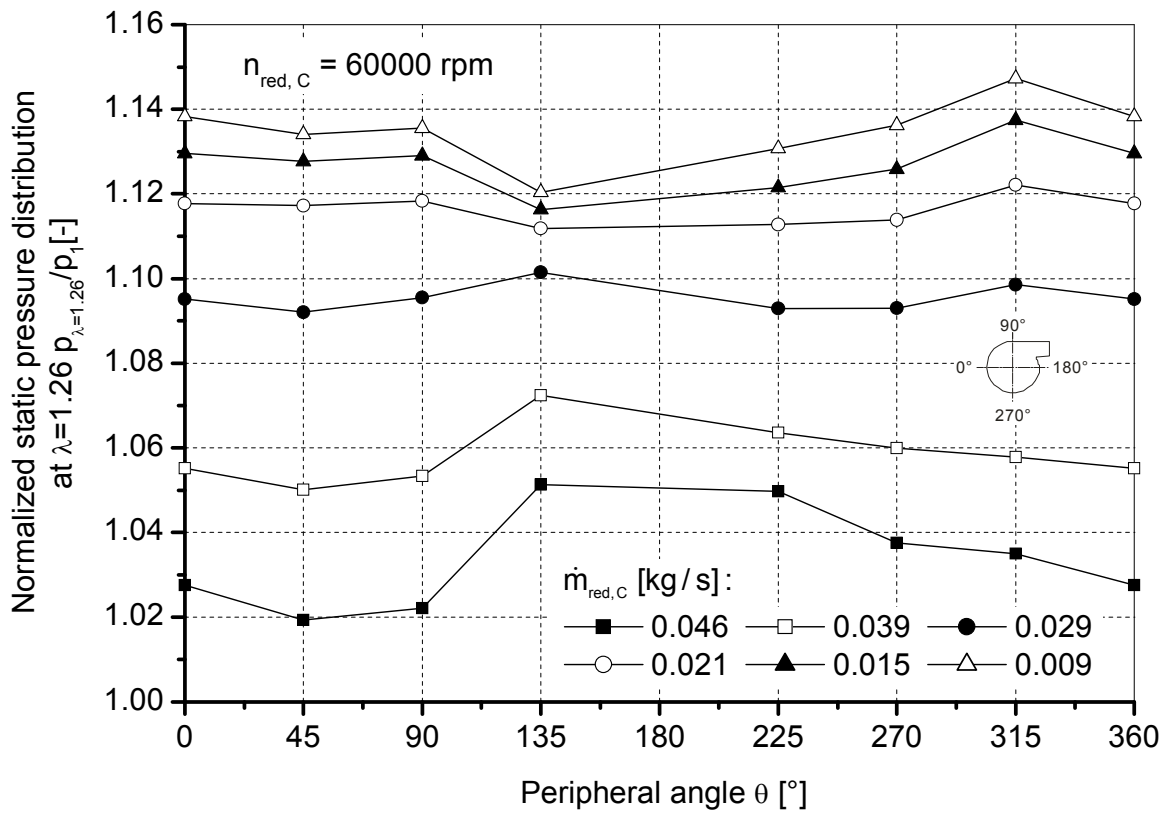


Figure A-35 Diffuser static pressure distribution at diameter ratios $\lambda=1.26$ and 1.6 for the GT1749V 70 Trim compressor at 60000 rpm

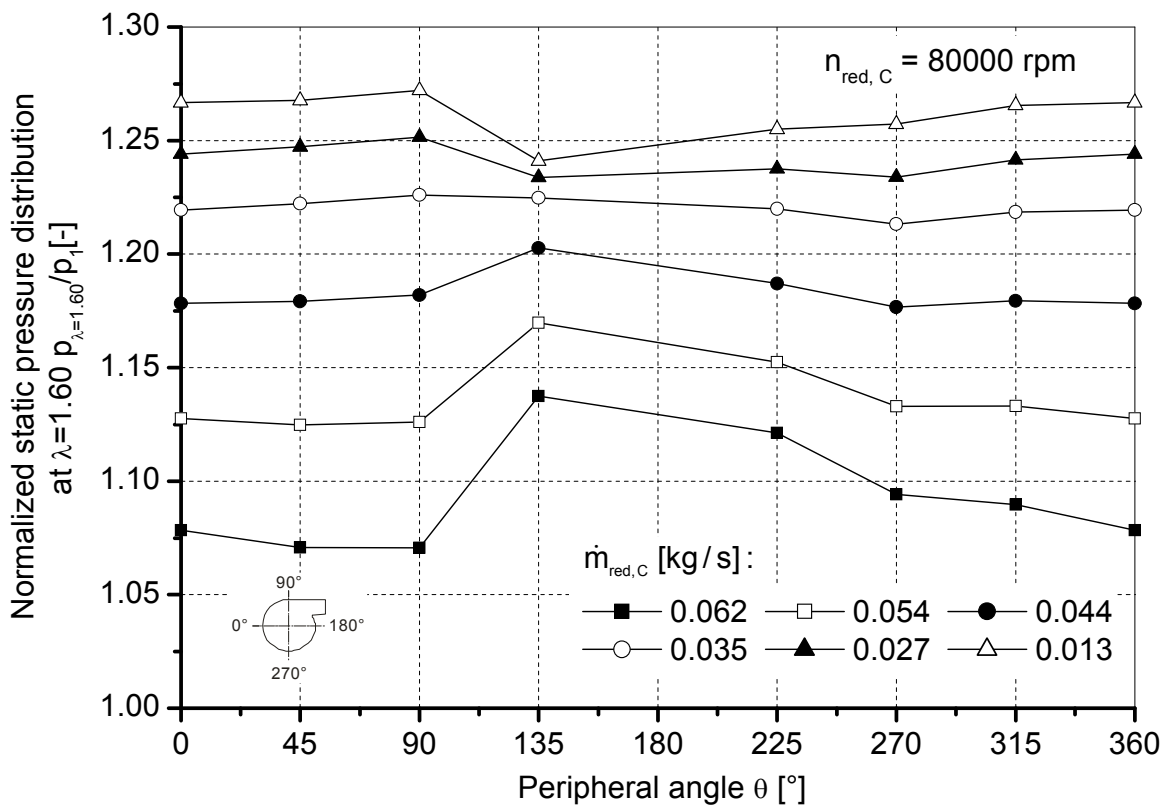
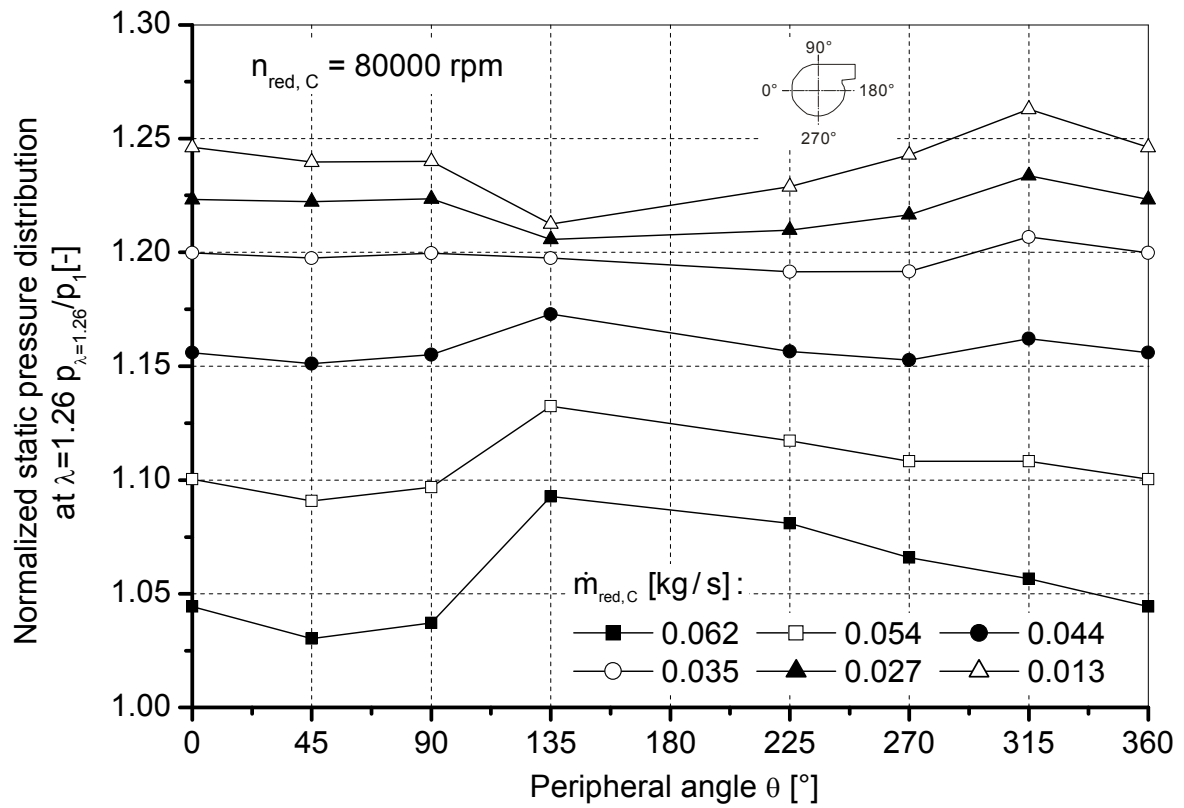


Figure A-36 Diffuser static pressure distribution at diameter ratios $\lambda=1.26$ and 1.6 for the GT1749V 70 Trim compressor at 80000 rpm

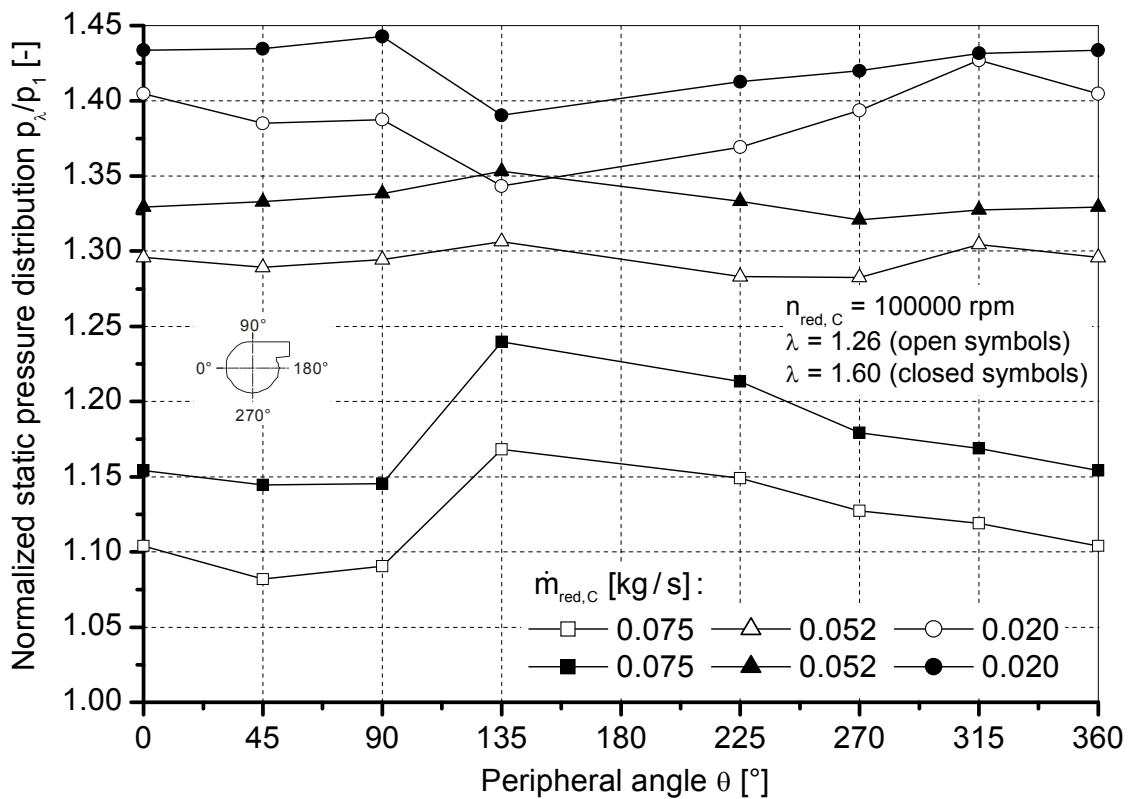
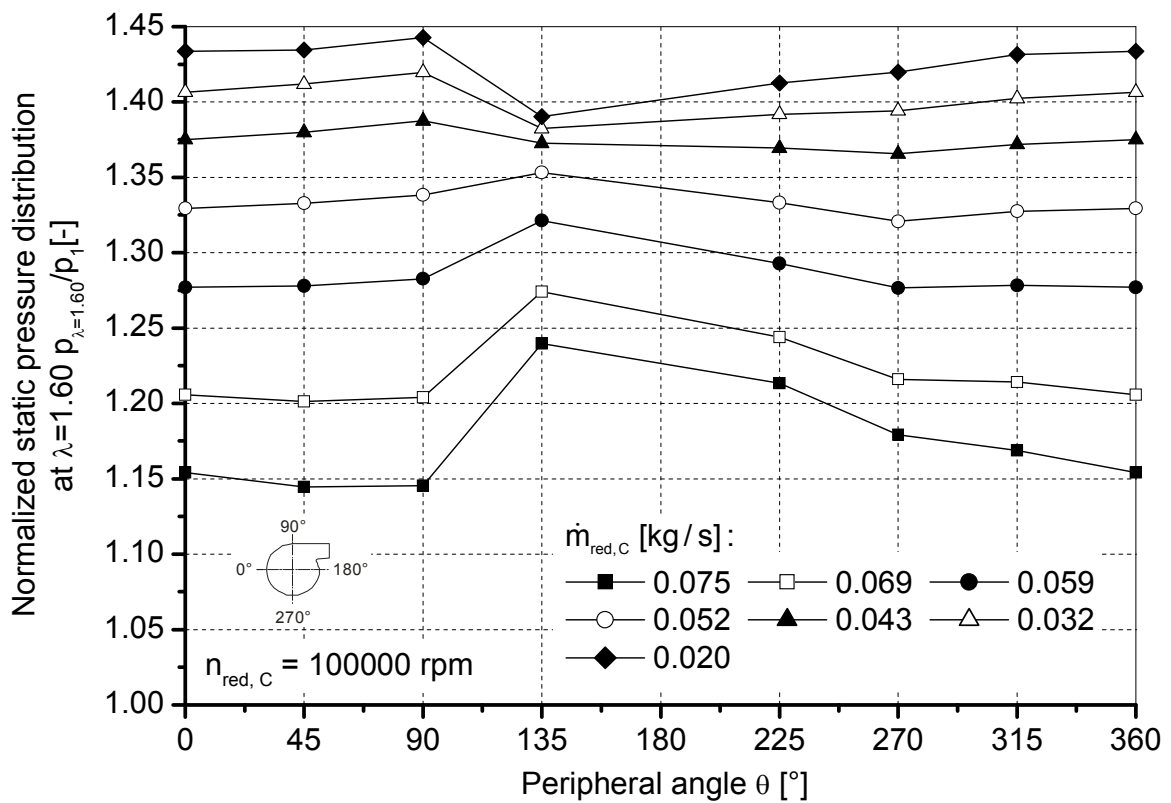


Figure A-37 Diffuser static pressure distribution at diameter ratios $\lambda=1.26$ and 1.6 for the GT1749V 70 Trim compressor at 100000 rpm

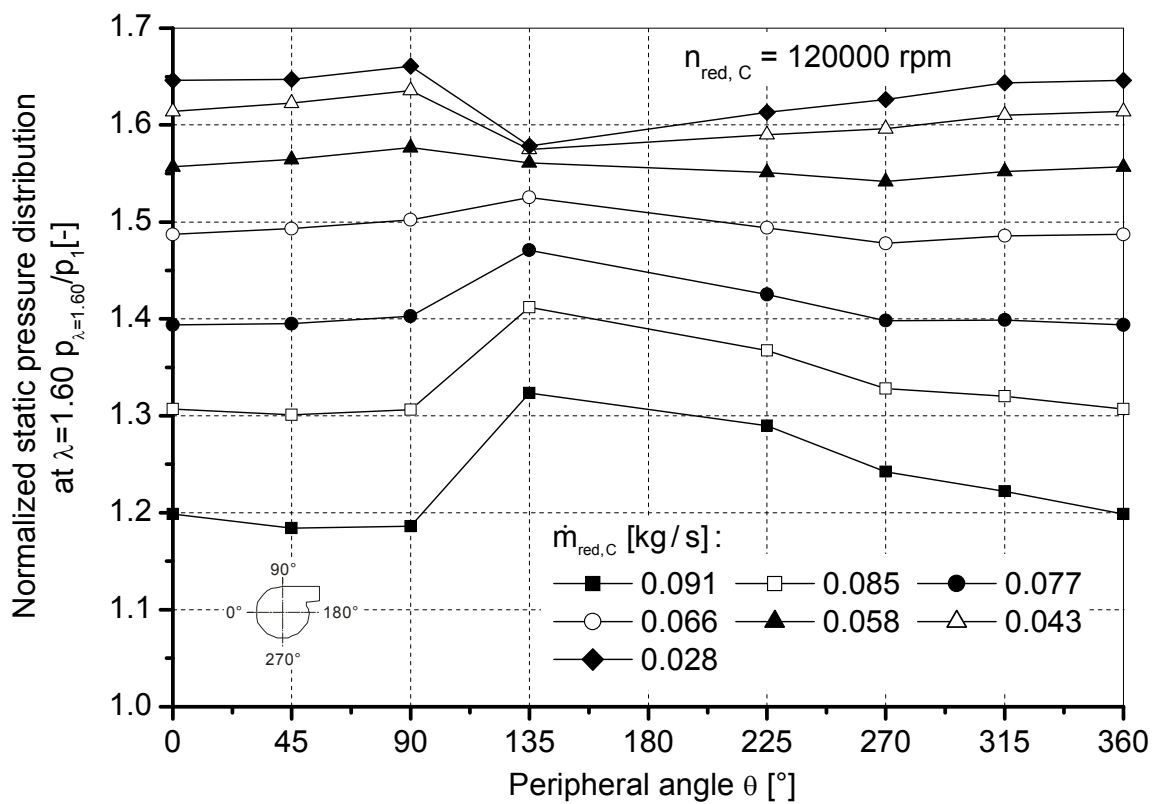
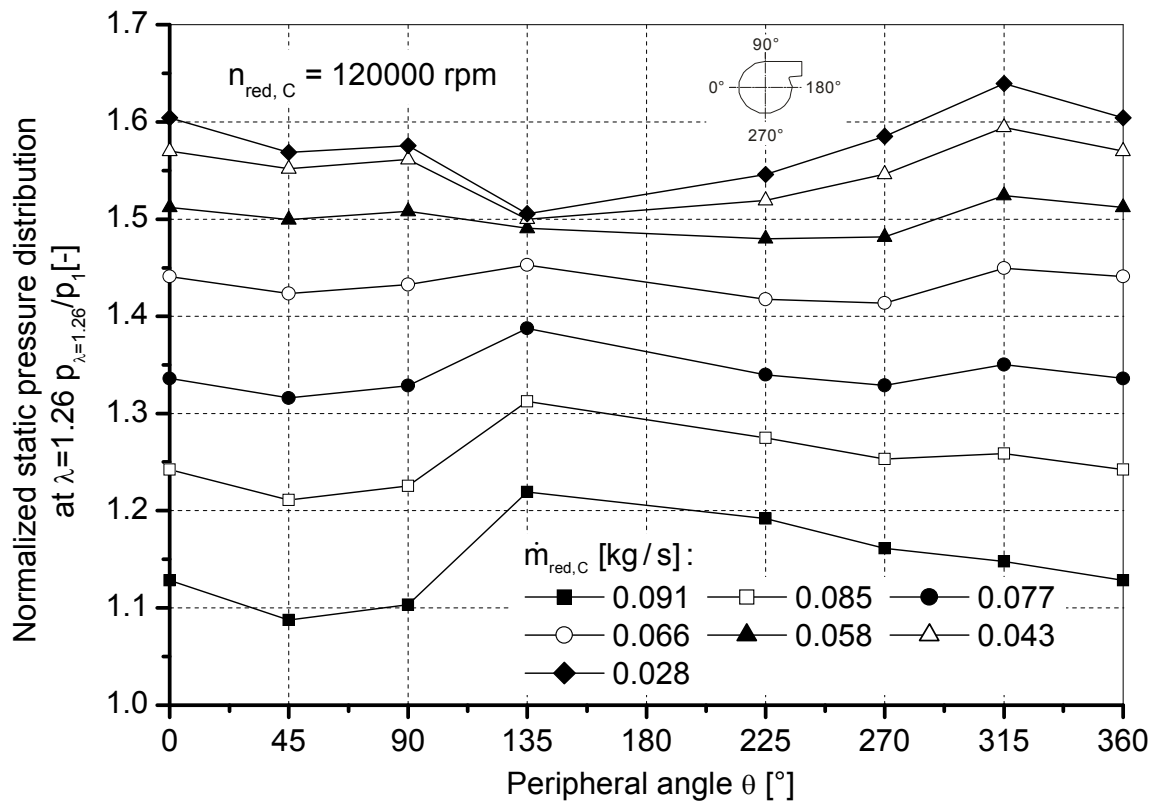


Figure A-38 Diffuser static pressure distribution at diameter ratios $\lambda=1.26$ and 1.6 for the GT1749V 70 Trim compressor at 120000 rpm

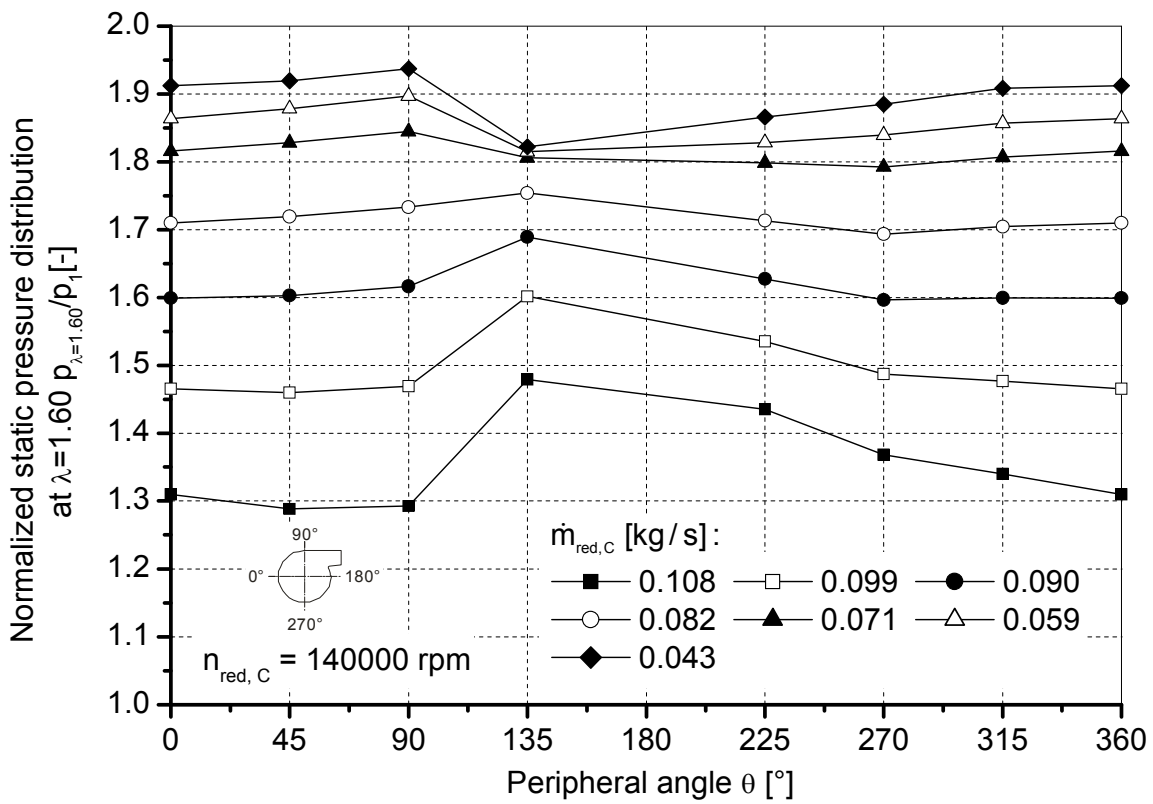
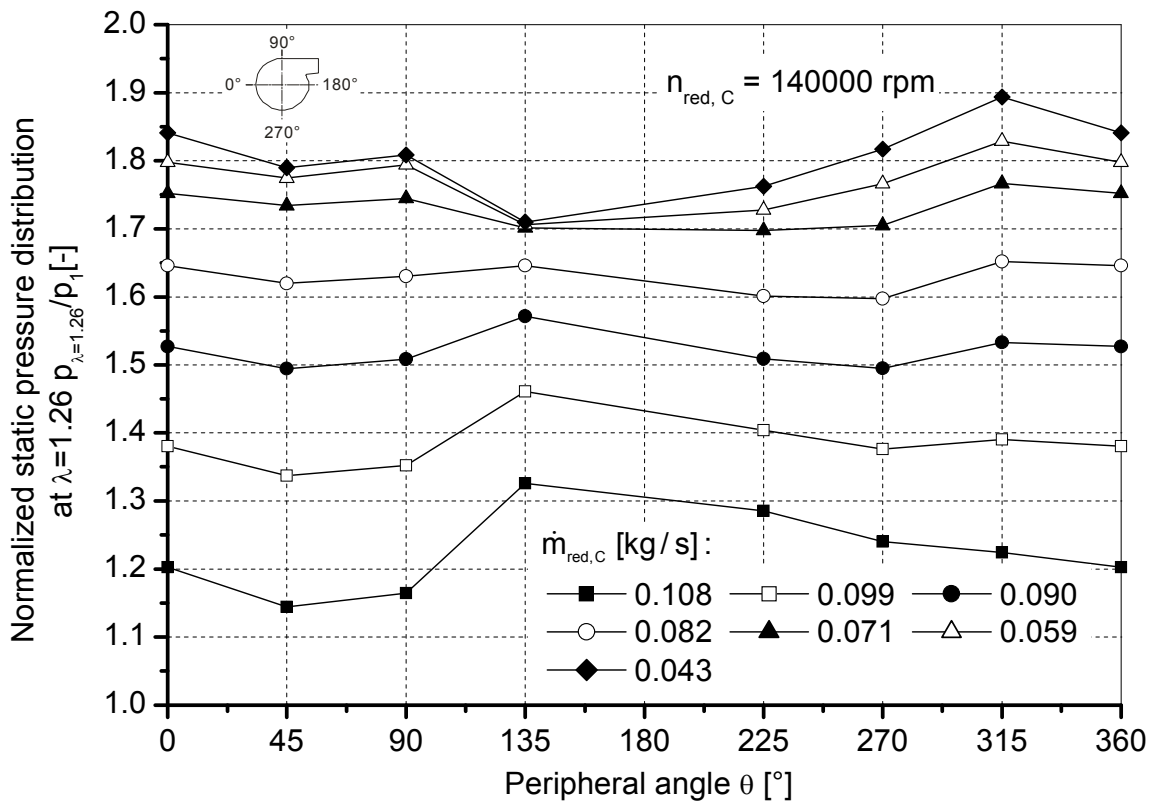


Figure A-39 Diffuser static pressure distribution at diameter ratios $\lambda=1.26$ and 1.6 for the GT1749V 70 Trim compressor at 140000 rpm

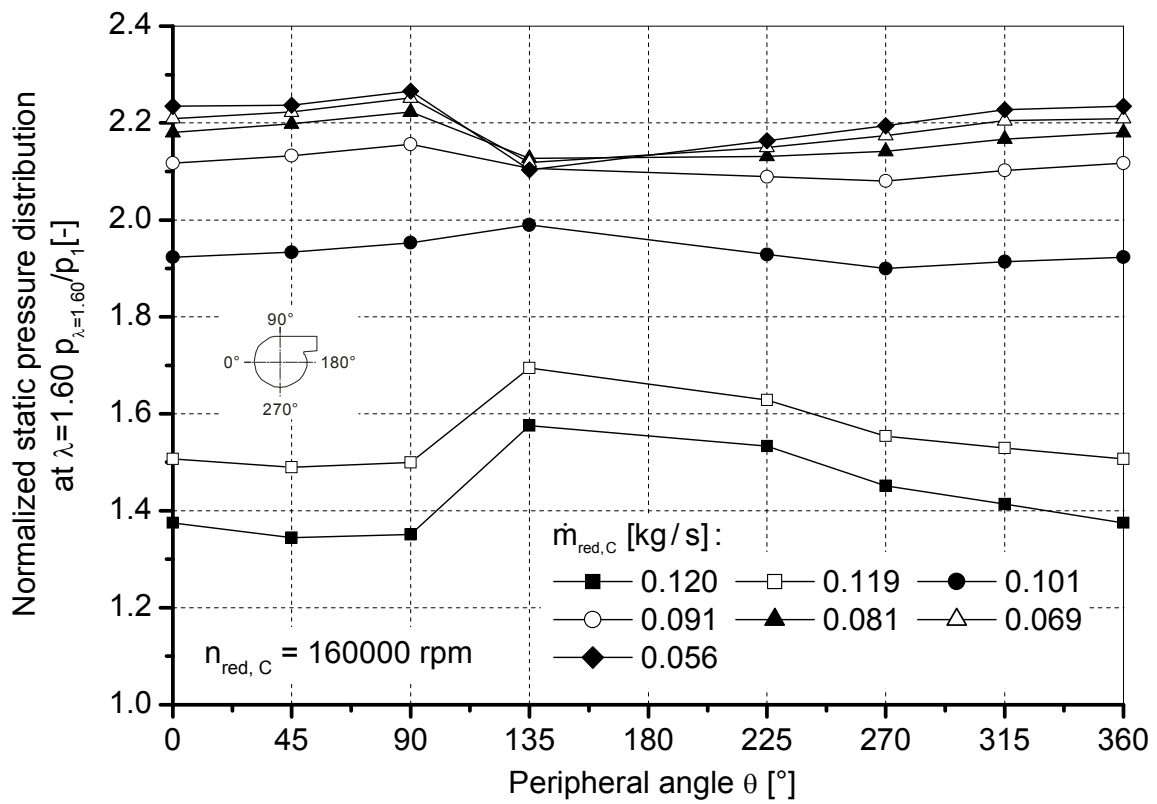
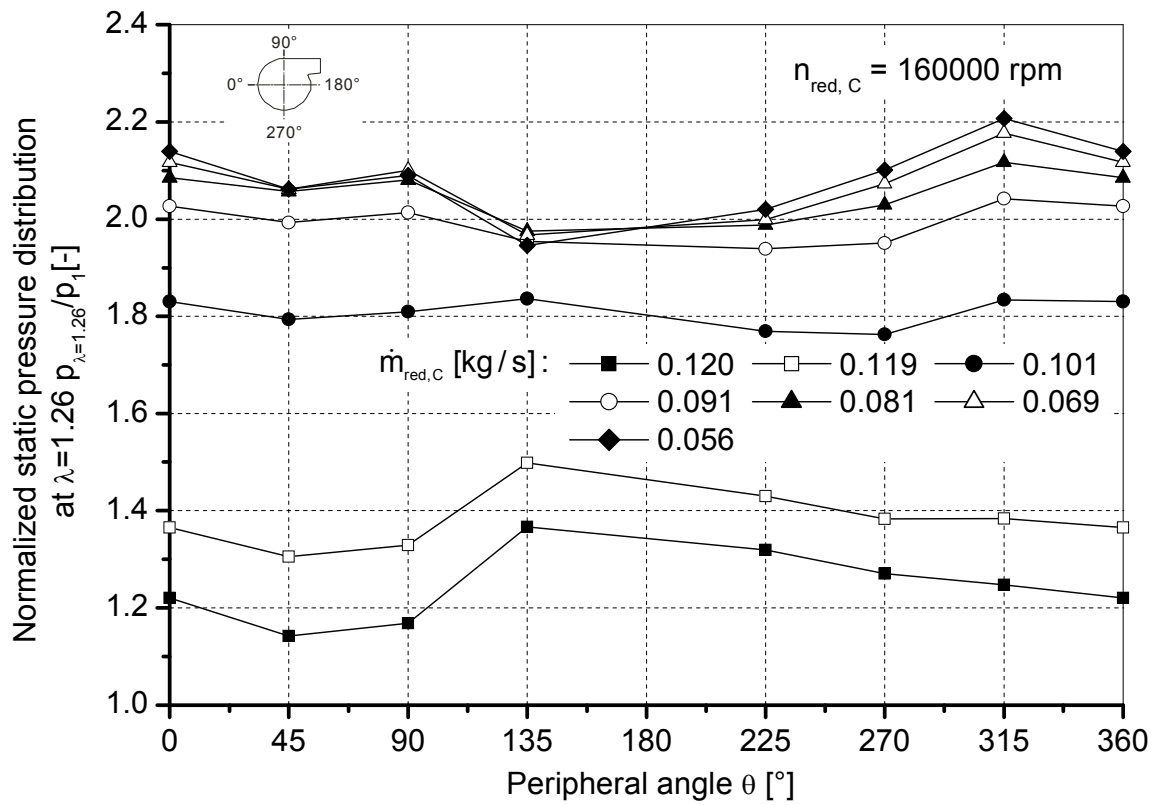


Figure A-40 Diffuser static pressure distribution at diameter ratios $\lambda=1.26$ and 1.6 for the GT1749V 70 Trim compressor at 160000 rpm

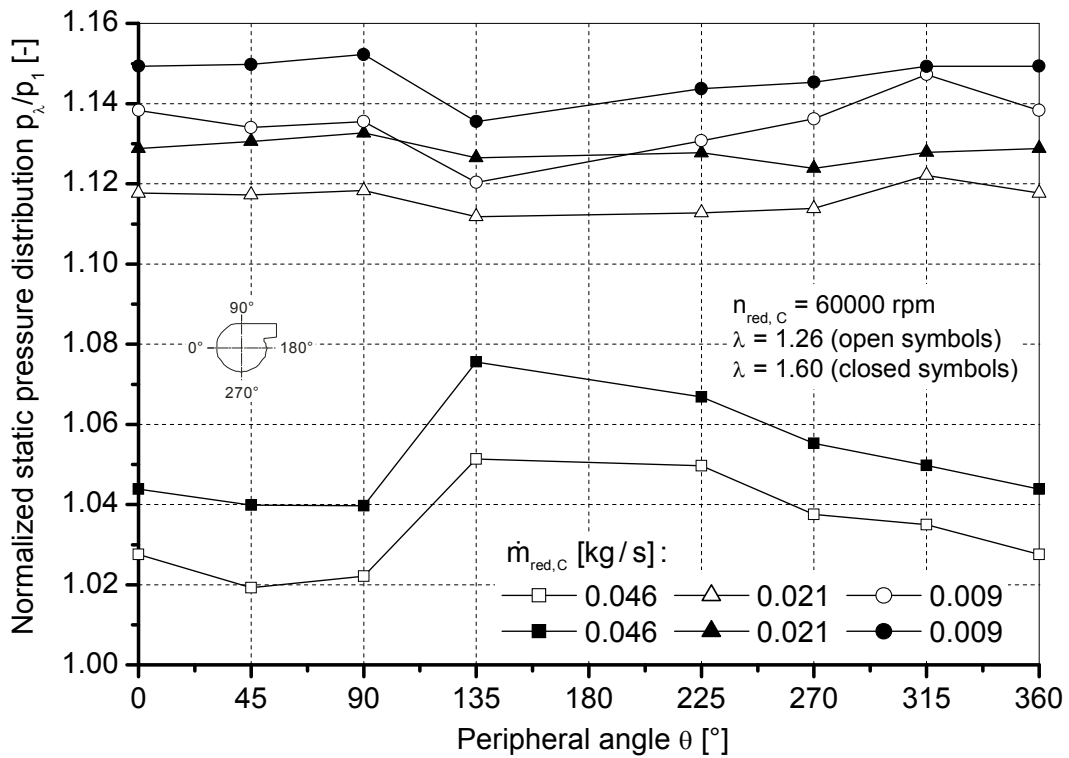


Figure A-41 Comparison between the static pressure distribution at diameter ratios $\lambda = 1.26$ and 1.6 for the GT1749V 70 Trim compressor at 60000 rpm

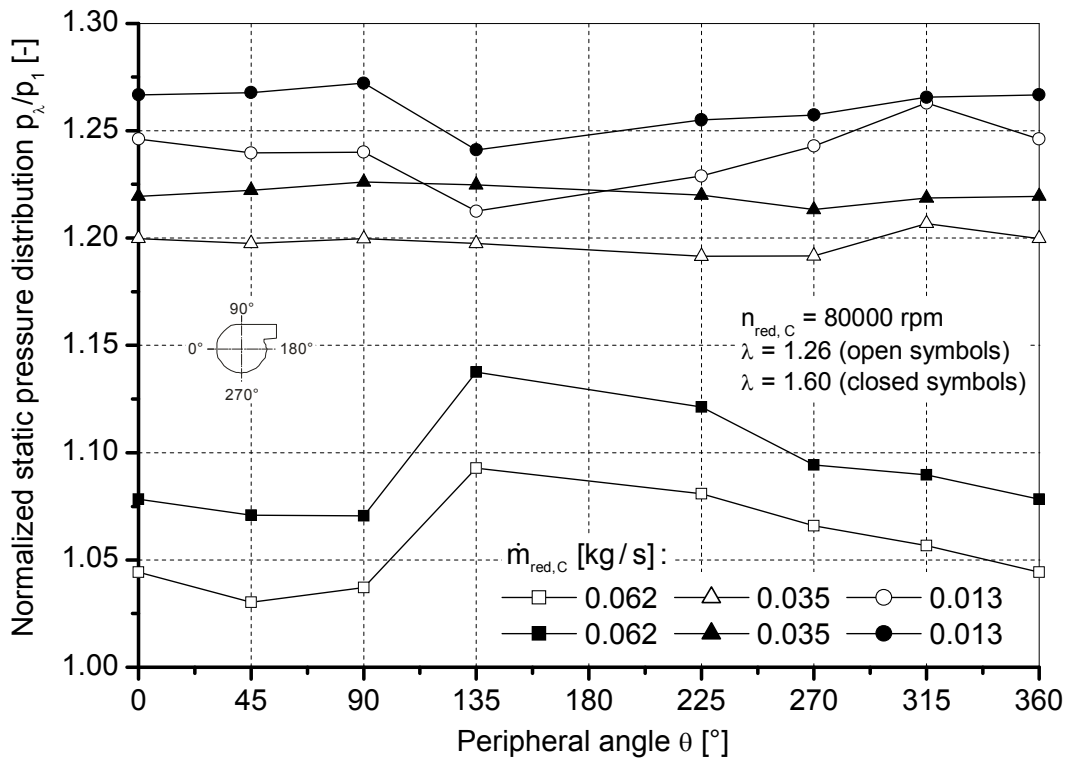


Figure A-42 Comparison between the static pressure distribution at diameter ratios $\lambda = 1.26$ and 1.6 for the GT1749V 70 Trim compressor at 80000 rpm

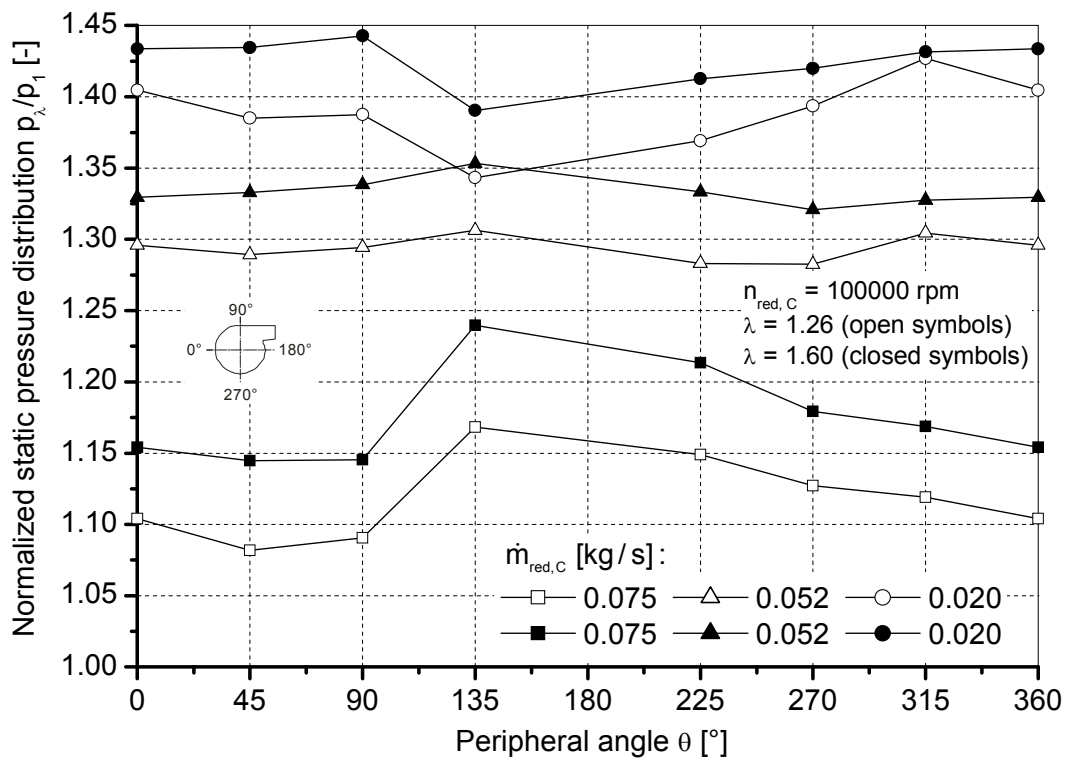


Figure A-43 Comparison between the static pressure distribution at diameter ratios $\lambda = 1.26$ and 1.6 for the GT1749V 70 Trim compressor at 100000 rpm

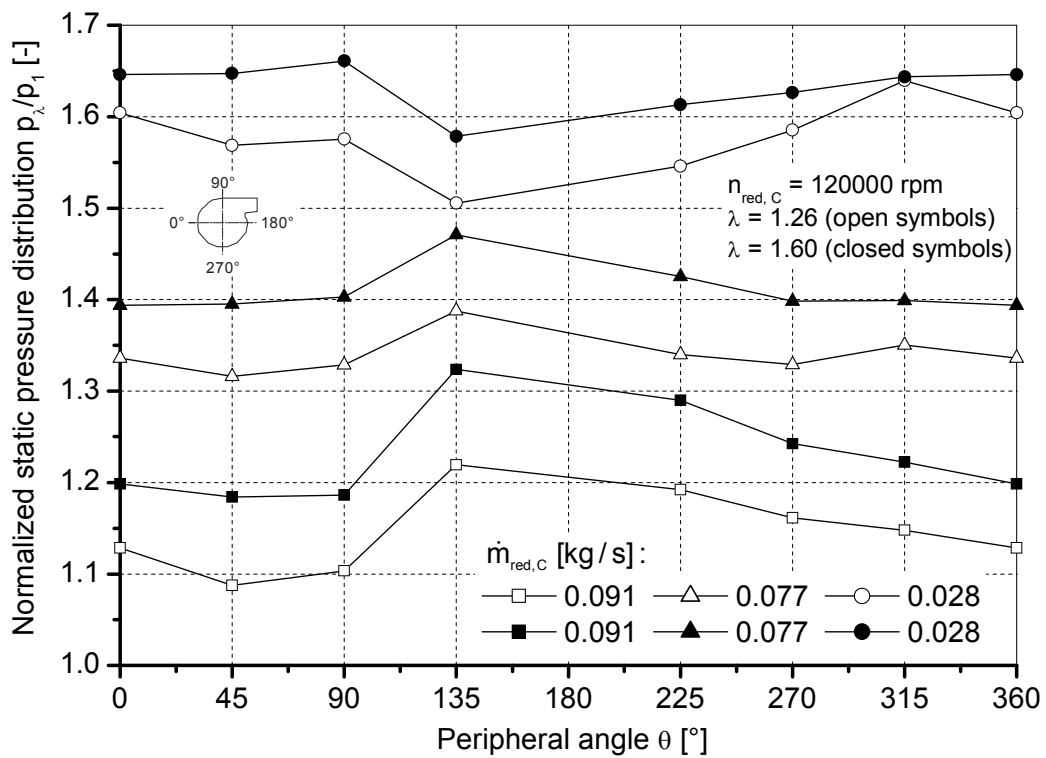


Figure A-44 Comparison between the static pressure distribution at diameter ratios $\lambda = 1.26$ and 1.6 for the GT1749V 70 Trim compressor at 120000 rpm

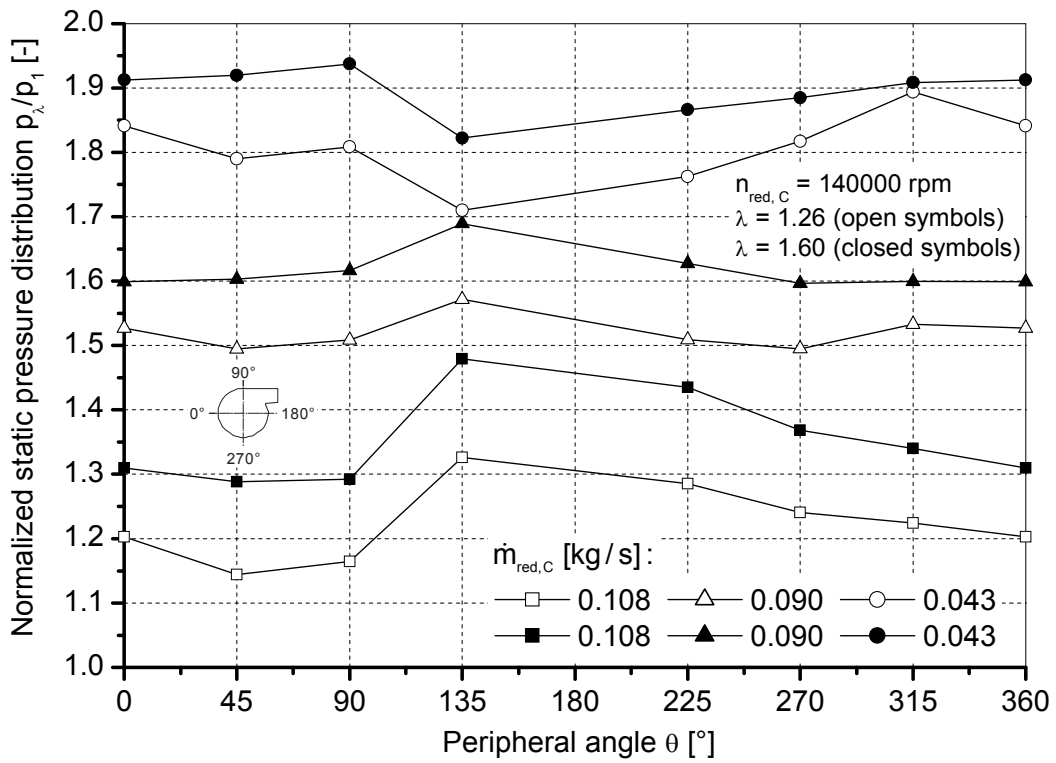


Figure A-45 Comparison between the static pressure distribution at diameter ratios $\lambda = 1.26$ and 1.6 for the GT1749V 70 Trim compressor at 140000 rpm

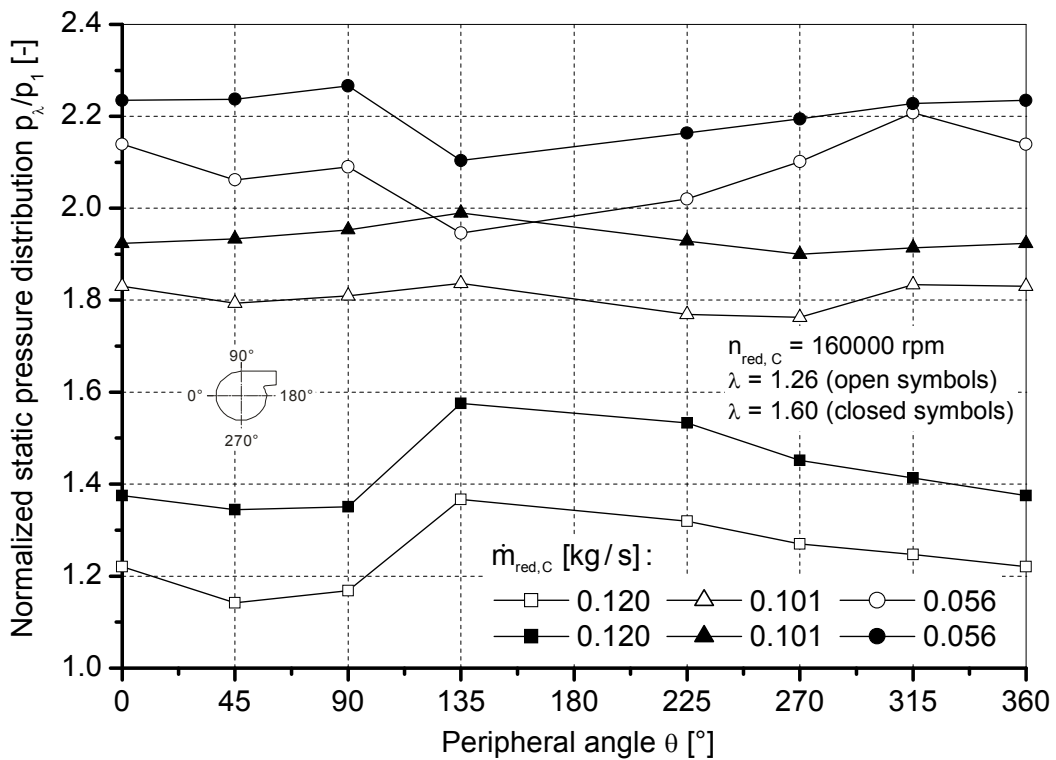


Figure A-46 Comparison between the static pressure distribution at diameter ratios $\lambda = 1.26$ and 1.6 for the GT1749V 70 Trim compressor at 160000 rpm

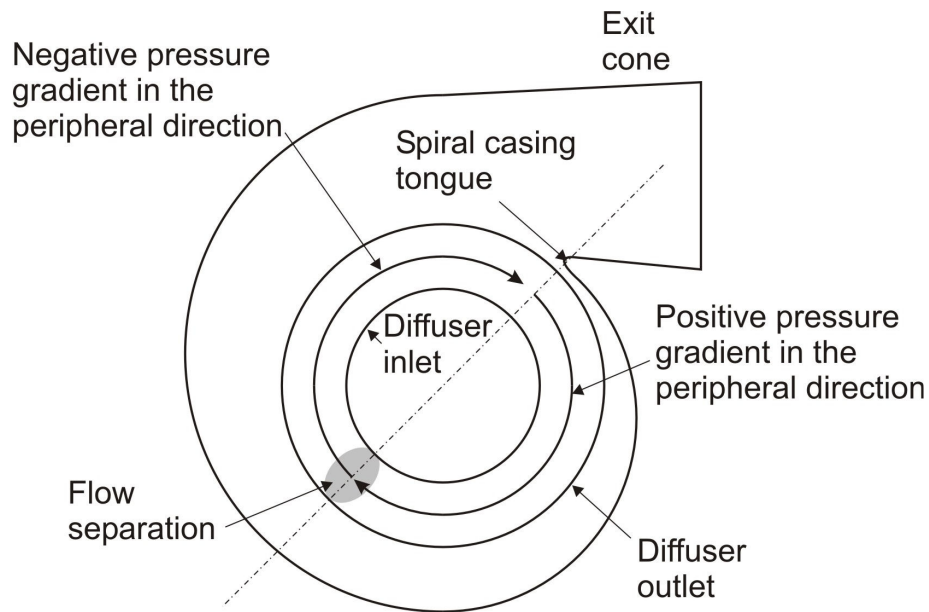


Figure A-47 Different flow regimes at the diffuser inlet along the compressor surge line

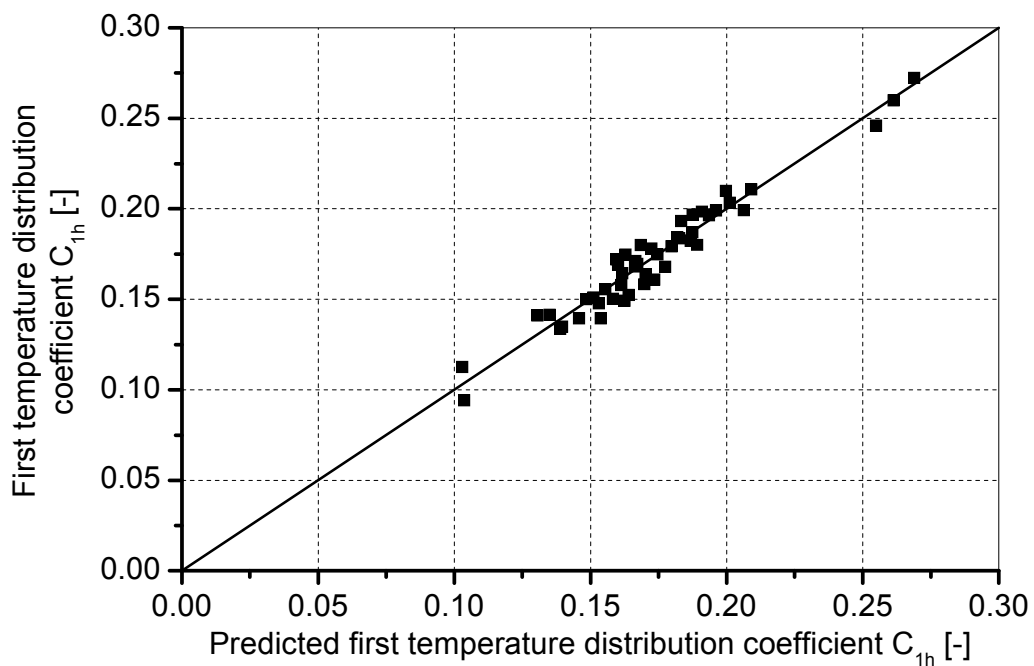


Figure A-48 Comparison between the estimated first temperature distribution coefficient and the predicted one

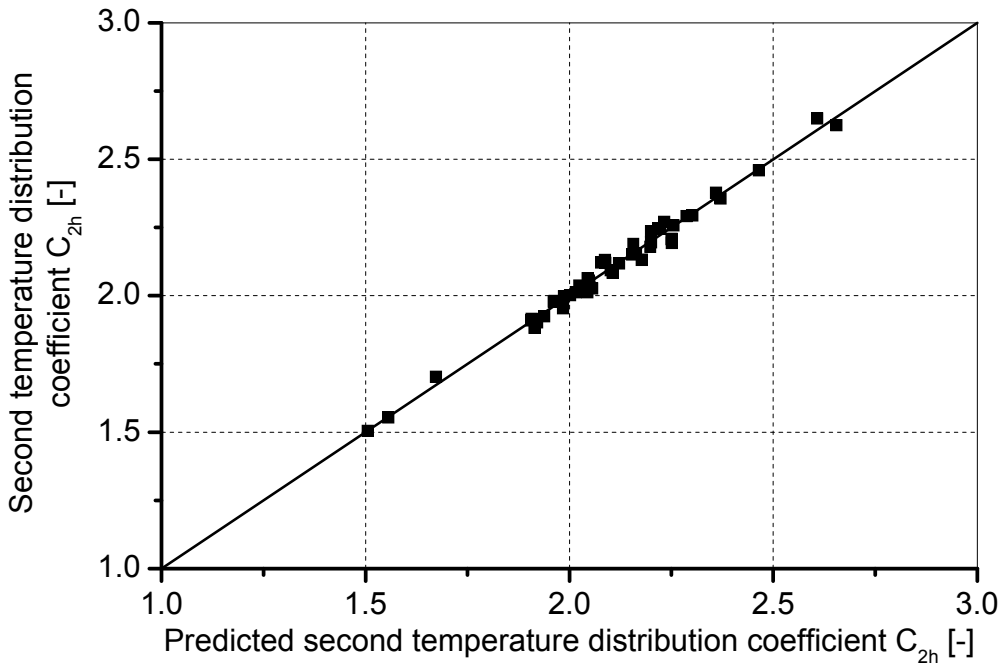


Figure A-49 Comparison between the estimated second temperature distribution coefficient and the predicted one

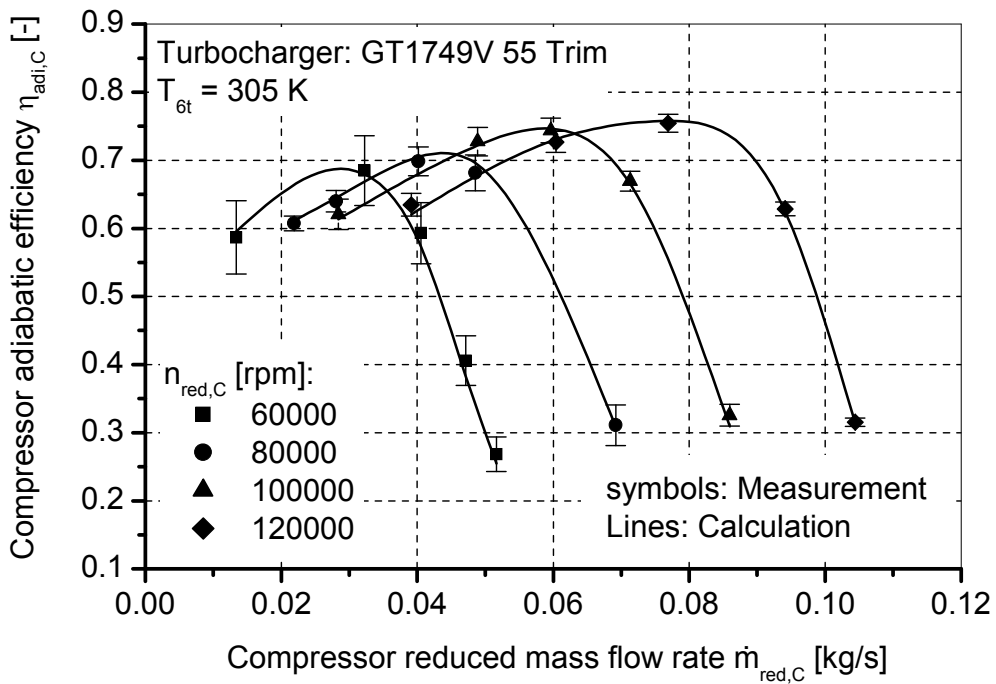


Figure A-50 Comparison between the measured compressor adiabatic efficiency and the calculated compressor adiabatic efficiency of the GT1749V 55 Trim compressor

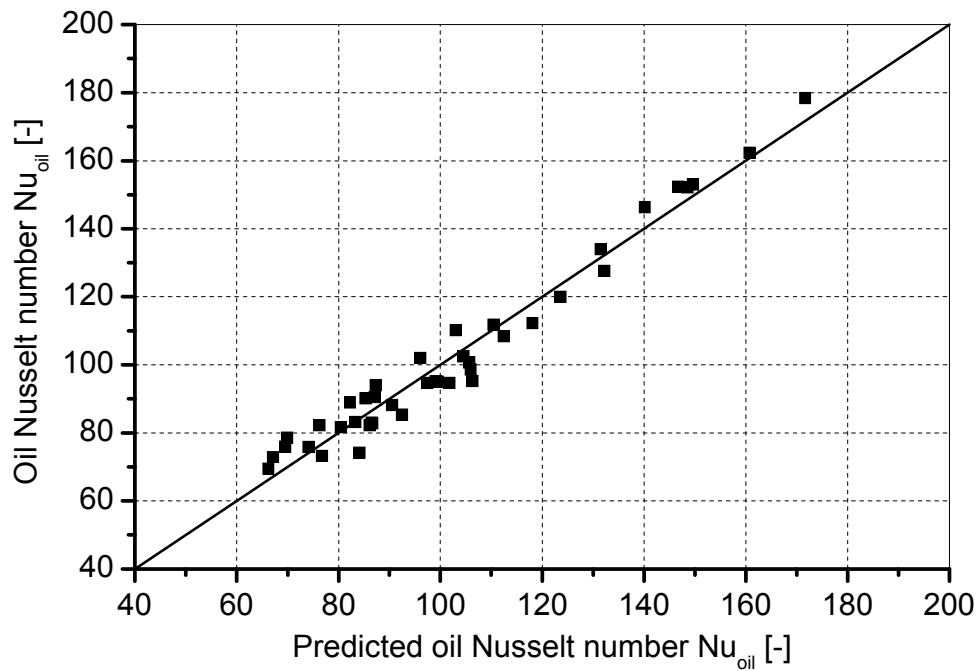


Figure A-51 Comparison between the predicted oil Nusselt number and the estimated oil Nusselt number

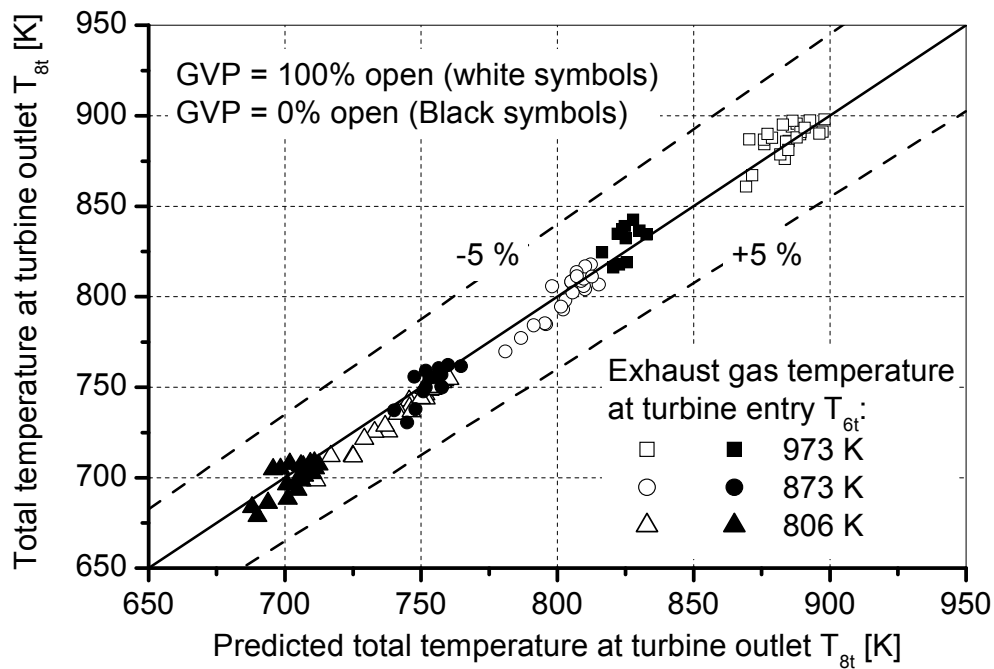


Figure A-52 Comparison between the measured total temperature at the turbine outlet and the estimated one for the GT1749V 55 Trim turbine

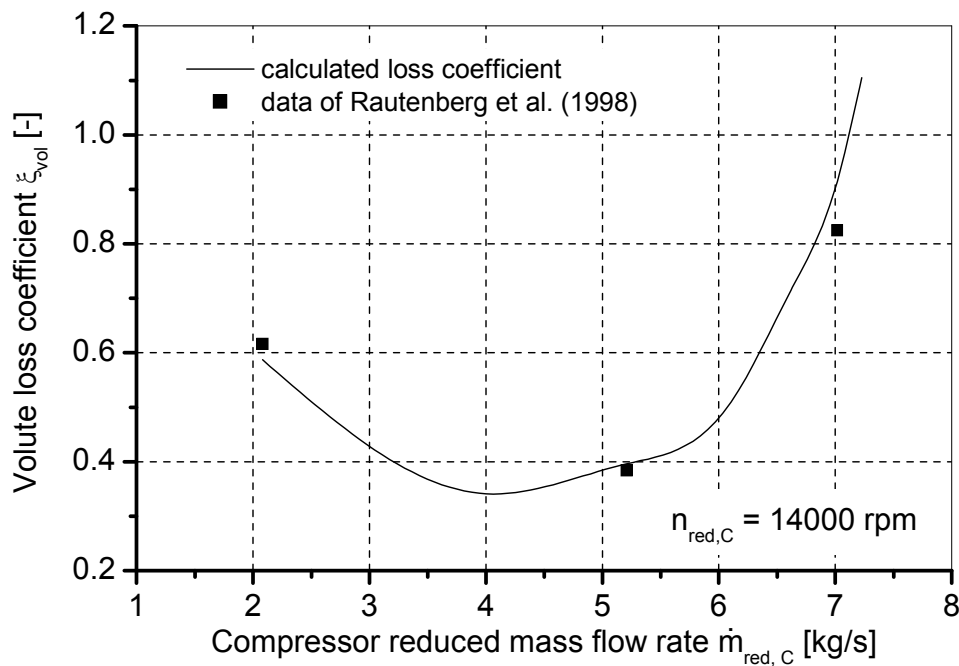


Figure A-53 Comparison between the measured volute loss coefficient and the calculated one for the large centrifugal compressor with external volute

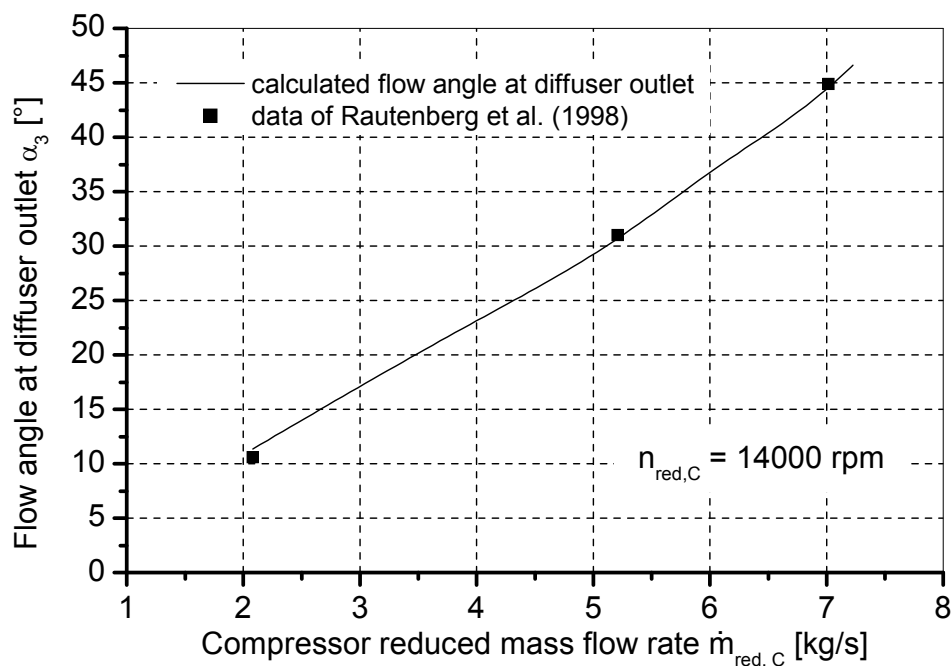


Figure A-54 Comparison between the measured flow angle at the volute inlet and the calculated one for the large centrifugal compressor with external volute

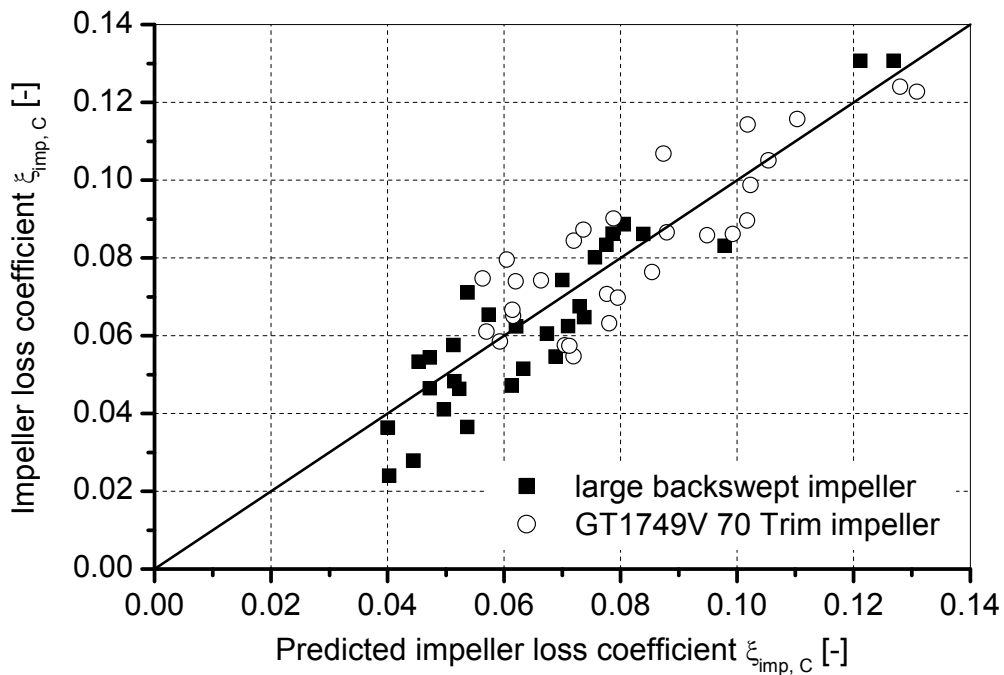


Figure A-55 Comparison between the estimated impeller loss coefficient using the program “V-Diffuser” and the calculated one

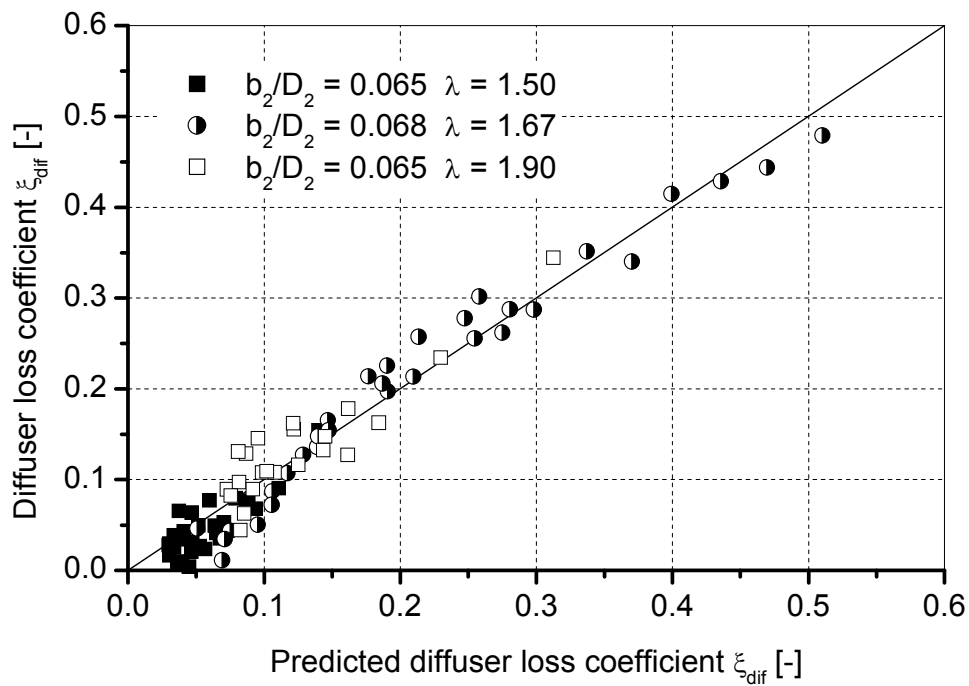


Figure A-56 Comparison between the estimated diffuser loss coefficient using the program “V-Diffuser” and the calculated one

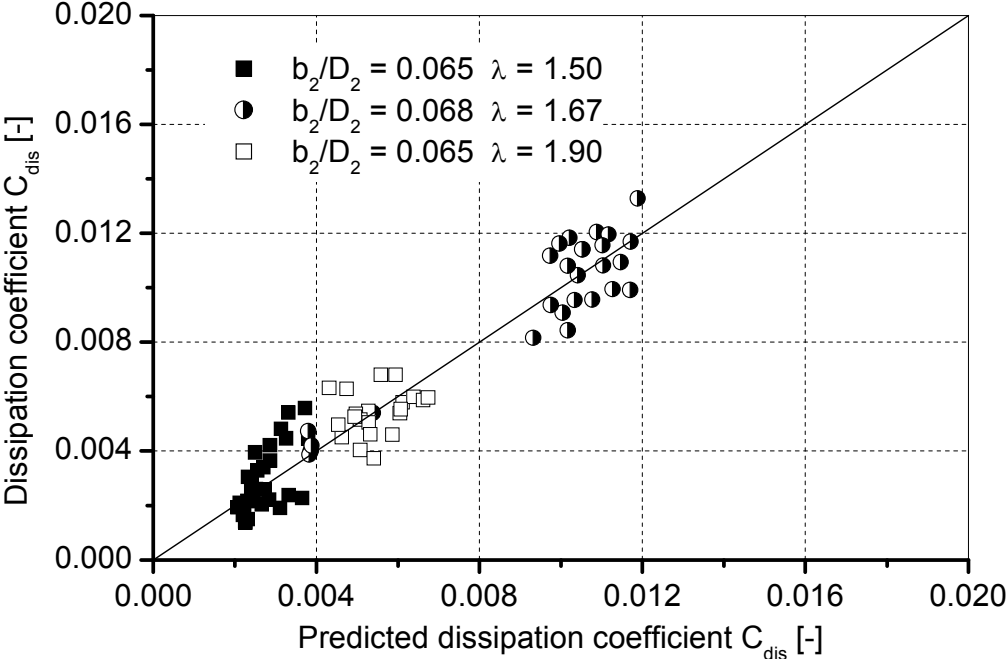


Figure A-57 Comparison between the estimated dissipation coefficient using the program “V-Diffuser” and the calculated one

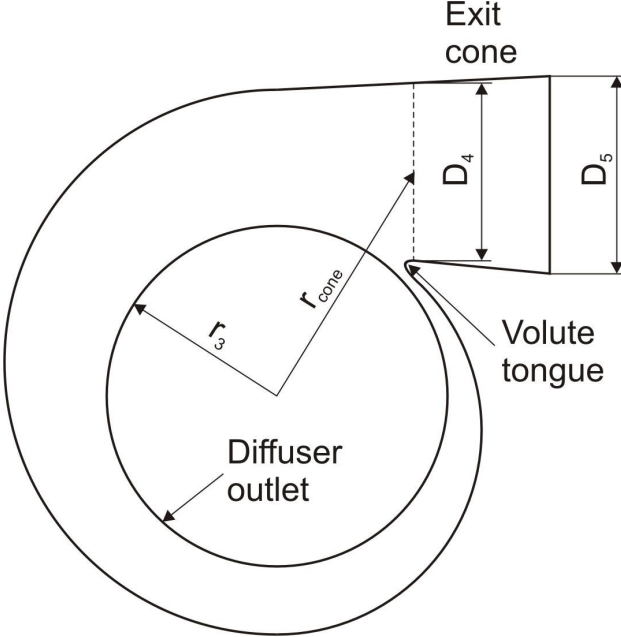


Figure A-58 Schematic diagram of the volute

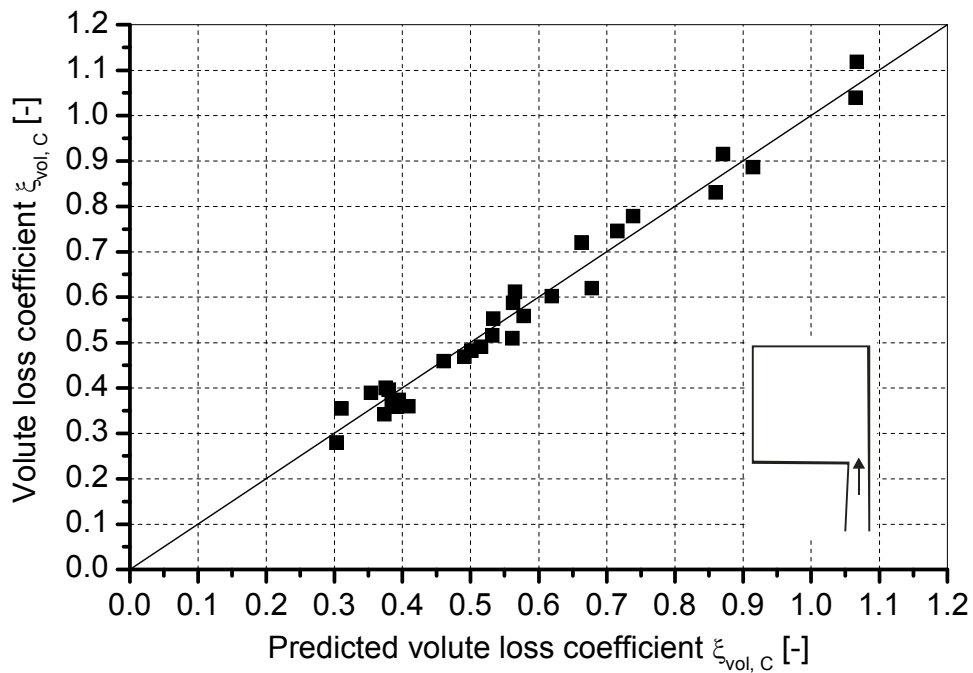


Figure A-59 Comparison between the measured volute loss coefficient and the calculated one for the large centrifugal compressor with external volute

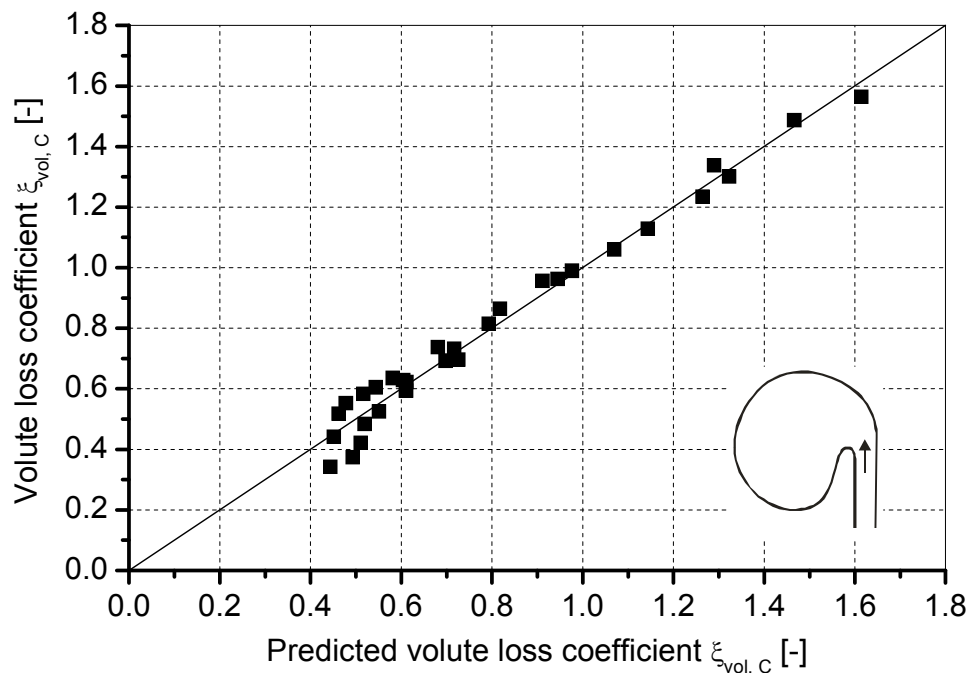


Figure A-60 Comparison between the estimated volute loss coefficient using the program "V-Diffuser" and the calculated one for the GT1749V 70 Trim compressor with central volute

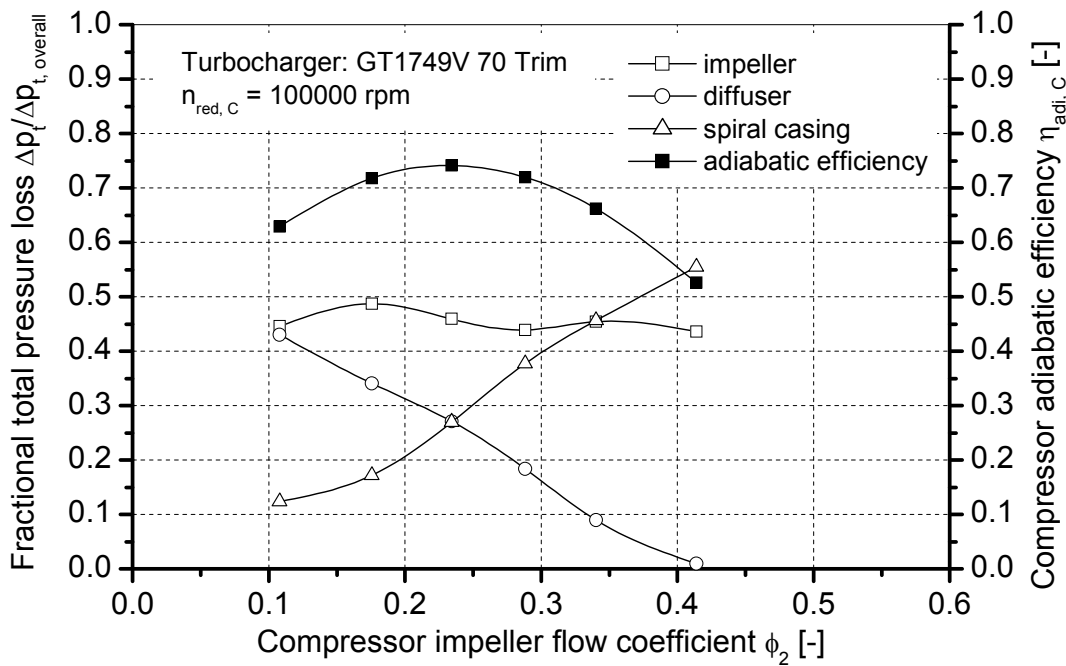


Figure A-61 Variation of the fractional total pressure loss and the compressor adiabatic efficiency with the impeller flow coefficient for the GT1749V 70 Trim compressor at 100000 rpm

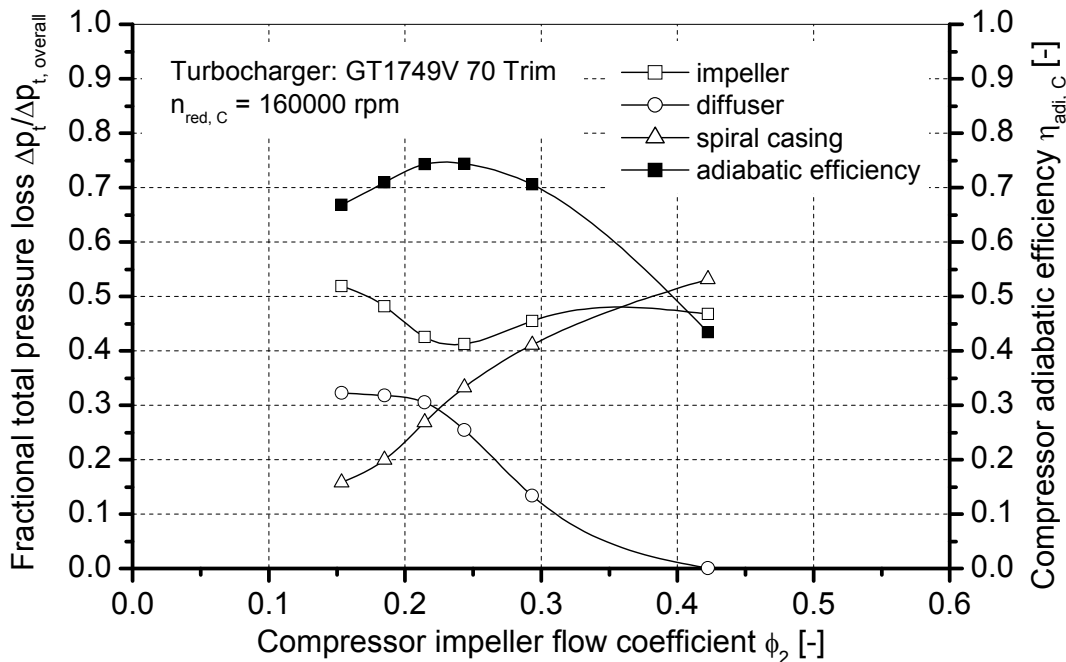


Figure A-62 Variation of the fractional total pressure loss and the compressor adiabatic efficiency with the impeller flow coefficient for the GT1749V 70 Trim compressor at 160000 rpm

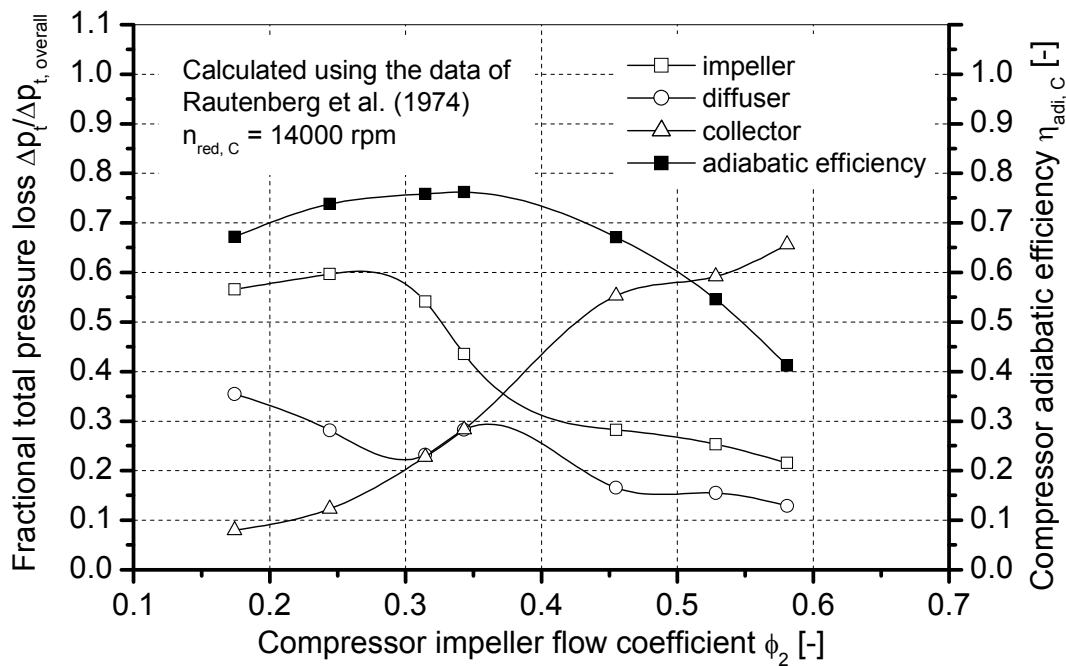


Figure A-63 Variation of the fractional total pressure loss and the compressor adiabatic efficiency with the impeller flow coefficient for the large centrifugal compressor with radial impeller

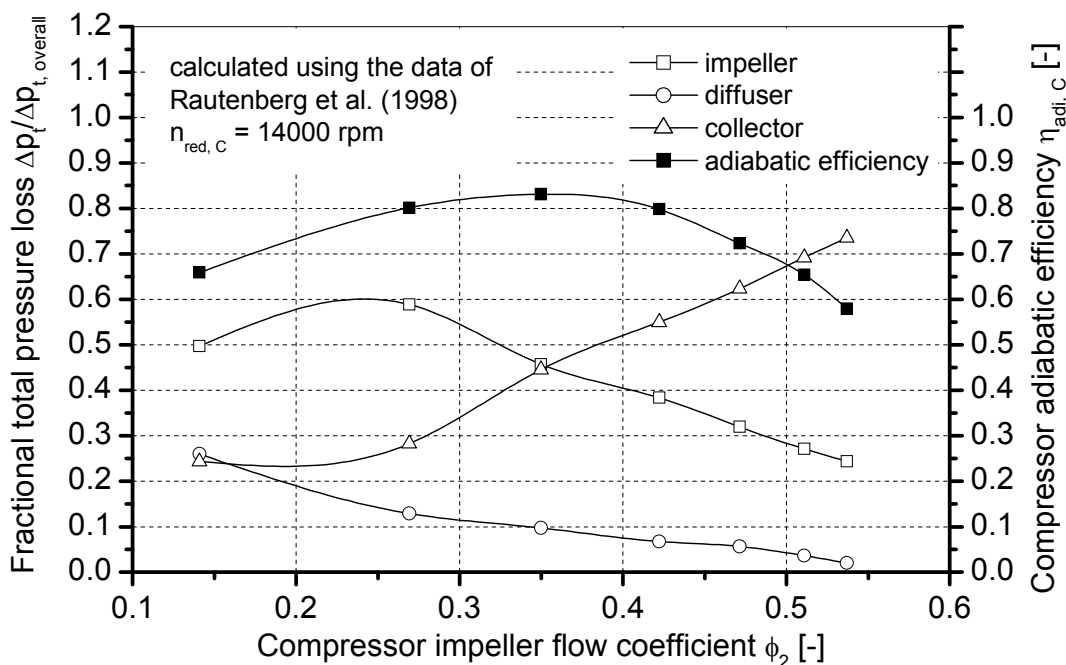


Figure A-64 Variation of the fractional total pressure loss and the compressor adiabatic efficiency with the impeller flow coefficient for the large centrifugal compressor with backswept impeller

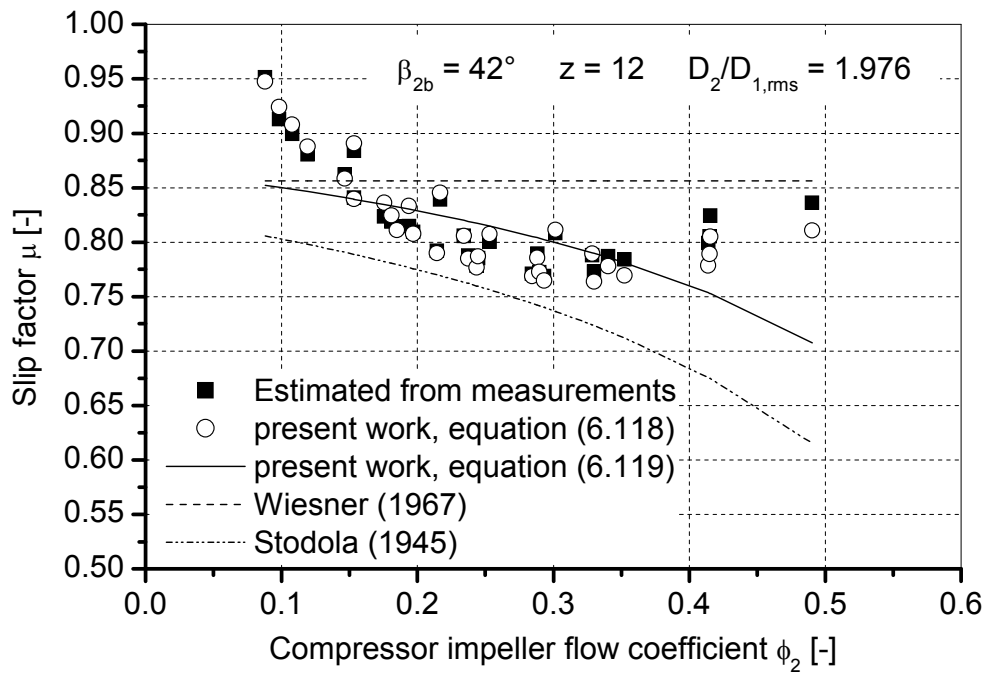


Figure A-65 Comparison between the estimated slip factor using the program “V-Diffuser” and the calculated one for the GT1749V 70 trim impeller

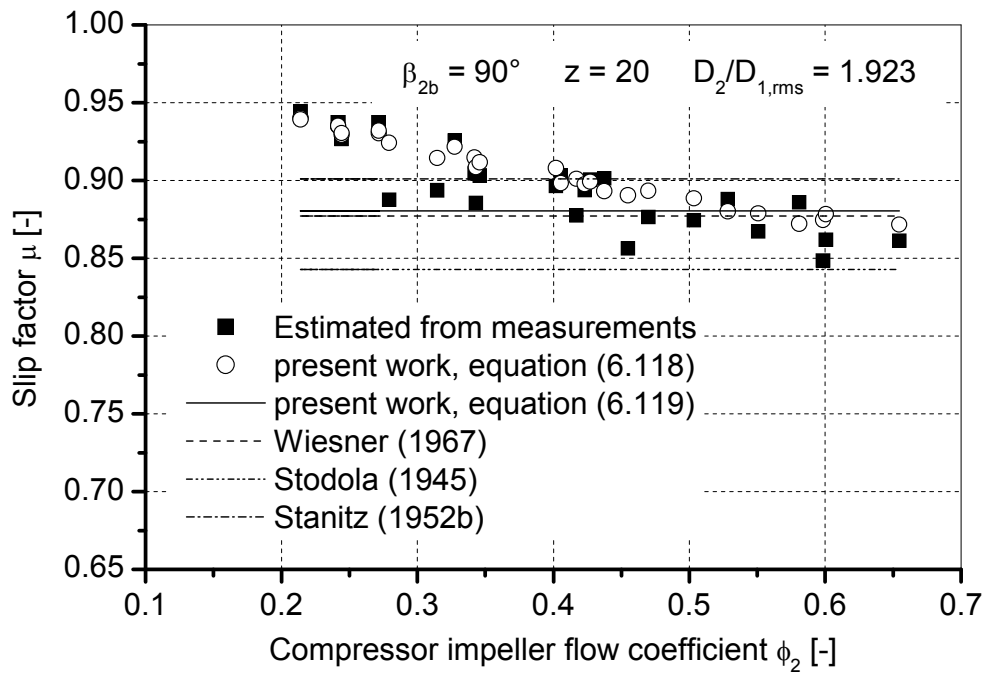


Figure A-66 Comparison between the estimated slip factor using the program “V-Diffuser” and the calculated one for the large radial impeller

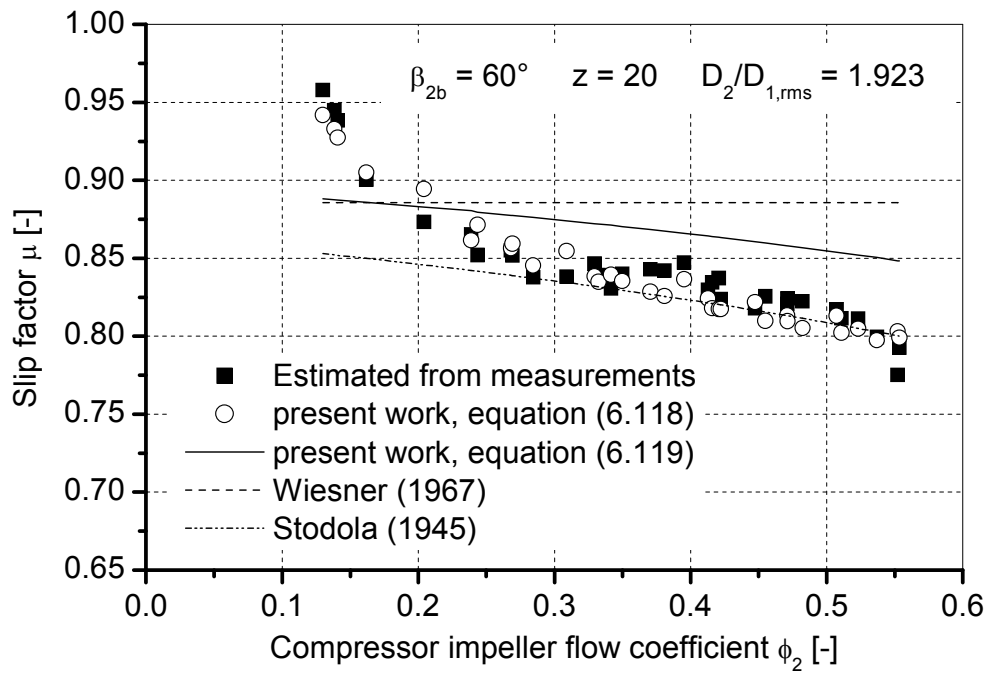


Figure A-67 Comparison between the estimated slip factor using the program “V-Diffuser” and the calculated one for the large backswept impeller

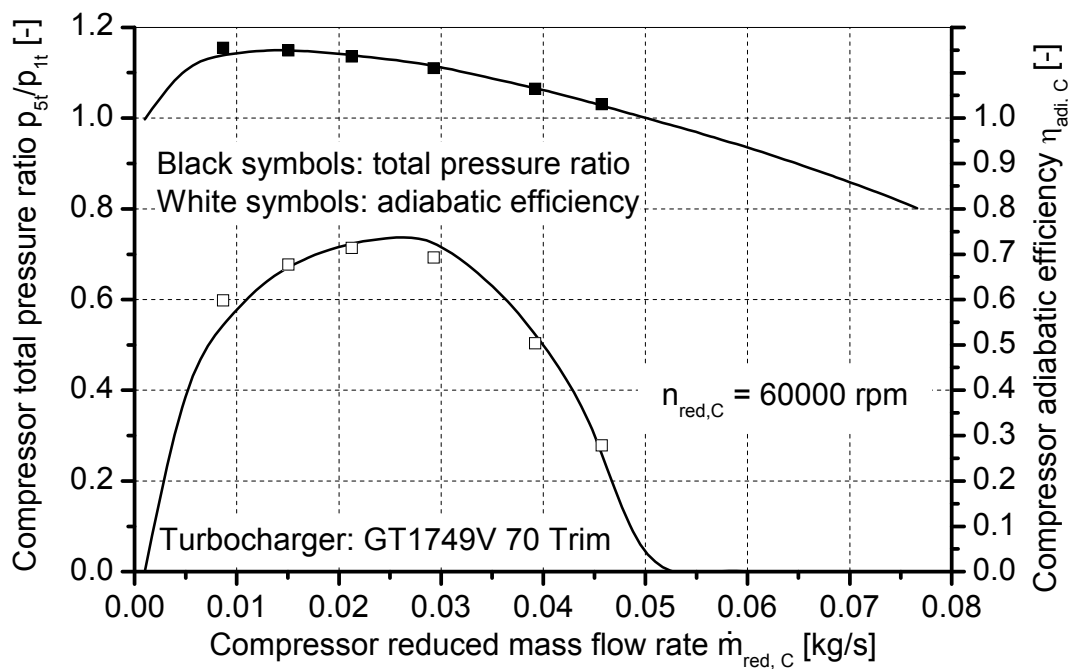


Figure A-68 Comparison between the predicted compressor performance and the measured compressors performance at 60000 rpm for the GT1749V 70 Trim compressor

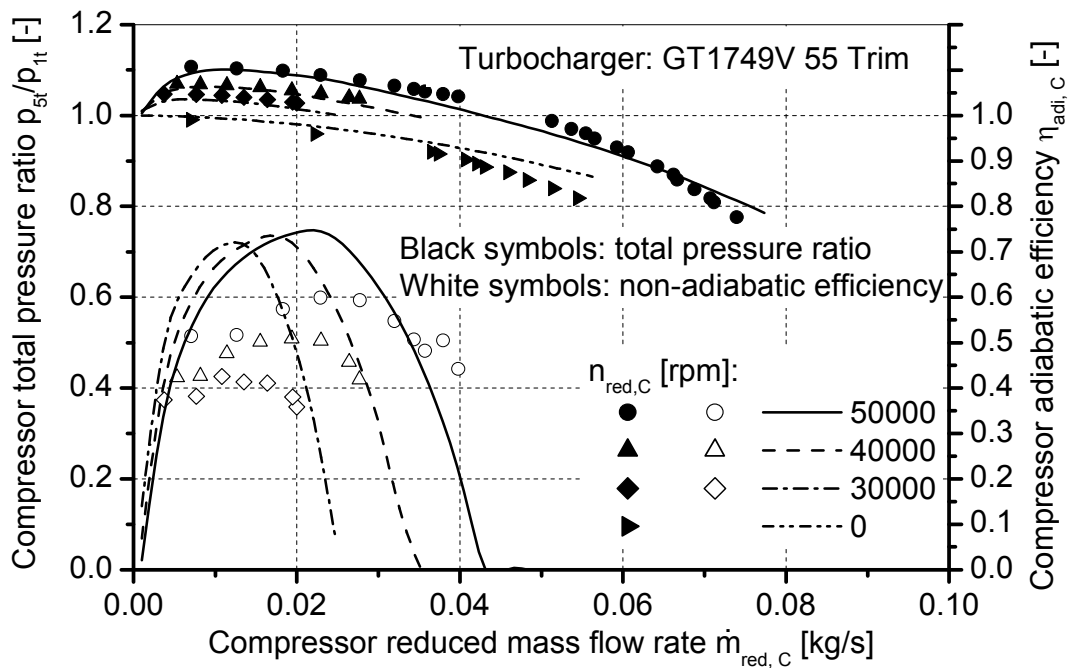


Figure A-69 Comparison between the predicted compressor performance and the measured compressors performance at 50000, and 0 rpm for the GT1749V 55 Trim compressor

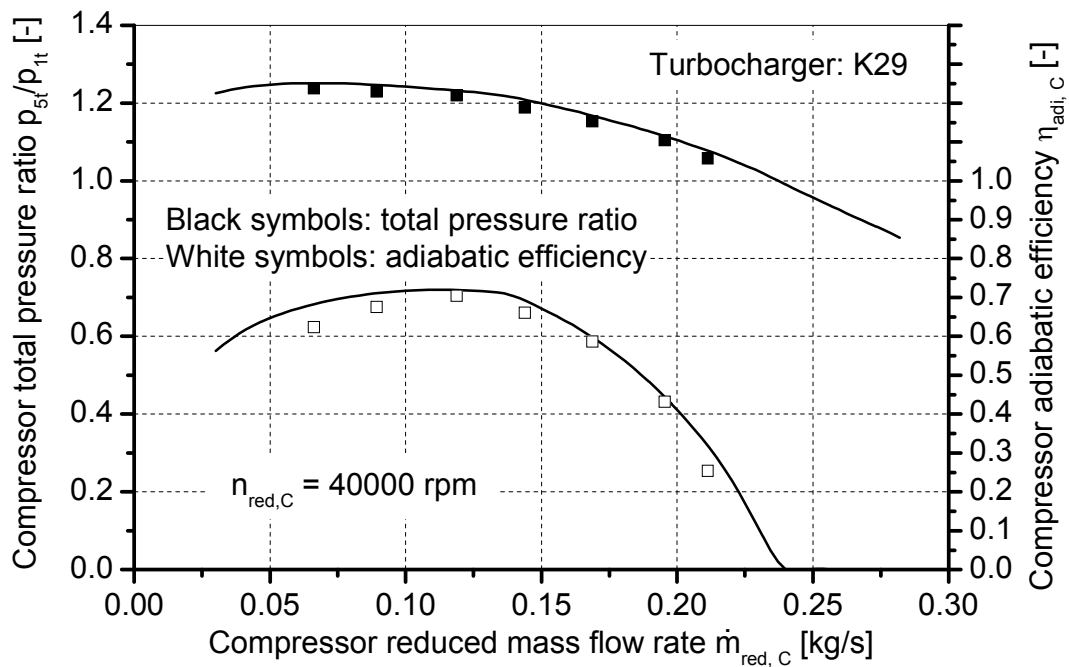


Figure A-70 Comparison between the predicted compressor performance and the measured compressors performance at 40000 rpm for the K29 compressor

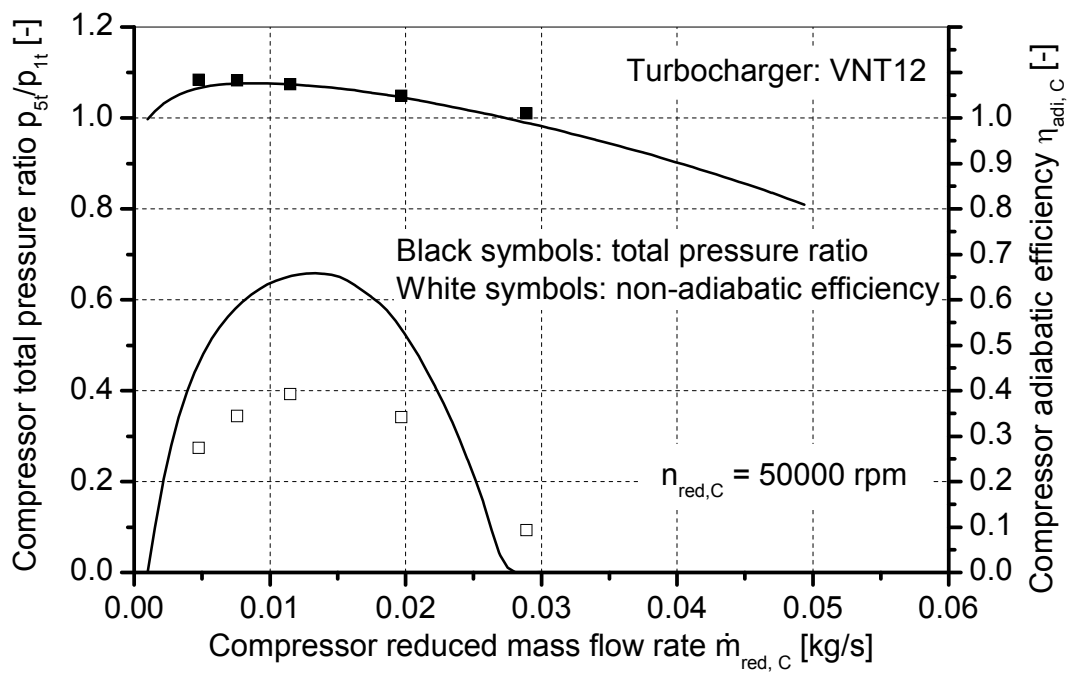


Figure A-71 Comparison between the predicted compressor performance and the measured compressors performance at 50000 rpm for the VNT12 compressor

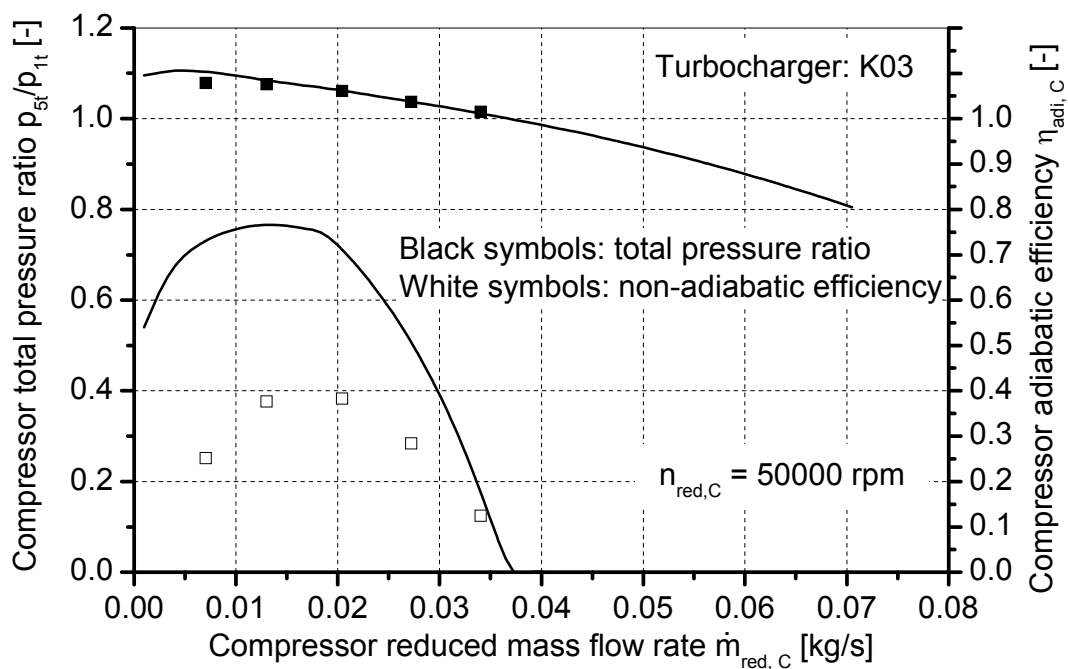


Figure A-72 Comparison between the predicted compressor performance and the measured compressors performance at 50000 rpm for the K03 compressor

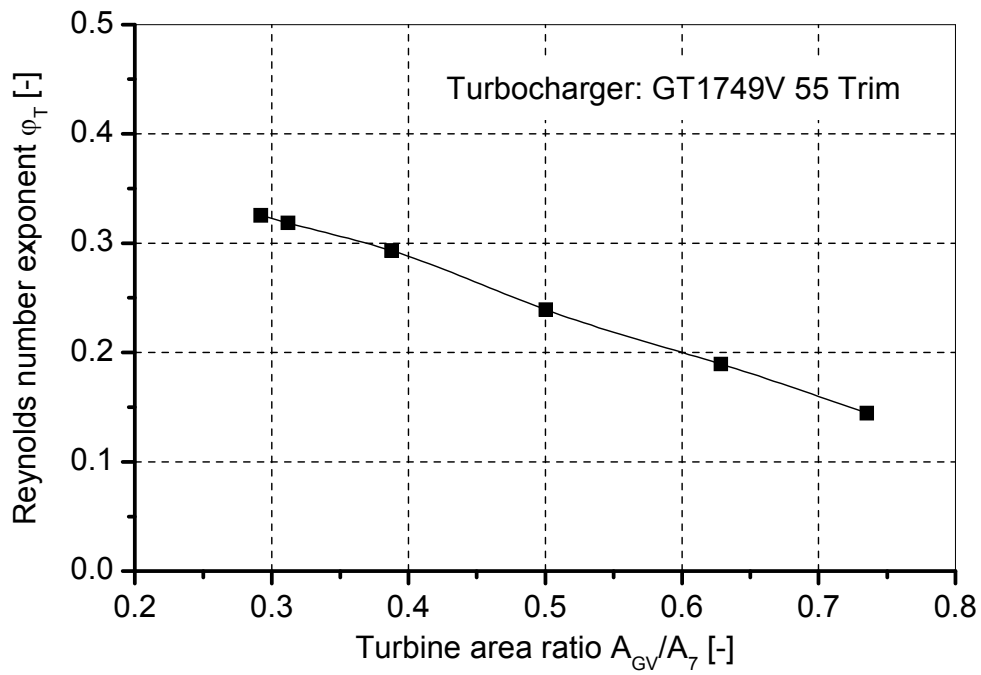


Figure A-73 Variation of the Reynolds number exponent with the turbine area ratio

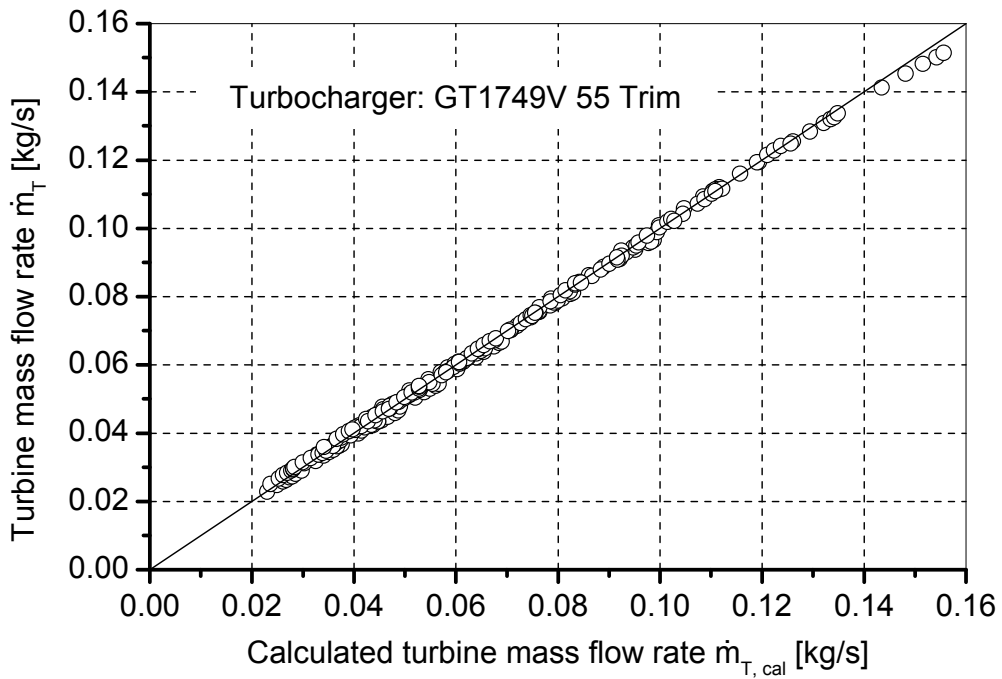


Figure A-74 Comparison between the measured turbine mass flow rate and the estimated turbine mass flow rate of the GT1749V 55 Trim turbine

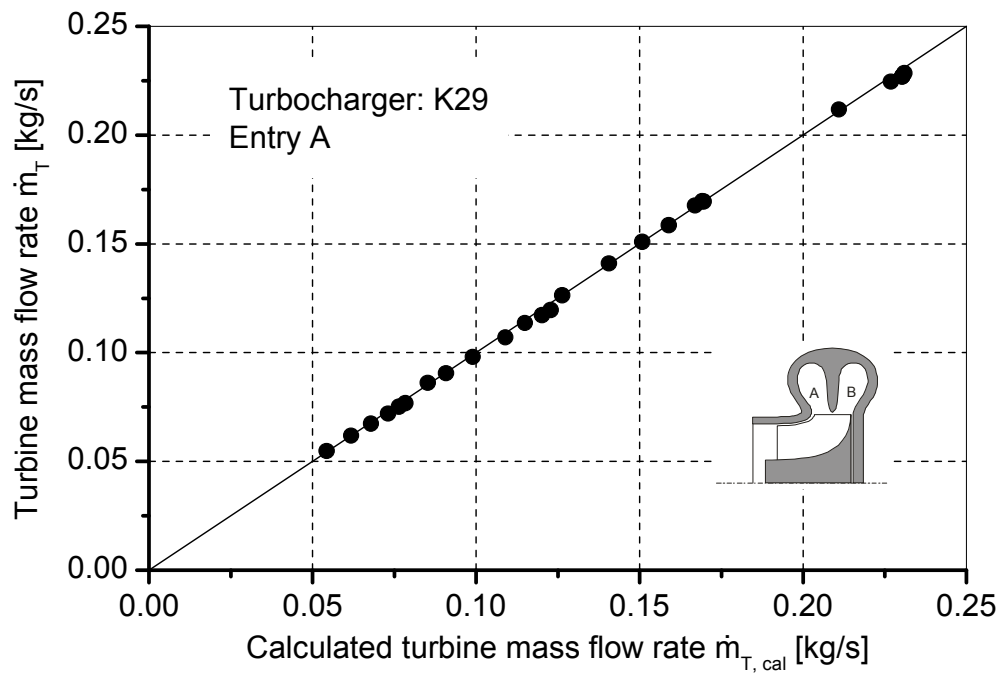


Figure A-75 Comparison between the measured turbine entry mass flow rate and the estimated turbine entry flow rate for entry A of the K29 turbine at entry pressure ratio 1.0

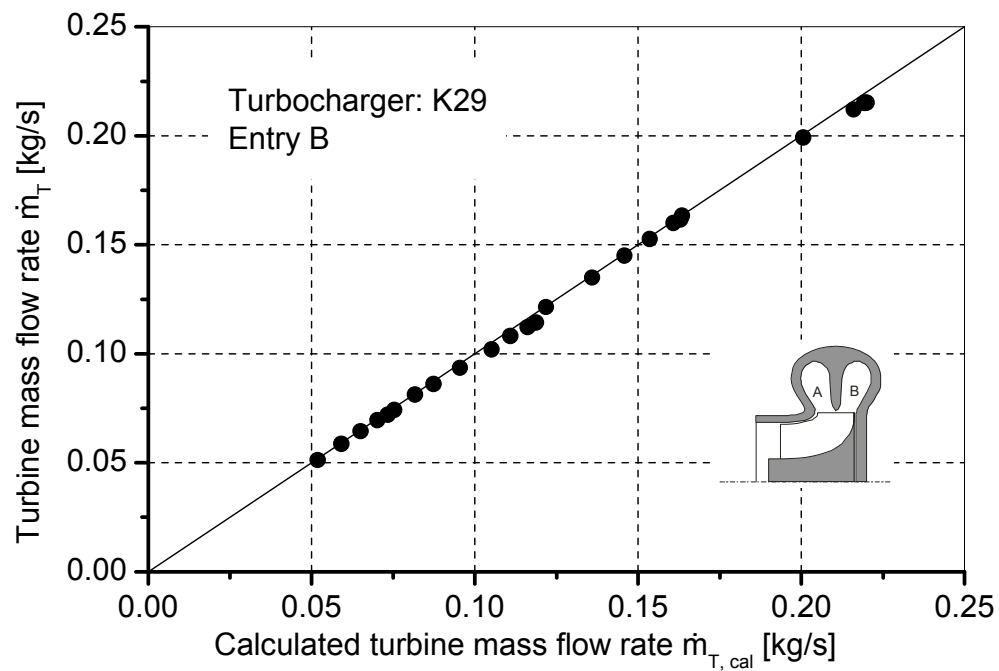


Figure A-76 Comparison between the measured turbine entry mass flow rate and the estimated turbine entry flow rate for entry B of the K29 turbine at entry pressure ratio 1.0

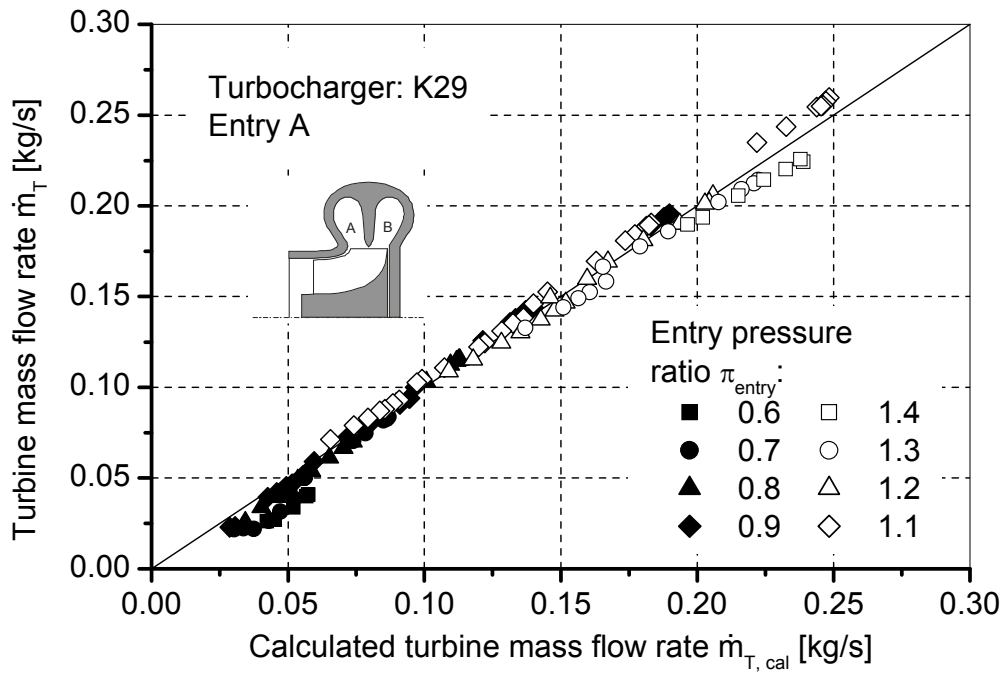


Figure A-77 Comparison between the measured turbine entry mass flow rate and the estimated turbine entry flow rate for entry A of the K29 turbine under partial admission conditions

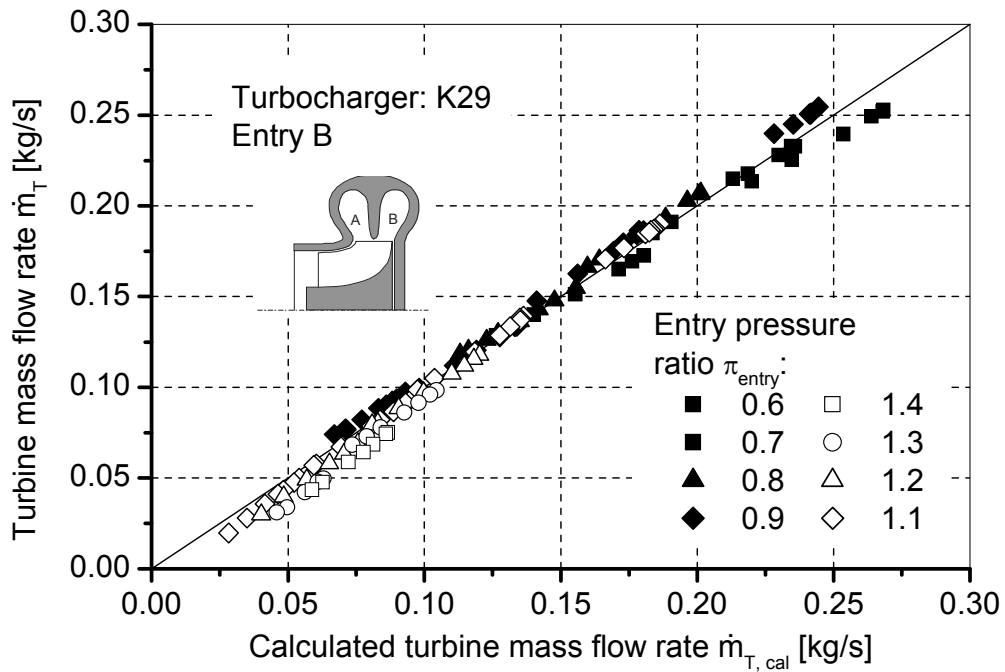


Figure A-78 Comparison between the measured turbine entry mass flow rate and the estimated turbine entry flow rate for entry B of the K29 turbine under partial admission conditions

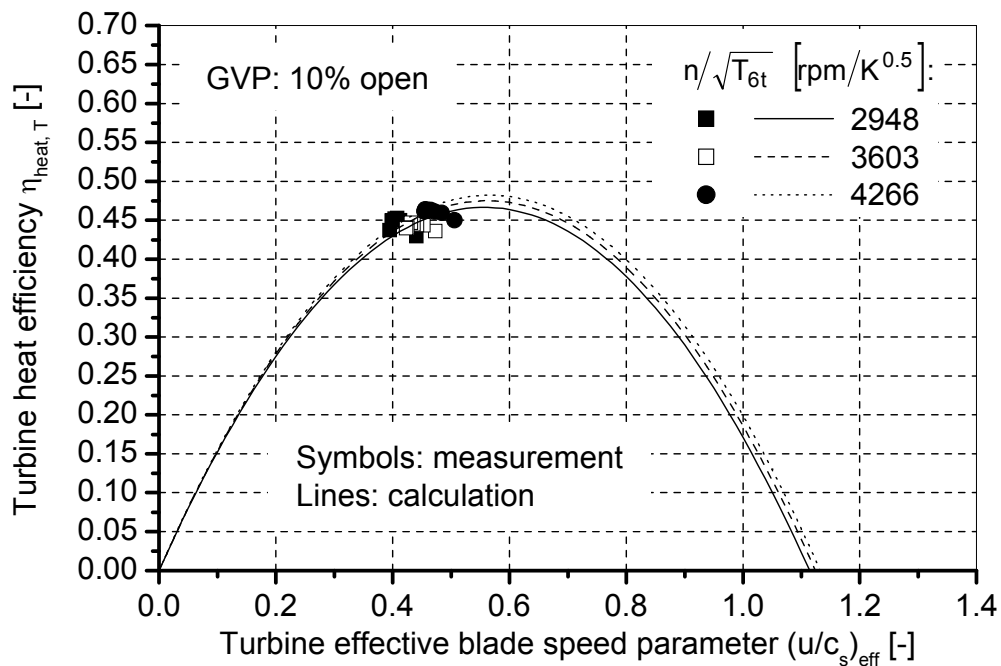


Figure A-79 Comparison between the actual heat efficiency of the GT1749V 55 Trim turbine and the calculated turbine heat efficiency at guide-vane position 10% open

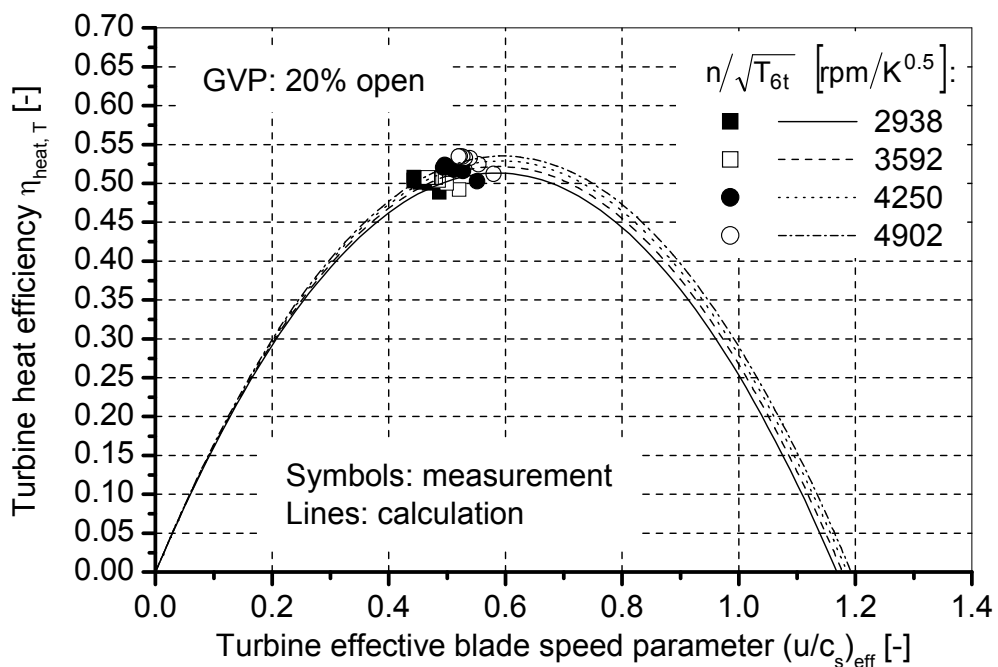


Figure A-80 Comparison between the actual heat efficiency of the GT1749V 55 Trim turbine and the calculated turbine heat efficiency at guide-vane position 20% open

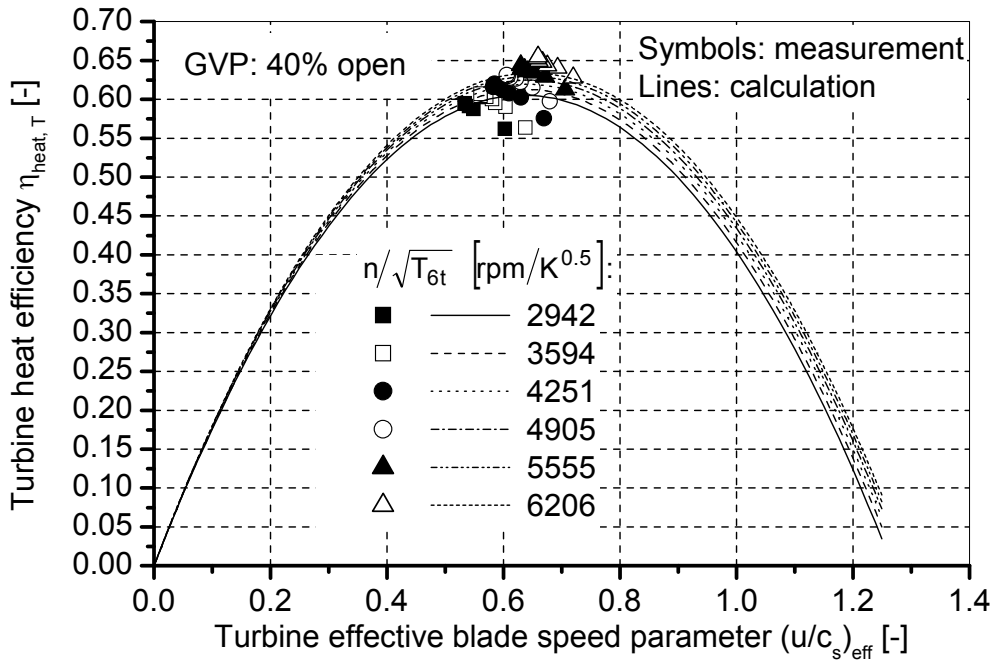


Figure A-81 Comparison between the actual heat efficiency of the GT1749V 55 Trim turbine and the calculated turbine heat efficiency at guide-vane position 40% open

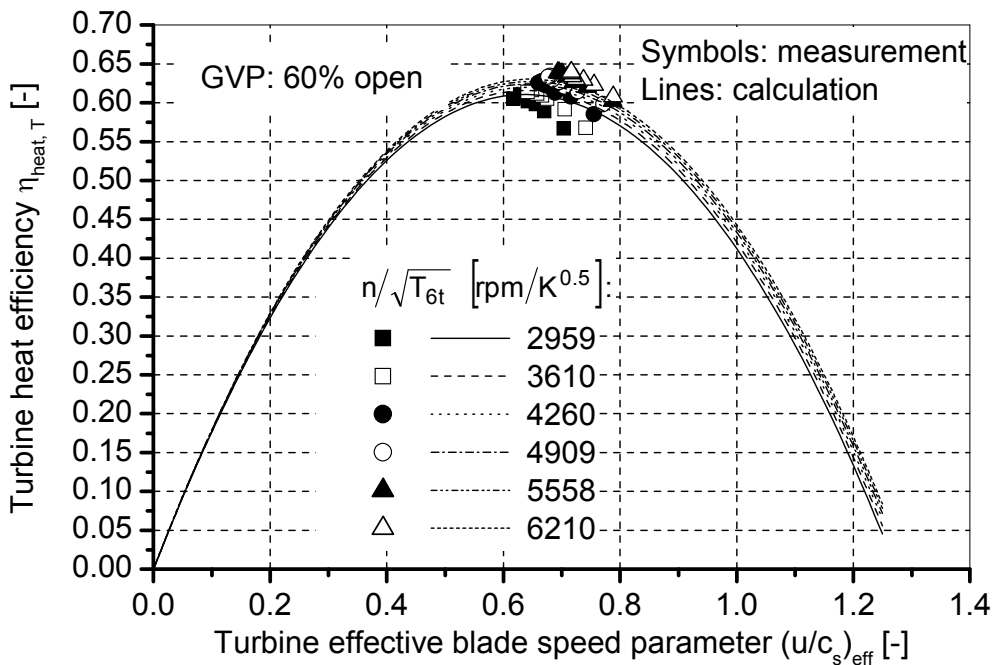


Figure A-82 Comparison between the actual heat efficiency of the GT1749V 55 Trim turbine and the calculated turbine heat efficiency at guide-vane position 60% open

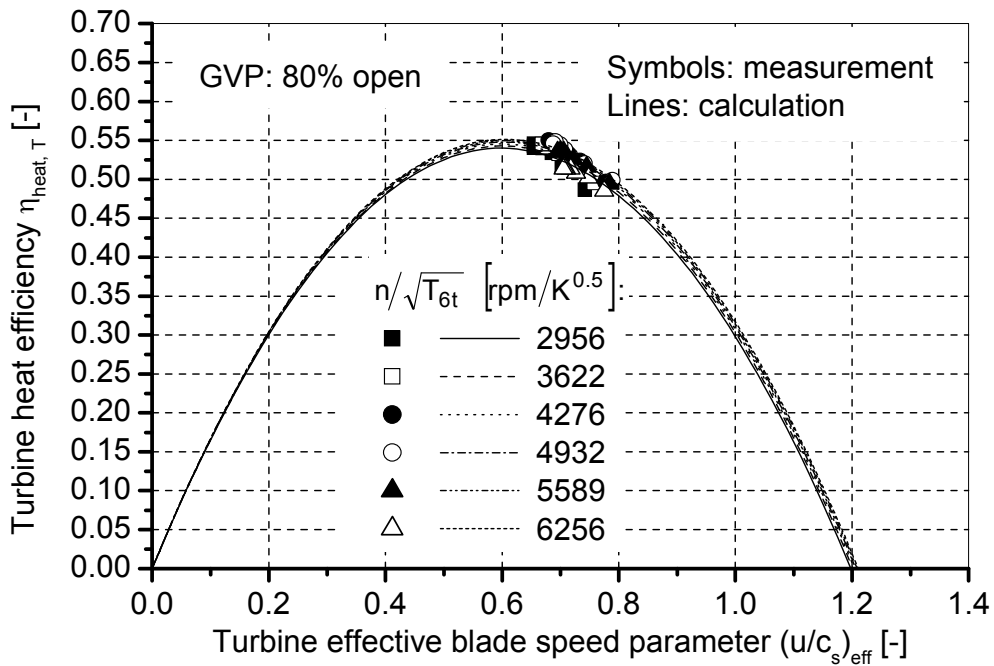


Figure A-83 Comparison between the actual heat efficiency of the GT1749V 55 Trim turbine and the calculated turbine heat efficiency at guide-vane position 80% open

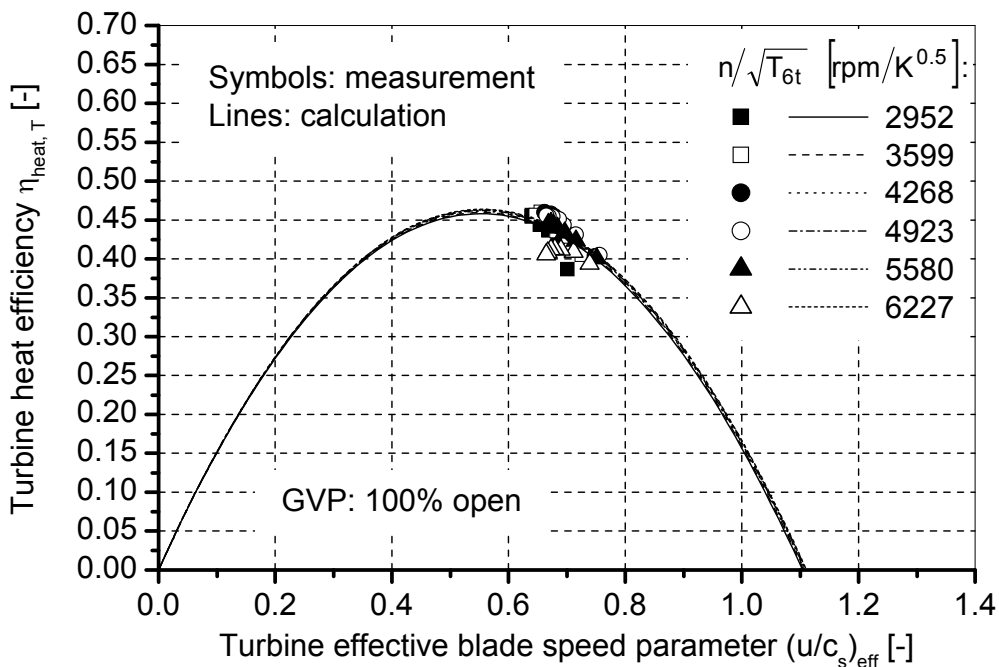


Figure A-84 Comparison between the actual heat efficiency of the GT1749V 55 Trim turbine and the calculated turbine heat efficiency at guide-vane position 100% open

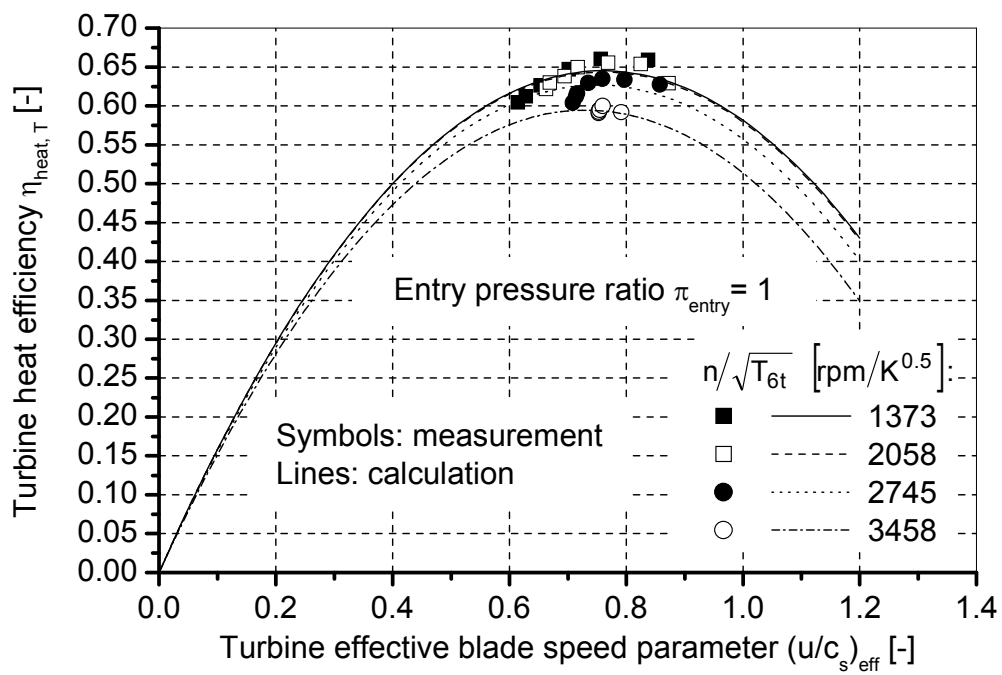


Figure A-85 Comparison between the actual heat efficiency of the K29 turbine and the calculated turbine heat efficiency

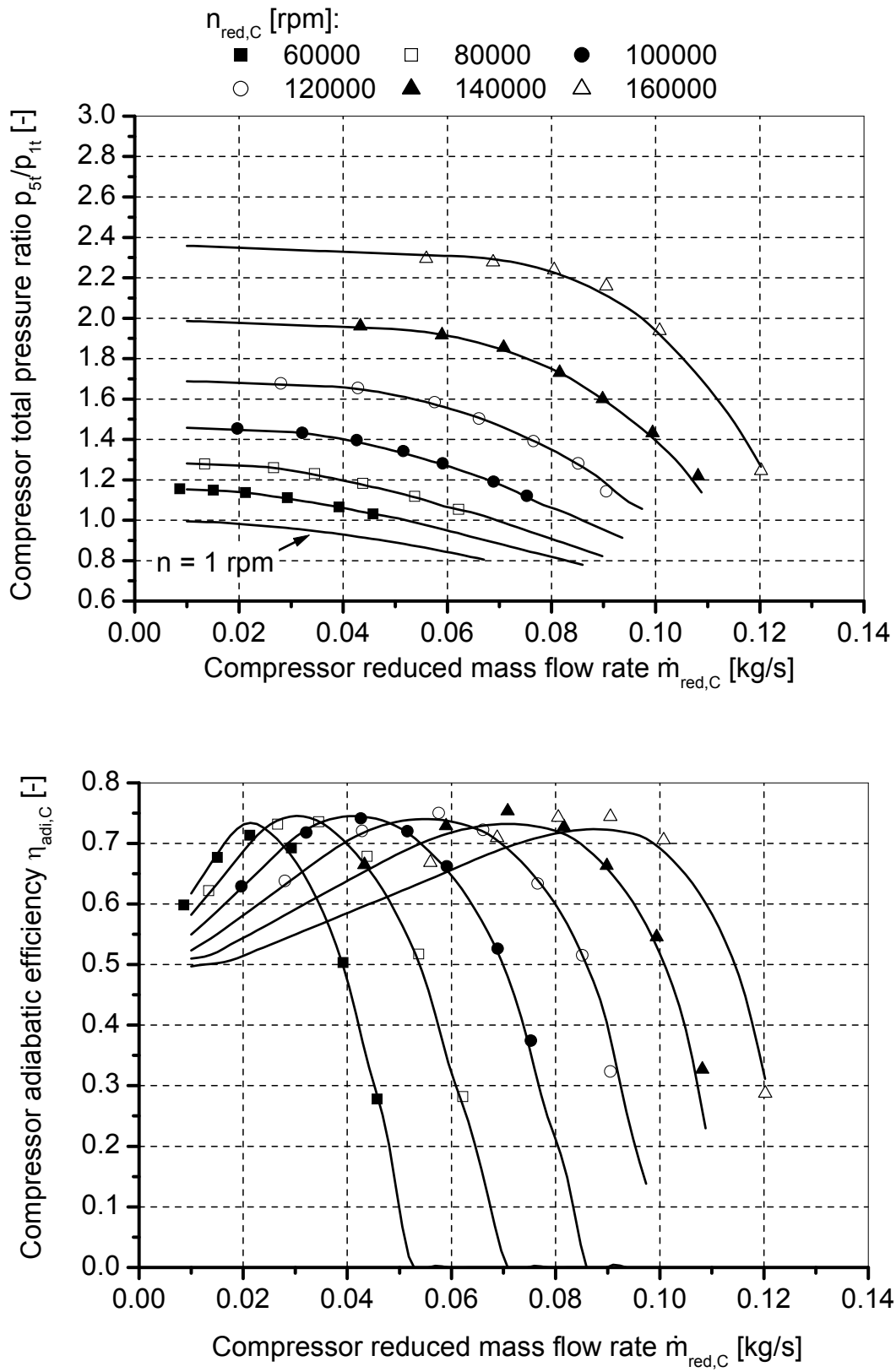


Figure A-86 Extended compressor performance map of the GT1749V 70 trim compressor at an exhaust gas temperature 305 K

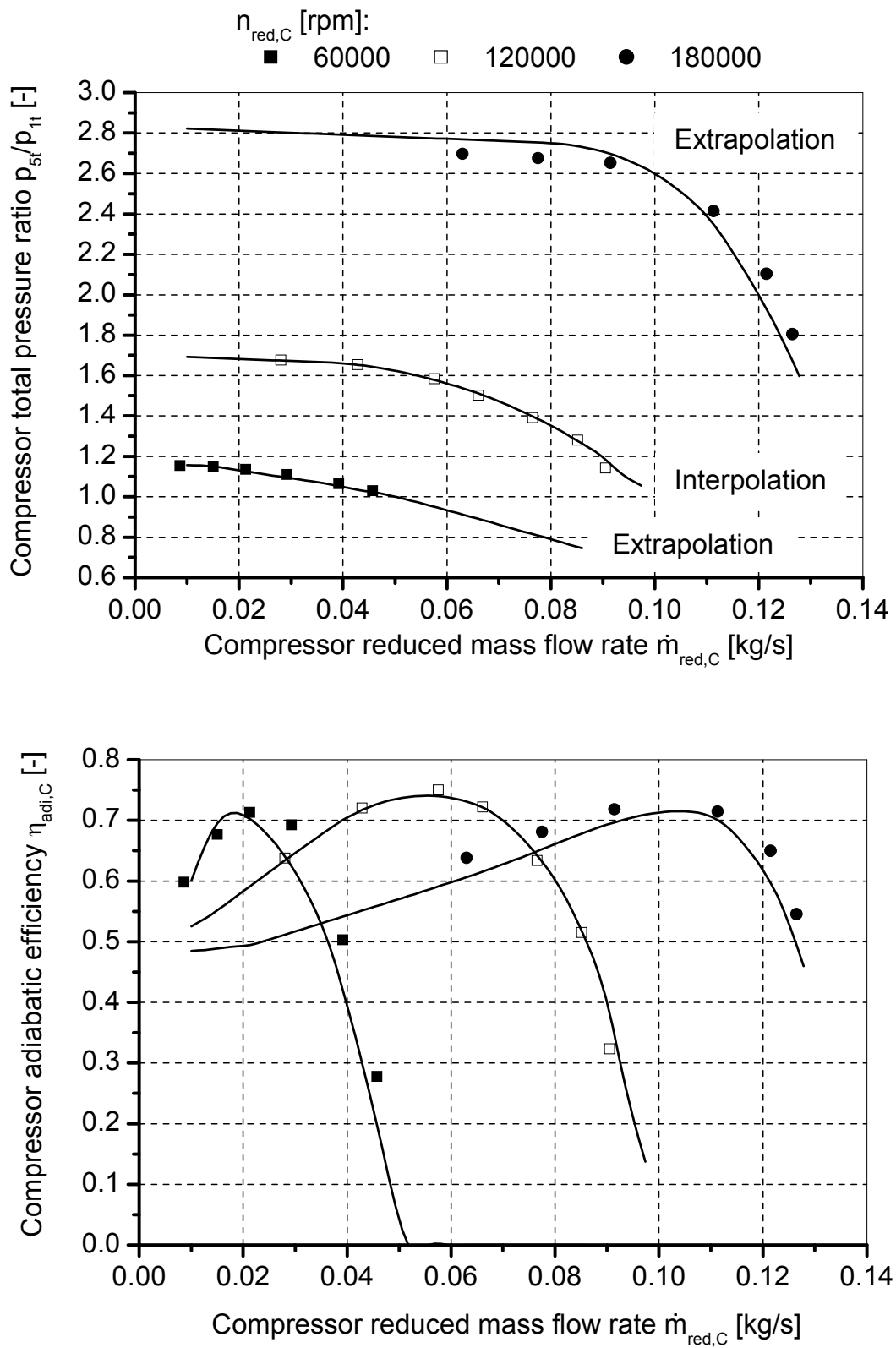


Figure A-87 Comparison between the measured performance lines and the extrapolated as well as the interpolated performance lines for the GT1749V 70 trim compressor

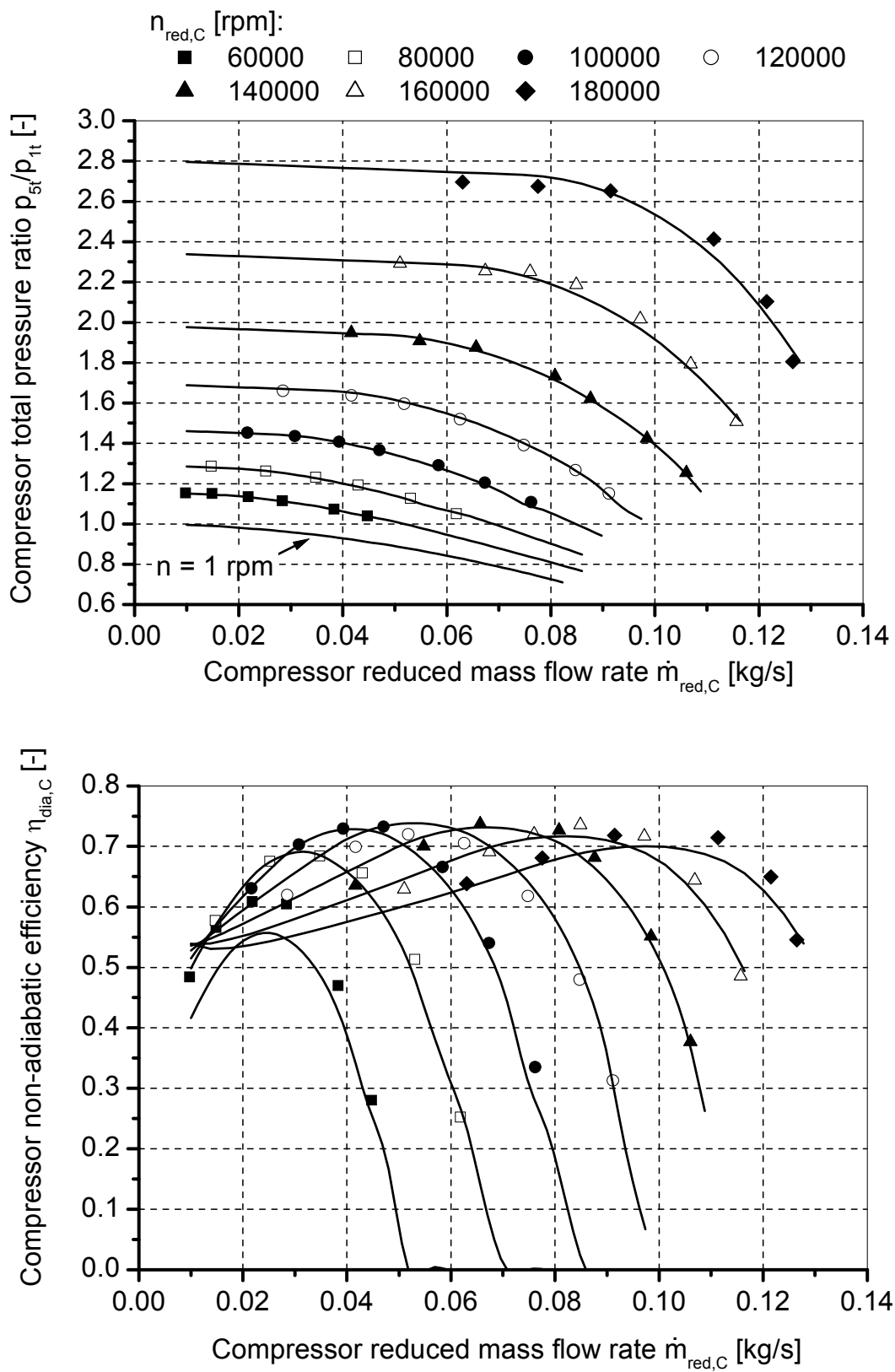


Figure A-88 Extended compressor performance map of the GT1749V 70 Trim compressor at an exhaust gas temperature 873 K

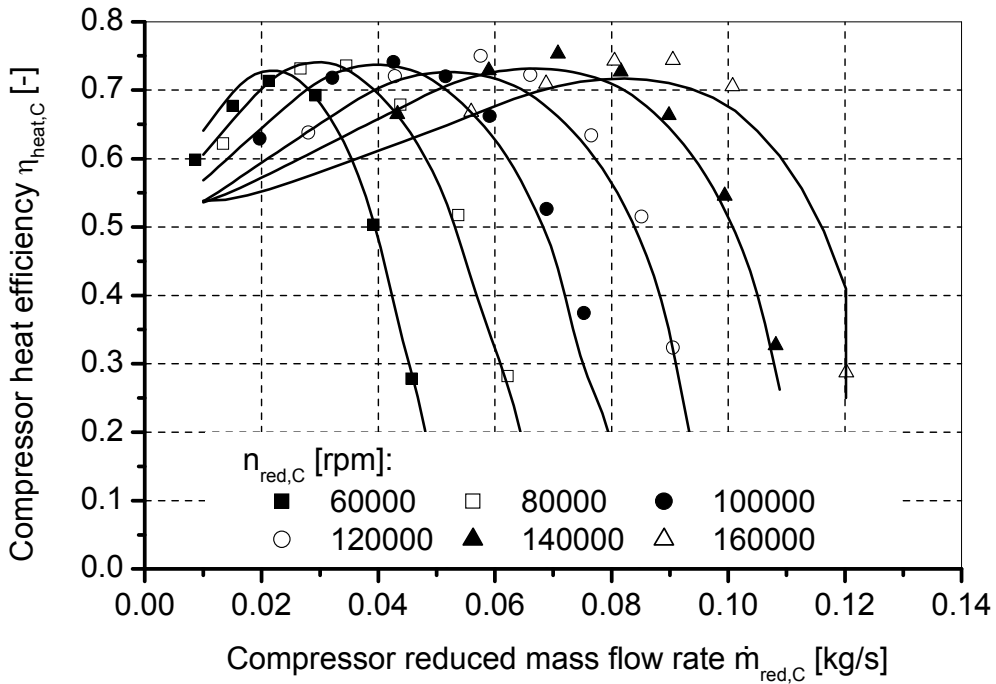


Figure A-89 Estimated compressor heat efficiency using the hot measurements as input to the program

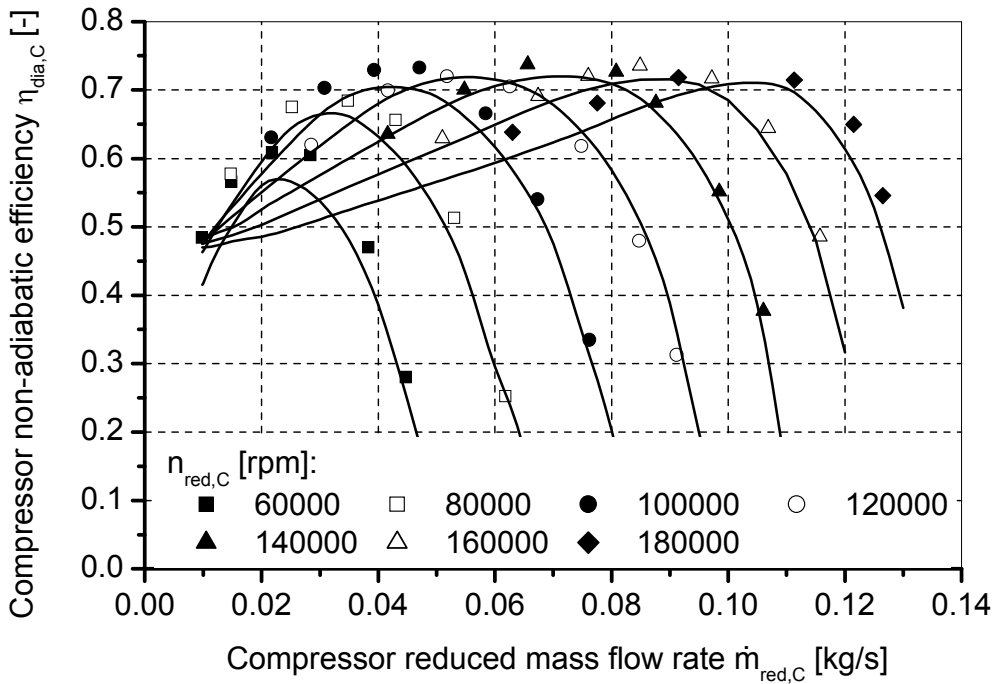


Figure A-90 Estimated compressor non-adiabatic efficiency using the cold measurements as input to the program

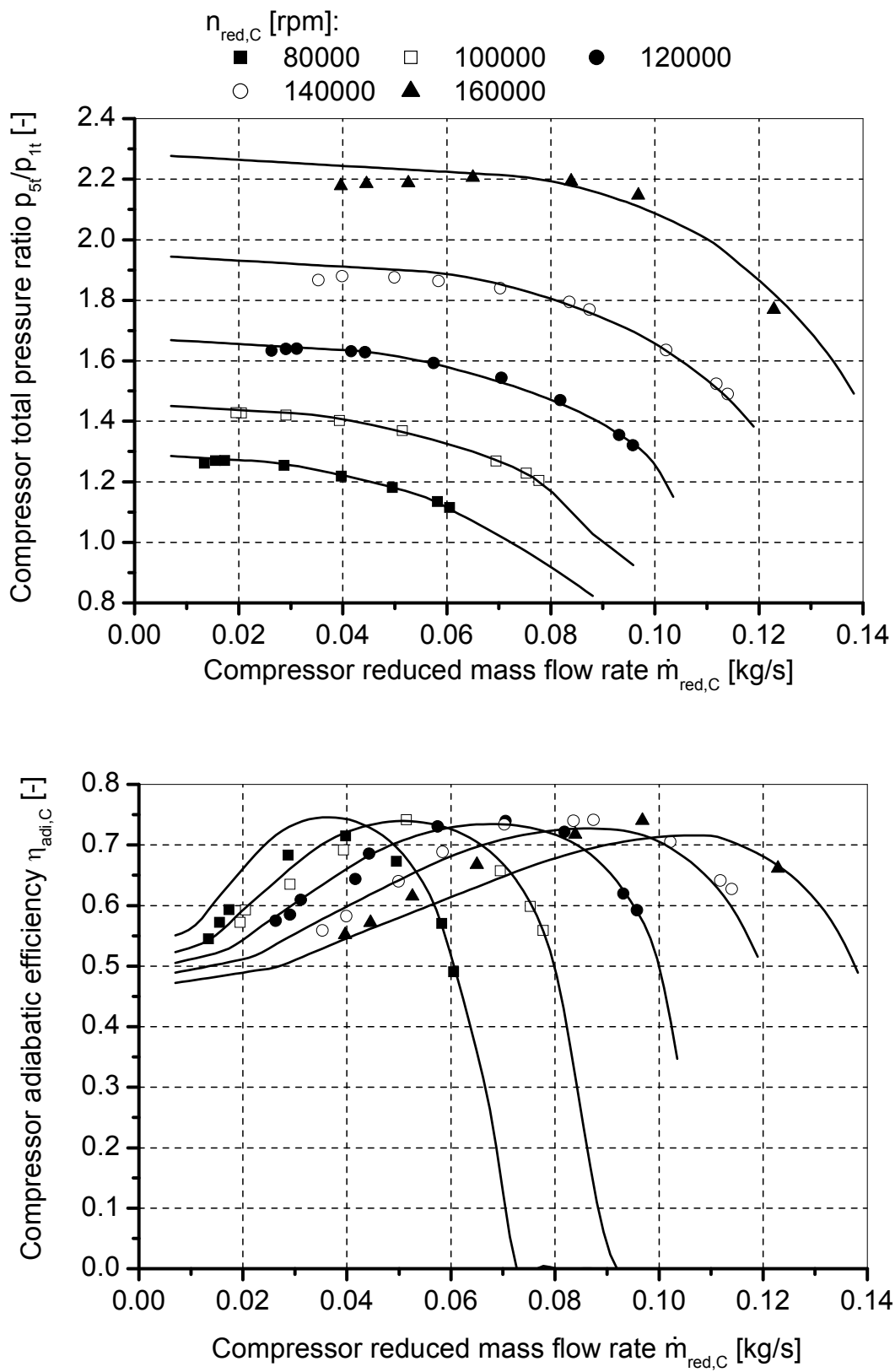


Figure A-91 Extended compressor performance map for the GT1749V 55 Trim compressor

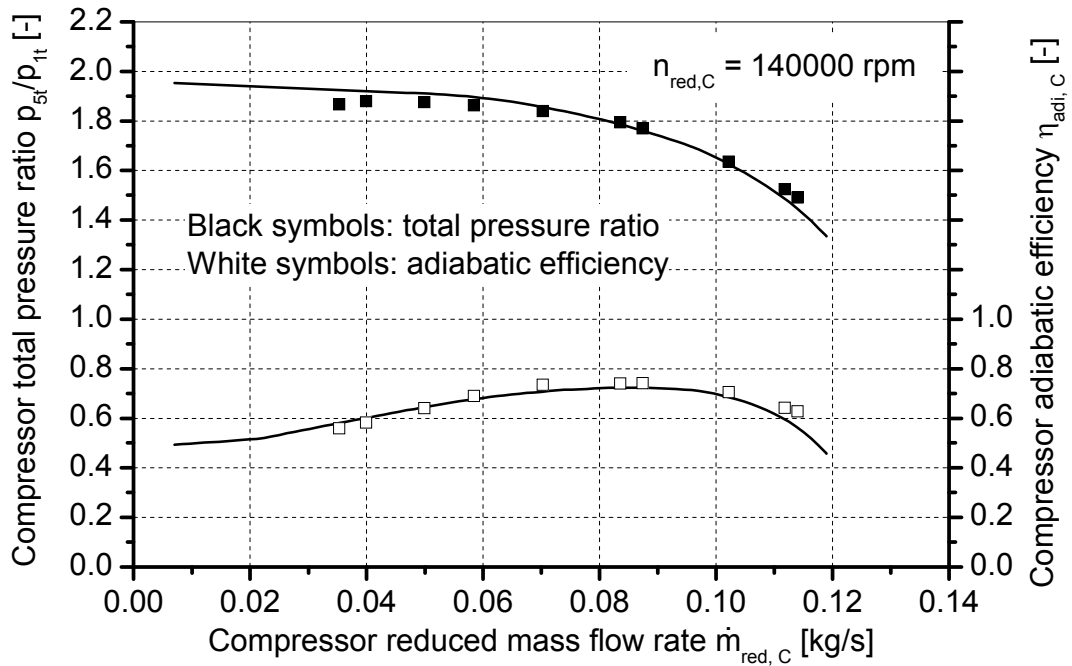


Figure A-92 Comparison between the interpolated performance line and the measured performance line of the GT1749V 55 Trim compressor at 140000 rpm

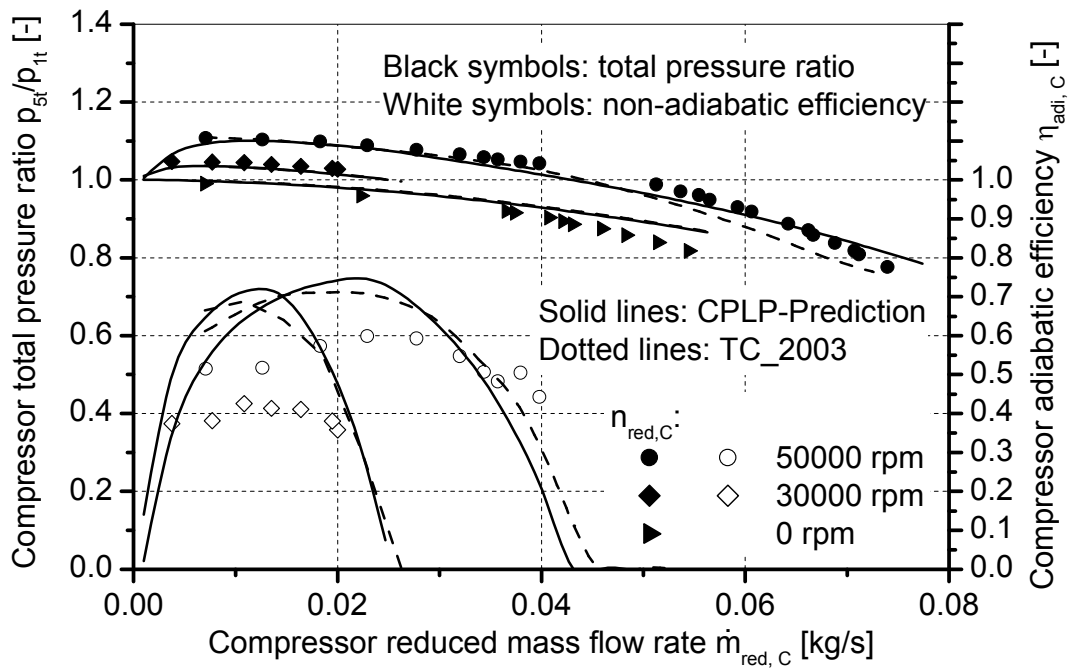


Figure A-93 Estimated compressor performance of the GT1749V 55 Trim compressor at very low rotational speeds and compressor operation in the forth quadrant of the map

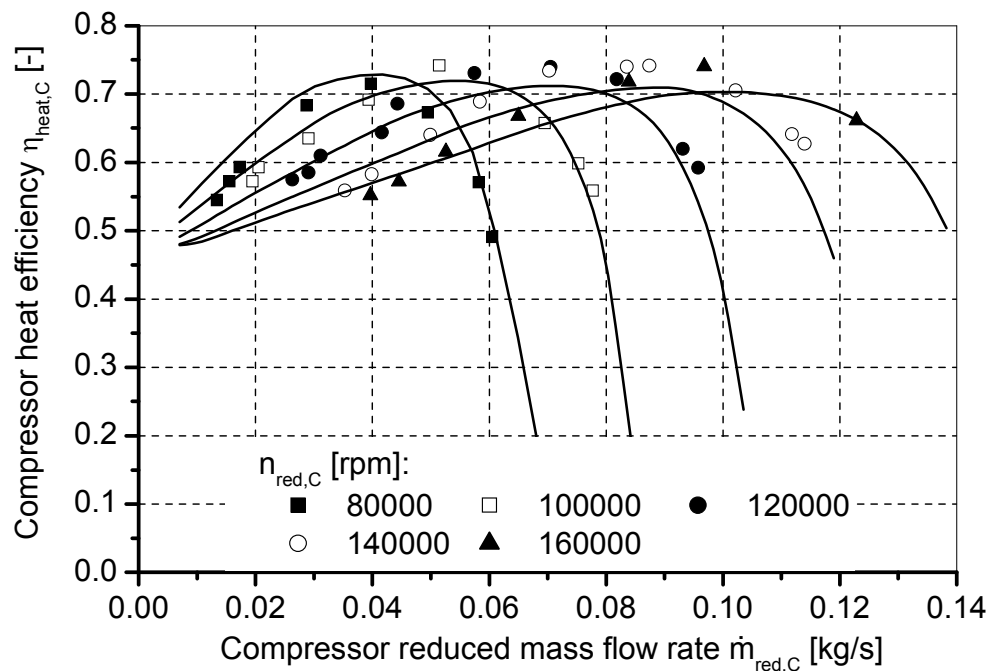


Figure A-94 Estimated compressor heat efficiency using the hot measurements as input to the program for the GT1749V 55 Trim compressor

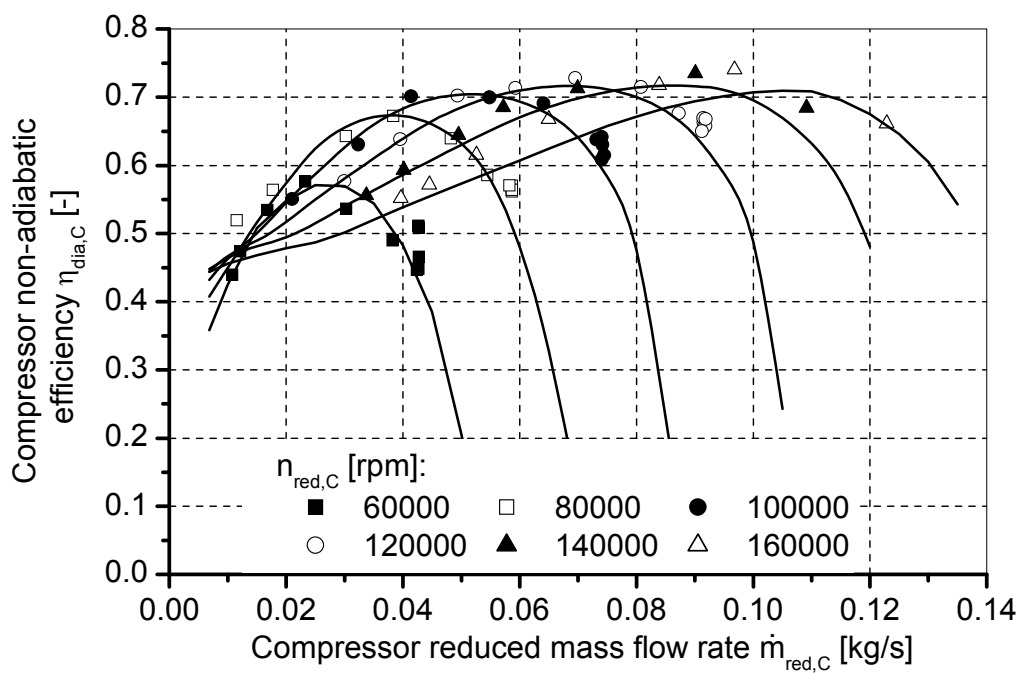


Figure A-95 Estimated compressor non-adiabatic efficiency using the cold measurements as input to the program for the GT1749V 55 Trim compressor

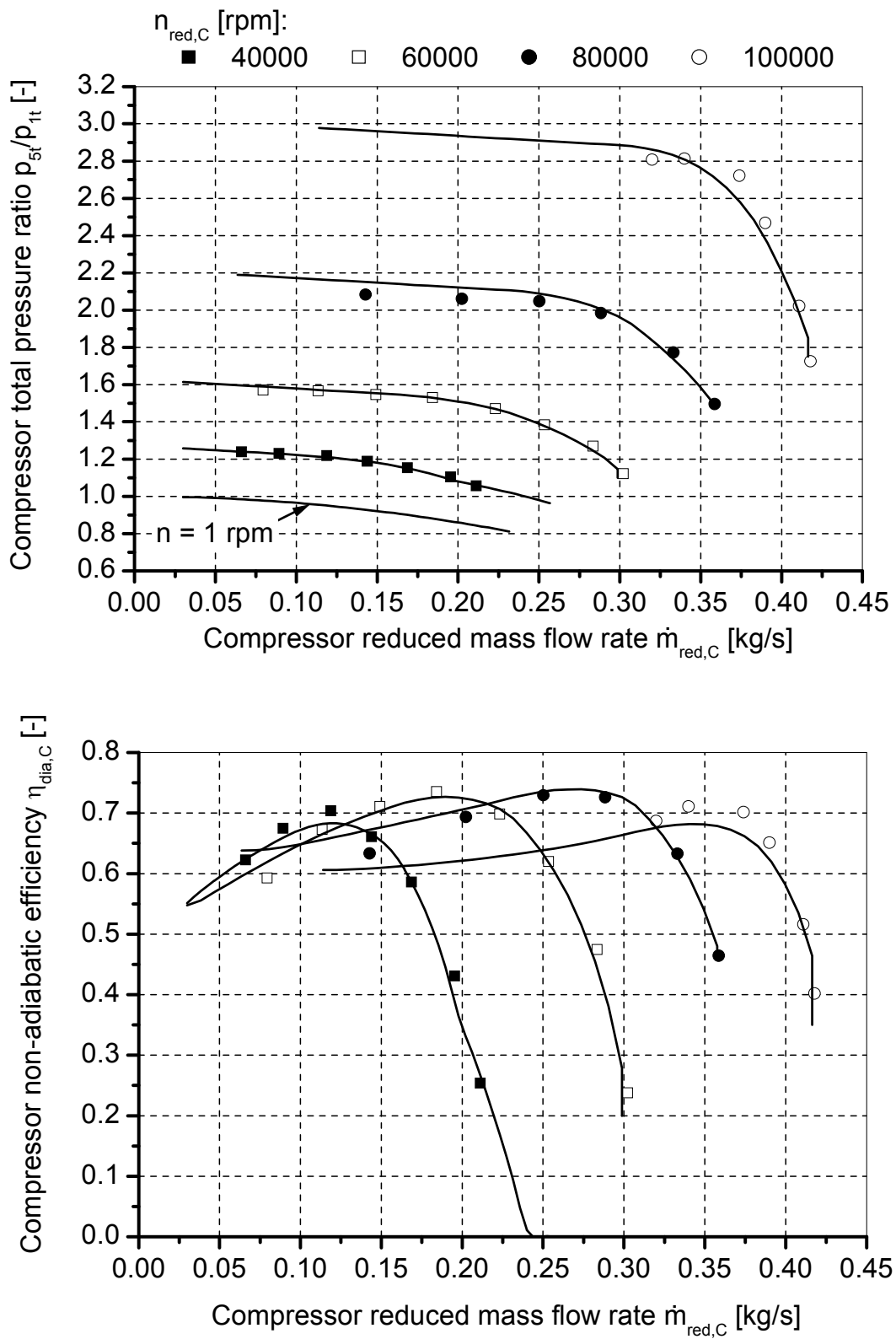


Figure A-96 Extended compressor performance map for the K29 compressor

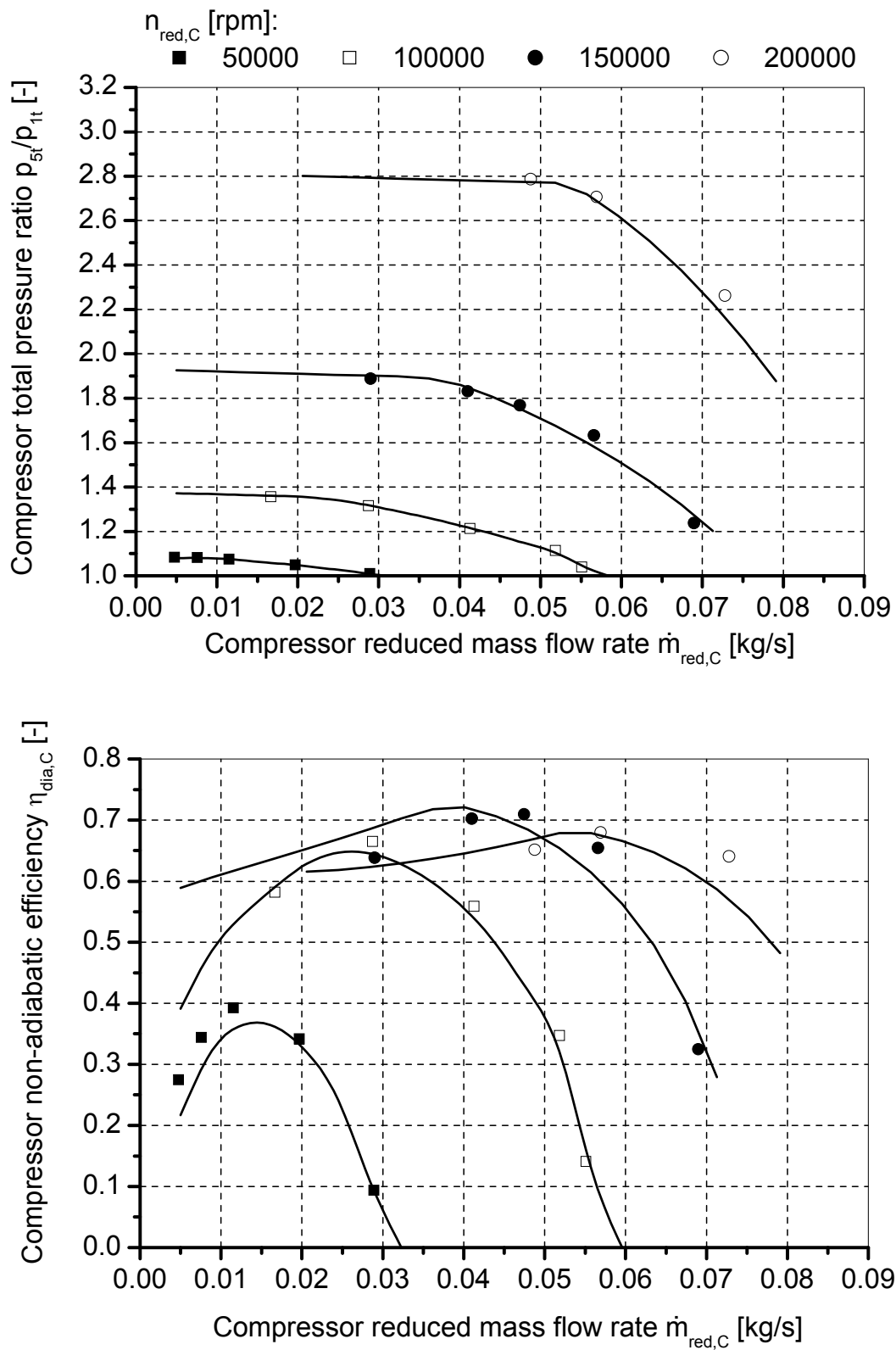


Figure A-97 Extended compressor performance map for the VNT12 compressor

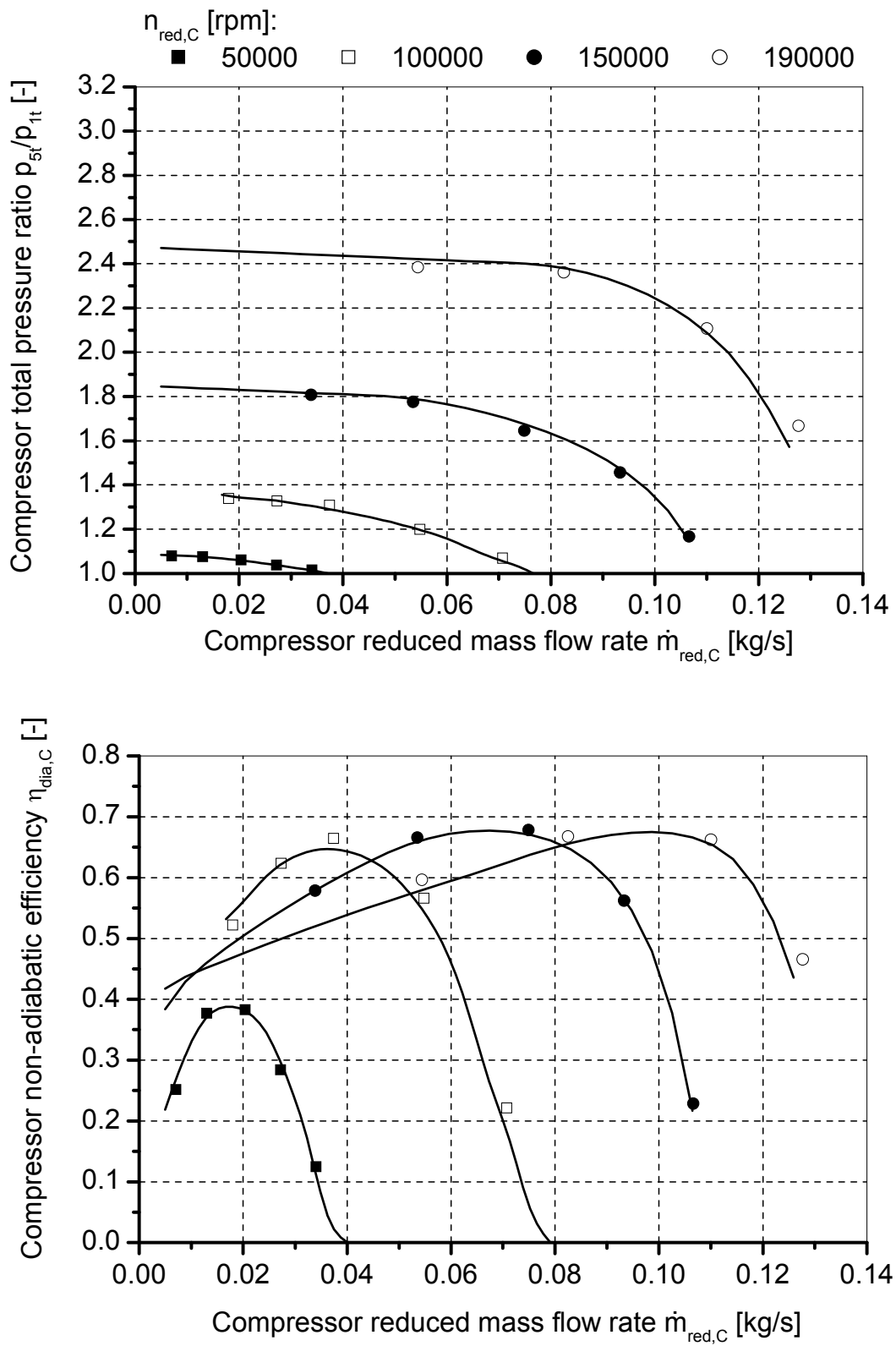


Figure A-98 Extended compressor performance map for the K03 compressor

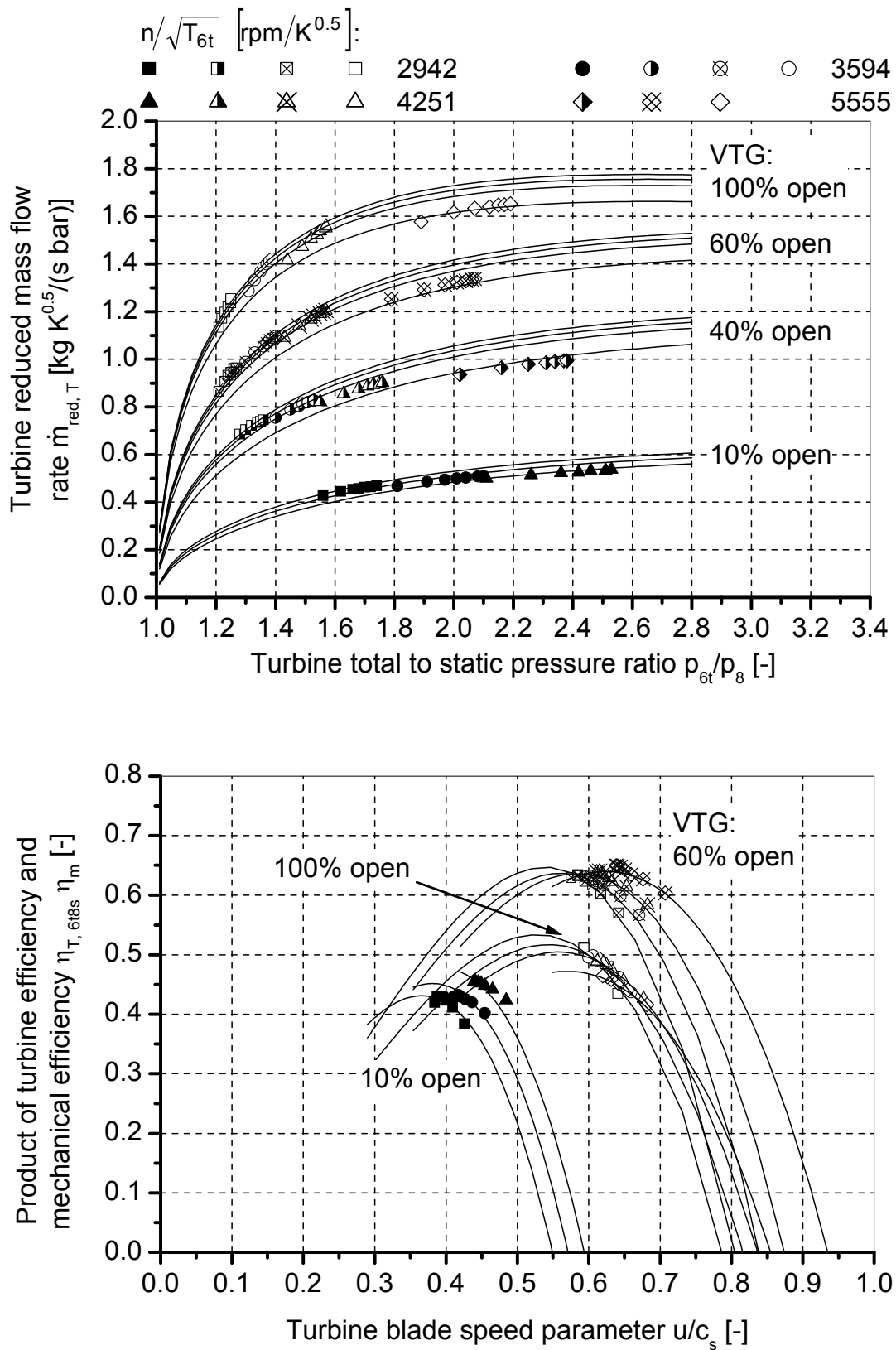


Figure A-99 Extended turbine performance map of the GT1749V 55 Trim turbine at an exhaust gas temperature 873 K

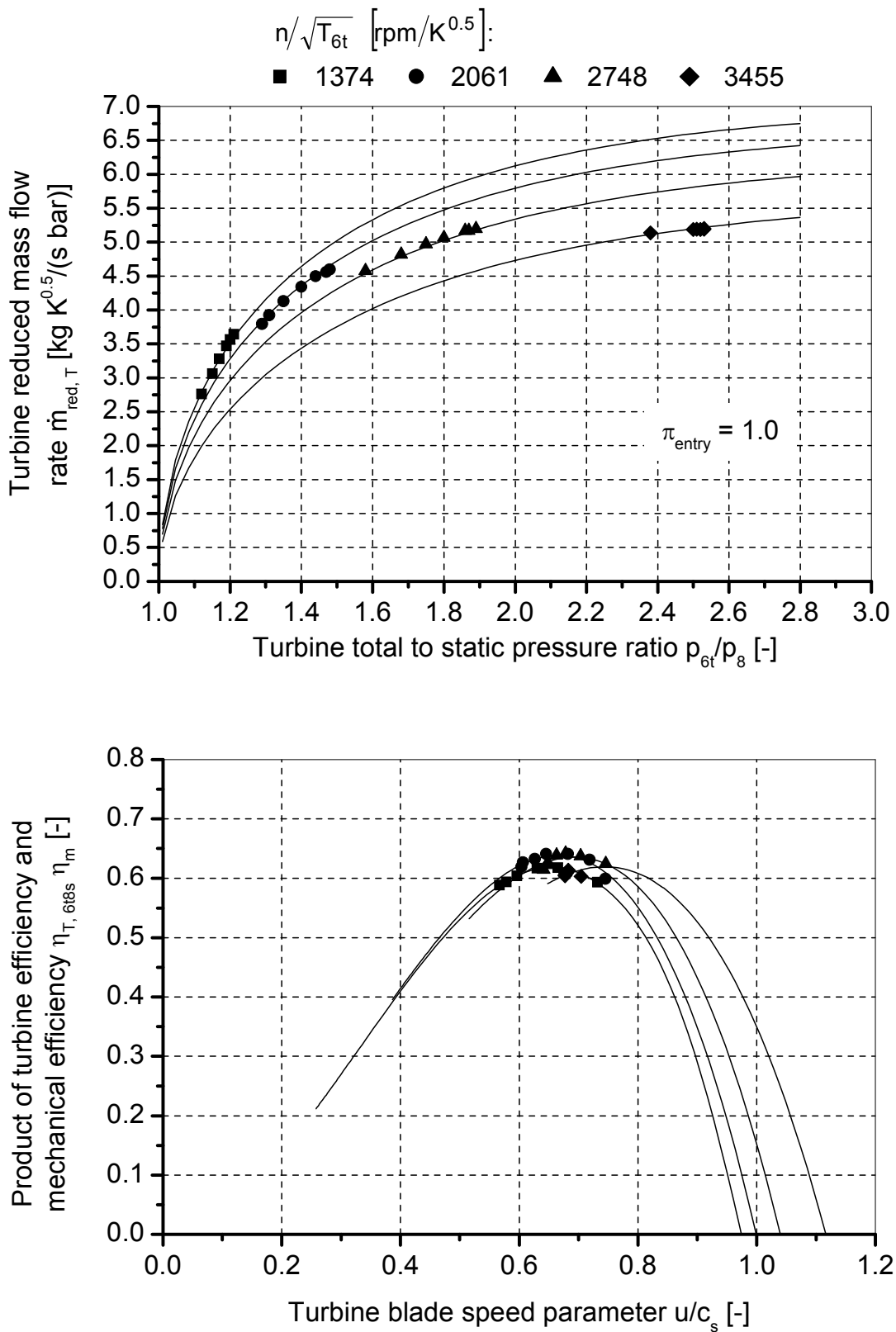


Figure A-100 Extended turbine performance map of the K29 turbine at an exhaust gas temperature 873 K and entry pressure ratio $\pi_{\text{entry}}=1$

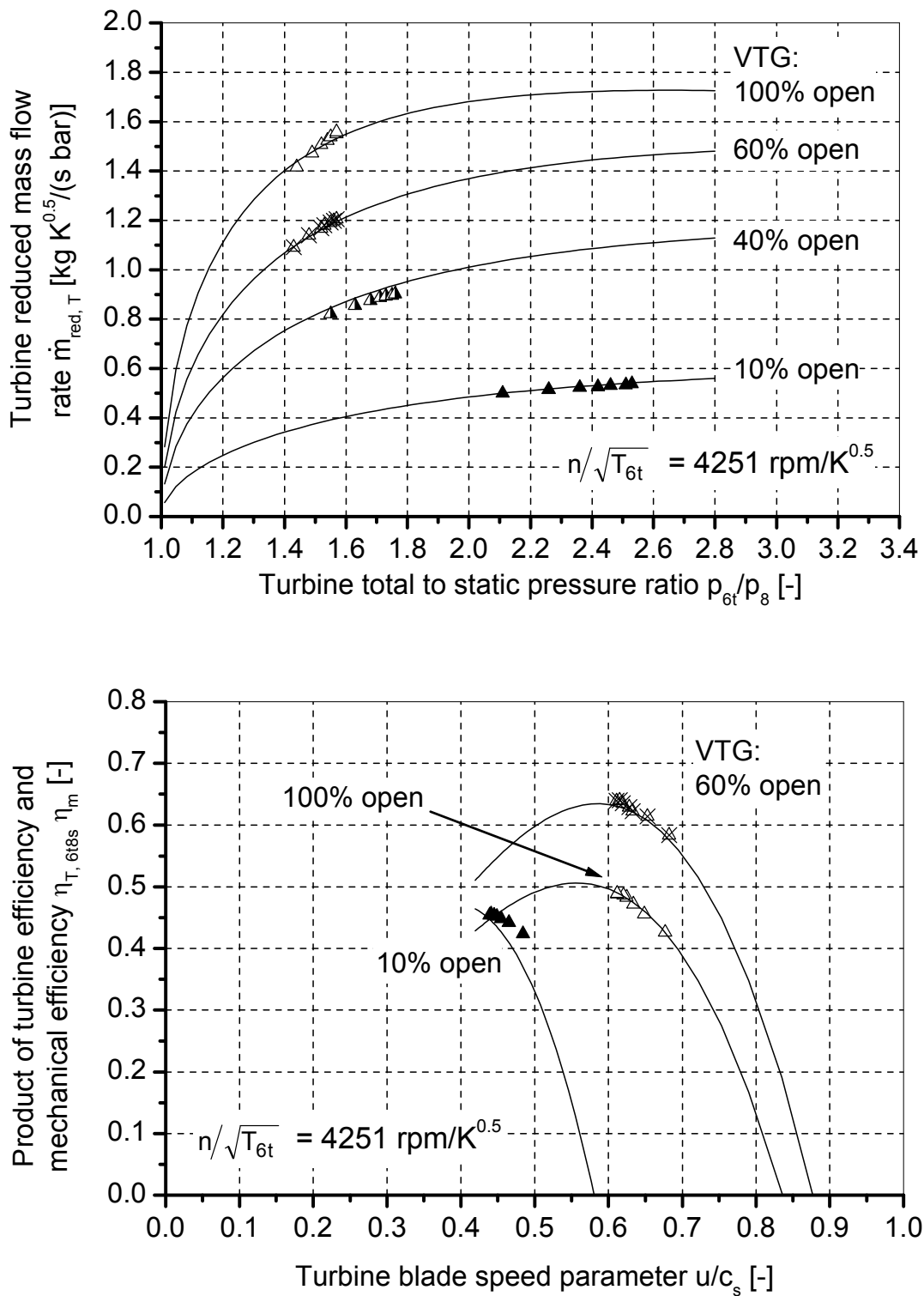


Figure A-101 Comparison between the measured turbine performance lines and the interpolated performance lines for the GT1749V 55 trim turbine

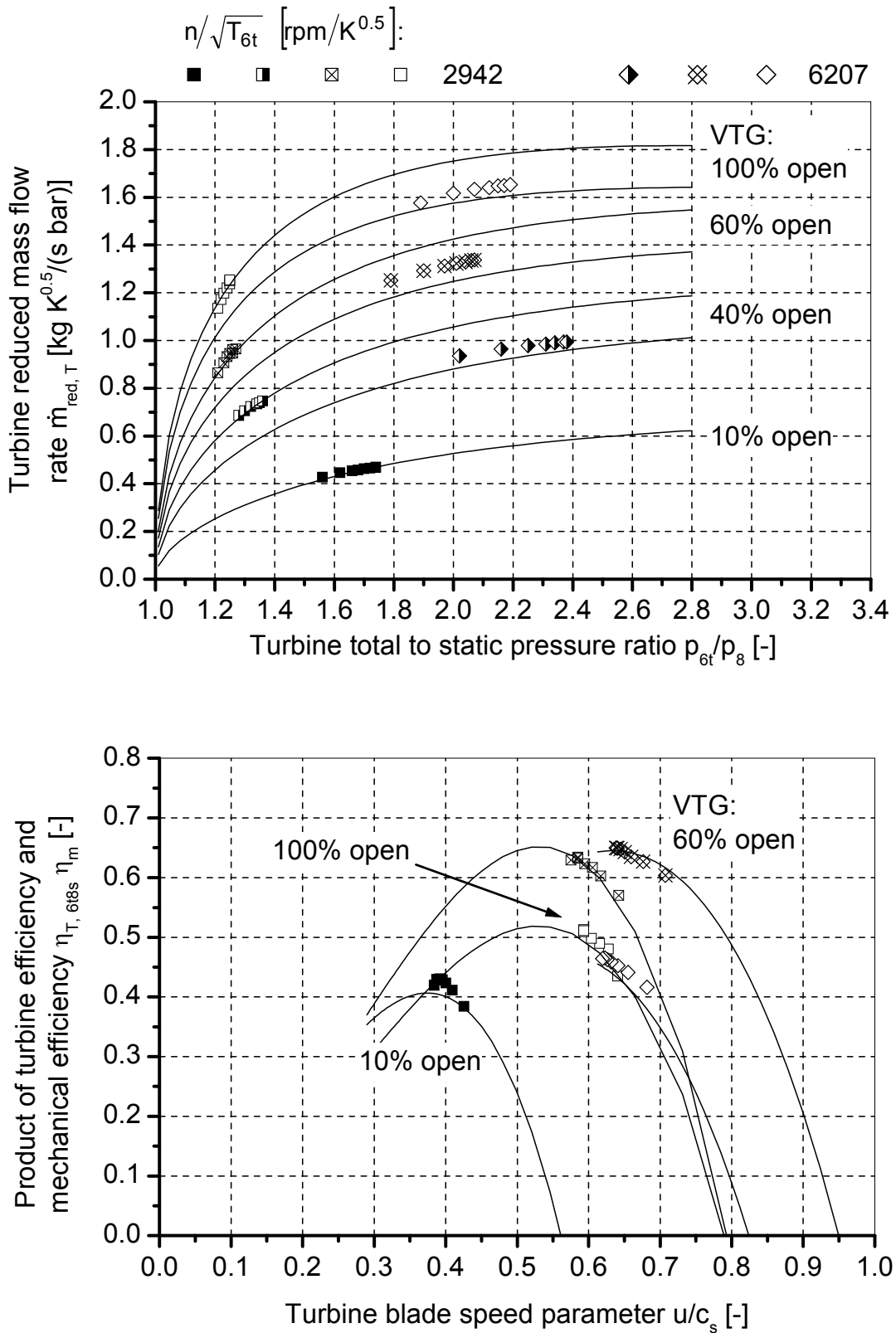


Figure A-102 Comparison between the measured turbine performance lines and the extrapolated performance lines for the GT1749V 55 trim turbine

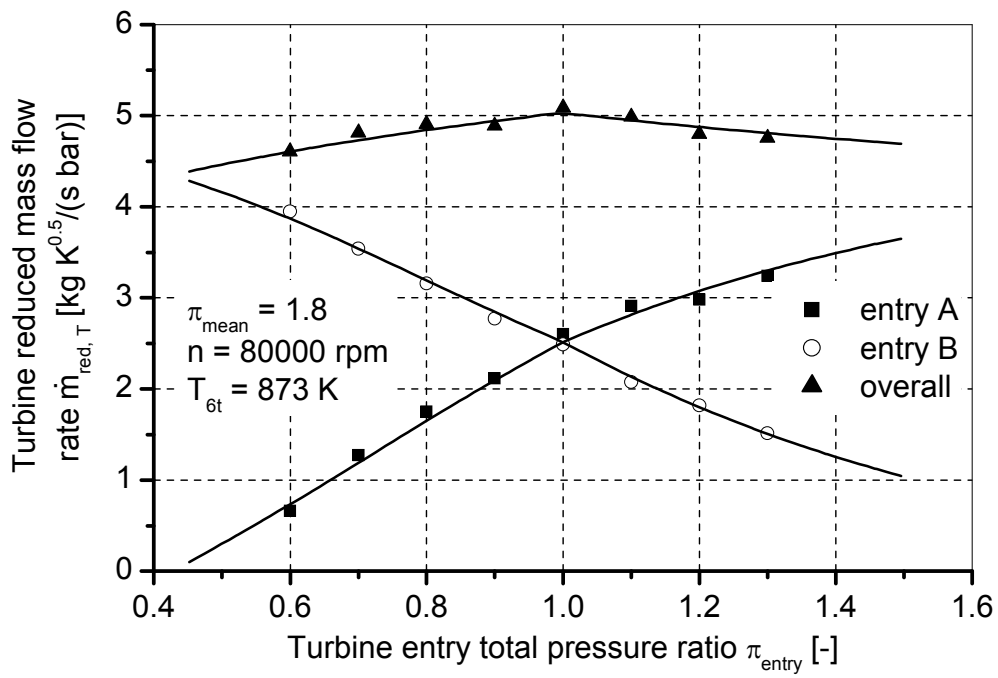


Figure A-103 Comparison between the measured turbine mass flow rate and the extrapolated mass flow rate for the K29 turbine under partial admission conditions

References

Aungier, R.H. (1995): Mean Streamline Aerodynamic Performance Analysis of Centrifugal Compressors. ASME Journal of Turbomachinery, Vol. 117, pp. 360-366.

Aungier, R.H. (2000): Centrifugal Compressors; a Strategy for Aerodynamic Design and Analysis. ASME PRESS, New York, ISBN 0 7918 0093 8.

Baar, R.; Lücking, M. (2002): Anforderung an zukünftige PKW-Aufladesysteme auf Basis der Energiebilanz eines Turboladers. 8. Aufladetechnische Konferenz, October 1-2, Dresden, Germany, pp. 243-264.

Baines, N.C. (1998): A Meanline Prediction Method for Radial Turbine Efficiency. IMechE 6th International Conference on Turbocharging and Air Management Systems, Paper No. C554/006/98, London, UK.

Balje, O.E. (1981): Turbomachines; a Guide to Design, Selection, and Theory. JOHN WILEY & SONS, New York, ISBN 0 471 06036 4.

Beckwith, T.G.; Buck, N.L.; Marangoni, R.D. (1982): Mechanical Measurements. 3rd Edition, Addison-Wesley Publishing Company, Reading, Massachusetts.

Bohn, D.; Heuer, T.; Moritz, N.; Wolff, M. (2003a): Modellierung des Wärmeflusses im und am System Turbolader. Final Report for Forschungsvereinigung Verbrennungskraftmaschinen FVV, FVV Project number 755, Heft 760.

Bohn, D.; Heuer, T.; Kusterer, K. (2003b): Conjugate Flow and Heat Transfer Investigation of a Turbocharger: Part I: Numerical Results. Proceedings of ASME Turbo Expo, Paper No. GT2003-38445, June 16-19, 2003, Atlanta, USA.

Bohn, D.; Heuer, T.; Kusterer, K. (2003c): Conjugate Flow and Heat Transfer Investigation of a Turbocharger: Part II: Experimental Results. Proceedings of ASME Turbo Expo, Paper No. GT2003-38449, June 16-19, 2003, Atlanta, USA.

Bulaty, T. (1974): Spezielle Probleme der schrittweisen Ladungswechselrechnung bei Verbrennungsmotoren mit Abgasturboladern. MTZ Motortechnische Zeitschrift 35 (1974) 6, pp. 177-185.

Busemman, A. (1928): Das Förderhöhenverhältnis radialer Kreiselpumpen mit logarithmisch-spiraligen Schaufeln. Zeitschrift für angewandte Mathematik und

Mechanik ZAMM, Vol. 8, pp. 372-384.

Came, P.M.; Swain, E.; Robinson, C.J.; Rutherford, M. S. (1996): An Integrated System for the Design of Radial Compressors and Turbines. IMechE 3rd International Conference on Computers in Reciprocating Engines and Gas Turbines, Paper No. C449/022, January 6-9, 1996, London, UK.

Challen, B.; Baranescu, R. (1999): Diesel Engine Reference Book. Butterworth-Heinemann, ISBN 0 7506 2176 1.

Chapman, K.S.; Nguru, R.; Shultz, J. (2002): Simplified Methodology to Correct Turbocharger Field Measurements for Heat Transfer and Other Effects. Final Report for Gas Research Institute, GRI-02/0156.

Chapman, K.; Brentano, T. (2000): Variable Geometry Turbocharger Shows Promise in Lab Evaluations. Pipe Line & Gas Industry Features, Vol. 83, No. 7, July, 2000.

Chen, H.; Winterbone, D.E. (1990): A Method to Predict Performance of Vaneless Radial Turbines under Steady and Unsteady Flow Conditions. IMechE 4th International Conference on Turbocharging and Turbochargers, Paper No. C405/008, May 22-24, London, UK.

Chesse, P.; Hetet, J.F.; Tauzia, X. (2000): Performance Simulation of Sequentially Turbocharged Marine Diesel Engines with Application to Compressor Surge. Journal of Engineering for Gas Turbines and Power, Vol. 122, pp. 562-569.

Daily, J.W.; Nece, R.E. (1960): Chamber Dimension Effects on Induced Flow and Frictional Resistance of Enclosed Rotating Discs. Trans. ASME, Journal of Basic Engineering, Vol. 82, pp. 217-232.

Denton, J.D. (1993): Loss Mechanisms in Turbomachines. AMSE Journal of Turbomachinery, Vol. 115, pp. 621-656.

Dou, H.S.; Mizuki, S. (1998): Analysis of the Flow in Vaneless Diffusers with Large Width-to-Radius Ratios. ASME Journal of Turbomachinery, Vol. 120, pp. 193-201.

Eckardt, D. (1980): Flow Field Analysis of Radial and Backswept Centrifugal Compressor Impellers; Part I: Flow Measurements Using a Laser Velocimeter. ASME 25th Annual International Gas Turbine Conference and Exhibit and the 22nd Annual Fluids Engineering Conference, March 9-13, Louisiana, USA, pp. 77-86.

Engeda, A. (1987): Untersuchungen an Kreiselpumpen mit offenen und geschlossenen Laufrädern im Pumpen- und Turbinenbetrieb", PhD Thesis, University of Hanover, Germany.

Fiaschi, D.; Manfrida, G.; Milani, A. (2001): A Systematic Analysis of Centrifugal Compressor Stages. 4th European Conference on Turbomachinery, March 20-23, Firenze, Italy, pp. 343-353.

Flotho, A.; Oelschlegel, H.; Schmidt, E.; Sumser, S. (2000): Turboaufladung für moderne Nutzfahrzeugmotoren. Haus der Technik e.V., Veranstaltungsunterlagen: Aufladung von Verbrennungsmotoren, March 30-31, Berlin, Germany.

General Electric (1943): The Turbosupercharger and the Airplane Power Plant. Technical Manual TM 1-404.

Ghasemi, S.; Shirani, E.; Benisi, A.H. (2002): Performance Prediction of Twin-Entry Turbocharger Turbines. Proceedings of ASME Turbo Expo, Paper No. GT-2002-30576, June 3-6, Amsterdam, Netherlands.

Gravdahl, J.T.; Egeland, O.; Vatland, S. (2002): Drive Torque Actuation in Active Surge Control of Centrifugal Compressors. *Automatica*, 38(11), pp. 1881-1893.

Gyarmathy, K. (1983): How does the Compres Pressure Wave Supercharger Work?. SAE Technical Paper Series 830234, International Congress & Exposition, Feb. 28-Mar. 4, Detroit, Michigan, USA.

Hagelstein, D.; Beyer, B.; Lübke, H.P.; Hasemann, H.; Baar, R.; Rautenberg M. (2000): Thermodynamik und Energietransport bei Abgasturboladern unterschiedlicher Regelungen. Haus der Technik E.V., Veranstaltungsunterlagen: Aufladung von Verbrennungsmotoren, March 30-31, Berlin, Germany.

Hagelstein, D.; Beyer, B.; Seume, J.; Haseman, H.; Rautenberg, M. (2002): Heuristical View on the Non-adiabatic Coupling System of Combustion Engine and Turbocharger. IMechE International Conference on Turbocharging and Turbochargers, London, UK.

Hagelstein, D.; Hillewaert, K.; Van den Braembussche, R.; Engeda, A.; Keiper, R.; Rautenberg, M. (2000): Experimental and Numerical Investigation of the Flow in a Centrifugal Compressor Volute. *ASME Journal of Turbomachinery*, Vol. 122, pp. 22-29.

Harada, H. (1988): Performance Characteristics of Two- and Three-Dimensional Impellers in Centrifugal Compressors. ASME Journal of Turbomachinery, Vol. 110, pp. 110-114.

Hemmerlein, N. (1994): Exhaust Gas Turbocharged SI Engines and their Ability of Meeting Future Demands. ImechE International Conference of Turbochargers and Turbocharging, Paper No. C484/039, June 7 – 9, London, UK.

Heyes, F.J.G. (1998): The Aerodynamic Design of the NAPIER 297 Compressor. IMechE 6th International Conference on Turbocharging and Air Management Systems, Paper No. C554/032/98, November 3-5, London, UK.

Hild, O.; Schlosser, A.; Fieweger, K.; Deutsch, G. (1998): PKW-Dieselmotor mit Abgasturboaufladung, variabler Turbinengeometrie/Abgasrückführung", Final Report for Forschungsvereinigung Verbrennungskraftmaschinen FVV, FVV Project number 651, Heft 665.

İçingür, Y.; Haşimoğlu, C.; Salman, S. (2003): Effect of Compex Supercharging on Diesel Emissions", Elsevier Science Ltd, Energy Conversion and Management, Vol. 44, pp. 1745-1753.

Japikse, D. (1984): Turbomachinery Diffuser Design Technology. Concepts ETI, Inc., ISBN 0 933283 00 8.

Japikse, D. (1996): Centrifugal Compressor Design and Performance. Concepts ETI, Inc., ISBN 0 933283 03 2.

Japikse, D. (2000): Characteristics of a Radial Inflow Turbine with Internal Component Measurements; Part I; Data Review. Proceedings of ASME Turbo Expo, Paper No. 2000-GT-0471, May 8-11, Munich, Germany.

Kirchhofer, H. (1977): Aufladung von Fahrzeugdieselmotoren mit Compex. Automobil-Industrie, No. 1.

Kirchhofer, H.; Spinnler, F. (1986): Druckwellenlader und kleinvolumiger Personenwagen-Dieselmotor für sparsames Fahren bei guter Fahrleistung. ATZ Automobiltechnische Zeitschrift 88 (1986) 4.

Kolmanovsky, I.; Moraal, P.; Nieuwstadt, M; Stefanopoulou, A.G. (1999): Issues in Modeling and Control of Intake Flow in Variable Geometry Turbocharged Engines. Hall/CRC Research Notes in Mathematics, pp. 436-445.

Kolmanovsky, I.; Stefanopoulou, A.G. (2000): Evaluation of Turbocharger Power Assist System Using Optimal Control Techniques. Society of Automotive Engineers SAE, Paper No. 2000-01-0519.

Kouremenos, D.A.; Hountalas, D.T.; Kotsiopoulos, P.N. (1994): Computer Simulation of Turbocharged Marine Diesel Engines and its Application for Engine and Turbocharger Diagnosis. IMechE Conference on Turbocharging and Turbochargers, Paper No. C484/008, pp. 13-20, London, UK.

Kurzke, J. (1996): How to Get Component Maps for Aircraft Gas Turbine Performance Calculations. ASME International Gas Turbine and Aeroengine Congress and Exhibition, Paper No. 96-GT-164.

Linnhoff, H.J. (1985): Die Berechnung des Ladungswechsels und Ansprechverhaltens von Verbrennungsmotoren mit Abgasturboaufladung. PhD Thesis, Ruhr-University of Bochum, Germany.

Logan, E.J. (2003): Handbook of Turbomachinery. 2nd edition, Marcel Dekker Inc., New York, ISBN 0 8247 0995 0.

Lohmberg, A.; Casey, M.; Ammann, S. (2001): Transonic Radial Compressor Inlet Design. 4th European Conference on Turbomachinery, March 20-23, Firenze, Italy, pp. 75-85.

Lüdtke, K. (1989): Industrial Centrifugal Compressors: The Influence of the Impeller Diffusion on the Stage Performance. ASME Conference on Gas Turbine and Aeroengine Congress and Exposition, Paper No. 89-GT-233, June 4-6, Toronto, Canada.

Lüdtke, K. (1999): Process Centrifugal Compressors - Latest Improvements of Efficiency and Operating Range. IMechE Transactions, Paper No. C556/014, pp. 219-234.

Malobabic, M. (1989): Das Betriebsverhalten leitschaufel- und bypassgeregelter PKW-Abgasturbolader. PhD Thesis, University of Hannover, Germany.

Malobabic, M.; Mobarak, A.; Rautenberg, M. (1983): Influence of heat transfer between turbine and compressor on the performance of small turbochargers. GTSJ International Gas Turbine Congress, pp. 566-574, Tokyo, Japan.

Malobabic, M.; Rautenberg, M. (1985): On Turbochargers with Variable Geometry.

ASME Gas Turbine Conference and Exhibit, Paper No. 85-GT-149, March 18-21, Texas, USA.

Malobabic, M.; Rautenberg, M. (1987): Adiabatic and Non-adiabatic Efficiencies of Small Turbochargers. International Gas Turbine Congress, Paper No. 87-Tokyo-IGTC-105, pp. 57-64, October 26-31, Tokyo, Japan.

Martin, C.S. (1983): Representation of Pump Characteristics for Transient Analysis. ASME Symposium on Performance of Hydraulic Turbines and Pumps, pp. 1-13, Boston, USA.

Martin, C.S. (2000): Water Hammer Potential in Pumps and Systems. Randall Publishing, Pumps & Systems magazine.

Mayer, A. (1981): Compres-supercharging for Vehicle Diesel Engines. Diesel and Gas Turbine Progress, May 1981.

Meese, H.M.; Swain, E. (2001): Analysis of Two Automotive Turbocharger Compressor Radial Vaneless Diffusers for Use in Improving a Performance Prediction Technique. Proceedings of ASME Turbo Expo, Paper No. 2001-GT-0319, June 4-7, Louisiana, USA.

Merker, G.P.; Kessen, U. (1999): Technische Verbrennung, Motorische Verbrennung. B. G. Teubner Stuttgart. Leipzig, ISBN 3 519 06381 6.

Merker, G.P.; Stiesch, G. (1999): Technische Verbrennung, Verbrennungsmotoren. B. G. Teubner Stuttgart. Leipzig, ISBN 3 519 06379 4.

Miersch, J.; Reulein, C.; Schwarz, C. (2000): Weiterentwicklung der Prozessrechnung für aufgeladene Ottomotoren. Haus der Technik; Aufladung von Verbrennungsmotoren, March 30-31, Berlin, Germany.

Mueller, M.; Hendricks, E.; Sorenson, S. C. (1998): Mean Value Modeling of Turbocharged Spark Ignition Engines. International Congress Exposition, Paper No. 980784, pp. 125-145.

Oh, J. (2001): Analysis of 8 Centrifugal Compressor Impellers Using Two Different CFD Methods; Part II: Blockage and Slip Characteristics. Proceedings of ASME Turbo Expo, Paper No. 2001-GT-0327, June 4-7, Louisiana, USA.

Oh, J.; Oh, K. (2000): Numerical Modeling of Some Parameters for Performance

Prediction of Centrifugal Impellers. ASME Turbo Expo, Paper No. 2000-GT-458, May 8-11, Munich, Germany.

Pischinger, F.; Wuensche, A. (1978): Untersuchung des Durchstroem- und Wirkungsgradverhaltens teilbeaufschlagter Abgasturbinen und des Einflusses dieser Randbedingungen auf das Betriebsverhalten abgasturboaufgeladener Verbrennungsmotoren; 1. Teilabschlussbericht: Das charakteristische Verhalten von kleinen Abgasturbinen und sein Einfluss auf den Arbeitsprozess von Dieselmotoren. Forschungsvereinigung Verbrennungskraftmaschinen FVV, FVV Project number 157, Heft 246.

Poling, B.E.; Prausnitz, J.M.; O'Connell, J.P. (2001): The Properties of Gases and Liquids. 5th Edition, McGraw Hill, ISBN 0 07 011682 2.

Press, W.H.; Teukolsky, S.A.; Vetterling, W.T.; Flannery, B.P. (1992): Numerical Recipes in Fortran, the Art of Scientific Computing. 2nd Edition, Cambridge University Press, ISBN 0-521-43064-X.

Pucher, H. (2000): Grundlagen der Aufladetechnik. Haus der Technik e.V., Veranstaltungsunterlagen: Aufladung von Verbrennungsmotoren, March 30-31, Berlin, Germany.

Pucher, H.; Berndt, R.; Grigoriadis, P.; Nickel, J.; Hagelstein, D.; Berndt, B.; Seume, J. (2001): Erweiterte Darstellung und Extrapolation von Turbolader-Kennfeldern als Randbedingung der Motorprozesssimulation. FVV Informationstagung Motoren, Heft R513, September 27, Frankfurt, Germany.

Pucher, H.; Berndt, R.; Grigoriadis, P.; Nickel, J.; Hagelstein, D.; Abdelhamid, S.; Seume, J. (2003a): Erweiterte Darstellung und Extrapolation von Turbolader-Kennfeldern als Randbedingung der Motorprozesssimulation. 5th Stuttgart International Symposium, February 18-20, Stuttgart, Germany, ISBN 3 8169 2180 9, pp. 140-156.

Pucher, H.; Berndt, R.; Grigoriadis, P.; Nickel, J.; Hagelstein, D.; Abdelhamid, S.; Seume, J. (2003b): Erweiterte Darstellung und Extrapolation von Turbolader-Kennfeldern als Randbedingung der Motorprozesssimulation. Final Report for Forschungsvereinigung Verbrennungskraftmaschinen FVV, FVV Project number 754, Heft 774.

Pucher, H.; Nickel, J. (2002): Vermessung erweiterter Kennfeldbereiche von Fahrzeugmotoren-Turboladern. 8. Aufladetechnische Konferenz, pp. 321-339,

October 1-2, Dresden, Germany.

Rautenberg, M.; Ayder, E.; Hillewaert, K.; Van den Braembussche, R.; Zeoli, D.; Seidel, U.; Hagelstein, D. (1998): Strömungsvorgänge in spiralförmigen Sammelräumen für Radialverdichterstufen. Final Report for Forschungsvereinigung Verbrennungskraftmaschinen FVV, FVV Project number 606, Heft 659.

Rautenberg, M.; Hass, U.; Kassens, K.; Knapp, P.; Mobarak, A.; Siegmann, W.; Wittekind, W. (1974): Untersuchung der Laufradströmung in hochbelasteten Radialverdichterrädern. Final Report for Forschungsvereinigung Verbrennungskraftmaschinen FVV, FVV Project number 83 and 115, Heft 115.

Rautenberg, M.; Kämmer, N. (1984): On the Thermodynamics of Non-adiabatic Compression and Expansion Processes in Turbomachines. 5th International Conference for Mechanical Power Engineering, October 13-15, Cairo, Egypt.

Riegler, C.; Bauer, M.; Kurzke, J. (2000): Some Aspects of Modeling Compressor Behavior in Gas Turbine Performance Calculations. Proceedings of ASME Turbo Expo, Paper No. 2000-GT-574, May 8-11, Munich, Germany.

Rodgers, C. (1984): Static Pressure Recovery Characteristics of some Radial Vaneless Diffusers. Canadian Aeronautics and Space Journal, Vol. 30, No. 1, pp. 42-54.

Rodgers, C. (1991): The Efficiency of Single-Stage Centrifugal Compressors for Aircraft Applications. ASME International Gas Turbine and Aeroengine Congress and Exposition, Paper No. 91-GT-77, June 3-6, Orlando, USA.

Rodgers, C. (2000): Effects of Blade Number on the Efficiency of Centrifugal Compressor Impellers. ASME Turbo Expo, Paper No. 2000-GT-455, May 8-11, Munich, Germany.

Rodgers, C. (2003): The Characteristics of Radial Turbines for Small Gas Turbines. Proceedings of ASME Turbo Expo, Paper No. GT2003-38026, June 16-19, Atlanta, USA.

Schlichting, H. (1968): Boundary Layer Theory. 6th Edition, McGraw-Hill.

Senoo, Y.; Ishida, M. (1986): Pressure Loss due to the Tip Clearance of Impeller Blades in Centrifugal and Axial Blowers. ASME Journal of Engineering for Gas Turbines and Power, Vol. 108, pp. 32-37.

Senoo, Y.; Ishida, M. (1987): Deterioration of Compressor Performance due to Tip Clearance of Centrifugal Impellers. ASME Journal of Turbomachinery, Vol. 109, pp. 50-60.

Senoo, Y.; Yamaguchi, (1986): A study on Unstable S-Shape Characteristic Curves of Pump Turbines at No Flow. ASME International Gas Turbine Conference and Exhibit, Paper No. 86-GT-17, June 8-12, Düsseldorf, Germany.

Seume, J.; Van den Braembussche, R.; Prinsier, J.; Kitzinger, J.; Steglich, T. (2003): Strömungsvorgänge in spiralförmigen Sammelräumen für Radialverdichterstufen. Final Report for Forschungsvereinigung Verbrennungskraftmaschinen FVV, FVV Project number 763, Heft 773.

Shell documentation: Ermittlung thermischer Größen von Mineralölen. DSAG CMI-T Sp 11/98

Sideris, M.; Van den Braembussche, R. (1986): Influence of a Circumferential Exit Pressure Distortion on the Flow in an Impeller and Diffuser. ASME International Gas Turbine Conference and Exhibit, Paper No. 86-GT-9, June 8-12, Düsseldorf, Germany.

Sideris, M.; Van den Braembussche, R. (1987): Influence of a Circumferential Exit Pressure Distortion on the Flow in an Impeller and Vaneless Diffuser. ASME Journal of Turbomachinery, Vol. 109, pp. 48-54.

Stanitz, J.D. (1952a): One-Dimensional Compressible Flow in Vaneless Diffusers of Radial- and Mixed-Flow Centrifugal Compressors Including Effects of Friction, Heat Transfer, and Area Change. NACA TN 2610.

Stanitz, J.D. (1952b): Some Theoretical Aerodynamic Investigations of Impellers in Radial and Mixed Flow Centrifugal Compressors. Transactions of the ASME, Vol. 74, pp. 473-497.

Staudacher, S.; Linke, A.; Fiola, R. (2003): A Comparison of Methods for the Extrapolation of Turbomachinery Performance maps for the Use in Performance Synthesis Programs. 5th European Conference on Turbomachinery Fluid Dynamics and Thermodynamics, March 17-22, Czech Republic.

Stodola, A. (1945): Steam and Gas Turbines. Peter Smith, New York.

Storset, O. F.; Stefanopoulou, A.G.; Smith, R. (2000): Air Charge Estimation for

Turbocharged Diesel Engines. Proceedings of American Control Conference, pp. 39-44.

Swain, E. (1990): A Simplified Method for Predicting Centrifugal Compressor Performance Characteristics. IMechE 4th International Conference on Turbocharging and Turbochargers, Paper No. C405/040, May 22-24, London, UK.

Swain, E.; and Connor, W.A. (1992): The Use of Simple Methods to Predict the Performance of Industrial Centrifugal Compressors. VDI Report No. 947.

Swain, E.; Meese, H. (1998): Extension of a Centrifugal Compressor Performance Prediction Technique. IMechE International Conference on Turbocharging and Turbochargers, Paper No. C555/008/98, London, UK.

Taylor, C.F. (1977): The Internal Combustion Engine in Theory and Practice, Volume 1: Thermodynamics, Fluid Flow, Performance. 2nd Edition, M.I.T. Press, ISBN 0 262 70015 8.

Traupel, W. (1962): Die Theorie der Strömung durch Radialmaschinen. Verlag G. Braun, Karlsruhe.

Traupel, W. (1977): Thermische Turbomaschinen. Springer-Verlag, ISBN 0 387 07939 4.

U.S. Environmental Protection Agency (EPA) (1998): Draft Regulatory Impact Analysis: Control of Emissions from Compression-Ignition Marine Engines. EPA 420-R-98-017.

Van den Braembussche, R. (1990): Design and Optimization of Centrifugal Compressors. Course Note 141/TU, von Karman Institute for Fluid Dynamics.

Van den Braembussche, R.; Ayder, E.; Hagelstein, D.; Rautenberg, D.; Keiper, R. (1999): Improved Model for the Design and Analysis of Centrifugal Compressor Volute. ASME Journal of Turbomachinery, Vol. 121, pp. 619-625.

Watson, N.; Janota, M.S. (1982): Turbocharging the Internal Combustion Engines. The MacMillan Press Ltd., ISBN 0 333 24290 4.

Weaving, J.H. (1990): Internal Combustion Engineering: Science & Technology. Elsevier Science Ltd., ISBN 1 85166 410 6.

Werner, K. (2001): Improved Gas Turbine Performance Prediction Using a Map Based Fleet Analysis. Proceedings of ASME Turbo Expo, Paper No. 2001-GT-0032, June 4-7, Louisiana, USA.

Whitfield, A.; Baines, N.C. (1990): Design of radial turbomachines. Longman Scientific & Technical and JOHN WILEY & SONS, New York, ISBN 0 470 21667 0.

Wiesner, F.J. (1967): A Review of Slip Factors for Centrifugal Impellers. ASME Journal of Engineering for Power, Vol. 89, pp. 558-572.

Willems, F.; Jager, B. (2000): One-sided Control of Surge in a Centrifugal Compressor System. Proceedings of ASME Turbo Expo, Paper No. 2000-GT-527, May 8-11, Munich, Germany.

Zangeneh, M.; Goto, A.; Harada, H. (1998): On the Design Criteria for Suppression of Secondary Flows in Centrifugal and Mixed Flow Impellers. ASME Journal of Turbomachinery, Vol. 120, pp. 723-735.

Ziegler, K.U.; Gallus, H.E.; Niehuis, R. (2002): A Study on Impeller-Diffuser Interaction; Part II: Detailed Flow Analysis. Proceedings of ASME Turbo Expo, Paper No. GT-2002-30382, June 3-6, Amsterdam, Netherlands.

Zinner, K. (1961) Diagramm zur Bestimmung des Betriebspunktes einstufiger Abgasturbolader. M.A.N. Forschungsheft 10.

Zinner, K. (1980): Aufladung von Verbrennungsmotoren. Springer-Verlag, ISBN 3 540 10088 1.

Lebenslauf

Name: Sameh Shaaban
Geburtsdatum: 01.02.1970
Geburtsort: Kairo, Ägypten
Familienstand: verheiratet, 1 Kind

Schulausbildung:
 1975-1981 Grundschule Lethè, Kairo-Ägypten
 1981-1984 Vorbereitungsschule Elkhofa, Kairo-Ägypten
 1984-1987 Hauptschule Elkoppa, Kairo-Ägypten
 Abschluss: Abitur

Studium:
 1987-1992 Maschinenbaustudium an der Helwan Universität,
 Vertiefungsrichtung: „Mechanical power engineering“.
 Abschluss: B. Sc. Maschinenbau

Militärdienst: 10.1992-11.1993

Weitere Ausbildung:
 1994-1995 Vorbereitungsvorlesungen zur Masterarbeit an der
 Helwan Universität
 1995-1997 Masterarbeit an der Helwan Universität
 Abschluss: M. Sc. Maschinenbau
 1999 Vorbereitungsvorlesungen zur Doktorarbeit an der
 Helwan Universität

Praktika:
 1990(15 Wochen) Ministerium für Elektrizität, Nordkairo
 Ausbildungszentrum bzw. Shobra Elkhema Kraftwerk.
 1991(2 Wochen) Suez Oil Company SOCo.

Berufstätigkeit:
 12.1993-05.2000 Wissenschaftlicher Mitarbeiter an der Helwan
 Universität
 05.2000-12.2003 Gastwissenschaftler an der Universität Hannover
 seit 01.2004 Wissenschaftlicher Mitarbeiter an der Universität
 Hannover